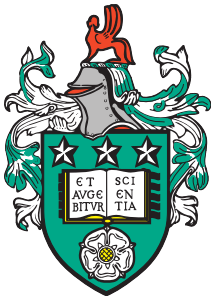
UNIVERSITY OF LEEDS

Radio Recombination Line Modelling of the Cometary Ultra-Compact HII Region DR21



Kingsley Ahenkora-Duodu

University of Leeds

School of Physics and Astronomy

Submitted in accordance with the requirements for the degree of

Doctor of Philosophy

November, 2025

This thesis is dedicated to my lovely wife, Racheal, and my beloved daughter, Racheal.

Intellectual Property Statement

The candidate confirms that the work submitted is his own and that appropriate credit has been given where reference has been made to the work of others.

This copy has been supplied on the understanding that it is copyright material and that no quotation from the thesis may be published without proper acknowledgement.

The right of Kingsley Ahenkora-Duodu to be identified as Author of this work has been asserted by him in accordance with the Copyright, Designs and Patents Act 1988.

© 2025 The University of Leeds and Kingsley Ahenkora-Duodu.

Acknowledgements

First and foremost, I give all glory and thanks to God Almighty for granting me strength, good health, and perseverance throughout my PhD journey. This path has been far from easy, but through God's unfailing grace and mercy, I have come this far.

I would like to express my deepest gratitude to my supervisor, Prof. Melvin Hoare, for his exceptional guidance, patience, and unwavering support throughout my studies. You have been not only an outstanding mentor but also a father figure and a true friend. I am sincerely grateful for the many opportunities you have provided me and for your encouragement during the most challenging periods of my research, particularly during the COVID-19 pandemic and the painful loss of my beloved daughter, Deborah. I am equally thankful to my co-supervisor, Prof. Julian Pittard, for his insightful guidance, constructive feedback, and for developing the hydrodynamic and radiative transfer code "HOPE", which has been instrumental in shaping the success of this work.

My heartfelt appreciation also goes to the DARA (Development in Africa with Radio Astronomy) project for sponsoring my studies and providing invaluable training and travel opportunities that enriched my academic experience.

To the staff and faculty of the School of Physics and Astronomy at the University of Leeds, I extend my sincere thanks for their assistance and for creating a supportive academic environment. I also wish to acknowledge my colleagues, both past and present, for their collaboration, encouragement, and friendship, which have made this journey a memorable one.

Finally, I express my deepest gratitude to my family and friends for their endless prayers, love, and encouragement. To my wonderful wife, Racheal, thank you for your unwavering love, patience, and joy. Your support and faith in me have been my greatest strength. To my precious baby girl, Racheal, named after my beautiful wife, you are

deeply loved, and you will always hold a special place in our heart. May God richly bless you all.

Abstract

This thesis presents the inaugural hydrodynamic modelling of cometary ultra-compact (UC) HII regions, with a direct comparison to observational kinematic data. The hydrodynamic models were applied to the cometary UCHII region DR21, offering the most precise comparison to date of the velocity structure of such regions. In these models, the star is offset from the cloud core, incorporating stellar winds and parameters specific to DR21. Through logical deduction, the density power law index value, α, was determined to be 1.0, the distance from the star to the cloud core, Rs, was 0.07 pc, and the initial number density at the star location, n_o, was 1.28×10^5 cm^{-3}. The thermal dust continuum emission from DR21 at 450μm was modelled to find the best-fit value for the density power law index. By overlaying and comparing the radio and dust continuum emissions of both the observed DR21 and the models, the distance between the star and the cloud core, Rs, was further validated. The cometary DR21 was determined to be 5 kyr old by comparing the model size to observations. The spectral energy distribution (SED) of the model and its turnover frequency fit the required density. The RRL radiative transfer code, developed by Steggles, was tested, modified, and compared to DR21 UCHII region observations. After identifying and correcting bugs in the code, the emission measure values obtained were consistent with literature test cases. Tests for expanding and contracting ionised gas under LTE and non-LTE conditions aligned well with previous literature results. The modified RRL radiative code modelled the radio recombination lines of the cometary UCHII region DR21, focusing on its velocity structure. Moment maps, position-velocity diagrams, and line profiles for both the observed DR21 and the models were examined within the context of DR21's cometary morphology. A comparison of the velocity structure for the observed DR21 and models projected at 30°, 45° and 60° showed reasonable agreement in the main body of the UCHII region, albeit with a $\approx$

5 km s^{-1}. This highlights the necessity for accurate stellar motion representation and support for the hybrid picture.

Contents

1 Introduction **1**

1.1 Star Formation . . . 2

1.1.1 Interstellar Medium . . . 2

1.1.2 Fundamentals of Star Formation . . . 4

1.1.3 Low-Mass Star Formation . . . 6

1.1.4 High-Mass Star Formation . . . 11

1.1.5 Evolutionary Stages of Massive Star Formation . . . 12

1.2 An Overview of Ultra-Compact HII Regions . . . 18

1.3 Radio Recombination Lines . . . 20

1.4 Models for Cometary Morphology . . . 22

1.5 DR21 Cometary UCHII Region . . . 24

1.6 Thesis Overview . . . 27

2 Radio Recombination Line Tests **29**

2.1 Introduction . . . 29

2.2 Numerical Methods and Simulation Setup . . . 30

2.2.1 The TORCH Radiation-Hydrodynamic Code . . . 30

2.2.2 Synthetic Observation using RadioRT . . . 31

2.2.3 Initial Testing and Code Correction . . . 32

2.2.4 Departure Coefficients Test . . . 33

2.2.5 Radio Continuum Aspect of the Code . . . 37

2.2.6 The Radio Recombination Aspect of the Code . . . 40

2.2.7 Radiative Transfer Methodology . . . 42

2.3 Test Cases . . . 43
2.4 Test Implementation . . . 45
2.5 Implementation Test for Emission Measure . . . 46
2.6 Implementation Test for Integrated Flux . . . 50
2.7 Modelling the Line Profile for H109α . . . 51
2.8 Expanding and Contracting Test of the Ionised Gas . . . 54
2.9 Conclusions . . . 58

3 Modelling of the Radio and Dust Continuum Emission from DR21 60
3.1 Introduction . . . 60
3.2 Hydrodynamic Model . . . 62
3.3 Hydrodynamic Model . . . 62
3.3.1 Density Distribution . . . 63
3.4 An Initial Model for DR21 . . . 64
3.5 The Radio Continuum Model . . . 66
3.5.1 Derivation of the preliminary Density Distribution for DR21 UCHII Region . . . 69
3.6 Dust-Continuum Emission of DR21 . . . 74
3.6.1 Astrometry of DR21 Dust-Continuum Emission . . . 76
3.7 Systematic Approach for Constraining Model Parameters of DR21 77
3.7.1 An Overview . . . 77
3.7.2 Derivation of the Separation Distance between the star and the cloud core, R_s . . . 77
3.7.3 Analysis of Dust Continuum Profiles and Density Power-Law Index Estimation . . . 82
3.7.4 Derivation of the Size (age) for DR21 . . . 86
3.8 Spectral Energy Distribution (SED) Fitting of the DR21 UCHII Region . . . 89
3.9 Conclusion . . . 92

4 Recombination Line Emission of Cometary DR21 UCHII Region 95
4.1 Introduction . . . 95
4.2 The Model . . . 96
4.3 Methodology . . . 97
4.3.1 Hydrodynamics . . . 98
4.3.2 Radiative Transfer . . . 98
4.3.3 Simulation Observation and Analysis . . . 99
4.3.4 Continuum Subtraction . . . 99
4.4 The Velocity Structure . . . 102
4.4.1 Velocity Field . . . 102
4.4.2 Position Velocity Diagram . . . 106
4.4.3 The Ionised Gas Motion . . . 113
4.4.4 Line Profile Analysis . . . 113
4.5 Numerical Methods and Code Improvements . . . 146
4.5.1 Overview of the HOPE Code . . . 147
4.5.2 Comparison Between HOPE and TORCH . . . 147
4.6 Benchmark Testing of the HOPE Code . . . 149
4.6.1 Model Setup . . . 149
4.6.2 Model Comparison . . . 150
4.6.3 Discussion of Results . . . 154
4.7 Inclusion of Stellar Velocity with a Non-uniform Environment . . . 155
4.8 Model Development for the DR21 Ultracompact HII Region . . . 156
4.8.1 Model Setup and Stellar Parameters . . . 156
4.8.2 Synthetic Observations and Comparison with DR21 . . . 166
4.9 Conclusions . . . 167

5 Conclusions 171
5.1 Summary . . . 171
5.2 An overview of this thesis . . . 172
5.3 Future Work and Improvement . . . 176

References 193

List of Figures

1.1 Schematic representation of the structures within molecular clouds, including Giant Molecular Clouds, Molecular Clouds, Molecular Clumps, and Hot Cores. Adapted from (Kim & Koo, 2001). . . . 3

1.2 A graphical representation illustrating the evolutionary stages of low-mass star formation, accompanied by their corresponding spectral energy distributions (SEDs) (Frost, 2019; Isella, 2007) 10

1.3 Schematic evolutionary sequence of massive star formation adapted from Motte *et al.* (2018); Tigé *et al.* (2017). The sequence progresses from Infrared Dark Clouds (IRDCs) to High-Mass Protostellar Objects (HMPOs), and finally to Hii regions (hypercompact, ultracompact, compact, and classical). 13

1.4 Kinematics of cometary models for HII Regions from (Cyganowski *et al.*, 2003). 23

1.5 DR21 cometary UCHII region observed in the hydrogen recombination line H66α at 22GHz using the Very Large Array (VLA) from Immer *et al.* (2014). 25

1.6 Displays the red and blue-shifted Gaussian fitting results in their respective locations shown as 'dots'. The sizes of the dots represent the logarithm amplitude of the Gaussian (Immer *et al.*, 2014). . . 26

2.1 The plot compares the variation of the free-free absorption coefficient with the Hnα line. This plot is taken from Figure 2.18 by Gordon & Sorochenko (2009b). 33

2.2 The two plots display the variation in the departure coefficients for a number of principal quantum levels of hydrogen with electron densities for electron temperature, $T_e = 10^4$ K at the top. The bottom plot shows the variation in the amplification factor for the principal quantum levels. This plot is taken from Figure 2.21 reported by Gordon & Sorochenko (2009b). 35

2.3 The plot showing the variation in the departure coefficients for a range of principal quantum numbers (n) of hydrogen with electron densities, N_e=10^4 cm^{-3} and electron temperature, $T_e = 10^4$ K. It compares the literature works done by Salem & Brocklehurst (1979); Seaton (1964); Sejnowski & Hjellming (1969); Storey & Hummer (1995). This plot is taken from Figure 2.22 by Gordon & Sorochenko (2009b). 36

2.4 This figure shows an observer looking along the centre of an inhomogeneous sphere with a Cartesian coordinate system. This schematic diagram was taken from Viner *et al.* (1979) and was used to model and solve the inhomogeneous sphere geometry. . . . 44

2.5 The figure displays the emission measure maps of Model 1 implementation with RadioRT at a viewing angle of 90°. 46

2.6 The figure shows the emission measure maps of Model 3 implementation with RadioRT at a viewing angle of 90°. 47

2.7 The figure illustrates the brightness temperature of the H109α radio recombination line at 5 GHz for Model 1, plotted as a function of velocity. The rest velocity is shown at 0 km s^{-1} for ray paths passing through the centre. This figure is adapted from Figure 2b in Viner *et al.* (1979). 52

2.8 The figure shows the radio recombination line brightness temperature as a function of velocity for H109α at 5GHz for model 1. The rest velocity was set at 0 kms^{-1} and projected at a viewing angle of 90° for comparison with Figure 2.7. 53

2.9 The constant radial expansion (model 4) and contraction (model 5) line profiles of H85α simulation of HII regions under LTE and non-LTE conditions. The line profiles for the LTE are the same and symmetric for Models 4 and 5, whilst the non-LTE for Models 4 and 5 are distinguishable and asymmetry. The test was conducted by Peters *et al.* (2012). 55

2.10 The verification of symmetric and asymmetric line profiles under LTE and non-LTE states, respectively, for H85α HII regions. RadioRT code developed by Steggles (2016) is modified to implement the expanding (Model 4) and contracting (Model 5) gas motion of H85α HII regions. The figure shows the symmetric nature of spherical HII regions under LTE and the asymmetric nature of HII regions under non-LTE conditions. 56

3.1 The combined image displays the radio continuum observation of the DR21 UCHII region (VLA 22 GHz, D-configuration) alongside the corresponding highlighted area selected for modelling. The left panel illustrates the large-scale structure of the DR21 UCHII region, with a marked section indicating the specific area of interest. The right panel presents a zoomed-in view of this highlighted region, which forms the focus of the modelling. It is important to note that the entire DR21 region was not modelled; only the zoomed-in subregion shown in the right panel will be analysed. The image is rotated by 100 degrees to enable comparison with the models. The data was taken from Immer *et al.* (2014) 61

3.2 The preliminary results of the hydrodynamics simulation of UCHII region for a star with mass $20M_{\odot}$ at a simulation time of 20kyrs in a local hydrogen number density, $n_{\star}, 1.28 \times 10^5$ cm^{-3}. Top left scale ($log_{10}(n_H)$ cm^{-3}), top right ($log_{10}(P)$ Ba), bottom left (log_{10}(T) K), bottom right ($log_{10}(n_{HII})$ cm^{-3}). The star is located at z_1=0.37 pc, r= 0.0 pc. The cloud core is at z_2=0.72 pc and r=0.0 pc. Hence Rs= 0.72 - 0.37 = 0.35 pc. 64

3.3 The radio continuum emission model at 22GHz generated for the initial hydrodynamic model in figure 3.2 for the cometary DR21 UCHII region. This figure has a viewing angle of 45°, at a distance of 1.5 kpc, contour levels at 0.2, 0.4, 0.6, and 0.8 Jy/beam, and is not smooth. 67

3.4 The radio spectrum fitting to DR21 UCHII region. The constant age (size) of 20kyrs is varied with the number densities, n_0. The black circles with error bars represent observational fluxes from Harris & Scott (1973). Model SEDs for three ambient densities generated using SED results from the hydrodynamic models are shown, with the best-fitting model ($n_0 = 1.28 \times 10^5$ cm^{-3}) highlighted in red. 68

3.5 The figure shows initial result with $\alpha = 1.5$ for the modelled dust continuum map smoothed to SCUBA 450μm resolution with number density, $n_\star = 1.28 \times 10^5$ cm^{-3} and age of 20kyrs to be used for further investigation. This is obtained by generating a column density map scaled to intensity[Jy/beam] and smoothed to 7.9" SCUBA 450μm resolution with an inclination angle of 45°. 73

3.6 Combined image showing the SCUBA 450μm dust continuum emission of DR21 and the corresponding Herschel 500μm data. The left panel presents the large-scale structure of DR21 with a zoomed-in view highlighting the DR21 UCHII region, while the right panel overlays the SCUBA 450μm (raster) and Herschel 500μm (magenta contour) data, as well as the SCUBA 450μm smoothed to 500μm resolution (black contour), to verify the astrometry of the SCUBA observation. 75

3.7 The figure shows an overlaid plot of the radio (displayed as a contour) and dust (displayed as a raster image) continuum emission from DR21 observations on the left, with a vertical slice through their peaks. The plot on the right is the corresponding line profiles showing the difference between the two peaks measured as 5.4″ for the radio and dust continuum emission. The overlaid radio and the dust images are rotated at 100 degrees to compare with the models. The data was taken from Immer *et al.* (2014) 78

3.8 The figure shows an overlaid plot for the models of the radio (displayed as a contour) and dust (displayed as a raster image) continuum emission from DR21 on the left, with a vertical slice through their peaks. The plot on the right is the corresponding line profiles showing the difference between the two peaks measured as 23.″. The models have initial number density, n_o= 1.28 × 10^5 cm^{-3}, Rs=0.35 pc, α= 1.5 at an age of 20kyrs and inclination angle of 45°. The contour levels for the radio are 0.2, 0.4, 0.6 and 0.8 Jy/beam. 79

3.9 This figure shows the results from slicing in the vertical plane for the overlaid dust (raster) and radio continuum (contour) observations, both rotated by 100° (labelled A), and the corresponding generated models (labelled C). The plot labelled B shows the distance between the two peaks for the observations and models for $\alpha = 1.5$, $R_s = 0.35$ at 20 kyr. The distance between the two peaks for the dust and radio continuum observations is 5.4″, and that of the models is 21.3″. This is used to constrain the distance between the star and the cloud core, R_s. 80

3.10 This figure is similar to Figure 3.9. Here, the best-fit model parameters of $\alpha = 1.0$, $n_o = 1.28 \times 10^5$ cm^{-3} at 5 kyr, with an inclination angle of 45°, are used for the models. The distance between the two peaks for the dust (raster) and radio (contour) continuum observations was measured as 5.4″, and the corresponding model value was estimated as 4.6 ± 0.8″. 81

3.11 The illustration presents the dust emission from DR21 as observed by SCUBA at a wavelength of 450μm, rotated by 100 degrees, with a horizontal slice through the midpoint displayed in the left panel. The red horizontal line mark indicates the slice taken through the map to extract the flux distribution used in the analysis. The intensity profile derived from this horizontal slice is shown in the right panel. This graph illustrates the variation of flux along the slicing direction and acts as a reference for comparison with models to determine the optimal value of α. 82

3.12 The figure shows the normalised dust column density for DR21 at 5kyrs with Rs=0.07 pc, n_o=1.28×10^5 cm^{-3}, inclination angle of 45°, and α=0.5 displayed at left-hand side. The line profile at the top-right corner shows the resulting plot for the horizontal slice through the midpoint of the modelled dust emission. 83

3.13 Same as figure 3.12 but with α of 1.0. The line profile at the top-right corner shows the resulting plot for the horizontal slice through the midpoint of the modelled dust emission. 84

3.14 Same as figure 3.12 but with α of 1.5. The line profile at the top-right corner shows the resulting plot for the horizontal slice through the midpoint of the modelled dust emission. 84

3.15 Same as figure 3.12 but with α of 2.0. The line profile at the top-right corner shows the resulting plot for the horizontal slice through the midpoint of the modelled dust emission. 85

3.16 A Plot of results from slicing in the horizontal plane for the models by varying α with constant Rs and n_o with 4 different models and compared to SCUBA 450μm data to estimate the value of α using the SCUBA 450μm as reference. The plot shows the normalised spatial intensity profiles for the values of α 0.5, 1.0, 1.5, and 2.0, with α=1.0 as the best fit for the spatial intensity profile of the SCUBA 450μm data. An error margin of 0.05 was applied in the computation of χ^2_ν. Note: the SCUBA 450μm observation used as reference was rotated at 100 degrees and sliced horizontally through the midpoints to compare like terms. 86

3.17 The plot shows an estimation of comparable size for the cometary DR21 UCHII region. The x-axis shows the distance from the peak intensity in arcseconds, and the y-axis shows the normalised intensity in Jy/beam. The figure displays the resulting plot from a horizontal slice through the midpoint of the observed DR21 and models at different ages (sizes) of 5kyr, 6kyr, 10kyr, 20kyr and 40kyr with constant n_o, of 1.28×10^5 cm^{-3}, Rs=0.07 pc, and α = 1.0 at an inclination angle of 45°. Note: the observed data was rotated at 100 degrees and sliced horizontally through the midpoint to compare with the models. The model maps were not smoothed to any specific resolution or beam width, except the 5 kyr, which was smoothed to match the 22 GHz resolution of the VLA D-configuration $\approx 2.8''$ beamwidth) using the CASA task IMSMOOTH 87

3.18 Comparison of the observed dust continuum profile of DR21 with the modelled profiles, analogous to Figure 3.17, focusing on identification of the best-fitting model. **Left panel:** Estimated size comparison of the cometary DR21 UCHII region from horizontal slices through the midpoint of observed data and models at ages of 5, 6, 10, 20, and 40 kyr. All normalised model profiles are overlaid on the observation, with Pearson correlation coefficients (r) shown in the legend. The 5 kyr model provides the best fit. **Right panel:** The best-fit model, determined by the highest Pearson correlation coefficient, is highlighted in red alongside the observed profile. This illustration allows direct comparison of model shapes and highlights the model that best reproduces the observed data. 89

3.19 The figure shows the derived SED fitting for the cometary DR21 UCHII regions. The black circles represent observed data from Harris & Scott (1973), while the lines correspond to the model fits for varying number densities. The derived model parameters of R_s=0.07 pc, α=1.0, inclined at 45° for 5kyrs were used while varying the number density for n_o, of $3.2\times10^4 cm^{-3}$, $6.40\times10^4 cm^{-3}$, $1.28\times10^5 cm^{-3}$, and $2.65\times10^5 cm^{-3}$ with their corresponding (χ^2_ν values captured in the plot. The log of the frequency against the log of the flux was plotted from Table 3.5. The constant error bars were estimated as 10% of the derived flux. 91

4.1 The observation of the cometary UCHII region DR21 by Immer *et al.* (2014) rotated at 100° to compare with models. The zoomed in figure region is the primary focus for the model with contour levels 0.2,0.4,0.6,0.8 Jy/beam. The figure on the right panel is the single-channel image, and the boxes show the areas of emissions summed to generate spectra for analysis in comparison with models. The synthesised beam of 3.4" is displayed at the bottom left corner of the right panel. 96

4.2 The diagram showcase the step-by-step approach in modeling the cometary UCHII region DR21. 97
4.3 Displays the modelled cometary UCHII region DR21 projected 45° with contour levels 0.2, 0.4, 0.6, 0.8 Jy beam^{-1}. The image shows the continuum-subtracted line data at 0 kms^{-1} at channel 31 out of 64. The rms of the resulting line image cube, away from the source is 3.5 $\times$ 10^{-3} Jy beam^{-1} compared to the observed line data at 7.4 $\times$ 10^{-3} Jy beam^{-1}. The synthesised beam of 3.4" is displayed at the bottom left corner. This object is obtained by following the methodology of Figure 4.2. 100
4.4 Moment 1 map showing the intensity-weighted radial velocity of the observed data by Immer *et al.* (2014) overlaid to the contour of the continuum emission to highlight the focus region of the southern area captured in the square of the cometary UCHII region compared to the models. The contour levels are 0.2, 0.4, 0.6, and 0.8 mJy beam^{-1}. Note that the Moment 1 map is not rotated. . . 101
4.5 Displays the simulated Moments 1 map of the cometary UCHII region DR21 projected at a viewing angle of 30°. Note that the head is at the top and the tail at the bottom. 103
4.6 Displays the simulated Moments 1 map of the cometary UCHII region DR21 projected at a viewing angle of 45°. Note that the head is at the top and the tail at the bottom. 104
4.7 Displays the simulated Moments 1 map of the cometary UCHII region DR21 projected at a viewing angle of 60°. Note that the head is at the top and the tail at the bottom. 105

4.8 The diagram shows a slice from the cometary head (positive) through the midpoint plane to the tail (negative) of the observed DR21 on the right-hand side and the corresponding Position Velocity (PV) diagram for the slice on the left-hand side. The PV diagram displays the distance along the slice and the velocity profile. Note that, the cometary UCHII region DR21 from Immer *et al.* (2014) is rotated at 100° to compared to models 106
4.9 The diagram shows a slice from the cometary head through the midpoint plane to the tail of the simulated DR21 on the right-hand side and the corresponding Position Velocity (PV) diagram for the slice on the left-hand side. The PV diagram displays the distance along the slice and the velocity profile for comparison to the observed data. The simulated DR21 is projected at a viewing angle of 30°. 107
4.10 The diagram shows the slice and the corresponding PV diagram as in Figure 4.9 for the simulated cometary UCHII region DR21 projected at a viewing angle of 45° 108
4.11 The diagram shows the slice and the corresponding PV diagram as in Figure 4.9 for the simulated cometary UCHII region DR21 projected at a viewing angle of 60° 109
4.12 Shows the positions and box sizes of the modelled cometary UCHII region DR21 projected at a viewing angle of 30°. 110
4.13 Shows the positions and box sizes of the modelled cometary UCHII region DR21 projected at a viewing angle of 45°. 111
4.14 Shows the positions and box sizes of the modelled cometary UCHII region DR21 projected at a viewing angle of 60°. 112
4.15 This plot corresponds to the 5M box position at the cometary head of the UCHII region DR21 and displays the overlaid spectra of the observed data alongside three model projections at inclination angles of 30°, 45°, and 60° for direct comparison. 117

4.16 Same as Figure 4.15 but for the box position 4M of the observed data and the models. 118
4.17 Same as Figure 4.15 but for the box position 3M of the observed data and the models. 119
4.18 Same as Figure 4.15 but for the box position 2M for the observed data and the models 120
4.19 Same as Figure 4.15 but for the box position 1M for the observed data and the models 121
4.20 Same as Figure 4.15 but for the box position 5R of the observed data and the models. 122
4.21 Same as Figure 4.15 but for the box position 4R of the observed data and the models. 123
4.22 Same as Figure 4.15 but for the box position 3R of the observed data and the models. 124
4.23 Same as Figure 4.15 but for the box position 2R for the observed data and the models. 125
4.24 Same as Figure 4.15 but for the box position 1R for the observed data and the models. 126
4.25 Same as Figure 4.15 but for the box position 5L of the observed data and the models. 127
4.26 Same as Figure 4.15 but for the box position 4L of the observed data and the models. 128
4.27 Same as Figure 4.15 but for the box position 3L of the observed data and the models. 129
4.28 Same as Figure 4.15 but for the box position 2L for the observed data and the models. 130
4.29 Same as Figure 4.15 but for the box position 1L for the observed data and the models. 131
4.30 Same as Figure 4.15 but for the box position 12BY4R for the observed data and the models 132

4.31 Same as Figure 4.15 but for the box position 12BY4L for the observed data and the models 133
4.32 This plot shows the 2 Gaussian fits for the box position 5M for the observed data of the cometary UCHII region DR21. The velocities, V_{vls}, obtained are 6.92 kms^{-1} and -9.00 kms^{-1} 136
4.33 This plot shows the 2 Gaussian fits for the box position 2M for the observed data of the cometary UCHII region DR21. The velocities, V_{vls}, obtained are -9.30 kms^{-1} and 5.07 kms^{-1} 137
4.34 This plot shows the 2 Gaussian fits for the box position 1M for the observed data of the cometary UCHII region DR21. The velocities, V_{vls}, obtained are -7.97 kms^{-1} and 16.73 kms^{-1} 138
4.35 The plot displays the peak velocities for the observed data and models with respect to the box positions, to investigate the motion of the ionised gas from the head (5R) to tail (1R) of the cometary UCHII region DR21 139
4.36 The plot displays the peak velocities for the observed data and models with respect to the box positions, to investigate the motion of the ionised gas from the head (5M) to the tail (1M) of the cometary UCHII region DR21 140
4.37 The plot displays the peak velocities for the observed data and models with respect to the box positions, to investigate the motion of the ionised gas from the head (5L) to tail (1L) of the cometary UCHII regions DR21 141
4.38 The plot displays the comparison of observed data and the models of the ionised gas motion viewed from below through the horizontal plane of the cometary UCHII regions DR21 142
4.39 Same as Figure 4.38 at different box positions of the cometary UCHII regions DR21 143
4.40 Same as Figure 4.38 at different box positions of the cometary UCHII regions DR21 144

4.41 Same as Figure 4.38 at different box positions of the cometary UCHII regions DR21 145
4.42 Comparison between HOPE and AH06 Model B at 10 kyr 151
4.43 Comparison between HOPE and AH06 Model B at 20 kyr 152
4.44 Comparison between HOPE and AH06 Model B at 40 kyr 153
4.45 Displays of the four panels of HOPE outputs at a simulation duration of 5 kyr. The **top-left** panel shows the logarithmic hydrogen number density, $\log_{10}(n_{\rm H})$ cm^{-3}. The **top-right** panel shows the logarithmic gas pressure, $\log_{10}(P)$ Ba. The **bottom-left** panel displays the logarithmic temperature, $\log_{10}(T)$ K, and the **bottom-right** panel presents the logarithmic ionised hydrogen number density, $\log_{10}(n_{\rm HII})$ cm^{-3}. The ionising star is located at coordinates $z = 0.0$ pc and $r = 0.0$ pc. The red arrows represent gas velocities in the range 30 km s^{-1} $< v <$ 2000 km s^{-1}, while the blue arrows correspond to lower-velocity gas with $v \leq 30$ km s^{-1}. 157
4.46 Same as Figure 4.45 HOPE output at simulation duration 10 kyr. 158
4.47 Same as Figure 4.45 HOPE output at simulation duration 15 kyr. 159
4.48 Same as Figure 4.45 HOPE output at simulation duration 20 kyr. 160
4.49 Displays of the four panels of HOPE outputs at a simulation time of 5 kyr, assuming a star moving at 10 km s^{-1}. 162
4.50 Similar to Figure 4.49 HOPE output at simulation duration 10 kyr, assuming a star moving at 10 km s^{-1}. 163
4.51 Similar to Figure 4.49 HOPE output at simulation duration 15 kyr, assuming a star moving at 10 $km\ s^{-3}$. 164
4.52 Same as Figure 4.49 HOPE output at simulation duration 20 kyr, assuming a star moving at 10 km s^{-1}. 165
4.53 Initial output model from the "Ray-Tracing" code at 5 kyr, processed with DS9 software. Shown is the 37th slice of 64 from the image cube, with the corresponding line profile displayed on the right. 166

4.54 Similar to Figure 4.53, this figure displays the line profile from a different region of the resulting image cube. 167
4.55 As in Figure 4.53, this figure shows the line profile from a different region of the resulting image cube. 168

List of Tables

1.1 Summary of low-mass star formation stages 7

2.1 Emission Measure (EM) results for Models 1 and 3 from this work compared with Table 2 of Viner *et al.* (1979). EM values labelled "SF1 (this work)" correspond to a sampling factor (SF) value of 1 used in the radiative transfer code. The columns under "Initial Test SF4" show EM values for Model 3 when SF was 4, about four times higher than SF 1. 48

2.2 The table shows the integrated flux results for the implementation of Model 3 and 1 of H109α, H85α and continuum emission in comparison to table 1 reported by Viner *et al.* (1979). 50

2.3 Model Parameters of H109α for Model 1 51

2.4 Model Parameters for Expanding and Contracting gas velocity of H85α 57

3.1 Flux density measurements of DR 21 at multiple frequencies. Flux densities are in units of 10^{-26} W m^{-2} Hz^{-1}. 70

3.2 Parameters of SED models for DR21 (Main) at 20 kyr. 71

3.3 Reduced χ^2_ν values for SED fitting of DR21. 72

3.4 Constraining the Model Parameters for DR21 76

3.5 Spectra Energy Distribution (SED) for DR21 observations and Models at 5kyr 90

3.6 Reduced Chi-square (χ^2_ν) values for different number densities at 5 kyr. 90

4.1 The radiative transfer code (RadioRT) model parameters for the Cometary UCHII Region DR21. 98
4.2 DR21 Observation compared to model at 30° projection angle . . 114
4.3 DR21 Observation compared to model at 45° projection angle . . 115
4.4 DR21 Observation compared to model at 60° projection angle . . 116

Abbreviations

CASA	Common Astronomy Software Application
CORNISH	Co-Ordinated Radio 'N' Infrared Survey for High-mass star formation
EUV	Extreme UltraViolet
FWHM	Full width at half maximum
GMC	Giant Molecular Cloud
HCHII	Hyper-Compact H II (region)
HMC	Hot Molecular Core
HOPE	Hydrodynamics of Photoionised Environments
ISM	Interstellar Medium
LTE	Local Thermodynamic Equilibrium
MYSO	Massive Young Stellar Object
NIR	Near InfraRed
RMS	Red MSX Source (survey)
RRL	Radio Recombination Line
RT	Radiative Transfer
SCUBA	Submillimetre Common-User Bolometer Array
SED	Spectral Energy Distribution
TORCH	The Operator-split Radiation, Cooling, Hydro-code
UCHII	Ultra-Compact H II (region)
UV	UltraViolet
VLA	Karl G. Jansky Very Large Array
YSO	Young Stellar Object
ZAMS	Zero Age Main Sequence

Chapter 1

Introduction

High-mass stars are formed deep within molecular clouds, where they inject powerful outflows of energy and radiative winds into their immediate surroundings. During their early stages of formation, these massive stars are heavily obscured by dust extinction. This obscuration, combined with the rarity of massive stars (due to their short lifespans), their rapid evolution through observable phases, and their complex environments, makes it challenging to observe, monitor, and construct a clear visualisation of their statistical evolutionary sequence Tan *et al.* (2014); Zinnecker & Yorke (2007). Despite these challenges, investigating the influence of massive stars on their immediate environment provides valuable insights into the physical and chemical parameters of star-forming regions, as well as a deeper understanding of high-mass star formation McKee & Ostriker (2007). Newborn massive stars emit copious amounts of ultraviolet radiation, which is capable of ionising the abundant hydrogen, forming HII regions, and heating the dust in the star-forming clouds. This process allows for probing these regions at infrared, sub-millimetre/millimetre, and radio wavelengths Churchwell (2002). Ultra-compact (UC) HII regions are particularly significant in the study of high-mass star formation. These regions are associated with the youngest massive stars ionising their immediate environments and represent an early evolutionary stage of HII regions. UC HII regions exhibit various regular morphologies and are longer-lived than initially expected (Wood & Churchwell, 1989b). This extended lifetime is attributed to the balance between the pressure

of the ionising radiation from the massive star and the surrounding dense molecular material, which slows the expansion of the ionised region Kurtz *et al.* (2000). The longer lifespan of UC HII regions, which can last up to 10^5 years, provides a dynamic environment where young massive stars continue to influence their surroundings Garay & Lizano (1999). This extended phase enables the study of the interactions between massive stars and their environments over a longer period, providing more detailed information on the physical and chemical dynamics at play. Furthermore, the evolutionary sequence of HII regions can be traced from the initial formation of UC HII regions to more evolved stages, where the regions expand and become less dense. Understanding the progression and characteristics of these stages is crucial for building a comprehensive picture of the formation and evolution of high-mass stars Hoare *et al.*.

The explosive death of massive stars forms shock waves that stir the interstellar medium, enriching it with heavy elements and potentially stimulating and triggering new generations of star formation Mac Low & Klessen (2004). This process underscores the cyclical nature of star formation and the significant role that high-mass stars play in the evolution of galaxies. This chapter will delve into the processes and characteristics of high-mass star formation, the influence of these stars on their surroundings, the extended lifetimes of UC HII regions, and the observational techniques used to study them. By examining these aspects, we aim to gain a deeper understanding of the complex and dynamic nature of high-mass star formation.

1.1 Star Formation

1.1.1 Interstellar Medium

Stars are formed from clouds of gas and dust, which are referred to as the interstellar medium (ISM). Star formation primarily occurs within this medium's cold, dense molecular regions. The ISM is predominantly composed of neutral hydrogen (HI), ionised hydrogen (HII), and molecular hydrogen (H_2). Various structures are embedded within the molecular clouds, including Giant Molecular

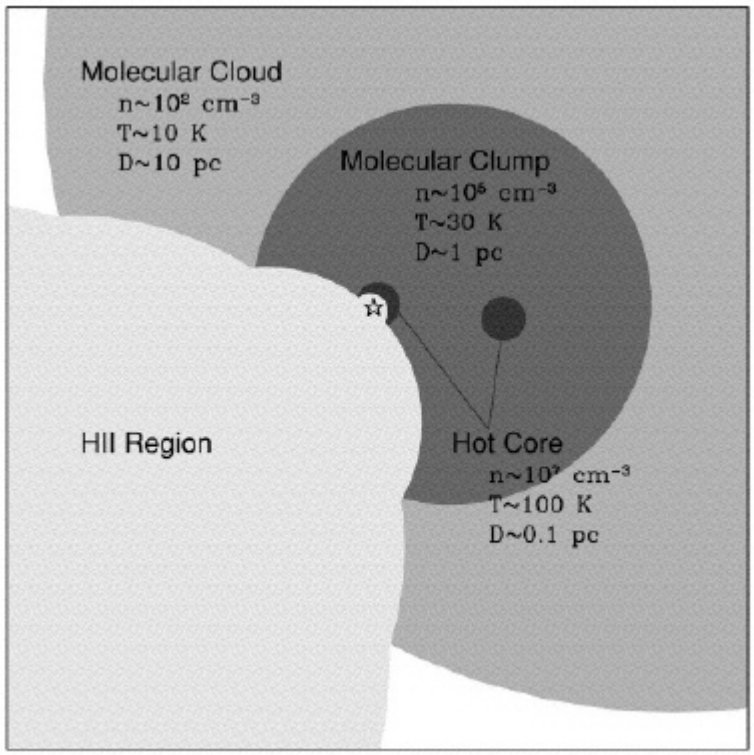


Figure 1.1: Schematic representation of the structures within molecular clouds, including Giant Molecular Clouds, Molecular Clouds, Molecular Clumps, and Hot Cores. Adapted from (Kim & Koo, 2001).

Clouds (GMCs), Molecular Clouds, Molecular Clumps, and Hot Cores.
These structures cover a wide range of physical conditions in terms of temperature, density, and sizes, as depicted schematically in Figure 1 from Kim & Koo (2001). The interstellar medium can be divided into several distinct phases, each defined by unique thermal states and size scales. Molecular clouds constitute the coldest and densest component, with temperatures typically ranging from 10 and 30 K. Their dimensions can vary from a few parsecs in the case of small isolated dark clouds to several tens of parsecs for giant molecular clouds, and they serve as the principal birthplaces of star formation. The cold neutral medium has slightly higher temperature, generally between 50 and 100 K, and densities of about 10

to 100 cm^{-3}. This phase commonly extends over scales of several tens of parsecs and is often observed as cold H I filaments within the galactic disk.
Thanks to the development of new observation techniques and technologies, like the Atacama Large Millimetre/submillimetre Array (ALMA) and James Webb Space Telescope(JWST), now we can gain deeper insight than ever before into what is happening out there by looking at this interstellar medium (ISM). For instance, Motte *et al.* (2018) demonstrated that high-resolution observations have unveiled complex substructures within molecular clouds, providing crucial insights into their fragmentation processes and the initial phases of star cluster formation. Additionally, André *et al.* (2014a) review the critical role of filaments in the ISM, which are ubiquitous in molecular clouds and appear to be the primary sites of star formation. The study of the ISM and its various components continues to be a vital area of research in understanding the complexities of star formation and the lifecycle of stars in our galaxy.

1.1.2 Fundamentals of Star Formation

Star formation is a fundamental process in the evolution of galaxies and the interstellar medium. It generally begins with the initial collapse of a molecular cloud and proceeds through the dynamical sequence of core collapse. This is a fundamental process in the evolution of galaxies and the interstellar medium. From Carroll & Ostlie (2007) on the significance of the Virial Theorem, for the collapse of a molecular cloud to be initiated, the condition $|P.E| > 2K.E$ must be satisfied, where the gravitational potential energy (P.E) is greater than twice the internal thermal energy (K.E). This equation is obtained by neglecting the influence of forces such as the magnetic field and the rotational field. The conditions necessary for the minimum mass of a cloud to collapse, Jean's criterion, where $M_c > M_J$, is given as

$$M_c > M_J \simeq \left(\frac{5kT}{G\mu m_H}\right)^{\frac{3}{2}} \left(\frac{3}{4\pi\rho_c}\right)^{\frac{1}{2}} \tag{1.1}$$

where μm_H is the mean molecular mass of the gas, ρ_c is the density of the cloud,

M_c and M_J being the mass of the cloud and Jean's mass, respectively. The equation implies that molecular clouds with a mass greater than the Jean's mass will commence collapse.

The evolutionary time scale for the collapse criteria is of great significance. Two time scales have been defined during the early phase of evolution, namely the free-fall time scale t_{ff} and the Kelvin-Helmholtz time scale t_{KH}. The free-fall time scale is defined as the time taken for a spherically symmetric cloud to collapse to the core with the influence of only gravitational force, ignoring internal pressure because gravity dominates. The t_{ff} is given by

$$t_{ff} = \sqrt{\frac{3\pi}{32G\rho_c}} \tag{1.2}$$

The time it takes for the cloud to radiate all its gravitational energy and eventually convert it to thermal energy is known as the Kelvin-Helmholtz time scale. It is the ratio of the gravitational potential energy to the luminosity of the cloud and is written as

$$t_{KH} \simeq \frac{3GM_\star^2}{10R_\star L_\star} \tag{1.3}$$

where $M_\star$, $R_\star$, and $L_\star$ are the mass, radius, and luminosity of the protostar, respectively. For low-mass stars, t_{ff} is less than t_{KH}, which implies that they begin hydrogen fusion after the collapse has concluded. On the other hand, for massive stars, the t_{ff} is greater than the t_{KH}, implying that they start hydrogen fusion whilst still accreting material onto the core. High-mass stars, therefore, emit intense photons (UV radiation) whilst still accreting materials, affecting the stellar environment. Additional processes, such as magnetic fields and turbulence, can also influence star formation. Recent studies have shown that magnetic fields can support gravitational collapse, affecting the formation and evolution of protostellar cores (Li *et al.*, 2014). Turbulence within molecular clouds can create density fluctuations, leading to localised regions of collapse and star formation (Krumholz *et al.*, 2019).

1.1.3 Low-Mass Star Formation

Why are low-mass stars important? Low-mass stars, such as those comparable to or smaller than the Sun, are more common and can be observed in more detail. They also live longer lives on average than do their more massive relatives. In addition, low-mass systems are usually easier to follow because of the lower surface temperatures, which make it possible for astronomers to track their evolution over longer time spans. So, a basic understanding of what goes on inside these minor stars serves as such an example for burgeoning theories concerning how even bigger ones come into being. Although massive and low-mass stars form through physical processes with distinct characteristics, and the earliest stages of high-mass star formation remain largely obscured, it is widely accepted that both types of stars share fundamentally similar formation mechanisms. However, low-mass stars offer an empirical framework and testbed for theories about high-mass star formation that is often difficult to find elsewhere (André *et al.*, 2014b; Ward-Thompson & Whitworth, 2011). A star begins to take shape within the cold, dense interior of a giant molecular cloud; these vast conglomerates of molecular gas and dust are found scattered along the spiral arms of galaxies (Solomon *et al.*, 1987). These clouds, composed mainly of hydrogen molecules (H_2) with some heavier molecules and dust grains, have typical temperatures of 10–20 K and densities around 10^2–10^4 cm^{-3}. Small perturbations in density within such environments can lead to gravity-dominated instabilities, provided the local mass reaches a critical value called the Jeans mass. The Jeans criterion sets out the point beyond which self-gravity exceeds internal gas pressure, initiating collapse. As shown in Equation 1.1, when $M_c > M_J$, hydrostatic equilibrium can no longer be maintained, and the cloud will collapse.

Core Formation and Core Collapse. Initial gravitational contraction develops in a pecking order, creating a network that resembles the structure of filaments and substructures within larger GMCs (André *et al.*, 2014b). These filaments provide a channel for gas to enter the dense areas, eventually giving rise to compact clumps and prestellar cores. A prestellar core is typically cold (∼10 K), gravitationally bound, and characterised by a slow, quasi-static con-

Table 1.1: Summary of the evolutionary stages of low-mass star formation, their characteristic physical properties, timescales, star formation efficiencies, and observational tracers. Evolutionary stages of low-mass star formation, and associated physical properties, timescales, star formation efficiencies and observational tracers

Stage	**Physical Characteristics**	**Lifetime**	**Efficiency**	**Observational Tracers**
Prestellar Core	Cold ($T \sim 10$ K), dense ($n > 10^{4-5}$ cm^{-3}), no central object.	10^5-10^6 yr	∼20-50% (core-to-star)	Submm dust continuum, NH_3, N_2H^+, inward motions in HCO^+
Class 0	Embedded protostar, envelope dominates mass, powerful jets and bipolar outflows, $L_{\rm submm}/L_{\rm bol} > 0.005$.	10^4-10^5 yr	Growing (majority of final mass accreted)	Strong submm continuum, CO outflows, weak IR, mm dust emission
Class I	Protostar + accreting disc, envelope dispersing, episodic accretion (e.g., FU Ori events), outflows carve cavities.	$\sim$ 0.5 Myr	Increasing stellar mass fraction	IR SED with shallow slope, near-IR reflection nebulae, CO outflows, scattered light cavities
Class II (T Tauri)	Optically visible PMS star + gas-rich disc, magnetospheric accretion, disc substructures visible (gaps/rings).	2-3 Myr (up to 10 Myr)	Most stellar mass assembled	Broad Hα, UV excess, IR excess from disc, ALMA submm continuum
Class III (Weak-line T Tauri)	PMS star with little/no disc, photospheric SED, strong magnetic activity, approaching ZAMS.	$<$ 1-2 Myr (before ZAMS)	Stellar mass essentially final	Weak Hα, no IR excess, strong X-ray emission

traction phase lasting hundreds of thousands of years. During this stage, thermal pressure, magnetic fields, and turbulence combined regulate the infall of the material.

Collapse in an Isothermal Phase and Adiabatic Phase Collapse. As the collapse proceeds, density rises to such a degree that radiative cooling becomes ineffective and the core is opaque to its own infrared emission. Initially, gas is approximately isothermal because radiation can be efficiently emitted during gravitational contraction. However, this is not the case when the optical depth becomes large enough that a significant amount of heat is trapped: the collapse then changes from isothermal to adiabatic process (Larson, 1969; Stahler *et al.*, 1980). A tiny hydrostatic structure, the *first hydrostatic core*, is thus formed. When the central temperature reaches about 2000 K, molecular hydrogen begins to dissociate. This absorbs energy, causing a secondary collapse and finally the birth of a true *protostar* at the core's centre.

Formation of the Protostar and Circumstellar Disk. The newly formed protostar remains deeply embedded within a dense envelope of infalling material. To conserve angular momentum, this gas will inevitably speed up the more it falls into itself. In this way, rotational motion becomes a uniform cylinder or disk around newborn stars called protostars (Hartmann, 2000; Stahler *et al.*, 1980). This disk serves as both a reservoir of material that feeds the central object and the potential birthplace of future planets. The geometry of the system also introduces some anisotropy, and the inflow along the rotational poles is less impeded; here, material can flow more freely. The centrifugal force also prevents direct infall in the equatorial plane of the disk, thus essentially preserving its shape.

Outflows, Jets, and Angular Momentum Regulation. When matter flows from the disk onto the protostar, some of it is also expelled as bipolar outflows and collimated jets. These outflows are magnetically driven, typically forming at the intersection of the protostar's magnetic field with that of its inner disk (Shu *et al.*, 1994). The creation of such jets provides an effective way to lose angular momentum, thus facilitating continued accretion from the disk. Observationally, these outflows give rise to dramatic features such as the Herbig-Haro objects,

which are shock-driven nebulae that form when jets collide with the surrounding gas (Frank *et al.*, 2014; Machida & Hosokawa, 2020).

Accretion and the Pre-Main-Sequence Phase. As it continues to accrete from the disk, the protostar gradually increases in mass. Meanwhile, its surrounding envelope evaporates away because both accretion and outflows serve as agents of dispersal. When most of its final mass has been accumulated, the protostar enters the *pre-main-sequence* (PMS) stage, in which contraction continues but accretion rates plummet. Now the object becomes optically visible, and its energy is supplied mainly by gravitational contraction rather than nuclear fusion. This phase is exemplified by classical T Tauri stars, which show strong Hα emission, light-curves and residual circumstellar disks (Bouvier *et al.*, 2006; Hartmann, 2000). Eventually, the temperature and pressure in the middle of the protostar become high enough for hydrogen fusion to start.

Evolutionary Classification. From an observational viewpoint, this theoretical sequence follows evolution in the source's spectral energy distribution (SED). The earliest of these deeply embedded objects, known as Class 0 sources, are seen predominantly in the far infra-red and sub-millimetre regions because of the cold, dense environments (Andre *et al.*, 1993). As evolution proceeds, the envelope dissipates, and the protostar comes to light as a Class I source, still heavily enshrouded but more visible at near infra-red wavelengths (Shu *et al.*, 1987). Objects of Class II qualified as the T Tauri phase, engaging with infrared emission dominated by the circumstellar disk. Finally, in the Class III period, the star has largely dissipated and left behind a tenuous debris disk or even no disk at all. The passage from Class 0 to Class III forms, therefore, the physical transformation: from a deeply embedded protostar to a true main-sequence star. Figure 1.2 presents a graphical representation of the evolutionary stages of low-mass star formation, along with their corresponding Spectral Energy Distributions (SEDs) for the different classes of low-mass stellar evolution (Frost, 2019; Isella, 2007). Additionally, as shown in Table 1.1, the formation of low-mass stars proceeds through a series of well-defined evolutionary stages, starting

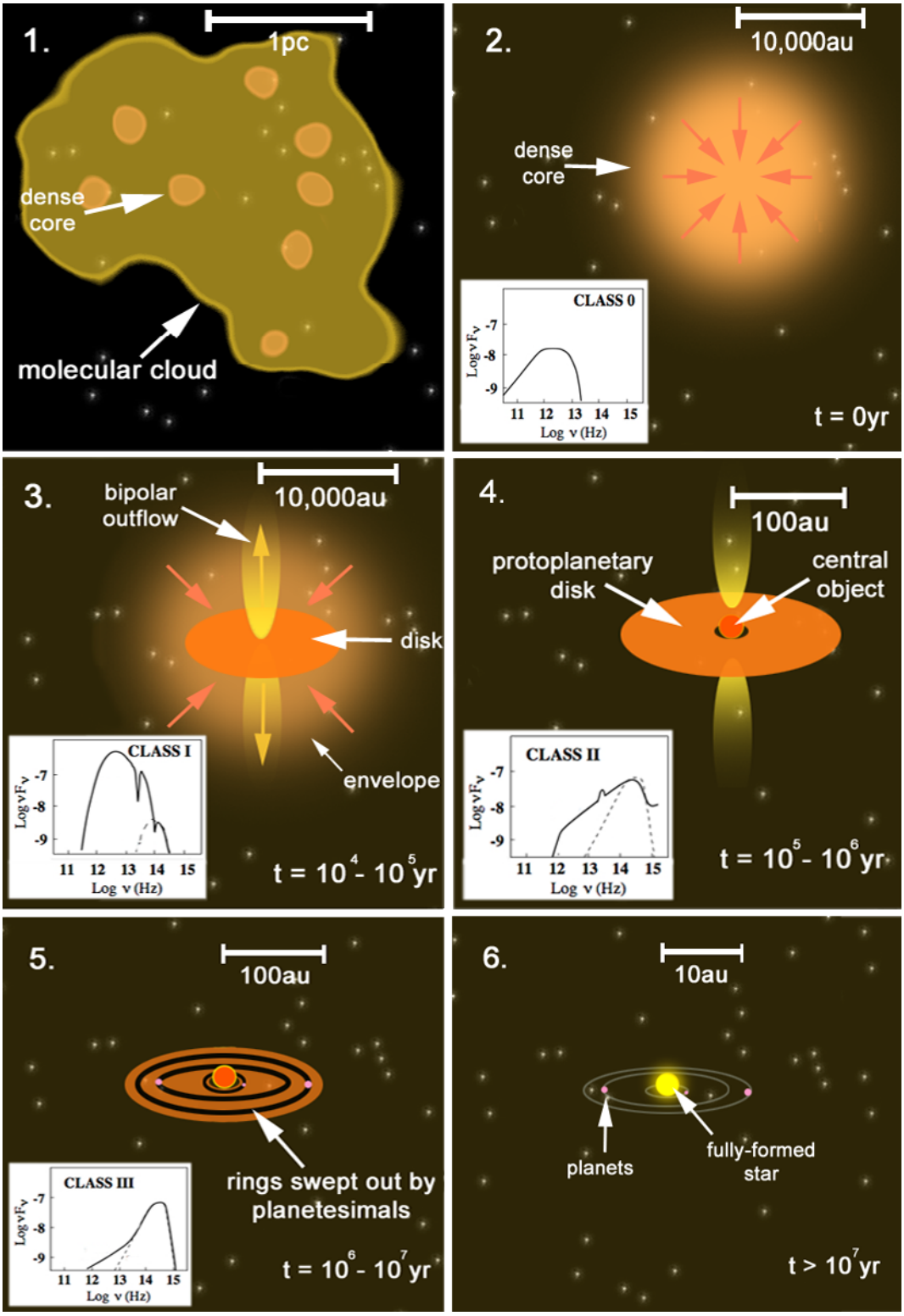


Figure 1.2: A graphical representation illustrating the evolutionary stages of low-mass star formation, accompanied by their corresponding spectral energy distributions (SEDs) (Frost, 2019; Isella, 2007)

from the prestellar core and culminating in the pre-main-sequence (PMS) phase. Each stage is characterised by distinct physical conditions, timescales, and observational tracers that reflect the gradual transformation from a cold, dense molecular core into a fully formed main-sequence star. This classification provides a coherent framework for linking theoretical models of collapse and accretion with multi-wavelength observations of young stellar objects.

1.1.4 High-Mass Star Formation

Massive stars are key drivers of galactic evolution through their strong radiation, winds, and eventual supernova explosions. Despite their importance, the formation of massive stars poses substantial theoretical and observational challenges. Their rarity, rapid evolution, large distances, and embedded formation environments complicate detailed studies. Massive stars form predominantly in clustered environments within giant molecular clouds (GMCs). The initial conditions for their birth differ markedly from those of low-mass stars: the dense gas clumps hosting massive star formation typically have masses of 10^2 to $10^5\,M_\odot$, sizes on the order of $\sim$ 1 to a few pc, and volume densities ranging from $n_\mathrm{o} \sim 10^4$ to $10^6\,\mathrm{cm}^{-3}$ (Motte *et al.*, 2018).

These clumps evolve rapidly, experiencing complex fragmentation and feedback mechanisms. Massive stars do not form in isolation but predominantly within stellar clusters. Both observations and simulations emphasise the importance of clustered environments, where competitive accretion and dynamical interactions influence the final mass distribution of the cluster members. Star-forming clumps typically host numerous dense cores, which simultaneously evolve to form massive stars alongside a population of lower-mass companions (Bonnell *et al.*, 2003; Lada & Lada, 2003; Motte *et al.*, 2018; Tan *et al.*, 2014). The competitive accretion of gas and dynamical interactions within these clusters influence individual stellar mass growth (Krumholz *et al.*, 2009). Accretion onto massive protostars proceeds predominantly via circumstellar disks, which funnel material inward while launching magneto-centrifugally driven outflows that help regulate angular momentum and enable mass growth (Motte *et al.*, 2018). These disks

have been observed with increasing clarity through high-resolution sub-millimetre interferometry, revealing Keplerian rotation signatures and disk-outflow systems (Cesaroni *et al.*, 2006; Johnston *et al.*, 2015; Zhang *et al.*, 2014). Numerical simulations also emphasise the crucial role of magnetically-launched disk winds and outflows in shaping the accretion process and feedback (Cunningham *et al.*, 2018). Radiative, mechanical (outflows, jets), and ionising feedback significantly reshape the natal cloud environment. These feedback processes both limit and regulate accretion rates, disperse residual gas, and influence cluster formation efficiency (Krumholz *et al.*, 2009; Motte *et al.*, 2018).

1.1.5 Evolutionary Stages of Massive Star Formation

Based on recent multi-wavelength surveys, high-angular resolution observations, and simulations, Motte *et al.* (2018); Tigé *et al.* (2017) propose an evolutionary sequence for massive star formation comprising several key stages as illustrated in Figure 1.3.

1. Infrared Dark Clouds (IRDCs)

IRDCs represent the earliest identifiable stage of massive star formation, characterised by cold ($\sim$ 10–20 K), dense molecular gas visible in silhouette against the bright Galactic mid-infrared background (Peretto & Fuller, 2010). These clouds harbour massive, often turbulent, clumps with densities $n_{\mathrm{H_2}} \gtrsim 10^5\,\mathrm{cm^{-3}}$ containing massive dense cores (MDCs) with masses $M_{\mathrm{core}} \sim 40\,M_\odot$ on scales ~ 0.1 pc (Rathborne *et al.*, 2006). These MDCs are the precursors to massive protostars.

2. High-Mass Protostellar Objects (HMPOs)

HMPOs are the deeply embedded young protostars accreting from MDCs, often invisible at optical wavelengths but bright in the far-infrared and (sub-)millimetre (Motte *et al.*, 2007). HMPOs can be sub-classified into *infrared-quiet* and *infrared-bright* sources based on the strength of their infrared emission, signalling different envelope dispersal stages (Mottram *et al.*, 2011). During the HMPO phase, accre-

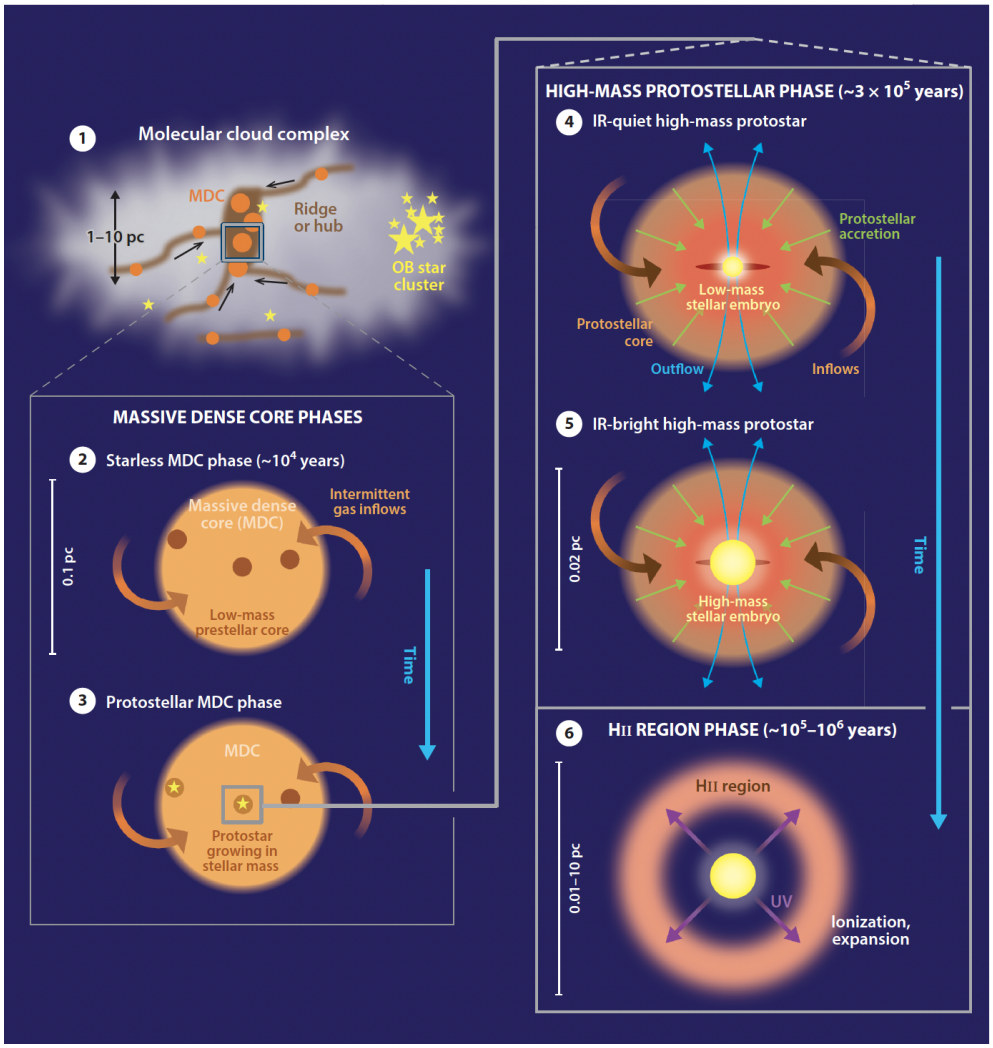


Figure 1.3: Schematic evolutionary sequence of massive star formation adapted from Motte *et al.* (2018); Tigé *et al.* (2017). The sequence progresses from Infrared Dark Clouds (IRDCs) to High-Mass Protostellar Objects (HMPOs), and finally to Hii regions (hypercompact, ultracompact, compact, and classical).

tion disks are present, and bipolar outflows are observed, indicating active mass ejection (Beuther *et al.*, 2002). Accretion rates peak in this phase, reaching values as high as $\sim 10^{-3}\,M_{\odot}\,\mathrm{yr}^{-1}$, sufficient to rapidly grow the stellar mass (Motte *et al.*, 2007).

3. HII Regions: From Hypercompact to Classical

As the protostar contracts and heats up, it begins ionising its surroundings, creating HII regions of increasing sizes categorised as follows (Churchwell, 2002; Kurtz *et al.*, 2000):

- **Hypercompact HII (HCHII) regions:** Sizes $\lesssim 0.01$ pc, extremely dense ($n_{\mathrm{e}} \sim 10^{6} - 10^{7}\mathrm{cm}^{-3}$), and often exhibiting broad radio recombination lines indicating dynamic gas flows (Hoare *et al.*, 2007b; Kurtz, 2005; Sewilo *et al.*, 2011).
- **Ultracompact HII (UCHII) regions:** With sizes of 0.01-0.1 pc, electron densities $n_{\mathrm{e}} \sim 10^{4} - 10^{5}\mathrm{cm}^{-3}$, and diverse morphologies (cometary, shell-like), these long-studied regions mark an established ionisation feedback phase (Churchwell, 2002; Hoare *et al.*; Wood & Churchwell, 1989b).
- **Compact HII regions:** Intermediate scale ionised regions, ranging from 0.1-0.5 pc, indicating expansion into less dense surroundings (Churchwell, 2002; Kurtz *et al.*, 1994; Wood & Churchwell, 1989b).
- **Classical HII regions:** The large, diffuse ionised nebulae representing mature massive stars that have emerged from their dense natal environment and photoionised large volumes of the interstellar medium (Churchwell, 2002; Osterbrock & Ferland, 2006).

The duration and transitions between these morphologies provide critical constraints on the feedback processes and the clearing of natal gas.

4. Emergence onto the Main Sequence and Cluster Assembly

By the end of the HII region phase, the massive star has typically reached the Zero Age Main Sequence (ZAMS) and has dispersed much of its dense envelope. The surrounding cluster continues to evolve with the formation of lower-mass stars and dynamical interactions (Motte *et al.*, 2018).

Massive star formation encapsulates a multiscale, multistage process involving cold infrared dark cloud (IRDC) clumps → massive protostars (HMPOs) with disks and outflows → growth of ionised HII regions (from HCHII to classical) → cluster emergence (Motte *et al.*, 2018; Tigé *et al.*, 2017). Despite significant progress, major uncertainties persist regarding the processes of fragmentation, variability in accretion, the influence of magnetic fields, and the regulation of feedback during massive star formation (Motte *et al.*, 2018). The synergy of cutting-edge observational facilities, such as Atacama Large Millimetre/submillimetre Array (ALMA) and James Webb Space Telescope (JWST), together with advanced magnetohydrodynamic simulations, offers promising avenues to deepen our understanding and resolve the outstanding challenges in the field.

Spontaneous Star Formation

In theory, the radiation pressure released from a protostellar object is capable of halting further accretion, leading to the question of how high-mass stars accumulate enough material to form. Several mechanisms have been proposed to explain how high-mass stars overcome this barrier. The three main concepts that have been developed to explain the formation of massive stars are (*a*) stellar collisions and mergers, (*b*) monolithic collapse, and (*c*) competitive accretion.

The *stellar collision and merger model* was an early solution proposed to address the radiation pressure problem. In this scenario, massive stars form by merging multiple low-mass or intermediate-mass stars in densely packed stellar clusters (Bally & Zinnecker, 2005; Bonnell *et al.*, 1998). This model is particularly relevant in extreme conditions, such as the dense environments of stellar clusters, where gravitational interactions and collisions are frequent enough to cause such mergers. However, this model is more applicable to regions with high stellar dens-

ities, such as starburst clusters, and may not account for massive star formation in most quiescent areas.

The *monolithic collapse model*, as originally proposed by McKee & Tan (2003), describes massive star formation through the collapse of a massive core with high, roughly spherical infall rates sufficient to assemble large stellar masses despite feedback. This model emphasises the necessity of elevated accretion rates to overcome the inhibitory effects of radiation pressure on dust grains. Subsequently, studies by Yorke & Sonnhalter (2002), Krumholz *et al.* (2009), and Kuiper *et al.* (2011) introduced the crucial role of circumstellar accretion disks in this process. Rather than a reduced radiation pressure in the equatorial plane, their multidimensional radiation-hydrodynamic simulations demonstrated that radiation preferentially escapes along the low-density polar regions perpendicular to the disk, while dense, infalling material continues to accrete through the disk plane. This anisotropic radiation field thus alleviates the radiation pressure barrier, enabling massive protostars to grow significantly by channelling accretion through the disk (Krumholz *et al.*, 2009; Kuiper *et al.*, 2011). Observations of accretion disks around young massive stars support this model Johnston *et al.* (2015); Zhang *et al.* (2014).

The *competitive accretion model* suggests that high-mass stars form in crowded stellar clusters, where stars compete for available materials from a shared reservoir of gas in the molecular cloud. In this model, stars closer to the centre and stars born earlier tend to have an advantage as they are more likely to gather a substantial portion of the competing materials (Bonnell *et al.*, 1997, 2001, 2004). This model emphasises that the position of a star within the cluster, as well as its formation time, affects its ability to gather material. Stars that form earlier and closer to the cloud's core are more likely to become massive. However, competitive accretion faces challenges in explaining the high accretion rates necessary for massive star formation, especially in lower-density environments (Krumholz *et al.*, 2005). More recent numerical simulations have emphasised the integral roles of magnetic fields, turbulence, and radiative feedback in regulating fragmentation and accretion. In particular, magnetohydrodynamic (MHD) simula-

tions by Kuiper & Hosokawa (2018) and Rosen & Krumholz (2020) reveal that magnetic fields can suppress small-scale fragmentation, promoting the growth of massive protostellar cores. In addition, feedback mechanisms in the form of outflows and stellar winds help regulate accretion and influence the surrounding environment; however, the exact interplay between these forces remains an active area of investigation.

Triggered Star Formation

The term triggered star formation refers to the process by which external forces, such as ionising radiation, stellar winds, or supernova explosions from a generation of massive stars, can initiate the formation of a new generation of stars. Elmegreen & Lada (1977) introduced the classical framework of triggered star formation, suggesting that feedback from massive stars can compress the surrounding molecular clouds, stimulating further star formation activities. In this scenario, the external pressure from massive stars compresses nearby gas and dust in molecular clouds, leading to gravitational collapse, giving rise to new protostellar objects. Two main mechanisms have been identified to explain triggered star formation: the radiation-driven implosion (RDI) model and the collect-and-collapse model.

The RDI model suggests that bright-rimmed clouds and pillars are produced when the ionisation front from massive stars ablates the surface of neighbouring molecular clouds. This process triggers star formation in the compressed regions of the clouds (Gritschneder *et al.*, 2009; Mellema *et al.*, 2006a; Miao *et al.*, 2006). These ionisation fronts, generated by inward-propagating shocks that compress the gas, induce gravitational instability and ultimately lead to star formation. Observational support for this process has been found in extended HII regions, where bright-rimmed clouds and pillar-like structures are associated with ongoing star formation (Getman *et al.*, 2007; Walborn *et al.*, 2002). The inward compressional shocks produced by the ionisation front are a key feature of the radiation-driven implosion (RDI) model and are frequently observed in regions

where massive stars interact with their environment, such as in the Eagle Nebula (M16) and the Carina Nebula (Smith, 2010; Smith *et al.*, 2010).

In the collect-and-collapse model, expanding HII regions, wind-blown bubbles, or supernovae shocks sweep up material into highly dense shells until it becomes gravitationally unstable and collapses, leading to the formation of new stars (Dale *et al.*, 2007; Whitworth *et al.*, 1994). This mechanism can lead to the formation of massive stars along the periphery of expanding HII regions, as observed in the RCW 79 and RCW 120 HII regions (Zavagno *et al.*, 2010). Observations of massive star-forming regions located at the edges of expanding HII regions further support the collect-and-collapse scenario (Zavagno *et al.*, 2010; Zinnecker & Yorke, 2007).

In a comprehensive survey of wind bubbles around massive stars, Deharveng *et al.* (2010) found that approximately 86% of the wind-blown bubbles contain HII regions and nearly 40% of these regions have cold dust, indicative of ongoing star formation. The detection of ultra-compact HII (UCHII) regions and methanol masers, commonly used as tracers of massive star formation, was found in 18 of the bubbles, providing compelling evidence that triggering occurs in fact along the periphery of these expanding regions. The identification of triggered star formation in these regions highlights the significant role that feedback from massive stars plays in regulating and inducing the birth of a new generation of stars. Triggered star formation plays a significant role in shaping the star formation process, especially in regions dominated by high-mass stellar populations. The feedback from these massive stars not only regulates the dynamics of molecular clouds but can also initiate the formation of new stellar systems, perpetuating the ongoing cycle of star formation in the galaxy.

1.2 An Overview of Ultra-Compact HII Regions

Almost all massive stars produce significant amounts of radiation beyond the Lyman limit, which heats and ionises the surrounding gas, forming an HII region. The ionised gas thus emits a radio continuum in the form of free-free radiation

that can propagate unimpeded through the interstellar medium. The HII regions are therefore a unique identifier of high-mass star formation. Most massive stars form UCHII regions shortly after birth expanding the ionised region into the classical HII regions.

Studies of Ultra-compact HII regions are therefore essential to understanding high-mass star formation as they may provide a lot of information about the early life of massive stars and their influence on their environments. Wood & Churchwell (1989b) and Kurtz *et al.* (1994), carried out surveys and classified UCHII regions into different types of morphologies having 26% cometary, 28% spherical, 17% core-halo, 3% shell-like and 26% irregular structures. They found that the ultra-compact HII regions are those with sizes $\leq$ 0.1pc, density $\geq 10^4 \mathrm{cm}^{-3}$ and emission measure $\geq 10^7 \mathrm{pc\ cm}^{-3}$. Walsh *et al.* (1998) found in their radio survey that most sources can be classified as either cometary or irregular.

In reviewing the differences in morphological surveys, Hoare *et al.* (2007) reported $\approx$ 40% cometary UCHII regions and argued that most of the shell-like morphologies can also be classified as cometary. Recent work by Emilova Kalcheva (2018) reported cometary dominance of approximately 70% in the Co-ordinated Radio 'N' Infrared Survey for High-mass star formation (CORNISH) Very Long Array (VLA) survey. The well-defined and regular shape of the cometary morphology HII regions must be due to the underlying physical processes, and make them ideal to investigate the dynamical evolution. Cometary UCHII region may also have a strong correlation to triggered star formation.

Cometary UCHII regions may exhibit a strong correlation with triggered star formation. The interaction between the stellar winds from massive stars and their surrounding environments can compress adjacent molecular clouds, leading to the formation of new stars (Elmegreen & Lada, 1977). Therefore, the study of UCHII regions not only contributes to our understanding of massive star formation but also sheds light on the intricate feedback mechanisms between stars and their environments.

1.3 Radio Recombination Lines

Radio Recombination Lines (RRLs) are spectral signatures that arise due to the continuous ionisation and recombination of electrons with ions, most prominently observed in the ionised nebulae such as HII regions. These lines are produced when electrons recombine with ions and cascade through different energy states, emitting radiation within the radio frequencies. The discovery of RRLs by Dravskikh & Dravskikh (1964) and Sorochenko & Borozich (1964) was pivotal in opening new possibilities for the study of ionised gas, especially in environments where optical observations are hindered by interstellar dust. Unlike optical and ultraviolet (UV) emission, radio waves can penetrate the dense clouds of gas and dust in star-forming regions. This makes RRLs an essential diagnostic for probing the physical conditions, structure, and kinematics of ionised gas across the galaxy.

RRLs serve as probes for studying the physical properties of ionised regions, as they provide direct insight into the electron density, temperature, and kinematics of the gas. Since these lines originate from transitions between high principal quantum numbers (for example, transitions between levels such as $n = 100$ and $n = 101$), RRLs are sensitive to the conditions in low-density plasma. This makes them a powerful diagnostic tool for astrophysical environments such as HII regions, planetary nebulae, and the ionised interstellar medium (ISM) (Osterbrock & Ferland, 2006). These regions are often optically thick at visible wavelengths but can be studied in detail through radio observations, allowing astronomers to map the distribution and kinematics of ionised gas in ways that are impossible with optical emission lines alone.

The sensitivity of RRLs to a wide range of physical conditions, including density, temperature, and turbulence, means that they can be used to study both large-scale structures and localised features. For example, they can trace the kinematics of ionised gas within star-forming regions and HII regions, providing insights into the velocity fields, turbulence motions, and large-scale outflows driven by massive young stars (Hoare *et al.*, 2007a). RRLs can also be used to estimate the electron temperature of ionised regions by comparing the intensities

of different recombination lines, a technique particularly useful for regions heavily obscured at optical and shorter wavelengths (Shaver, 1975).

In addition to providing information on the general properties of ionised gas, RRLs are sensitive to departures from Local Thermodynamic Equilibrium (non-LTE) effects, pressure broadening, and Doppler shifts produced by gas motions. Non-LTE conditions arise when the population of atomic energy levels do not follow what would be expected in a gas in thermal equilibrium, typically due to the influence of radiation fields and collisions in HII regions (Salem & Brocklehurst, 1980). These effects lead to subtle changes in the observed line strengths and profile shapes of recombination lines.

Pressure broadening arises when collisions between particles in the plasma cause shifts in atomic energy levels, altering the profile of RRLs. These effects become relevant in regions with high electron densities, where increased collisions broaden the lines and make their detection more difficult at low spectral resolution. However, advancements in modern radio telescopes such as the Very Large Array (VLA) and the Atacama Large Millimetre/submillimeter Array (ALMA) now allow high-angular resolution observations of these broadened features, enabling more detailed investigation of the plasma conditions (Wilson *et al.*, 2013).

Advances in radio astronomy have significantly enhanced the ability to observe and interpret RRLs. Modern radio telescopes equipped with state-of-the-art receivers and advanced data processing techniques allow for the detection of RRLs with unprecedented sensitivity and resolution. This has enabled detailed studies of the internal structure of HII regions, the kinematics of ionised gas, and the feedback effects of massive stars on their environments. RRL observations also provide valuable information into the chemical composition of the interstellar medium, since recombination lines from various elements such as hydrogen, helium, and carbon can be observed (Gordon & Sorochenko, 2009a). The application of RRLs has moved beyond simply characterising the properties of ionised gas to exploring phenomena such as feedback from massive stars, ionised winds, and even the evolution of galaxies through extragalactic RRL studies (Alves *et al.*, 2010).

In summary, RRLs have become a fundamental tool in modern radio astronomy, providing essential information about the physical conditions and dynamics of ionised gas across diverse astrophysical environments.

1.4 Models for Cometary Morphology

There are several models proposed to explain the cometary appearance of HII regions. Three main models have been proposed and progressively debated. The champagne flow model evolved from the "blister" model for cometary HII regions (Israel, 1978; Tenorio-Tagle, 1979). This model postulates the appearance of cometary HII regions when ionised gas that lies near the edge of the molecular cloud expands rapidly towards the less dense medium. In this model, the cometary morphology is due to the steepness of the density gradient within the cloud. The velocity of the ionised gas close to the head of the cometary region should be close to that of the densest molecular gas while the ionised gas accelerates down the tail at high velocities of $\approx 30\text{km s}^{-1}$ through the "nozzle" (Bodenheimer *et al.*, 1979; Yorke *et al.*, 1983).

Van Buren *et al.* (1990) introduced the bow shock model in explaining the cometary morphology of some compact HII regions due to stellar motion. According to Mac Low *et al.* (1991); Reid & Ho (1985); Van Buren & Mac Low (1992), the newborn star moves supersonically through a uniform medium, creating a bow shock ahead of the star as the ram pressure produced by the ambient flow balances the stellar wind arising from the star. The limb-brightening found in the bow shock model is a result of the stellar winds sweeping up materials between the star and the paraboloidal shell wind-blown bubbles. Limb-brightening is a major feature seen in the radio continuum images of cometary UCHII regions. The kinematics of the bow shock model predicts high ionised gas velocities at the head of the cometary region, close to the velocity of the ionising star, with lower velocities near the tail region. The pure bow shock model looks attractive since it easily reproduces the limb-brightening structure seen in continuum images while the pure champagne flow model shows such features by incorporating stellar winds.

The hydrodynamics models of Arthur & Hoare (2006) with the inclusion of stellar motions and stellar winds produced similar morphologies, suggesting that morphological types are not unique indicators of the physical conditions of UCHII regions. To differentiate between these two models in predicting the cometary shape of UCHII region, the kinematics of the ionised gas is analysed.

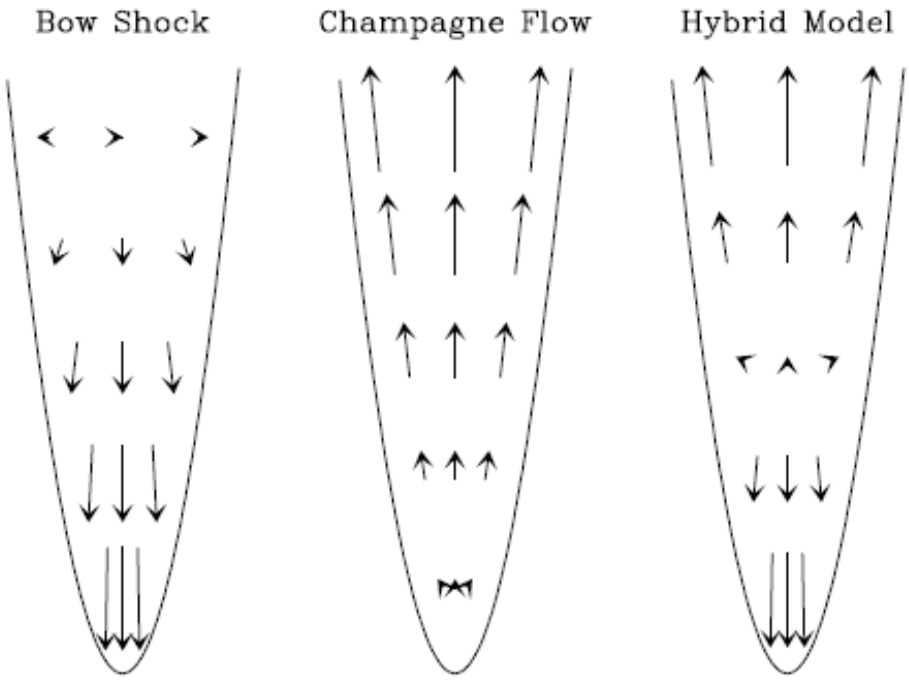


Figure 1.4: Kinematics of cometary models for HII Regions from (Cyganowski *et al.*, 2003).

The Hybrid model makes use of these two models and their kinematics to explain the cometary shape of UCHII regions. According to Lumsden & Hoare (1996, 1999) on reproducing the velocity structure of the cometary G29.96 − 0.02 UCHII region, both champagne flow and bow shock models individually poorly describe the velocity structure of the object. Hoare *et al.* (2007) argued that the UCHII region G29.96 − 0.02 requires a hybrid model since the velocity structure features can best be explained by both champagne flow and bow shock models. In the in-

vestigation of the hybrid models, Arthur & Hoare (2006) incorporated champagne flow plus stellar wind and a combination of pure champagne and pure bow shock models while varying the stellar wind and density gradient. They noted that the pure champagne flow plus stellar wind produced limb-brightening morphologies. The line widths are highest ahead of the cometary head and highest in the cometary tail for the pure bow shock and pure champagne flow respectively (Arthur & Hoare, 2006). The authors reported that, with the hybrid model, a slow-moving ionising star in a steep gradient possessed higher velocity widths down the tail, while a fast-moving star in a relatively shallow density gradient, the highest velocity widths found nearer to the ionising star. Figure (1.4), displays the three cometary UCHII region models; the bow shock model (*left*), the champagne flow model (*middle*), and the hybrid model (*right*) taken from (Cyganowski *et al.*, 2003).

1.5 DR21 Cometary UCHII Region

DR21 is a well-studied massive star formation region with two cometary HII regions, that are aligned perpendicular to each other. This alignment of two cometary provides a distinctive approach to distinguish between the models of cometary HII regions (Cyganowski *et al.*, 2003). Figure 1.5, shows an image of the DR21 cometary HII region. Studies by Cyganowski *et al.* (2003); Harris & Scott (1973); Immer *et al.* (2014) collectively identified DR21 as containing dual cometary regions. Their observations revealed a compact northern component and a more extended southern region consisting of three compact condensations. The observation of two hydrogen recombination lines and two NH_3 transitions conducted by Cyganowski *et al.* (2003) was used to investigate the gas kinematics of the DR21 HII regions. In Cyganowski *et al.* (2003) analysis, they noticed that the northern cometary head was red-shifted with respect to the molecular gas, but that of the southern cometary head was blue-shifted. This supersonic velocity difference between the two compact heads of the cometary region is consistent with the simple bow shock model. However, towards the tail of the southern

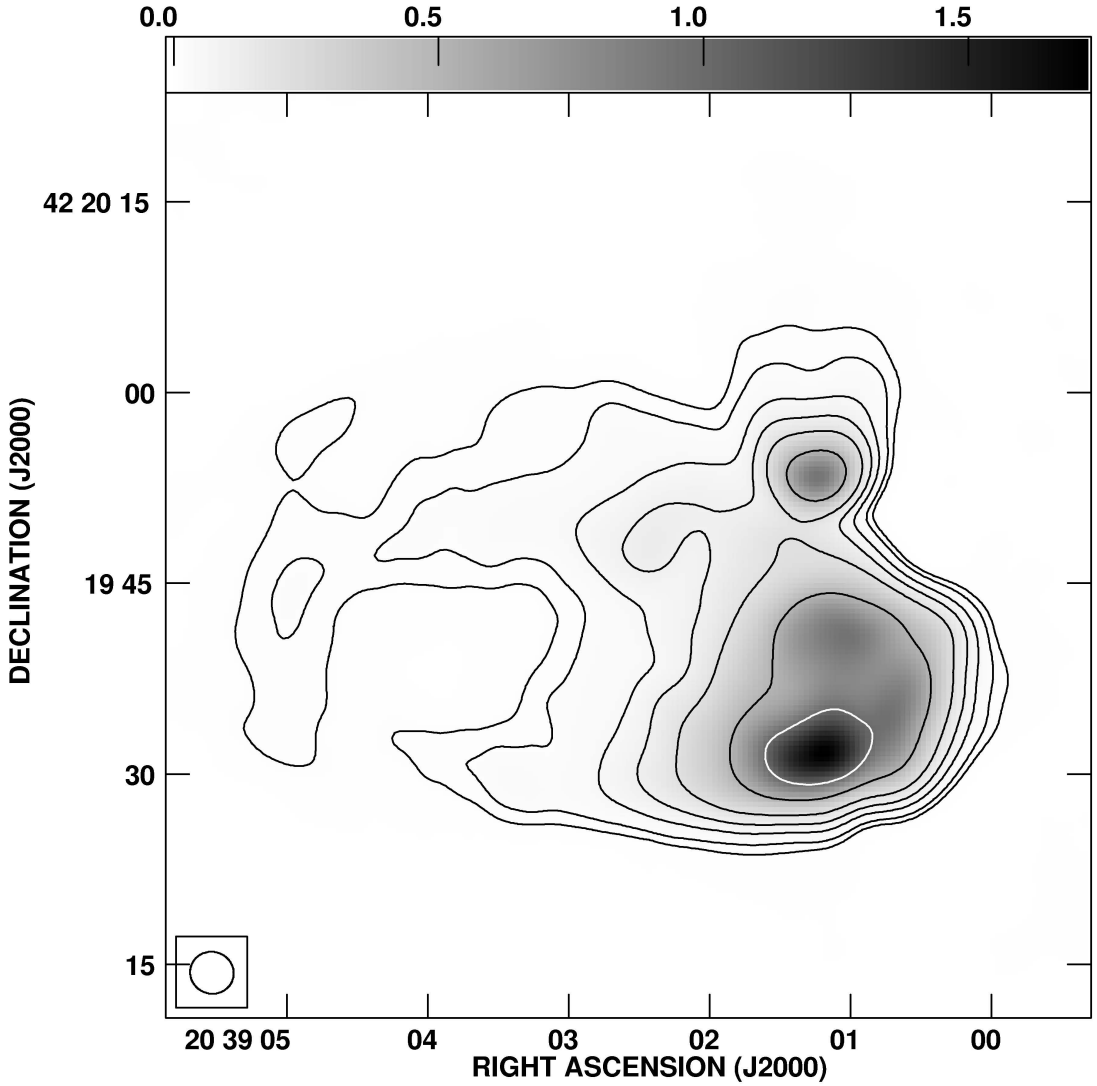


Figure 1.5: DR21 cometary UCHII region observed in the hydrogen recombination line H66α at 22GHz using the Very Large Array (VLA) from Immer *et al.* (2014).

HII region, Cyganowski *et al.* (2003) noted the velocity of the ionised gas "drifts past" the ambient molecular material using the NH_3 velocities. The H76α line observation of Roelfsema *et al.* (1989) also reported ionized material "drift past" the ambient molecular material farther down the tail of DR21. This suggests the initial pressure-driven outflow towards the tail as indicated by the champagne flow model, due to the density gradient. The pure bow shock model and simple champagne flow model operating in the same cometary HII region led the authors to conclude a hybrid model for the cometary shape of DR21.

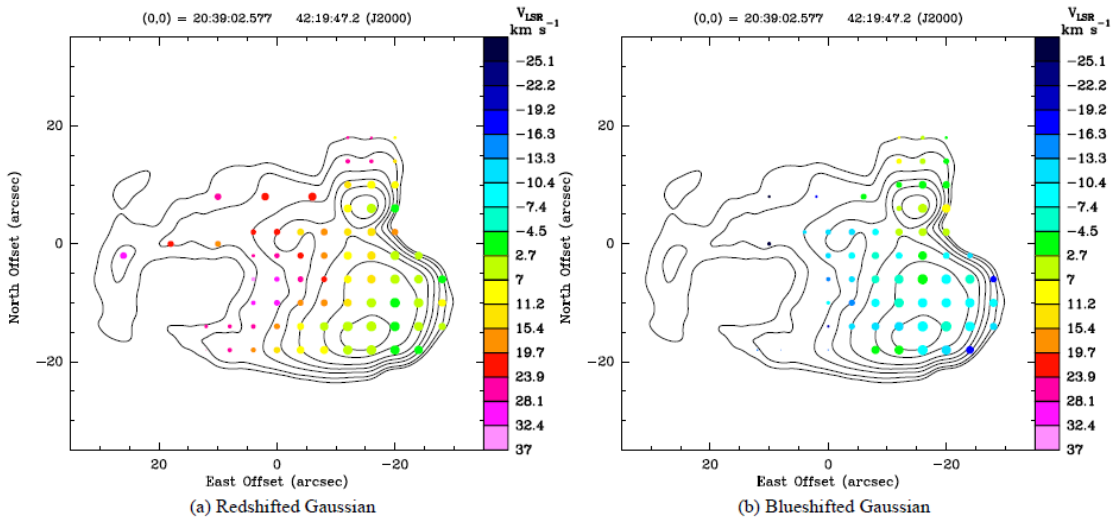


Figure 1.6: Displays the red and blue-shifted Gaussian fitting results in their respective locations shown as 'dots'. The sizes of the dots represent the logarithm amplitude of the Gaussian (Immer *et al.*, 2014).

A follow-up H66α recombination line observation of DR21 was conducted by Immer *et al.* (2014) who presented a detailed investigation of the velocity structure of the cometary HII region. Radio emission was detected towards the tail of the southern HII region at relatively higher velocities than Cyganowski *et al.* (2003). Immer *et al.* (2014) reported that the southern and northern HII regions are consistent with the champagne flow model, which may be caused by the density

gradient of the molecular cloud. The bow shock produced in the molecular cloud ahead of the ionising star could be a result of the star moving towards the southern HII region direction. There was an indication of rotational flow possibly caused by the velocity gradient between the eastern and western sides of the northern HII region (Immer *et al.*, 2014).
The detection of the two velocities (the red and blue shifted velocity component) structures of DR21 in the northern and southern HII regions by Immer *et al.* (2014) indicate the presence of strong stellar winds giving rise to the flow of ionised material along a cone-like shell, with the interior of the cone occupied with less dense gas. Figure 1.6 displays the red- and blue-shifted Gaussian fitting results respectively. The cometary shape of the DR21 HII region is believed to be a hybrid model with stellar winds and or stellar motions in defining the kinematics and inconsistent with the hydrodynamic models by Arthur & Hoare (2006).

1.6 Thesis Overview

This thesis is geared towards studying high-mass star formation at the Ultra-compact (UC) HII region stage of evolution and the influence on its environment through testing, modifying and comparing models tailored to observations. The remainder of this thesis is structured as follows. Chapter 1 details a review of the relevant literature. In Chapter 2, the radiative transfer code, RadioRT, developed by Steggles (2016) to model radio recombination lines (RRLs) for the first time, is tested and used to describe the RRLs with focus on the implementation and comparison of test cases to literature. The conditions under which to expect the observation of line profile asymmetries are investigated and compared to the literature. In Chapter 3, the methodology used to simulate and model an object tailored to cometary DR21 UCHII region is described in full, alongside the modelled continuum dust emission of DR21 to investigate and constrain the density distribution of the ionised and molecular gas within the context of the cometary hydro models. In Chapter 4, the procedure and results for modelling DR21 simulated spectra are presented. A detailed comparative analysis of the

velocity structure for DR21 UCHII region is investigated, and the trends found between them are described. The testing and implementation of stellar motion modules within the new hydrodynamics code HOPE and the radiative transfer code Ray-Tracing are also discussed. Finally, in Chapter 5, the thesis is concluded, and possible areas of future work and improvement are presented.

Chapter 2

Radio Recombination Line Tests

2.1 Introduction

Many Radio Recombination Lines (RRLs) are not significantly affected by interstellar dust. If an optical or infrared emission line encounters dust along your line of sight, it will be obscured; though peripheral, the situation is quite similar to that encountered in dust clouds. Radio emissions, on the other hand, pass right through these dusty environments with hardly any attenuation. Thus, the observed line parameters (e.g. line widths, peak velocities, and intensities) can be unambiguously attributed to intrinsic properties of the ionised gas itself. RRLs are consequently an invaluable tool for studying the physical conditions and inner structure of ionised hydrogen areas throughout the interstellar medium.

The advent of radio telescopes with increasingly sensitive detectors and more sophisticated bandwidths has led us to study RRLs with far greater scope than ever before. These advances in technology have enabled systematic investigations into such line properties as thermal and turbulent broadening, optical depth effects, or deviations from Local Thermodynamic Equilibrium (LTE). It is now common practice to test theoretical velocity distributions of ionised gas against observed line shapes.

Ultra-compact (UC) HII regions, in particular, serve as an excellent central point for RRL research. The only thing necessary for an RRL study of most UCHII regions is that the RRL profiles be optically thin, and usually, this condition is

fulfilled. At both radio and submillimetre wavelengths, observers may therefore collect hydrogen recombination lines to diagnose key parameters such as electron temperature, density, velocity fields, and the roles of feedback mechanisms from massive stars (Gordon & Sorochenko, 2009b). Using different frequency line diagnostics, one can discriminate physical effects such as non-LTE departures, pressure broadening, and general and other bulk motions such as expansion, contraction, or outflow on a large scale.

Over the past few decades, several radiative transfer codes have been developed to interpret and model observational data of ionised and molecular regions. One of the most notable is MOLLIE, described extensively by Keto (1990); Keto & Rybicki (2010); Keto *et al.* (2004), which is capable of performing radiative transfer calculations in both molecular and ionised environments. Another significant code is the one developed by Martín-Pintado *et al.* (1993), which simulates recombination line observations within ionised regions. RADMC-3D is an adaptive mesh radiative transfer code that models stars and ionised gas, employing mesh refinement techniques to capture detailed structures across ionisation fronts (Peters *et al.*, 2012). Additionally, TORCH is a three (and 2D)-dimensional Eulerian fixed-grid hydrodynamics simulator that incorporates radiation and cooling processes inherently. Finally, RadioRT is a specialised radiation transport code designed to post-process TORCH outputs specifically for radio recombination line (RRL) studies (Steggles, 2016). All of these codes have played a role in advancing the understanding of ionised gas, but they differ significantly in approach and capabilities.

2.2 Numerical Methods and Simulation Setup

2.2.1 The TORCH Radiation-Hydrodynamic Code

The simulations presented in this study were performed using TORCH (The Operator-split Radiation, Cooling, Hydrocode), a two-dimensional axisymmetric Eulerian fixed-grid radiation-hydrodynamic (RHD) code. The development and detailed description of TORCH can be found in Steggles *et al.* (2017)

and Steggles (2016). This code self-consistently couples hydrodynamics with photoionisation, radiative transfer, and detailed heating and cooling processes, thereby capturing the complex interaction of ionising radiation with the ambient gas. TORCH employs an operator-split methodology (Strang, 1968) that sequentially solves hydrodynamics, ionisation, and thermal balance within each timestep to maintain numerical stability and computational efficiency. Hydrodynamics computations are performed on a two-dimensional axisymmetric cylindrical grid (Falle, 1991), utilising a hybrid Riemann solver combining the Harten-Lax-van Leer Contact (HLLC) and Harten-Lax-van Leer (HLL) schemes to accurately capture fluid shocks and discontinuities.

Radiation transport and photoionisation are implemented via an explicit ray-tracing scheme that enables precise tracking of ionisation front propagation and quantification of energy deposition from Lyman continuum photons (Mellema *et al.*, 2006b). Implicit treatment of ionisation and recombination processes ensures stability over long time steps. Heating and cooling rates, including collisional excitation and recombination cooling, follow the approaches presented by Henney *et al.* (2009).

The simulation grid models a cylindrically symmetric molecular cloud with a prescribed density gradient. The ionising star is intentionally offset from the geometric centre of the cloud to induce a natural density contrast in the surrounding gas. Combined with stellar winds and ionising radiation, this asymmetric setup reproduces cometary morphologies observed in ultracompact HII (UCHII) regions. Consistent with previous models of UCHII regions (Arthur & Hoare, 2006; Mac Low *et al.*, 1991), several simplifications are adopted: the ionising star is held fixed (no proper motion), and both gravitational forces and magnetic fields are neglected. These assumptions isolate the dominant dynamical influences of photoionisation and stellar winds on the evolution of the ionised region.

2.2.2 Synthetic Observation using RadioRT

The post-processing of TORCH simulation outputs for observational comparison is conducted using the RadioRT code developed by Steggles (2016). This

specialised radiation transport code generates synthetic radio continuum and radio recombination line (RRL) observations by projecting integrated intensities, optical depths, and emission measures along rays traced through the simulation grid, following the method developed by Dougherty *et al.* (2003). Although RadioRT was designed to produce RRL simulations in astrophysical contexts, the original implementations of TORCH and RadioRT have not yet been fully validated against actual observational data. In this work, we extend and modify these codes to rigorously test the accuracy of RRL predictions by comparing synthetic spectra to established theoretical models from the literature. Together, the enhancements in TORCH and RadioRT enable a detailed and self-consistent investigation of the dynamical and radiative processes governing the evolution of ultracompact HII regions and facilitate direct comparisons with observational diagnostics through synthetic radio recombination line data.

2.2.3 Initial Testing and Code Correction

First initial tests revealed that the line strengths produced by RadioRT were approximately 10^4 times weaker than expected. This significant discrepancy was traced back to an error in the original code where the principal quantum number of the upper energy level was erroneously fixed at a static value of 1, instead of dynamically reflecting the actual quantum number relevant to each transition. This oversight in handling the level populations and line broadening terms led to incorrect radiative transfer calculations. After identifying and correcting this error to allow the code to accept and properly utilise the actual quantum numbers, RadioRT was rigorously tested against established benchmark models from the literature. These tests included scenarios involving single ions in static and expanding gas, as well as LTE and non-LTE conditions in HII regions, confirming the reliability and accuracy of the corrected code. As an expansion of the RadioRT code and its assembly validation in this study, we aim to make it into a useful tool for observing the ionised gas movements and physical conditions. This provides the starting point for bringing it into play with more complex astrophysical systems, such as ultra-compact HII regions, where feedback from massive

stars can trigger star formation, and dynamic gas motions are at a premium in shaping the interstellar environment.
A detailed investigation was performed to assess the influence of the upper energy level input values on the departure coefficients.

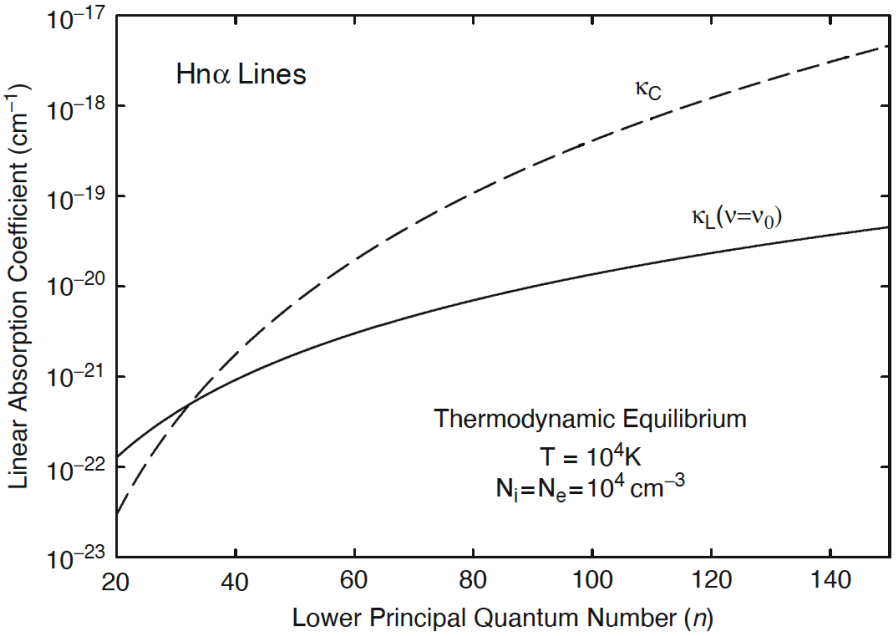


Figure 2.1: The plot compares the variation of the free-free absorption coefficient with the Hnα line. This plot is taken from Figure 2.18 by Gordon & Sorochenko (2009b).

2.2.4 Departure Coefficients Test

A test was conducted on the resulting emission, absorption, and departure coefficients to determine whether the aspect of the code works correctly as expected. This was done by comparing the printout statements from the radiative transfer code to the literature and/or calculations. The initial radiative transfer code printout values for the emission, absorption and departure coefficients were in-

consistent with the literature. After carefully analysing the line-by-line code of the radiative transfer, it was deduced that the principal quantum level, n_1 in the radiative transfer code, was being set to $n = 1$ rather than $n = 85$ requested. The principal quantum number was appropriately defined to allow multiple transitions to be recorded, and the resulting values were then compared with those reported in the literature.

The free-free Absorption coefficient, line absorption coefficient at the line centre, and departure coefficients integrated into RadioRT to reproduce the simulated spectra were investigated by comparing the results to Gordon & Sorochenko (2009b); Salem & Brocklehurst (1979); Seaton (1964); Sejnowski & Hjellming (1969); Storey & Hummer (1995). The free-free absorption coefficient (Gordon & Sorochenko, 2009b) is given by

$$\kappa_c = 9.770 \times 10^{-3} \frac{N_e N_\iota}{\nu^2 T^{\frac{3}{3}}} \left[17.72 + \ln \frac{T_e^{\frac{3}{2}}}{\nu} \right] \tag{2.1}$$

where $\mathrm{N}_e = \mathrm{N}_\iota$ is the electron density, T is the temperature and ν is the frequency. The free-free absorption coefficient of the radiative transfer code (RadioRT) was checked and verified for the implementation of Model 3. Given T=10^4 K, N_e=5 $\times 10^4$ cm^{-3} and $\nu = 10.522 \times 10^9$ Hz for H85α gives κ_c value of 7.37 $\times 10^{-19}$ cm^{-1}.

This value corresponds well to the values obtained from the radiative transfer code for κ_c and also for Hnα where n=85 in Figure 2.1, reasonably agree with the calculated value, plot and the values obtained from the RadioRT code.

A similar approach was conducted for the line absorption coefficient (Gordon & Sorochenko, 2009b) given as follows:

$$\kappa_L \approx 3.469 \times 10^{-12} \phi_\nu Z^2 \Delta n \frac{f n_1, n_2}{n_1} \times \left(1 - \frac{3\Delta n}{2 n_1} \right) \frac{N_e N}{T^{\frac{5}{2}}} exp \left(\frac{Z^2 E n_1}{kT} \right) \tag{2.2}$$

where $f n_1, n_2$ is the absorption oscillator strength, ϕ_ν is the line profile, ϕ_ν= 1 Hz^{-1}, $E n_1$ is the energy of the level n_1 below the continuum and Δn is the transition change. The values obtained from the RadioRT code for κ_L were

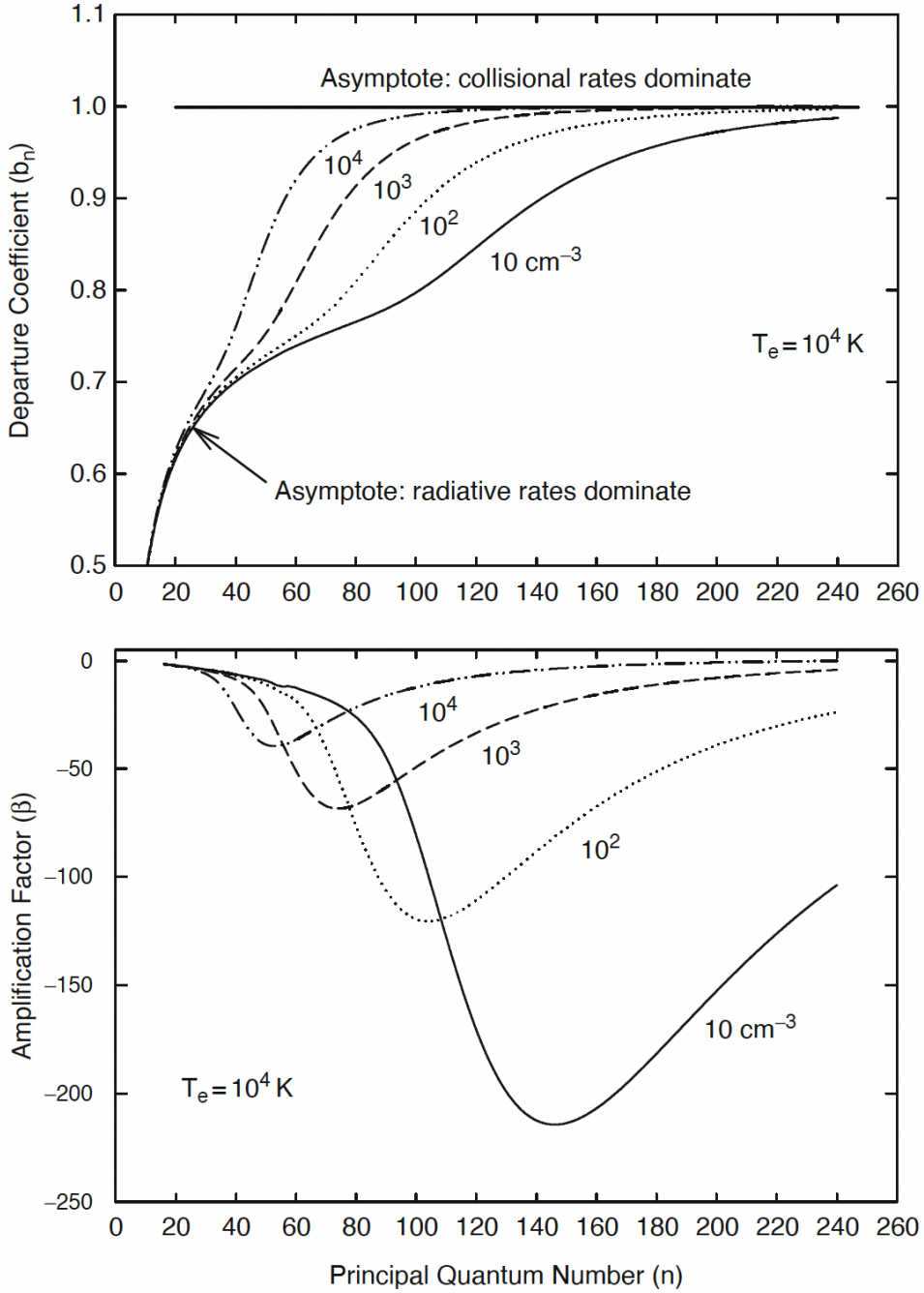


Figure 2.2: The two plots display the variation in the departure coefficients for a number of principal quantum levels of hydrogen with electron densities for electron temperature, $T_e = 10^4$ K at the top. The bottom plot shows the variation in the amplification factor for the principal quantum levels. This plot is taken from Figure 2.21 reported by Gordon & Sorochenko (2009b).

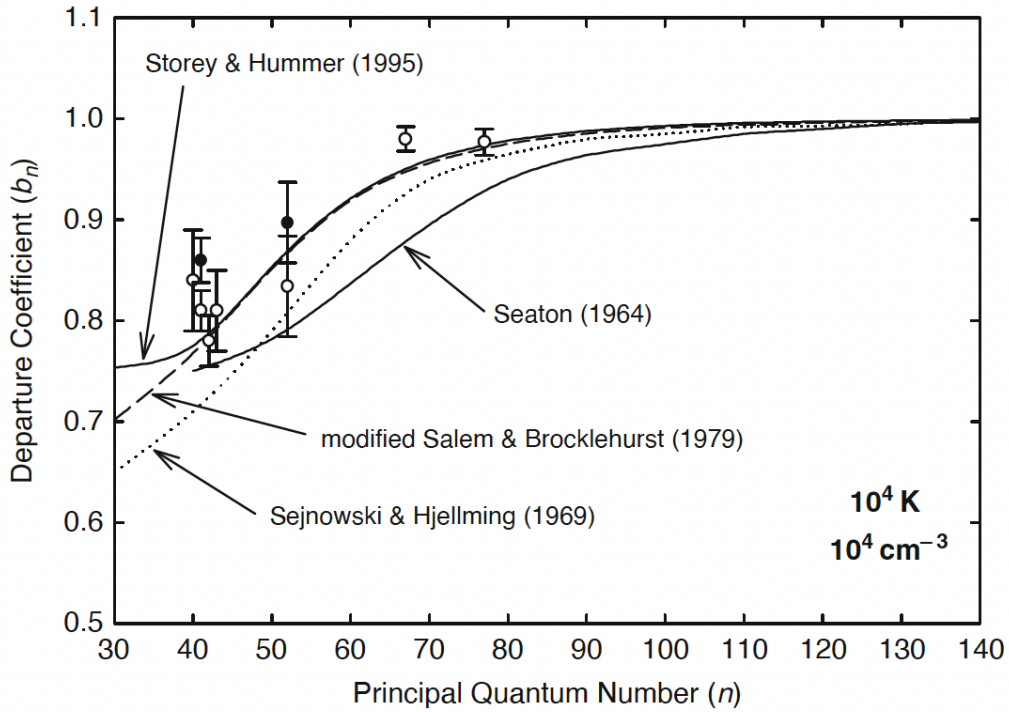


Figure 2.3: The plot showing the variation in the departure coefficients for a range of principal quantum numbers (n) of hydrogen with electron densities, N_e=10^4 cm^{-3} and electron temperature, T_e = 10^4 K. It compares the literature works done by Salem & Brocklehurst (1979); Seaton (1964); Sejnowski & Hjellming (1969); Storey & Hummer (1995). This plot is taken from Figure 2.22 by Gordon & Sorochenko (2009b).

found to be on the order of 10^{-21} for H85α, which was in good agreement with the Figure 2.1 by Gordon & Sorochenko (2009b) comparing the variation of the free-free absorption coefficient with the Hn line α.
The departure coefficient (b_n), integrated in RadioRT, was tested and verified by implementing Model 3 for H85α at 10.522 GHz. The resulting departure coefficients of the radiative transfer code were compared with Figures 2.2 and 2.3, and the resulting values for b_n were in the range of $0.9 > 1.0$, which were in good agreement.

2.2.5 Radio Continuum Aspect of the Code

The hydrodynamic code (TORCH) and the radiation transfer code (RadioRT) developed by Steggles (2016) are run independently, and the hydrodynamic output is read into the RadioRT code. The codes are run with the continuum set up to simulate and model HII regions. The radio continuum aspect of the code is described below as seen in Steggles (2016);
For a moving non-relativistic electric field of a system with charges, neglecting the contribution of the velocity field and retardation effects, it is given by

$$\vec{E}_{\rm rad}(\vec{r},t) = \sum_i \frac{q_i}{4\pi\varepsilon_0} \frac{1}{\left|\vec{R}_i\right| c^2} \hat{R}_i \times \left(\hat{R}_i \times \ddot{\vec{r}}_i\right), \tag{2.3}$$

where q_i are the charge particles, $\vec{R}_i$ are the separation distance between the particle positions $\vec{r}_i$ and the field position $\vec{r}$. By definition, the dipole moment is given by

$$\vec{d} = \sum_i q_i \vec{r}_i, \tag{2.4}$$

with the corresponding electric field given by

$$\vec{E}_{\rm rad}(\vec{r},t) = \frac{1}{4\pi\varepsilon_0} \frac{1}{|\vec{R}|c^2} \hat{R} \times \left(\hat{R} \times \ddot{\vec{d}}_i\right), \tag{2.5}$$

and the magnetic field is

$$\vec{B}_{\rm rad}(\vec{r},t) = \frac{1}{c}\hat{R} \times \vec{E}_{\rm rad}(\vec{r},t), \tag{2.6}$$

To obtain the free-free volume emissivity $j_v^{\rm ff} = dW/dVdtdv$, the rate of electromagnetic energy transfer dW/dt per unit area dA is deduced by:

$$\frac{dW}{dtdA} = \frac{1}{\mu_0 c}\left|\vec{E}_{\rm rad}\right|^2 = \frac{\mu_0}{16\pi^2 c}\frac{|\ddot{\vec{d}}|^2}{|\vec{R}|^2}\sin^2\theta, \tag{2.7}$$

here, θ is the separation angle between $\hat{R}$ and $\dot{\vec{v}}$. Larmor formula is obtained after integrating equation 2.7 is given by

$$\frac{dW}{dt} = \frac{\mu_0|\ddot{\vec{d}}(t)|^2}{6\pi c}. \tag{2.8}$$

Introducing Parseval's theorem gives

$$\int_{-\infty}^{+\infty}|\ddot{\vec{d}}(t)|^2dt = \int_{-\infty}^{+\infty}|\ddot{\vec{d}}(\omega)|^2d\omega = 2\int_{0}^{+\infty}|\ddot{\vec{d}}(\omega)|^2d\omega, \tag{2.9}$$

The Fourier transform is differentiated twice with respect to time to give

$$\frac{dW}{d\omega} = \frac{\mu_0}{3\pi c}|\ddot{\vec{d}}(\omega)|^2 = \frac{\mu_0}{3\pi c}\omega^4|\vec{d}(\omega)|^2. \tag{2.10}$$

Defining Bremsstrahlung with respect to an electron moving past an ion with an impact parameter, b, gives

$$\vec{d}(\omega) = \frac{e}{2\pi\omega^2}\int_{-\infty}^{\infty}\dot{\vec{v}}e^{i\omega t}dt \tag{2.11}$$

Now, with the interaction between the electron and the ion over, the integral of equation 2.11 gives

$$\vec{d}(\omega) = \begin{cases} \frac{e}{(2\pi)^{1/2}\omega^2}\Delta\vec{v}, & \text{if } \omega t \ll 1 \\ 0, & \text{if } \omega t \gg 1 \end{cases}$$

We, therefore, get a radiation spectrum of

$$\frac{dW}{d\omega} = \begin{cases} \frac{\mu_0 e^2}{6\pi^2 c\omega^2}|\Delta\vec{v}|^2, & \text{if } \omega t \ll 1 \\ 0, & \text{if } \omega t \gg 1 \end{cases}$$

The largest aspect of acceleration is perpendicular to the path of the electron with a change in velocity, Δv, yielding

$$\Delta v \approx \frac{1}{4\pi\varepsilon_0}\frac{Ze^2}{m_e}\int_{-\infty}^{+\infty}\frac{b}{\left(b^2+v^2t^2\right)^{3/2}}dt = \frac{1}{4\pi\varepsilon_0}\frac{Ze^2}{m_e}\frac{2}{bv}, \tag{2.12}$$

and

$$\frac{dW}{d\omega} \approx \begin{cases} \frac{1}{(4\pi\varepsilon_0)^3}\frac{8Z^2e^6}{3\pi c^3 m_e^2 b^2 v^2}, & \text{if } \omega t \ll 1 \\ 0, & \text{if } \omega t \gg 1 \end{cases} \tag{2.13}$$

The total spectrum for the gas is obtained by multiplying equation 2.13 by the flux of electrons $n_e v$ and integrating over the area at the ion density, n_i, to give

$$\frac{dW}{d\omega dV dt} \approx \frac{1}{(4\pi\varepsilon_0)^3}\frac{16 n_e n_i Z^2 e^6}{3c^3 m_e^2 v}\ln\left(\frac{b_{\max}}{b_{\min}}\right) \tag{2.14}$$

where, n_e is the electron density and v is the electron speed, $b_{\min}$ is the minimum impact parameter, $b_{\max}$, is the maximum impact parameter.
We then obtain a Gaunt factor expressed as,

$$g_{\mathrm{C}}(v,\omega) = \frac{\sqrt{3}}{\pi}\ln\left(\frac{b_{\max}}{b_{\min}}\right) \tag{2.15}$$

The free-free volume emissivity becomes

$$\frac{dW}{d\omega dV dt} \approx \frac{1}{(4\pi\varepsilon_0)^3}\frac{16\pi n_e n_i Z^2 e^6}{3^{3/2}c^3 m_e^2 v} g_{\mathrm{ff}}(v,\omega). \tag{2.16}$$

It must be noted that if $v < (2hv/m)^{1/2}$, no photons are created, as well as $d\omega = 2\pi dv$. By averaging the free-free volume emissivity over a thermal distribution of

speeds, we obtain the equation below that is captured in the RadioRT code by Steggles (2016)

$$j_{v,\mathrm{C}} = \frac{dW}{dV\,dt\,d\nu} = \frac{1}{(4\pi\varepsilon_0)^3}\frac{32\pi e^6}{3m_e^{3/2}c^3}\sqrt{\frac{2\pi}{3k_{\mathrm{B}}T}}Z^2 n_e n_i \exp\left(\frac{-h\upsilon}{k_{\mathrm{B}}T}\right) g_{\mathrm{ff}}(\upsilon,\omega). \quad (2.17)$$

Now, by taking into account that the source function, $\mathrm{S}_{v,C}$, the corresponding thermal free-free volume absorption coefficient is also obtained as the equation below, which is captured in RadioRT code developed by Steggles (2016)

$$\alpha_{v,\mathrm{C}} = \frac{1}{(4\pi\varepsilon_0)^3}\frac{16\pi e^6}{3m_e^{3/2}ch\upsilon^3}\sqrt{\frac{2\pi}{3k_{\mathrm{B}}T}}Z^2 n_e n_i \left(1-\exp\left(-\frac{h\upsilon}{k_{\mathrm{B}}T}\right)\right) g_{\mathrm{ff}}(\upsilon,\omega). \quad (2.18)$$

2.2.6 The Radio Recombination Aspect of the Code

The radiative transfer code, RadioRT developed by Steggles (2016) has the capability of generating recombination lines. This was derived and integrated into RadioRT code by Steggles (2016) as follows;
When an electron falls from a principal quantum state m to n, the corresponding absorptivity is given by

$$\alpha_{v,\ \mathrm{L}} = \frac{h\upsilon}{4\pi}\left(N_n B_{nm} - N_m B_{mn}\right)\phi(\upsilon), \quad (2.19)$$

where h is the Planck Constant, B_{nm} and B_{mn} are Einstein B-coefficients for absorption and stimulated emission, N_n and N_m are number densities of the atoms n and m respectively and $\phi(\upsilon)$ is the line profile function. The Einstein coefficient for spontaneous emission is given by

$$A_{mn} = \frac{2h\upsilon^3}{c^2}B_{mn}, \quad (2.20)$$

and the Einstein coefficients satisfy the relation,

$$g_n B_{nm} = g_m B_{mn} \quad (2.21)$$

Now, equation 2.19 can be expressed as

$$\alpha_{v,\,\mathrm{L}} = \frac{c^2 N_n g_m}{8\pi v^2 g_n n_v^2} A_{mn} \left(1 - \frac{g_n N_m}{g_m N_n}\right) \phi_{mn}(v), \tag{2.22}$$

where n_v is the index of refraction, g_n are the statistical weights of energy level n, and N_n is the population of electrons at level n and on the assumption of local thermodynamic equilibrium (LTE), we obtained the Saha-Boltzmann equation

$$N_n^{\mathrm{LTE}} = \frac{N_e N_i h^3}{(2\pi m_e k_{\mathrm{B}} T_e)^{3/2}} \frac{g_n}{2} \exp\left(-\frac{E_n}{k_{\mathrm{B}} T_e}\right), \tag{2.23}$$

where E_n is the energy of level n with sign convention $E_n < 0$. Using 2.23 we obtain

$$\frac{g_n N_m^{\mathrm{LTE}}}{g_m N_n^{\mathrm{LTE}}} = \exp\left(-\frac{h v_0}{k_{\mathrm{B}} T}\right). \tag{2.24}$$

From equation 2.22 and 2.24, the absorption coefficient can be obtained as

$$\alpha_{v,\,\mathrm{L}}^{\mathrm{LTE}} = \frac{c^2 N_n^{\mathrm{LTE}}}{8\pi v^2} A_{n+1,n} \left(1 - \exp\left(-\frac{h v_0}{k_{\mathrm{B}} T}\right)\right) \phi(v), \tag{2.25}$$

This finally leads to the Einstein A-coefficient given as

$$A_{n+1,n} \approx \frac{64\pi^6 m_e e^{10}}{3\,(4\pi\varepsilon_0)^6\, c^3 h^6 n^5}. \tag{2.26}$$

The departures from the local thermodynamic equilibrium, thus departure coefficients, are considered and implemented in the radiation transfer code, RadioRT. This is obtained by dividing the actual population in level k by the population predicted under LTE conditions and is given as

$$b_k \equiv \frac{N_k}{N_k^{\mathrm{LTE}}}. \tag{2.27}$$

The departure coefficients are calculated from the code developed by Gordon

& Sorochenko (2009b), and the non-LTE absorptivity is obtained by using the formula

$$\alpha_{v,\ \mathrm{L}} = \frac{b_n - b_{n+1}\exp\left(-\frac{hv_0}{k_\mathrm{B}T}\right)}{1-\exp\left(-\frac{hv_0}{k_\mathrm{B}T}\right)}\alpha^{\mathrm{LTE}}_{v,\ \mathrm{L}} \tag{2.28}$$

and the non-LTE emissivity is also given as

$$j_{v,\ \mathrm{L}} = b_{n+1} j^{\mathrm{LTE}}_{V,\ \mathrm{L}}. \tag{2.29}$$

2.2.7 Radiative Transfer Methodology

To generate the synthetic HII regions, Steggles (2016) employed the ray tracing scheme in the appendix of Dougherty *et al.* (2003) with the capabilities of generating radio recombination lines. Steggles (2016) developed the "The Operator-split Radiation, Cooling, Hydrocode" (TORCH) and the RRL radiative transfer code (RadioRT). The RadioRT code traces rays from the TORCH outputs with the emission and absorption coefficients calculated to accumulate the intensity. Following the RadioRT code developed by Steggles (2016), the source function is defined by

$$S_v \equiv \frac{j_v}{\alpha_v}, \tag{2.30}$$

where j_v, is the emission coefficient and α_v, absorption coefficient. The optical depth is defined by

$$\tau_v = \int \alpha_v ds \tag{2.31}$$

It must be noted that ds is denoted in the code as

$$ds = \frac{\Delta l}{sampling factor}. \tag{2.32}$$

where Δl is the change in length with respect to the number of grid samples

(sampling factor).
Now, we introduce the general radiative transfer equation given as

$$\frac{dI_v}{d\tau_v} = S_V - I_V \tag{2.33}$$

Multiplying equation 2.33 by the integrating factor of e^{τ_v} gives

$$e^{\tau_v}\frac{dI_v}{d\tau_v} + e^{\tau_v}I_v = \frac{d\left(e^{\tau_v}I_v\right)}{d\tau_v} = e^{\tau_v}S_v, \tag{2.34}$$

Integrating this over a path segment gives

$$I_v = e^{-\Delta\tau_v}I_0 + e^{-\Delta\tau_v}\int_0^{\Delta\tau_v} e^{\tau}S_v d\tau, \tag{2.35}$$

where the $\Delta\tau_v$ is the optical depth across the segment path, and I_0 is the initial intensity at the path segment and the change in the intensity in the model grid is given as

$$I_V - I_0 = \left(1 - e^{-\Delta\tau_v}\right)\left(S_V - I_0\right). \tag{2.36}$$

2.3 Test Cases

A numerical code was developed by (Viner *et al.*, 1979) to model an inhomogeneous spherical region, capable of calculating both radio continuum and hydrogen recombination line emission. The schematic diagram in Figure 2.4 shows the Cartesian system involved in modelling and solving the inhomogeneous sphere geometry by Viner *et al.* (1979). The numerical code developed by Viner *et al.* (1979) for the estimation of continuum and recombination line emission is used to investigate the effects of radial variation of the physical model parameters on the line profiles from the emission of HII regions. Peters *et al.* (2012) used the adaptive-mesh radiation transfer code RADMC-3D to present the significance of

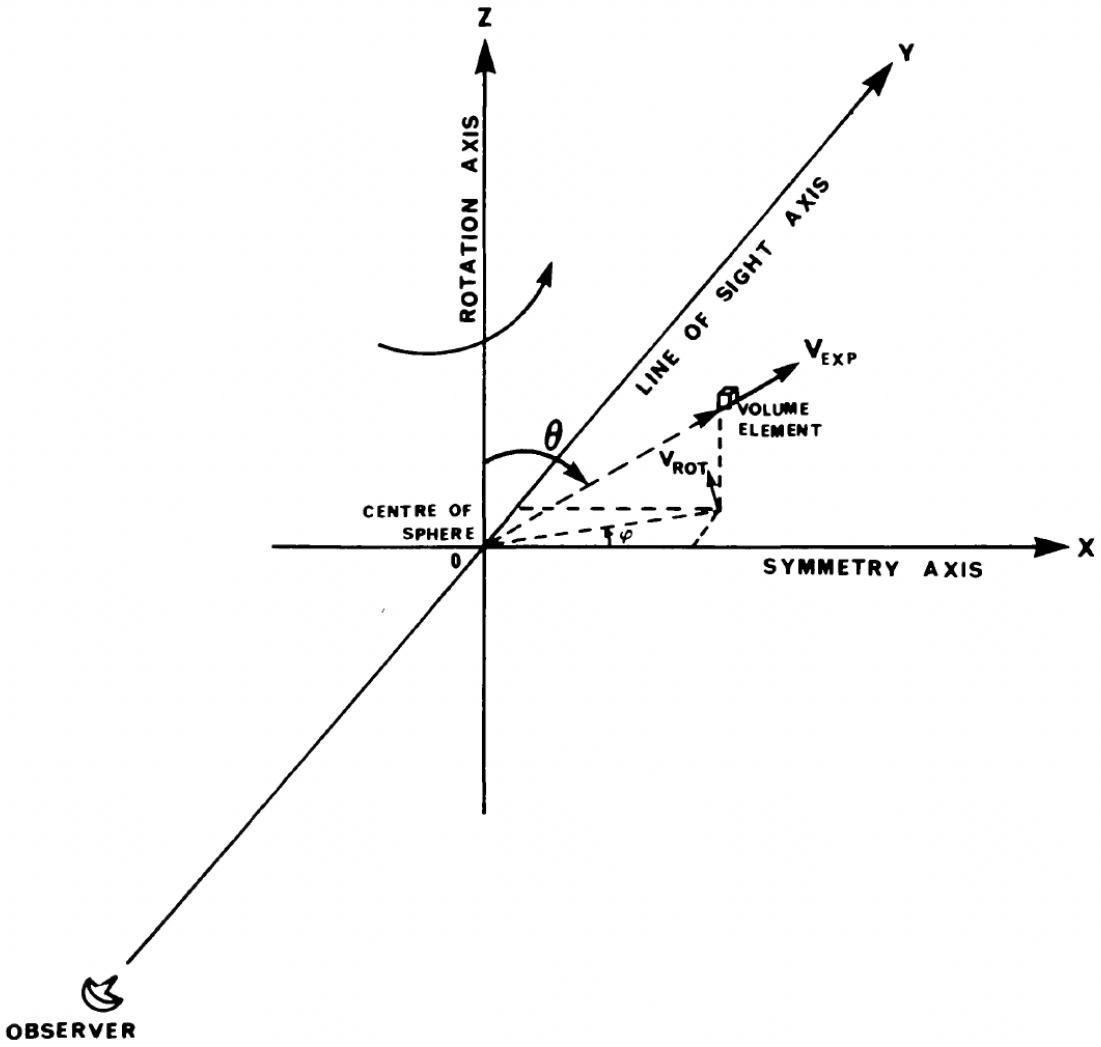


Figure 2.4: This figure shows an observer looking along the centre of an inhomogeneous sphere with a Cartesian coordinate system. This schematic diagram was taken from Viner *et al.* (1979) and was used to model and solve the inhomogeneous sphere geometry.

non-local thermodynamical equilibrium (non-LTE) modelling in the implementation of their simulated hydrogen recombination lines emission.
The radiative transfer code (RadioRT), developed by Steggles (2016), was employed in this chapter and modified to test the code and strength of the Hydrogen recombination line profiles against the series of tests conducted by Viner *et al.* (1979) and Peters *et al.* (2012).

2.4 Test Implementation

The initial test is to verify the implementation of the radial dependence on the electron density using the radiative transfer code, RadioRT (Steggles, 2016), against the series of tests conducted by Viner *et al.* (1979) and Peters *et al.* (2012). Models 1 and 3 from Viner *et al.* (1979) and Peters *et al.* (2012) are selected to verify this implementation. A constant gas temperature, T= 10^4 K and turbulent velocity, V_T= 15 kms^{-1} are considered with no rotation, expansion or contraction, and the background temperature is negligible as reported by Viner *et al.* (1979) and Peters *et al.* (2012). The radial dependence of the number density for Models 1 and 3 is defined as follows:

1. Model 1

$$n_e = \begin{cases} 28 \times (r)^{-2} & 0.02pc \leq r \leq 0.4pc \\ 0 & \text{otherwise,} \end{cases} \tag{2.37}$$

2. Model 3

$$n_e = \begin{cases} 5 \times 10^4 cm^{-3} & r \leq 0.24\text{pc} \\ 0 & \text{otherwise,} \end{cases} \tag{2.38}$$

RadioRT was modified, and Models 1 and 3 are implemented separately within the radiative transfer code to simulate the radio recombination lines. RadioRT was modified such that the output of the hydro models in terms of the number density, turbulence broadening and frequency was replaced with the analytic expression for Models 1 and 3.

2.5 Implementation Test for Emission Measure

The general formula to estimate emission measures (EM) is given as

$$EM = \int {n_e}^2 ds \tag{2.39}$$

where n_e is the electron density integrated along the line of sight (cm^{-6} pc). To see the structure of optically thin UCHII regions, the RadioRT code by Steggles (2016) was used to generate EM maps. Viner *et al.* (1979) estimated the EM through the centre (cm^{-6} pc) and average EM across the source (cm^{-6} pc) using their code for Models 1 and 3.

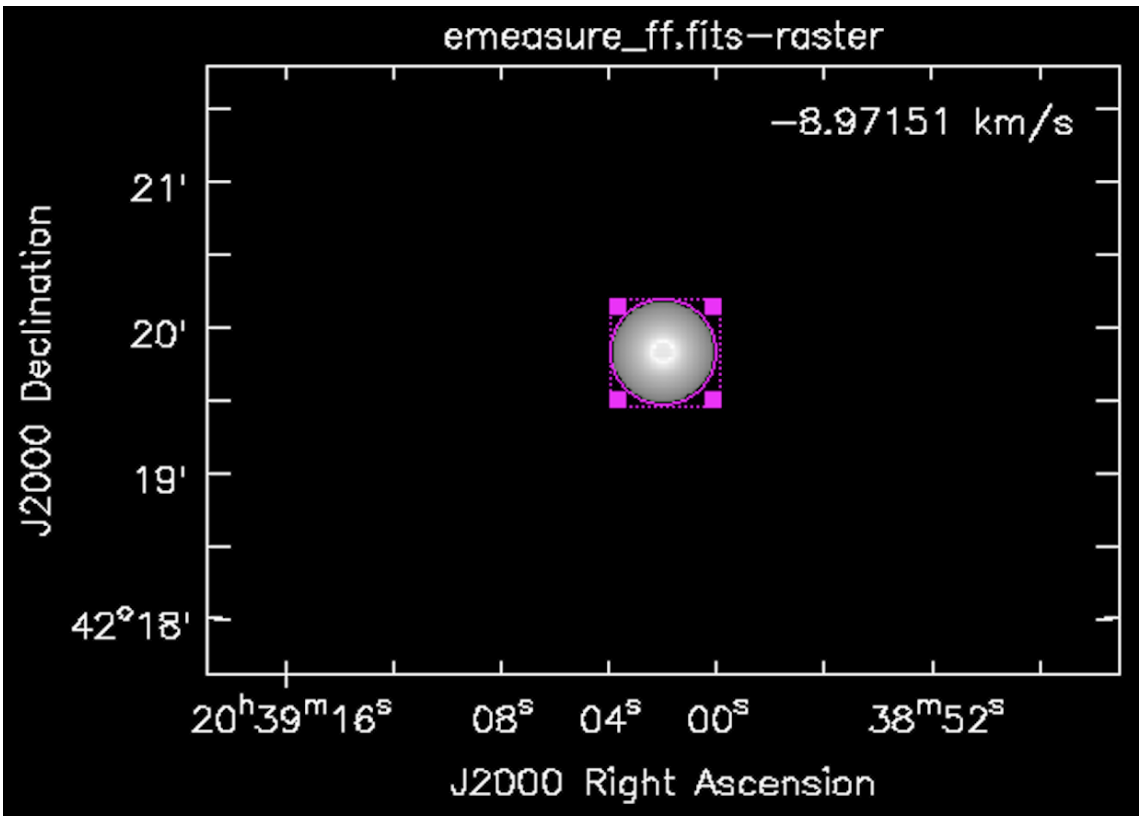


Figure 2.5: The figure displays the emission measure maps of Model 1 implementation with RadioRT at a viewing angle of 90°.

A test was conducted to verify the EM aspect of the code using RadioRT by

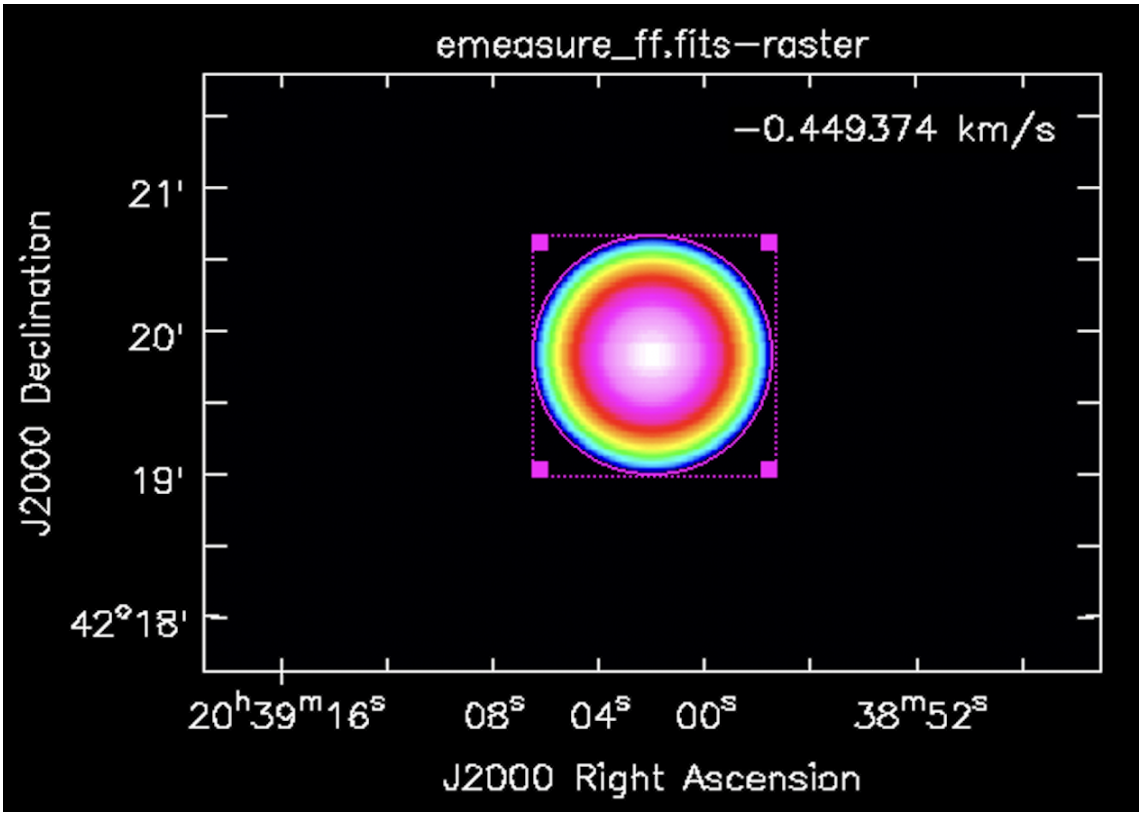


Figure 2.6: The figure shows the emission measure maps of Model 3 implementation with RadioRT at a viewing angle of 90°.

Table 2.1: Emission Measure (EM) results for Models 1 and 3 from this work compared with Table 2 of Viner *et al.* (1979). EM values labelled "SF1 (this work)" correspond to a sampling factor (SF) value of 1 used in the radiative transfer code. The columns under "Initial Test SF4" show EM values for Model 3 when SF was 4, about four times higher than SF 1.

Model	EM through centre (cm^{-6} pc)			Average EM across source (cm^{-6} pc)		
	SF1 (this work)	Viner et al.	Initial Test SF4	SF1 (this work)	Viner et al.	Initial Test SF4
Model 1	1.2×10^{8}	8.1×10^{7}	–	1.1×10^{7}	1.6×10^{7}	–
Model 3	1.2×10^{9}	1.3×10^{9}	4.8×10^{9}	7.8×10^{8}	7.7×10^{8}	3.1×10^{9}

implementing Models 1 and 3. Models 1 and 3 were implemented within the RadioRT code to generate emission measure maps for UCHII regions projected at a viewing angle of 90°. Figure 2.5 and Figure 2.6 show the EM maps generated for Model 1 and Model 3 of the simulated continuum HII regions. The astronomical software CASA was used to image the resulting EM maps and the maximum and mean intensities corresponding to emission measure through the centre and average emission measure across the source were obtained respectively by drawing an ellipse to cover the overall emission measure of the modelled EM maps for the HII regions as shown in Figure 2.5 and Figure 2.6. The results from the implementation test of Models 1 and 3 were compared to the emission measure values recorded in Table 2 of Viner *et al.* (1979).

The initial results for the continuum emission from the implementation of Model 3 within the radiative transfer code exhibited intensities higher than expected, with no expected fall-off at the edges of the spherical models observed at 90°. It was found that the model was optically thicker than expected, resulting in excessively strong continuum emission. Further analysis revealed that the emission measure was overestimated by approximately a factor of 4 compared to analytic solutions and results reported by Viner *et al.* (1979). This discrepancy was traced to the scaling parameter termed the *sampling factor* in the radiative transfer configur-

ation. Originally set to 4, reducing the sampling factor to 1 resolved the issue, yielding emission measure values for Models 1 and 3 that aligned closely with those documented in Table 2 of Viner *et al.* (1979). The columns labelled "Initial Test SF4" and "SF1 (this work)" in Table 2.1 correspond to emission measures computed using sampling factors of 4 and 1, respectively, with the sampling factor of 1 adopted for the primary analysis in this work.

It is presumed that the sampling factor was introduced by Steggles (2016) to enhance the numerical integration accuracy along the line of sight by increasing the number of samples per grid cell. However, the code appears to be missing an associated renormalisation factor corresponding to this oversampling, which results in an artificial amplification of the emission measure when the sampling factor is greater than 1. Despite a thorough examination, this normalisation correction could not be located in the code base.

Given the sufficiently fine resolution of the computational grid employed in this work, a sampling factor of 1 provides adequate numerical accuracy and stability. Therefore, we adopt this value for all subsequent models to ensure the fidelity of the synthetic continuum emission calculations.

Table 2.1 compares the emission measure values obtained using the models of the RadioRT code to the values reported by Viner *et al.* (1979). The values obtained for the implementation of Model 3 (SK1) with a constant electron density, n_e=50 $\times$ 10^4 cm^{-3}, are 1.2 $\times$ $10^9 cm^{-6}pc$ and 7.8 $\times$ 10^8 $cm^{-6}pc$ for emission measure through the centre and average emission measure across the source respectively. These values agree reasonably well with the literature as seen in Table 2.1. The values obtained for model 1 also agreed reasonably well, as noted from Table 2.1. From the recorded values obtained for the emission measure, the test implementation of Models 1 and 3 using the modified version of RadioRT code is considered adequate and a true reflection for simulating emission measure maps for HII regions.

2.6 Implementation Test for Integrated Flux

In this section, the test was carried out with a focus on H109α, H85α and the continuum emission with their corresponding frequencies, 5008.9 MHz, 10522 MHz and 100000 MHz, respectively, as seen in Table 1 by Viner *et al.* (1979) and reconstructed in the test case of Appendix B by Peters *et al.* (2012). The simulated HII regions from the radiative transfer code were processed with the CASA astronomical software and used to image the resulting HII regions. The flux for the corresponding models was then determined by drawing an aperture around the source.

Table 2.2: The table shows the integrated flux results for the implementation of Model 3 and 1 of H109α, H85α and continuum emission in comparison to table 1 reported by Viner *et al.* (1979).

Radio Recombination Line	Rest Frequency (MHz)	Model 1		Model 3	
		Integrated Flux, S_ν (Jy)	Viner value: Flux, S_ν (Jy)	Integrated Flux, S_ν (Jy)	Viner value: Flux, S_ν (Jy)
H109α	5008.9	1.696	0.864	–	–
H85α	10522.0	4.1	2.734	1990	1339.0
Continuum	100000.0	37.47	24	10200	9300

Table 2.2 presents a comparison between the radiative transfer results produced with the RadioRT code and the test calculations reported by Viner *et al.* (1979). For Model 1, the integrated fluxes obtained are 1.7 Jy for H109α, 4.1 Jy for H85α, and 37.47 Jy for the continuum. The Model 3 values obtained from using RadioRT for H85α and the continuum are 1990 Jy and 10200 Jy. These values are slightly higher than those results obtained by Viner *et al.* (1979). This could be as a result of using different atomic data than Viner *et al.* (1979). These values are, however, comparable to Table 1 reported by Viner *et al.* (1979).
In terms of checking the resulting integrated flux density, a hands-on calculation using similar spherical model estimations from equation A-13 of Mezger &

Henderson (1967) is used to verify the flux density for the continuum emission of Model 3 with an estimated value of $\approx$ 9000 Jy comparable to the value of 9300 Jy published by Viner *et al.* (1979).

Table 2.3: Model Parameters of H109α for Model 1

H109α Model Parameters	
Rest Frequency	5.0089 GHz
Bandwidth	1.5 MHz
Number of channels, nchan	64
Principal Quantum Number, n	109
Turbulence broadening	15 kms^{-1}
Line of Sight Velocity, v$_{los}$	0 kms^{-1}
Distance, d	1 kpc
Sampling factor	1
Inclination angle	90°

2.7 Modelling the Line Profile for H109α

The line profile for the radio recombination line (RRL) of H109α was modelled using Model 1 and compared to Figure 2b of Viner *et al.* (1979) as shown in Figure 2.7. The radio recombination line transfer code, RadioRT, developed by Steggles (2016), was modified to produce a synthetic observation of model HII region for H109α line profile. The model parameters were set as seen in table 2.3 for comparison with table 1 for H109α reported by Viner *et al.* (1979) with a rest frequency of 5 GHz. It must be noted that the number of channels was set to 64 channels and a bandwidth of 1.5 MHz for 23.4 kHz/channels (0.3 kms^{-1}/channel) with an inclination angle of 90°. The astronomical software CASA was used to produce the line profile as shown in Figure 2.8. An aperture was drawn to cover the radio emission for the generated model to produce the brightness temperature

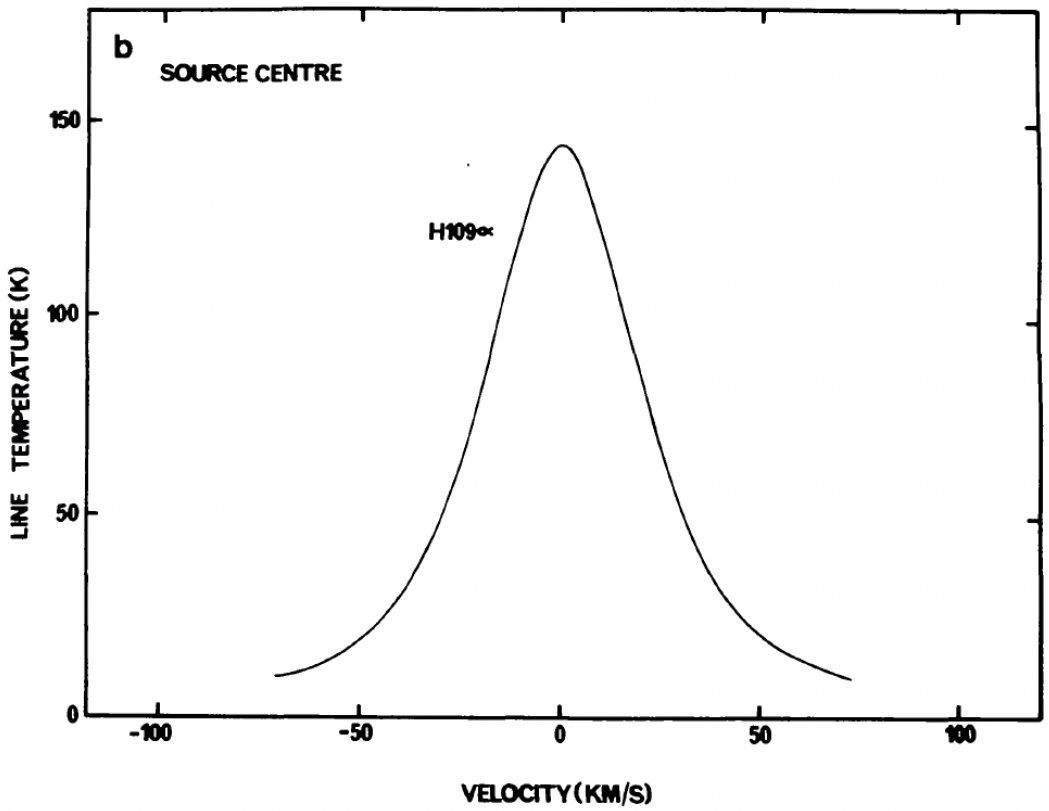


Figure 2.7: The figure illustrates the brightness temperature of the H109α radio recombination line at 5 GHz for Model 1, plotted as a function of velocity. The rest velocity is shown at 0 km s^{-1} for ray paths passing through the centre. This figure is adapted from Figure 2b in Viner *et al.* (1979).

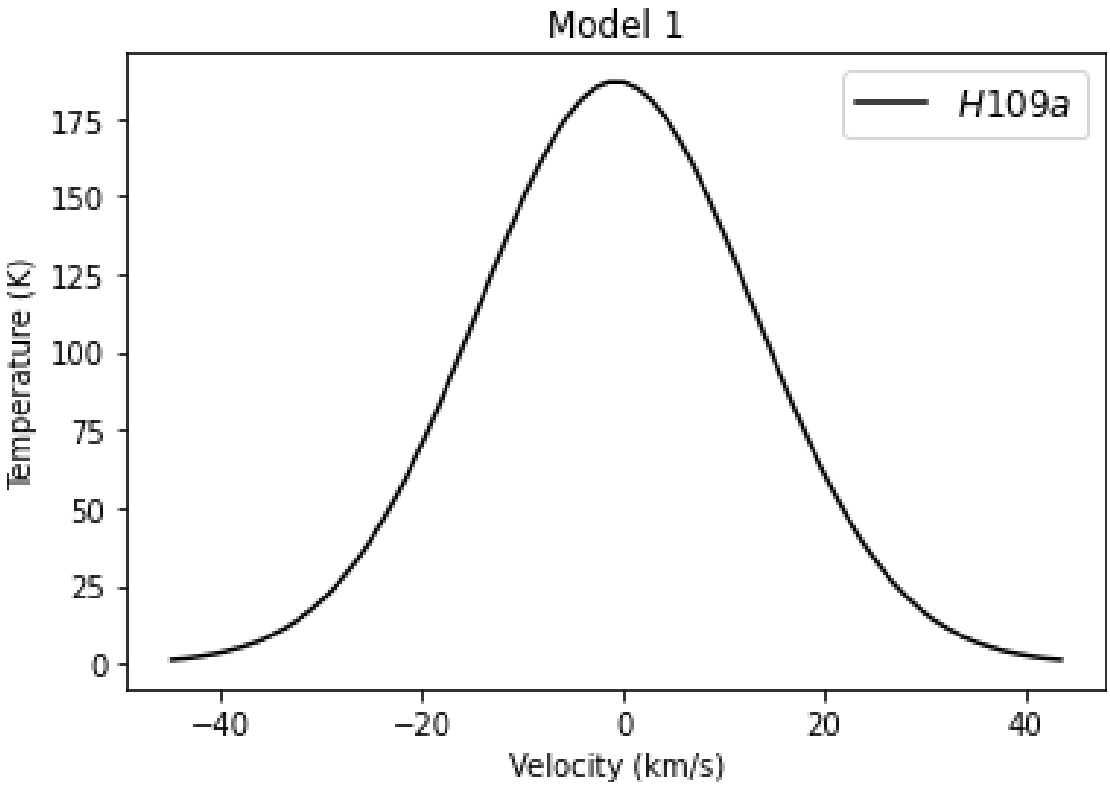


Figure 2.8: The figure shows the radio recombination line brightness temperature as a function of velocity for H109α at 5GHz for model 1. The rest velocity was set at 0 kms^{-1} and projected at a viewing angle of 90° for comparison with Figure 2.7.

in kelvin, K, for the recombination line at 5 GHz as a function of velocity in kilometres per second for ray paths through the centre of model 1. It was noted that the brightness temperature for the model (Figure 2.8) was slightly higher ($\approx$ 190 K) than that of Viner *et al.* (1979) shown as Figure 2.7. However, the full width at half maximum (FWHM) for Figure 2.7 was slightly higher as compared to the generated line profile shown in Figure 2.8. This could be a result of the non-local thermodynamic equilibrium (non-LTE) effects, which can extremely affect the line shapes and produce asymmetric line profiles from radially symmetric HII regions (Peters *et al.*, 2012; Viner *et al.*, 1979).

2.8 Expanding and Contracting Test of the Ionised Gas

1. Model 4

$$n_e = \begin{cases} 28 \times (r)^{-2} & 0.02pc \leq r \leq 0.4pc \\ 0 & \text{otherwise,} \end{cases} \quad V_r = 80kms^{-1} \tag{2.40}$$

2. Model 5

$$n_e = \begin{cases} 28 \times (r)^{-2} & 0.02pc \leq r \leq 0.4pc \\ 0 & \text{otherwise,} \end{cases} \quad V_r = -80kms^{-1} \tag{2.41}$$

A test was conducted using the RadioRT code developed by Steggles (2016) to examine the conditions under which the line profiles of symmetric H II regions appear symmetric or asymmetric. Under LTE conditions, the profiles from symmetric H II regions are expected to remain symmetric about the rest frequency, regardless of optical depth effects. In contrast, non-LTE conditions produce asymmetric line profiles (Peters *et al.*, 2012; Viner *et al.*, 1979).
The adaptive-mesh radiation transfer code RADMC-3D was used to test the effects of constant radial expansion (Model 4) and contraction (Model 5) on gas

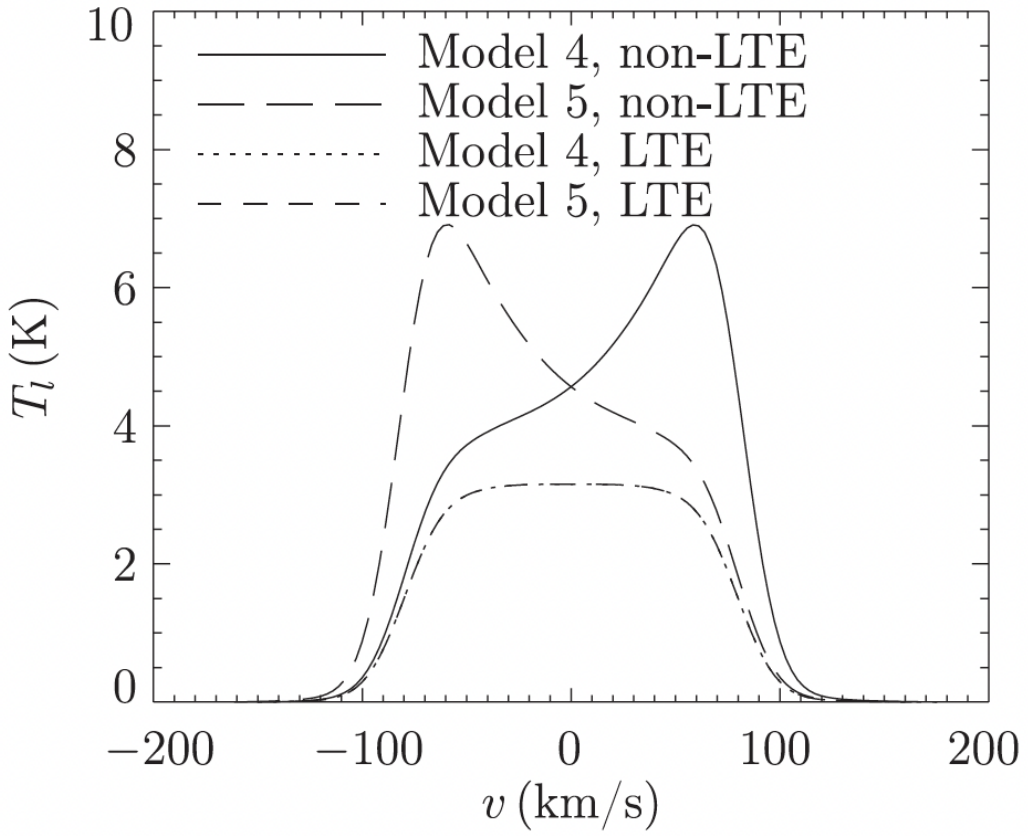


Figure 2.9: The constant radial expansion (model 4) and contraction (model 5) line profiles of H85α simulation of HII regions under LTE and non-LTE conditions. The line profiles for the LTE are the same and symmetric for Models 4 and 5, whilst the non-LTE for Models 4 and 5 are distinguishable and asymmetry. The test was conducted by Peters *et al.* (2012).

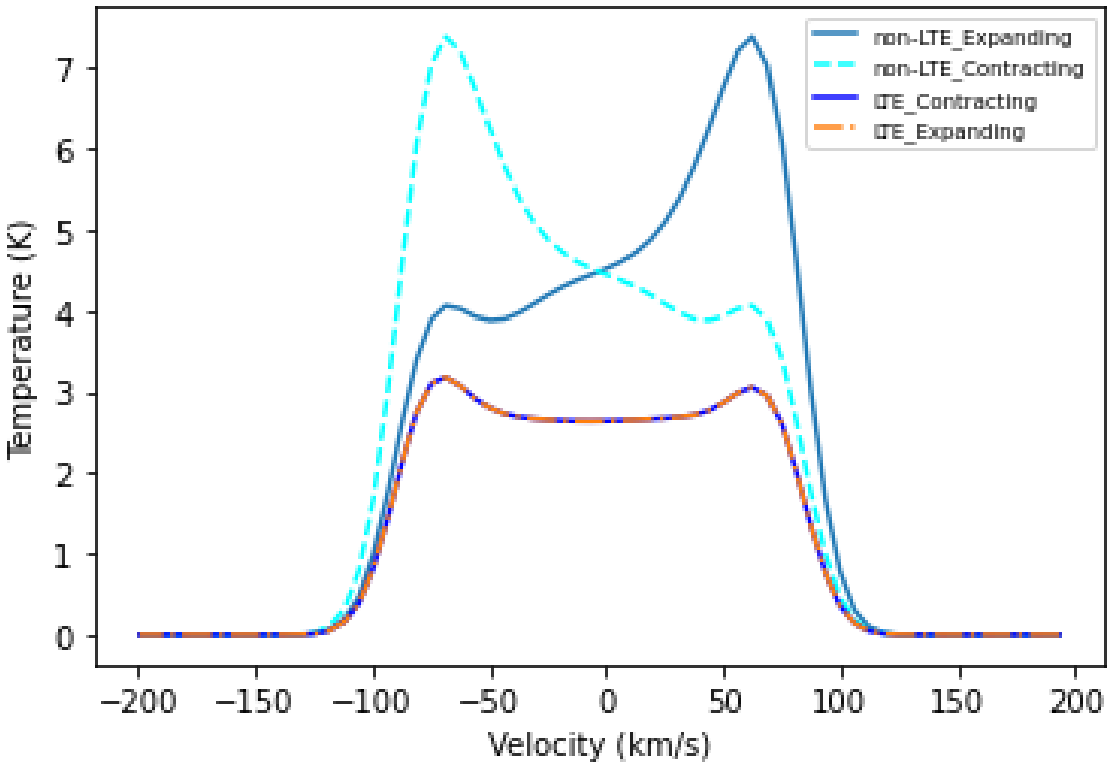


Figure 2.10: The verification of symmetric and asymmetric line profiles under LTE and non-LTE states, respectively, for H85α HII regions. RadioRT code developed by Steggles (2016) is modified to implement the expanding (Model 4) and contracting (Model 5) gas motion of H85α HII regions. The figure shows the symmetric nature of spherical HII regions under LTE and the asymmetric nature of HII regions under non-LTE conditions.

Table 2.4: Model Parameters for Expanding and Contracting gas velocity of H85α

H85α Model Parameters	
Rest Frequency	10.524 GHz
Bandwidth	14.0 MHz
Number of channels, nchan	64
Principal Quantum Number, n	85
Turbulence broadening	15 kms^{-1}
Line of Sight Velocity, v$_{los}$	0 kms^{-1}
Distance, d	1 kpc
Sampling factor	1
Inclination angle	90°

motion, allowing the influence of optical depth to be examined under both LTE and non-LTE conditions for simulated H85α symmetric H II regions (Peters *et al.*, 2012). Their results show clearly the symmetric line profiles for the LTE condition and asymmetric line profiles for the non-LTE state, as expected, as seen in Figure 2.9.

A test with RadioRT code was conducted to confirm the symmetric and asymmetric line profiles for LTE and non-LTE conditions by implementing Models 4 and 5 using H85α simulation of HII regions. Models for expanding (Model 4) and contracting (Model 5) gas velocities are considered similar to Model 1 but with a constant radial gas velocity, V$_r$, incorporated in the RadioRT code. The model parameters for simulating the H85α observations of the HII regions are given in Table 2.4. The bandwidth for the model was 14.0 MHz, divided into 64 channels as seen in Table 2.4, resulting in a spectral resolution of 218.75kHz/channel (2.9 kms^{-1}/channel). The line of sight velocity, V$_{los}$, was set at 0 kms^{-1} at a distance of 1 kpc. The sample factor corrected value of 1 was set to generate the models. The gas motion was traced for H85α using the line profiles for LTE and non-LTE conditions.

The results of the test conducted to investigate the symmetric and asymmetric line profiles under LTE and non-LTE conditions (see Figure 2.10) show great

significance in using the non-LTE conditions for simulating radio recombination lines. The symmetric nature of the spherical symmetric HII region was evidenced from the implementation test of expanding (Model 4) and contracting (Model 5) gas velocities, which have identical and symmetric line profiles under LTE conditions. The expanding and contracting gas velocities under non-LTE states are evidently asymmetric and distinguishable as seen in Figure 2.10 by implementation with the RadioRT code. The results are in good agreement with Figure 5 reported by Viner *et al.* (1979) and Figure 2.9 showing that line profiles are good indicators for the expanding and contracting of gas motion. It also confirms the significance of implementing non-LTE conditions in simulating radio recombination line profiles.

2.9 Conclusions

The results of the validation tests show that the modified RadioRT code can reproduce most of the main observational features of RRLs over a wide range of physical parameters. Tests on static symmetric H II regions showed that the profiles of lines remain symmetric in LTE after taking into account optical depth effects, while treated under non-LTE conditions, they naturally result in asymmetries expected from theory. The expanding and collapsing sphere models also showed systemic shifts and profile deformations that can be well matched to the results of Viner *et al.* (1979) and Peters *et al.* (2012).

Good agreement with synthetic line profiles and published results demonstrates the quality of the radiative transfer and non-LTE physics implemented in RadioRT. These tests also highlight the sensitivity of RRL to bulk gas motions and radiative transfer effects, thus their usefulness as diagnostics of kinematics and physical properties in ionised regions. Of particular interest, the capability to reproduce asymmetric profiles gives us confidence that the code can be used to interpret the dynamics of UCHII regions: ultra-compact H II (UCHII) regions are significantly affected by expansion, turbulence and feedback from massive stars on gas morphology.

Moreover, the code's success at capturing turbulence and velocity gradient effects indicates its applicability to more general physics like radiatively driven ionised winds, triggered star formation, and the extragalactic environment of ionised gas. This makes RadioRT a valuable tool to connect observations with theoretical models in studies concerning Galactic and extragalactic star formation regions. In this section, we have described a suite of verification tests of the modified RadioRT code that are designed to be specific for responding to radio recombination line profiles under well-defined physical conditions. The key conclusions are:

- The code can reproduce symmetric line profiles for static H II regions in LTE, and the accuracy of the radiative transfer part of the equation is tested this way.
- Non-LTE effects produce asymmetric shapes of the lines, which is in agreement with previous theoretical results, and it confirms our level population calculations.
- Simulations of expanding and contracting ionised gas spheres exhibit the expected systematic asymmetries in line profiles, which are consistent with those of published simulations.
- The code implements the effects of turbulence and velocity gradients on the emergent line properties, enhancing its applicability for physical conditions occurring in astrophysical objects.

The confidence we have in the competency of RadioRT in reproducing the kinematics and thermodynamical properties of ionised gas has been given new grounds by these results. With the validity of the implementation established, it remains to be used in real observational data of UCHII regions, where it will provide a tool to explore in detail their dynamics and feedback processes, as well as their participation in massive star formation.

Chapter 3

Modelling of the Radio and Dust Continuum Emission from DR21

3.1 Introduction

The DR21 (Downes and Rinehart 21) region is recognised as one of the most luminous and extensively researched massive star-forming complexes situated within the Cygnus X molecular cloud complex. Initially detected as a prominent radio continuum source at 5 GHz by Downes & Rinehart (1966), DR21 gained attention due to its significant microwave emissions and expansive structure. Further high-resolution studies conducted by Ryle & Downes (1967) classified DR21 as one of the earliest compact HII regions, affirming its role as a site for massive star formation embedded within dense molecular material. Located at an estimated distance of approximately 1.5 kpc based on trigonometric parallax measurements of 6.7 GHz methanol masers (Rygl *et al.*, 2012), DR21 resides within the Cygnus X complex, which is one of the most substantial molecular cloud complexes in our Milky Way galaxy. The region contains a series of dense clumps and cores that extend over several parsecs, acting as active star formation sites (Schneider *et al.*, 2010). The primary ridge of DR21 runs north-south and stands out for its strong continuum emission and robust molecular outflows, which have been examined across various wavelengths, including radio, submillimetre, and infrared spectra (Garden & Carlstrom, 1992; Jakob *et al.*, 2007).

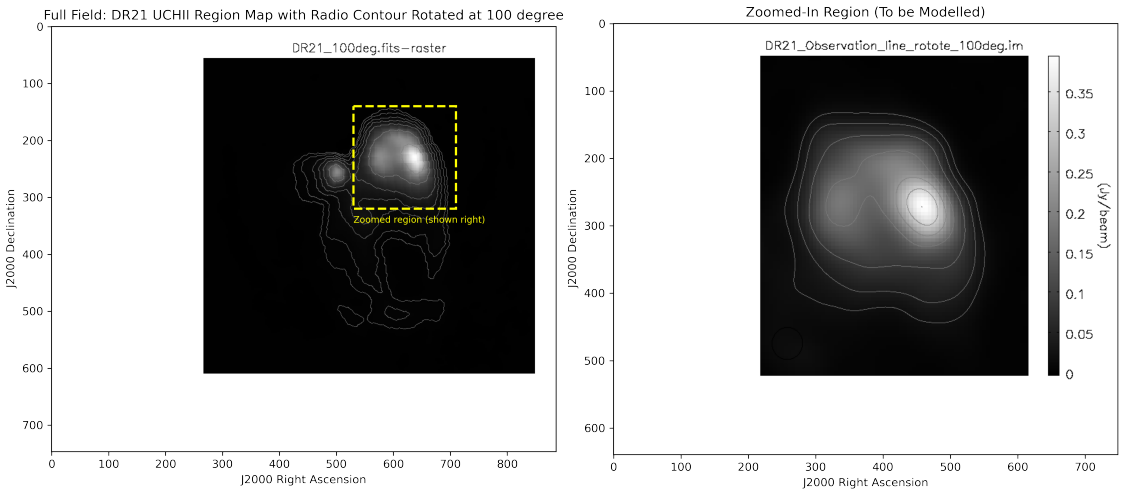


Figure 3.1: The combined image displays the radio continuum observation of the DR21 UCHII region (VLA 22 GHz, D-configuration) alongside the corresponding highlighted area selected for modelling. The left panel illustrates the large-scale structure of the DR21 UCHII region, with a marked section indicating the specific area of interest. The right panel presents a zoomed-in view of this highlighted region, which forms the focus of the modelling. It is important to note that the entire DR21 region was not modelled; only the zoomed-in subregion shown in the right panel will be analysed. The image is rotated by 100 degrees to enable comparison with the models. The data was taken from Immer *et al.* (2014)

The morphology of the DR21 complex is diverse, featuring multiple compact and ultra-compact HII (UCHII) regions, ionised jets, and dusty envelopes that illustrate the intricate relationship between massive star formation and the surrounding interstellar medium (ISM). Notably, the DR21 (Main) region has been identified as a cometary UCH II area due to its arc-like shape and density gradient (Cyganowski *et al.*, 2003; Immer *et al.*, 2014). These structures are believed to be influenced by stellar winds and ionisation fronts that interact with uneven ambient materials, resulting in distinct morphologies such as cometary shapes,

shell-like forms, and core-halo configurations (Wood & Churchwell, 1989b).
Figure 3.1 presents the DR21 UCH II region, with the right panel showing a zoomed-in view of the highlighted area that serves as the focus for the modelling. It is important to note that the image was rotated by 100 degrees to match the model's orientation for comparison. The data were obtained from Immer *et al.* (2014). The distinctive configuration of DR21, coupled with its strong free-free radio continuum emissions and extensive dust envelope, offers a valuable opportunity for examining the physical processes that govern the interaction between ionised gas and surrounding molecular matter. The radio wavelength continuum emission primarily arises from free-free emissions originating from ionised hydrogen gas, whereas the submillimetre and far-infrared emissions result from thermal radiation emitted by dust grains intermixed with molecular gas (Churchwell, 2002; Hoare *et al.*, 2007b). Consequently, modelling DR21 across multiple wavelengths can provide essential insights into the spatial distribution, along with density and temperature characteristics of both ionised and neutral components.
This chapter's main objective is to simulate and model both radio frequency and dust continuum emissions emanating from the cometary UCH II region of DR21. By juxtaposing synthetic radio continuum maps with observed spectral energy distributions (SEDs) related to dust emissions against actual observational data, we aim to refine our understanding of density structures along with temperature distributions, in addition to emission characteristics of DR21. This research employs radiative transfer simulations alongside comparisons to hydrodynamic models to interpret observed morphological features to test theoretical models of cometary UCHII regions.

3.2 Hydrodynamic Model

3.3 Hydrodynamic Model

To investigate the cometary morphology of the DR21 UCHII region, we perform cylindrical two-dimensional axisymmetric radiationâ€“hydrodynamic simulations

using the TORCH code (Steggles *et al.*, 2017). TORCH self-consistently couples hydrodynamics, photoionisation, radiative transfer, and thermal processes via an operator-split scheme to ensure numerical stability and efficiency. The simulation setup models a symmetric molecular cloud with a density gradient, offsetting the ionising star from the centre to reproduce the characteristic cometary shape observed in DR21. As with previous UCHII models (Arthur & Hoare, 2006; Mac Low *et al.*, 1991), gravity, magnetic fields, and stellar motion are neglected to focus on the effects of photoionisation and stellar winds. Details of the numerical methods, including hydrodynamic solvers, radiative transfer implementation, and thermal physics, are provided in Steggles (2016). The main parameters of the hydrodynamic code to simulate the time evolution of an HII region are described below.

3.3.1 Density Distribution

The position of a massive star with respect to the density distribution can affect the dynamical evolution of its stellar environment (Arthur & Hoare, 2006; Franco *et al.*, 1990, 2000, 2007; Tenorio-Tagle, 1979). Hofner *et al.* (2000) in their observational studies of the molecular clouds, suggested strong density gradients within the molecular clouds. Observations indicate that a more varied distribution of ambient density within the surrounding molecular cloud might be essential for creating a more accurate model (Gaume *et al.*, 1994). It is therefore necessary to set realistic density distribution parameters in models tailored to observations. The general density distribution, n(r), from the molecular cloud core centre is given by the formula;

$$n_{(r)} = n_o \left[1 + \left(\frac{r}{r_c}\right)^2\right]^{-\alpha}, \tag{3.1}$$

where the value of n_o, is the number density at the centre of the cloud core, r_c is the radius of a small flat section at the core set as 0.01 pc, r is the radius from the molecular cloud core center and the exponent is the density distribution power law index, α. Different values for the power law index have been reported using

different techniques from a range of 1 to 3 (Arquilla & Goldsmith, 1985; Franco *et al.*, 2000; Hatchell & Van der Tak, 2003; van der Tak *et al.*, 2000).

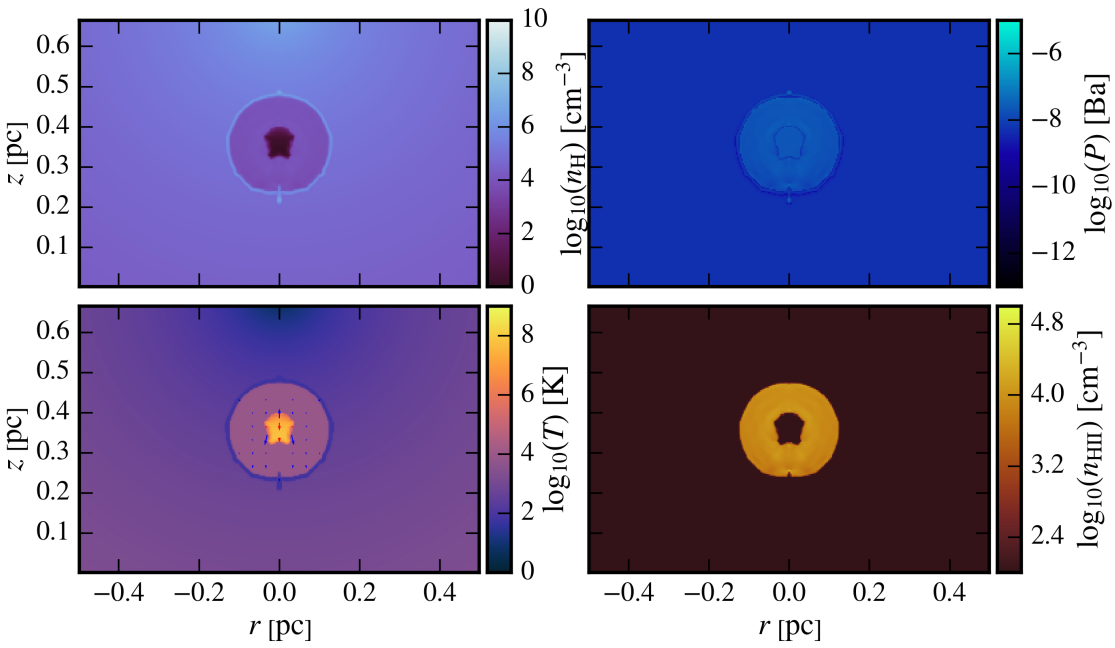


Figure 3.2: The preliminary results of the hydrodynamics simulation of UCHII region for a star with mass $20M_{\odot}$ at a simulation time of 20kyrs in a local hydrogen number density, $n_{\star}$, 1.28×10^5 cm^{-3}. Top left scale ($log_{10}(n_H)$ cm^{-3}), top right ($log_{10}(P)$ Ba), bottom left (log_{10}(T) K), bottom right ($log_{10}(n_{HII})$ cm^{-3}). The star is located at z_1=0.37 pc, r= 0.0 pc. The cloud core is at z_2=0.72 pc and r=0.0 pc. Hence Rs= 0.72 - 0.37 = 0.35 pc.

3.4 An Initial Model for DR21

An initial model was selected from the grid of models in Steggles *et al.* (2017). To obtain suitable stellar parameters of DR21, the total luminosity, $L_{\star}$ was taken as $\approx 3 \times 10^4$ L$_{\odot}$ from the RMS survey by Mottram *et al.* (2011). This corresponds to a mass of M$_{\star}$ of 20M$_{\odot}$ reported by Steggles *et al.* (2017) with an ionising photon rate of 4.9 $\times 10^{48}$ s^{-1}. Following Steggles *et al.* (2017), the mass-loss rate,

$\dot{M}_w$ of 2.57 $\times 10^{-8}$ $M_\odot yr^{-1}$ and terminal velocity, V_∞, of 2.86 $\times 10^3$ kms^{-1}, which are the stellar wind parameters were estimated using the recipe of Vink *et al.* (2001) and were taken from Steggles *et al.* (2017).

The initial gas density at the star's position follows Model F, where the star is offset from the centre of the cloud core, as described by Arthur & Hoare (2006). The corresponding density profile is implemented in TORCH following the formulation presented by Steggles *et al.* (2017), given by:

$$n_\star = n_o \left[1 + \left(\frac{R_s}{r_c}\right)^2\right]^{-\alpha} \tag{3.2}$$

The star in this model is offset from the cloud centre at a distance, Rs, of 0.35 pc taken from (Steggles, 2016) with an initial power law index, α, which assumes $\alpha = 1.5$ for the test model. It must be noted that Steggles *et al.* (2017) theoretically stated the exponent as $\frac{-\alpha}{2}$ where the code was $-\alpha$.

One set of parameters for the ionising star included a temperature of 300 K at the star's position, with temperatures decreasing toward the cloud core and increasing away from it. The simulation grid comprised, $N_r = 150$ radial and $N_z = 200$ axial cells within a box size of $L_r = 0.5, \mathrm{pc}$. The hydrodynamics simulation was run for 200 kyr, outputting data every 2 kyr, generating a total of one hundred snapshots.

Figure 3.2 shows preliminary results at an evolutionary age of 20 kyr, displaying the total number density (top left), temperature (bottom left), pressure (top right), and ionised hydrogen number density (bottom right). These correspond to a star of mass, $M_\star = 20, M_\odot$ with an initial number density at the stellar location of $n_o = 1.28 \times 10^5, \mathrm{cm}^{-3}$. The 20 kyr snapshot was chosen as it captures an early but dynamically important phase where photoionisation and stellar winds start significantly influencing the surrounding gas, shaping the characteristic cometary morphology without having yet dispersed the dense core (Arthur & Hoare, 2006).

3.5 The Radio Continuum Model

The radiative transfer ray-tracing code developed by Dougherty *et al.* (2003) was enhanced by Steggles *et al.* (2017) to post-process hydrodynamic outcomes and model radio continuum emission. This upgraded code generated the radio continuum representation for DR21, as illustrated in Figure 3.3. An inclination angle, i, of 45° was selected as the initial condition for the model, since the morphology of the continuum emission excludes a face-on orientation ($i = 0°$), which would appear circular, while the observed RRL velocity gradient rules out an edge-on orientation ($i = 90°$), as that would result in no overall velocity gradient. The initial radio continuum model for DR21, illustrated in Figure 3.3, was generated using the radiative transfer code.

The preliminary hydrodynamic model results are read out into the radiative transfer code. Expressing the radiative transfer equation in terms of optical depth gives

$$\frac{dI_\nu}{d\tau_\nu} = \frac{\xi_v}{\alpha_\nu} - I_{\nu o} \tag{3.3}$$

where $\frac{\xi_v}{\alpha_\nu}$ is the Source function, S_ν. The optical depth, τ_ν is given by

$$\tau_\nu = \int \alpha_\nu ds \triangle\tau_\nu = \alpha_\nu \triangle s \tag{3.4}$$

By multiplying equation (3) by an integrating factor $\exp \tau_\nu$ and integrating by over a path segment gives

$$I_{\nu(\,\tau_\nu)} = I_{\nu o} \exp -\triangle\tau_\nu + \int_0^{\triangle\tau_\nu} S_{\nu(\,\tau_\nu)} \exp -(\,\tau_\nu - \triangle\tau_\nu\,) d\tau \tag{3.5}$$

Since the S_ν is constant over the path length, $\triangle s$, the emergent intensity will then be

$$I_i = I_{i-1} \exp -\alpha_\nu \triangle s + \frac{\xi_v}{\alpha_\nu}(\,1 - \exp -\alpha_\nu \triangle s\,) \tag{3.6}$$

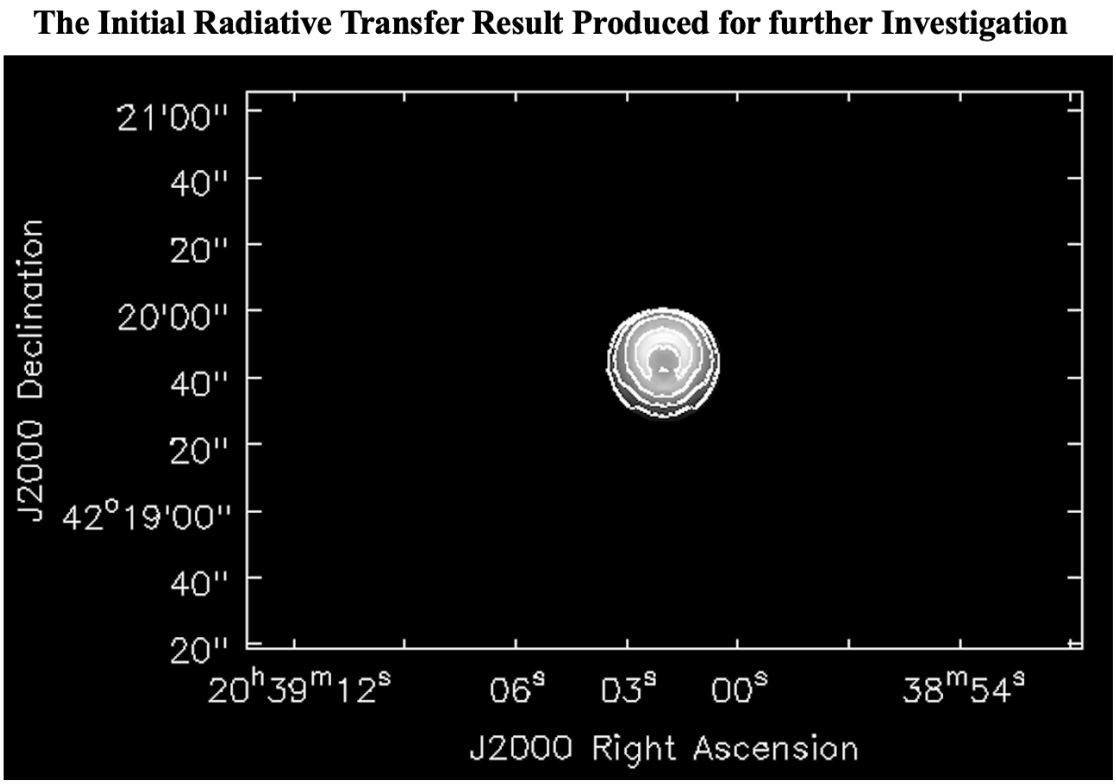


Figure 3.3: The radio continuum emission model at 22GHz generated for the initial hydrodynamic model in figure 3.2 for the cometary DR21 UCHII region. This figure has a viewing angle of 45°, at a distance of 1.5 kpc, contour levels at 0.2, 0.4, 0.6, and 0.8 Jy/beam, and is not smooth.

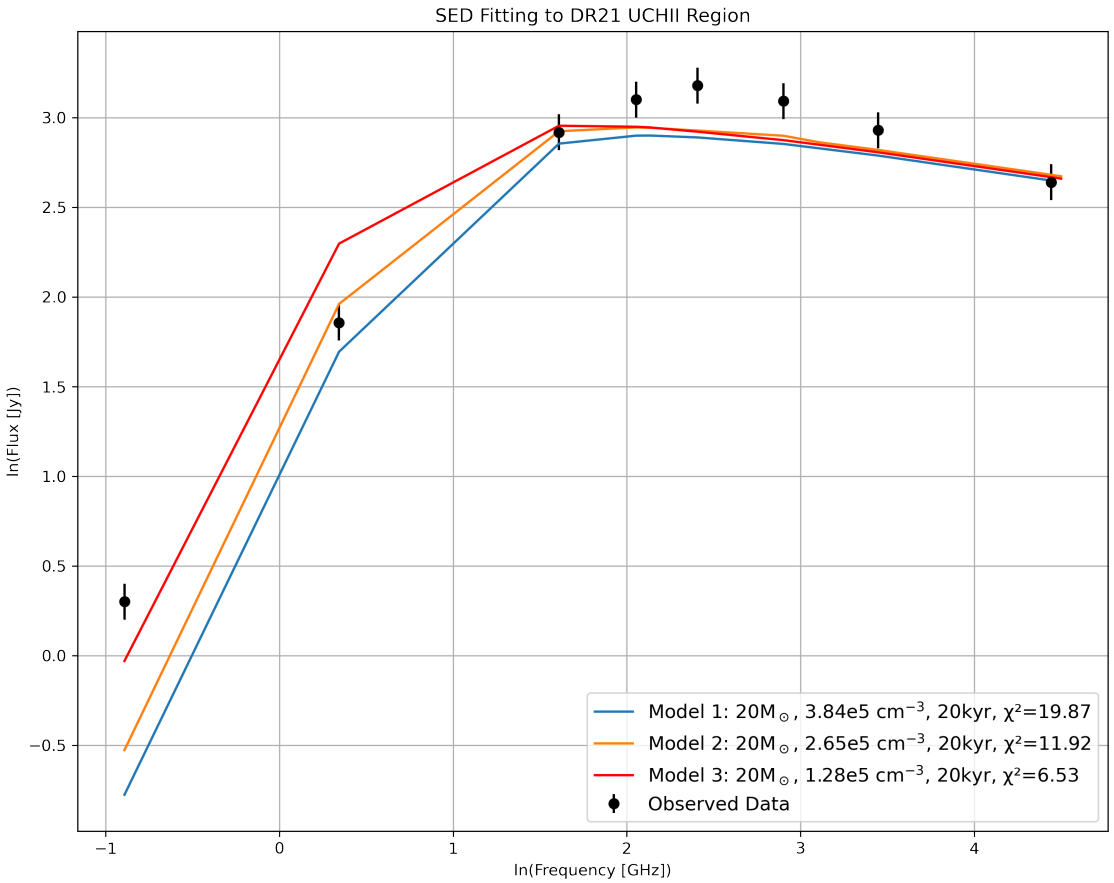


Figure 3.4: The radio spectrum fitting to DR21 UCHII region. The constant age (size) of 20kyrs is varied with the number densities, n_0. The black circles with error bars represent observational fluxes from Harris & Scott (1973). Model SEDs for three ambient densities generated using SED results from the hydrodynamic models are shown, with the best-fitting model ($n_0 = 1.28 \times 10^5$ cm^{-3}) highlighted in red.

3.5.1 Derivation of the preliminary Density Distribution for DR21 UCHII Region

By referring to the spectral energy distribution (SED) of DR21 taken from Harris & Scott (1973), a density for DR21 was obtained by fitting the SED models for 20kyrs of DR21 to the observations, as shown in Figure 3.4. The total model fluxes were obtained by drawing an aperture to cover the radio continuum emission for the corresponding fluxes, frequencies, and values noted for the model SED plots. To model the physical conditions within the DR21 ultra-compact HII region, a preliminary density distribution was derived based on the observed spectral energy distribution (SED) and radiative transfer simulations. The goal was to estimate the ambient number density (n_0) of the ionised gas that best reproduces the observed radio fluxes. The method involved the following steps:

1. **Compilation of Observational Data:** Flux densities at multiple radio frequencies were compiled from Harris & Scott (1973). The spectral energy distribution of the compact HII region DR 21 has been extensively studied across a broad frequency range, employing various radio telescopes with different beamwidths and resolutions. Here we summarise the key observational results relevant for SED construction, focusing on antenna types, frequencies, flux densities, beamwidths, and limitations associated with these data. Below is the observational data extracted from Figure 2 in Harris & Scott (1973).

    - **Haystack 120-foot Antenna**: Used by Dent (1972) for measurements at 7.8 GHz (3.8 cm) and 15.5 GHz (1.9 cm) with beamwidths approximately $6'$ at 7.8 GHz and $2'2''$ at 15.5 GHz.
    - **NRAO 36-foot Antenna**: Employed for millimetre-wave measurements at 31.4 GHz (9.5 mm) with a beamwidth near $2'2''$ Dent (1972); Downes *et al.* (1970). Observations at 85.0 GHz with a $1.2'$ beamwidth were also carried out Downes *et al.* (1970).
    - **Cambridge 1-mile Radio Telescope**: Used by Ryle & Downes (1967) and Wynn-Williams (1971) for lower-frequency observations at

0.408 and 1.407 GHz with beam half-power beamwidths (HPBW) of $80'' \times 118''$ at 0.408 GHz, and $23'' \times 34''$ at 1.407 GHz.

- **Cambridge 5-km Telescope**: Harris & Scott (1973) provided flux densities at 5.0 GHz with very high spatial resolution having synthesised beam of $2.0'' \times 3.0''$.

Table 3.1 summarises the flux density measurements, frequencies, beamwidths/resolutions, and observatory details for DR 21 from the listed references.

Table 3.1: Flux density measurements of DR 21 at multiple frequencies. Flux densities are in units of 10^{-26} W m^{-2} Hz^{-1}.

Frequency (GHz)	Flux Density	Beamwidth / Resolution
0.408	1.35 (combined components A & B)	$80'' \times 118''$
1.407	6.4 (component A)	$23'' \times 34''$
2.7	∼16	few arcseconds (implied)
5.0	18.5	$2.0'' \times 3.0''$ (Cambridge 5 km telescope)
7.8	∼22	$6'$
15.5	∼20	$2'2''$
31.4	18.7	$2'2''$ (Haystack)
85.0	∼14	$1.2'$

The flux densities reveal that above ∼3 GHz the emission from DR21 remains approximately constant near 20 flux units (1 flux unit = 10^{-26} W m^{-2} Hz^{-1}), consistent with thermal bremsstrahlung from compact H II regions (Dent, 1972; Downes *et al.*, 1970). A slight decline at higher frequencies (31.4 and 85 GHz) aligns with the expected spectral behaviour of such sources. The beamwidth variation implies differing spatial resolutions across frequencies: lower-frequency observations exhibit broader

beams, leading to blending of multiple components and extended emission (e.g., at 0.408 GHz and 1.407 GHz), which may result in overestimation of compact component fluxes. Conversely, higher frequencies with smaller beams (down to a few arcseconds) resolve these compact components more cleanly. Cross-comparison of flux densities should be treated with caution without beam-matching, as differing spatial scales can bias the SED shape. Overall, these factors necessitate careful consideration when plotting and modelling the SED of DR 21 to avoid misinterpretations of its thermal emission spectrum.

All fluxes were converted into logarithmic space, $\log S_\nu$ vs. $\log \nu$, to facilitate comparison with theoretical SEDs. Table 3.1 shows the compilation of the SED for the observed data. For ease of comparison with the models, constant error values (0.1) were adopted for the flux measurements.

2. **Selection of Model Parameters:** Radiative transfer models were constructed for a central star of mass $M_* = 20\ M_\odot$ and an evolutionary age of 20 kyr. The density of the ambient hydrogen number n_0 was treated as a free parameter and varied systematically over a plausible range:

$$n_0 = 3.84 \times 10^5,\ 2.65 \times 10^5,\ 1.28 \times 10^5\ \text{cm}^{-3}. \tag{3.7}$$

Three models were considered, each with the same stellar mass (20 $M_\odot$) and evolutionary age of 20 kyr, but differing in their initial ambient number density (n_0). These models are summarised in Table 3.2.

Table 3.2: Parameters of SED models for DR21 (Main) at 20 kyr.

Model	Stellar Mass ($M_\odot$)	Ambient Density (n_0 [cm^{-3}])	Age (kyr)
A	20	3.84×10^5	20
B	20	2.65×10^5	20
C	20	1.28×10^5	20

3. **Comparison with Observations:** For each model, the synthetic SED was calculated at each observed frequency. The reduced chi-square statistic

(χ^2_ν) was calculated to quantify the goodness of fit:

$$\chi^2_\nu = \frac{1}{N-1}\sum_{i=1}^{N}\left(\frac{\log S_{\nu,\mathrm{obs},i} - \log S_{\nu,\mathrm{model},i}}{\sigma_i}\right)^2, \tag{3.8}$$

where N is the number of data points, and σ_i is the observational uncertainty. The results are summarised in Table 3.3.

Table 3.3: Reduced χ^2_ν values for SED fitting of DR21.

Model	n_0 (cm^{-3})	Reduced χ^2_ν
Model 1	3.84×10^5	19.87
Model 2	2.65×10^5	11.92
Model 3	1.28×10^5	6.53

4. **Identification of Best-Fit Density:** The model with ambient density $n_0 = 1.28 \times 10^5$ cm^{-3} provides the lowest reduced chi-square and reproduces the observed SED most accurately as shown in Figure 3.4. This model correctly matches the flux turnover near 5-10 GHz, corresponding to the transition from optically thick to optically thin free-free emission. Models with higher densities underestimate the low-frequency flux, while models with intermediate densities still produce higher χ^2_ν values than the best-fit model.

In conclusion, preliminary SED analysis indicates that the DR21 UCHII region is best described by a 20 $M_\odot$ star embedded in a medium of density $n_0 \approx 1.28 \times 10^5$ cm^{-3} at an age of $\sim$ 20 kyr. This configuration successfully reproduces both the shape and magnitude of the observed SED, consistent with a moderately dense cometary ultra-compact HII region as indicated in Figure 3.4. The results obtained using radio spectrum fitting reveal a relatively high density and young age, indicating an early stage in massive star formation. The generated hydrodynamic results at 20kyrs are read out into the radio transfer code with the observational parameters (frequency of observation, bandwidth, line-free channels, distance, etc) taken from the deep H66α observations of the cometary

HII regions in DR21, at 22GHz obtained with the Very Long Array (VLA) by Immer *et al.* (2014) to reproduce the initial synthetic DR21 UCHII region as shown in Figure 3.3 for further investigation. Figure 3.3, displays the model radio continuum image of the cometary DR21 UCHII region with the mass of $20M_{\odot}$, inclined at an angle of 45° at 20kyrs. The star in this model is offset from the cloud centre at a distance, Rs, of 0.35 pc taken from (Steggles, 2016) with an initial power law index, α, which assumes $\alpha = 1.5$ for the test model.

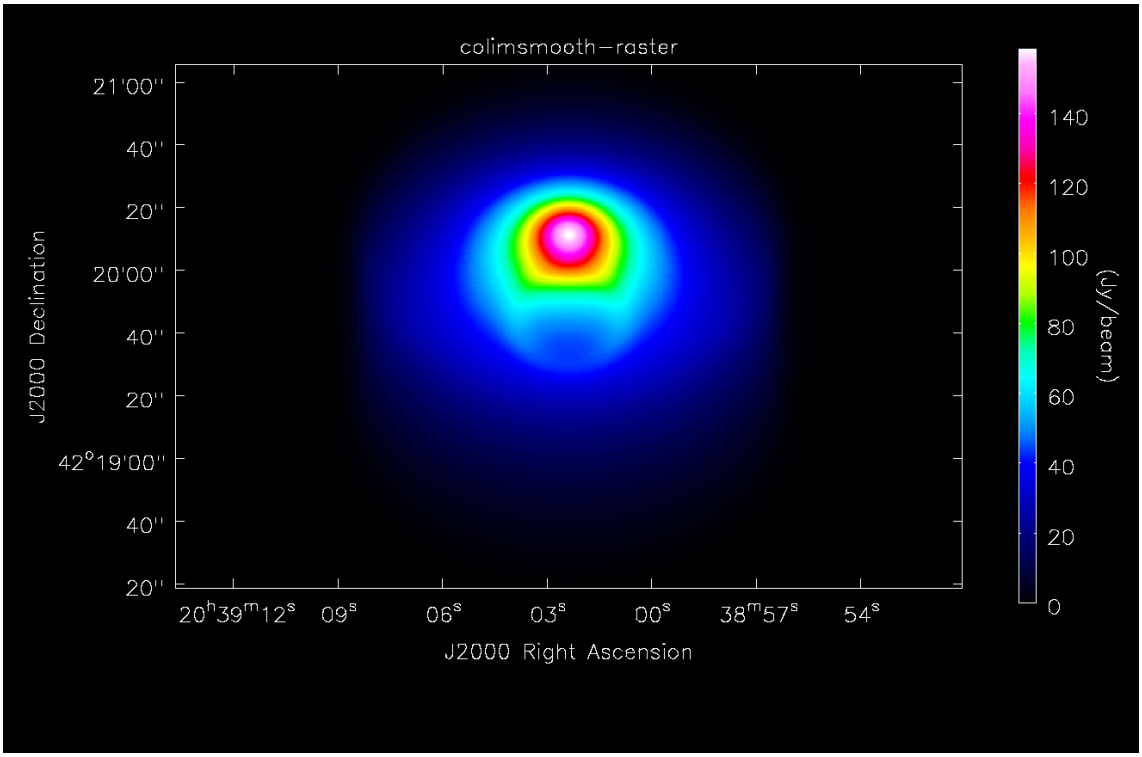


Figure 3.5: The figure shows initial result with $\alpha = 1.5$ for the modelled dust continuum map smoothed to SCUBA 450μm resolution with number density, $n_{\star}$ = 1.28×10^5 cm^{-3} and age of 20kyrs to be used for further investigation. This is obtained by generating a column density map scaled to intensity[Jy/beam] and smoothed to 7.9" SCUBA 450μm resolution with an inclination angle of 45°.

3.6 Dust-Continuum Emission of DR21

The parameters for the density distribution of the molecular cloud, which forms an integral part of the dynamics of DR21 as shown in equation 3.1, Rs and α, must be constrained for the models. The Sub-millimetre dust emission can be used to probe the molecular cloud environment. The thermal dust continuum emission from DR21 was modelled with reference to the Sub-millimetre Common User Bolometric Array (SCUBA) at 450μm observation of DR21. The radiative transfer code of Steggles (2016) was modified to calculate a column density image at a particular viewing angle.

To model the synthetic dust continuum map of DR21, the column density, N_{H2}, the map generated from the radio transfer code follows the general equation given by:

$$N_{H_2} = \int_0^s n_{H_2} ds \tag{3.9}$$

To enable a direct comparison between the flux densities of the modelled dust continuum maps and the observed SCUBA 450 μm data of DR21, the column density maps were converted to intensity units [Jy beam^{-1}], denoted as S_ν. This conversion was performed using the relation from Urquhart *et al.* (2013), originally derived by Hildebrand (1983), expressed as:

$$S_v = \frac{N_{H_2} \Omega \kappa_\nu \mu m_H B_v \left(T_{dust}\right)}{\gamma} \tag{3.10}$$

Here, γ is the gas-to-dust mass ratio, taken as 100; $B_\nu(T_{\rm dust})$ is the Planck function; $T_{\rm dust}$ is the dust temperature; Ω represents the solid angle of the 7.9$''$ beam for SCUBA at 450 μm; $m_{\rm H}$ is the mass of a hydrogen atom; μ is the mean molecular weight of the gas, adopted as 2.8; and κ_ν is the dust absorption coefficient. A value of $\kappa_\nu = 1.85$ cm^2, g^{-1} was adopted from Schuller *et al.* (2009). Although this opacity coefficient was originally derived for observations at 870 μm, it was applied here as an approximate value for the SCUBA 450 μm data of DR21 due to the absence of directly measured κ_ν at this wavelength in the literature. It should be noted that there is considerable uncertainty associated with opacity

values; therefore, our analysis primarily relies on normalised intensity profiles to constrain the density distribution, thereby minimising the impact of the absolute opacity uncertainty. This assumption provides a reasonable estimate for comparing modelled and observed fluxes while maintaining consistency with previous submillimeter studies. A uniform dust temperature, T_{dust}, was assumed, and a value of 36K for DR21 was taken from Roy *et al.* (2011). To compare the model to the observation, the intensity map was smoothed to 7.9″ SCUBA 450μm resolution as shown in Figure 3.5. The derived peak flux density, $S_{\nu,\mathrm{peak}} = 140 \pm 2.5$ mJy for the observed dust continuum emission, is in close agreement with the modelled value of ∼142 mJy obtained for the simulated dust continuum map of DR21, indicating a good consistency between the observational and modelled results.

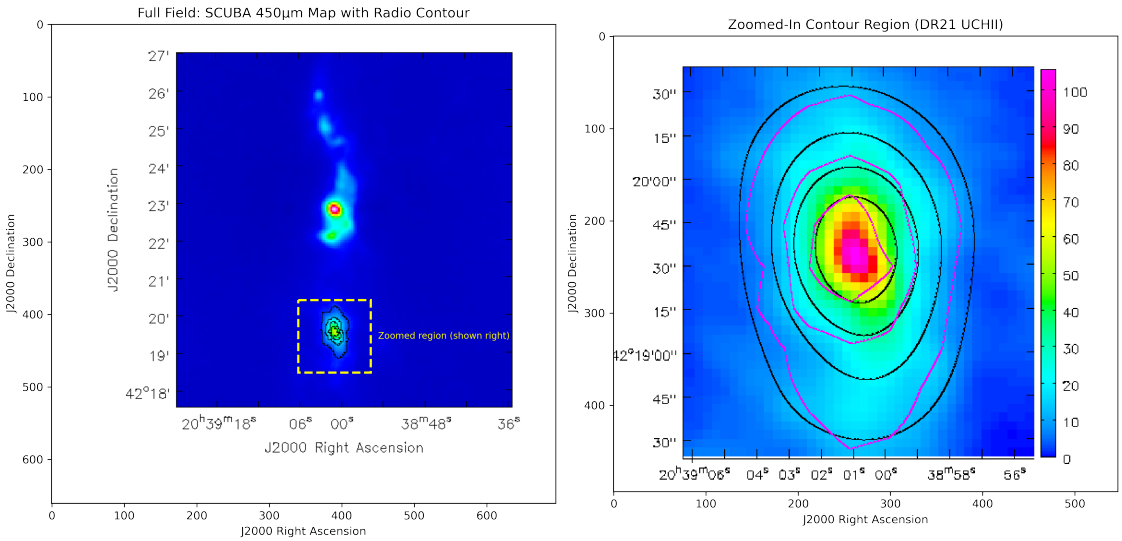


Figure 3.6: Combined image showing the SCUBA 450μm dust continuum emission of DR21 and the corresponding Herschel 500μm data. The left panel presents the large-scale structure of DR21 with a zoomed-in view highlighting the DR21 UCHII region, while the right panel overlays the SCUBA 450μm (raster) and Herschel 500μm (magenta contour) data, as well as the SCUBA 450μm smoothed to 500μm resolution (black contour), to verify the astrometry of the SCUBA observation.

3.6.1 Astrometry of DR21 Dust-Continuum Emission

To verify the SCUBA 450μm data for DR21 used to estimate the value of Rs, to model the synthetic cometary DR21 UCHII region, it is essential to check the astrometry of the observations to confirm that it falls within the expected uncertainty. The astrometry of the SCUBA 450μm observation of DR21 is checked by overlaying on the lower resolution, but better astrometry Herschel 500μm data of DR21 and smoothing the SCUBA 450μm data to the Herschel 500μm resolution as shown in Figure 3.6. The CASA task Imfit is used to determine the offsets at Right Ascension, $\alpha = 1.8''$ and Declination, $\delta = 1.4''$ for the position of DR21 SCUBA 450μm data Herschel 500μm observation of cometary DR21 UCHII region. The estimated offsets are within the expected astrometry uncertainty for the Herschel 500μm with an absolute pointing accuracy between $\approx$ 2" (Pascale *et al.*, 2011; Pilbratt *et al.*, 2010).

Table 3.4: Constraining the Model Parameters for DR21

Observations/Model Constrain	Primary Parameter	Secondary Parameter
Radio Horizontal Slice Profile	Age (size)	number density, n_o
Dust Horizontal Slice Profile	Power Law Index, α	Distance between the star and the cloud core, Rs
Vertical Slice between Radio and Dust	Distance between the star and the cloud core, Rs	Angle of inclination, ι
Spectral Energy Distribution (SED)	number density, n_e	Age (size)

3.7 Systematic Approach for Constraining Model Parameters of DR21

To accurately reproduce the observed dust and radio continuum structures of the DR21 UCHII region, a systematic and iterative modelling approach was employed to constrain the relevant parameters. The process followed a logical progression, comparing key observational diagnostics with their modelled counterparts to refine the physical parameters of the source progressively. Table 3.4 serves as a guide, summarising the relationships between each observational constraint and the primary or secondary model parameters affected.

3.7.1 An Overview

The modelling process began with the parameters obtained from the literature, particularly those of Steggles (2016), which provided the foundation for the density, source size, and flux distributions. As shown in Figure 3.4, the optimal density was determined to be $n_0 = 1.28 \times 10^5$ cm^{-3}. In addition, a range of density power-law indices, $\alpha = 0.5,\ 1.0,\ 1.5$, and 2.0, was explored to assess their effect on the spatial and flux distributions of the modelled emission. The initial distance between the ionising star and the cloud core, $R_s = 0.35$, adopted from Steggles (2016), was also examined and refined based on the spatial separation between the radio and dust continuum peaks. Furthermore, the initial model age of 20 kyrs was varied to evaluate its influence on the overall morphology and to constrain the evolutionary stage of DR21 UCHII region. These initial parameters were tested to provide a baseline for comparison.

3.7.2 Derivation of the Separation Distance between the star and the cloud core, R_s

Vertical slices through the radio and dust continuum peaks were used to determine the offset and geometry between the emission regions by comparing observations

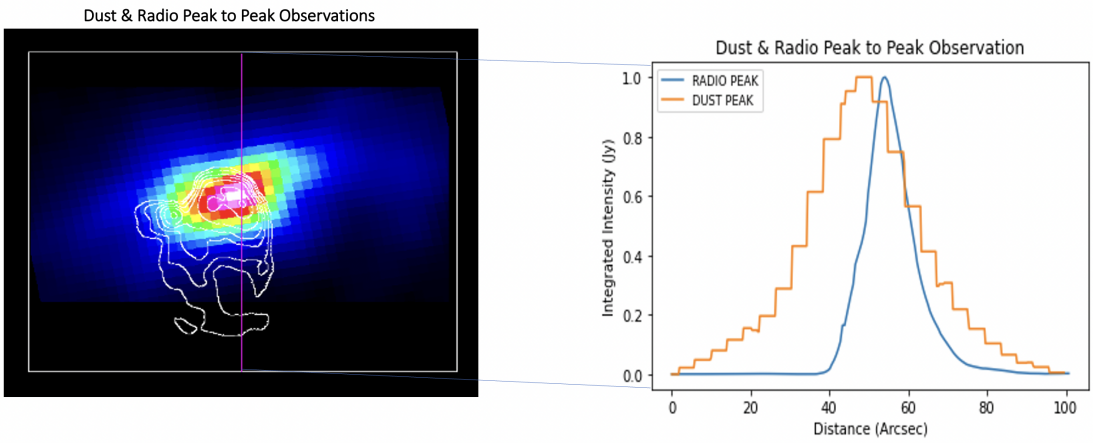


Figure 3.7: The figure shows an overlaid plot of the radio (displayed as a contour) and dust (displayed as a raster image) continuum emission from DR21 observations on the left, with a vertical slice through their peaks. The plot on the right is the corresponding line profiles showing the difference between the two peaks measured as 5.4″ for the radio and dust continuum emission. The overlaid radio and the dust images are rotated at 100 degrees to compare with the models. The data was taken from Immer *et al.* (2014)

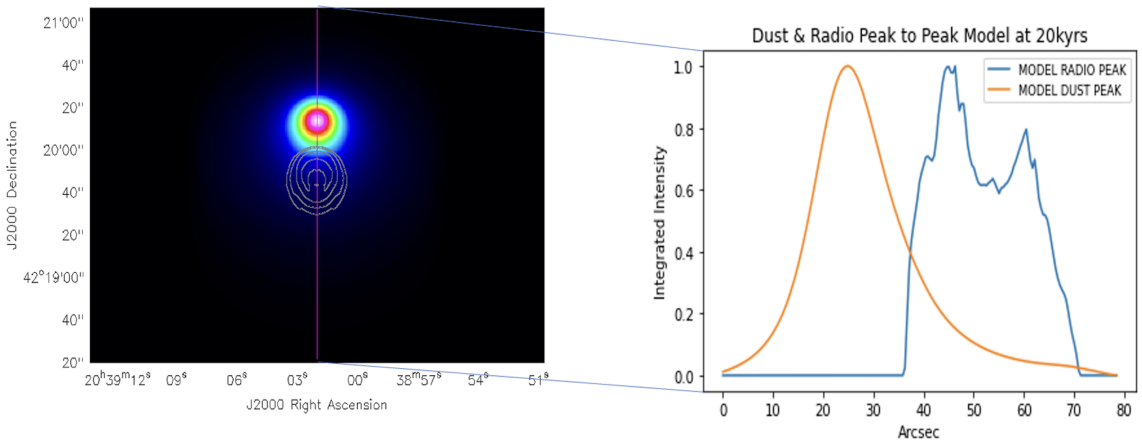


Figure 3.8: The figure shows an overlaid plot for the models of the radio (displayed as a contour) and dust (displayed as a raster image) continuum emission from DR21 on the left, with a vertical slice through their peaks. The plot on the right is the corresponding line profiles showing the difference between the two peaks measured as 23.″. The models have initial number density, n_o= 1.28 × 10^5 cm^{-3}, Rs=0.35 pc, α= 1.5 at an age of 20kyrs and inclination angle of 45°. The contour levels for the radio are 0.2, 0.4, 0.6 and 0.8 Jy/beam.

(radio continuum (VLA 22 GHz) and dust continuum (SCUBA 450 μm)) to the models, as shown in Figure 3.7 for the observed data and Figure 3.8 for the models. These slices constrained the distance between the ionising star and the cloud core, R_s and the inclination angle ι, as they directly affect the spatial offset between the radio and dust peaks. Observations revealed a peak separation of 5.4″, as shown in Figure 3.7, whereas models with $R_s = 0.35$ pc produced a separation of 21.3″ (see Figure 3.8), indicating that smaller R_s values and adjustments to the inclination angle are necessary.

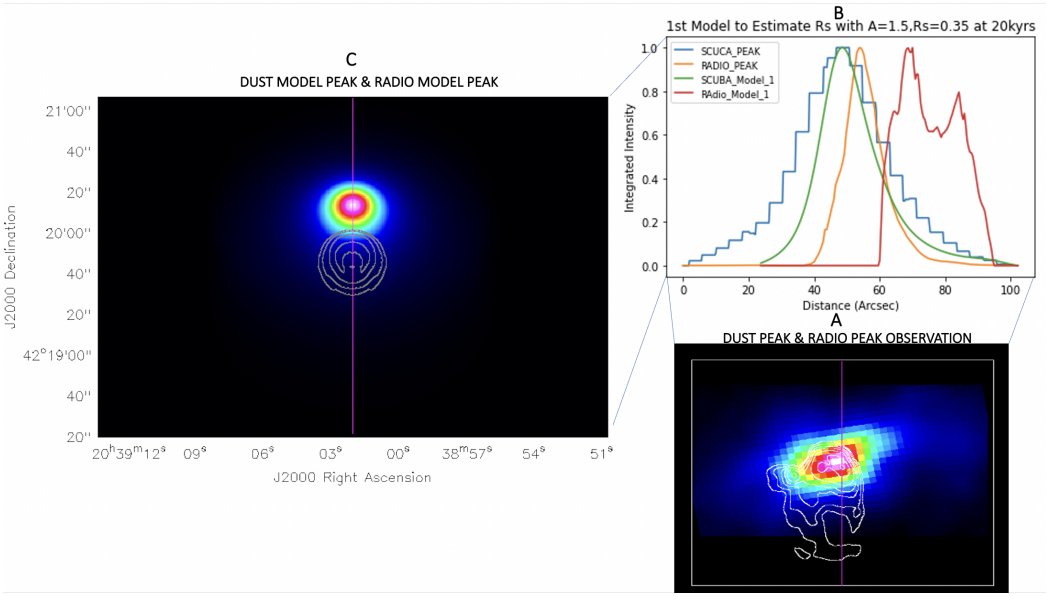


Figure 3.9: This figure shows the results from slicing in the vertical plane for the overlaid dust (raster) and radio continuum (contour) observations, both rotated by 100° (labelled A), and the corresponding generated models (labelled C). The plot labelled B shows the distance between the two peaks for the observations and models for $\alpha = 1.5$, $R_s = 0.35$ at 20 kyr. The distance between the two peaks for the dust and radio continuum observations is 5.4″, and that of the models is 21.3″. This is used to constrain the distance between the star and the cloud core, R_s.

Figures 3.9 and 3.10 show the slice through the vertical plane of the overlaid

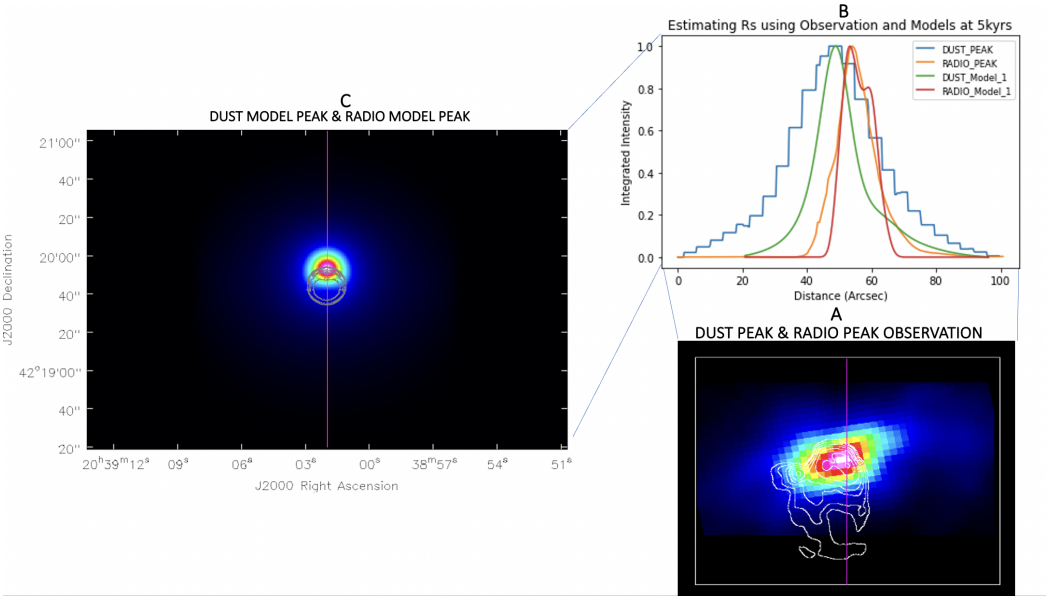


Figure 3.10: This figure is similar to Figure 3.9. Here, the best-fit model parameters of $\alpha = 1.0$, $n_o = 1.28 \times 10^5$ cm^{-3} at 5 kyr, with an inclination angle of 45°, are used for the models. The distance between the two peaks for the dust (raster) and radio (contour) continuum observations was measured as 5.4″, and the corresponding model value was estimated as 4.6 ± 0.8″.

SCUBA 450μm data and Very Large Array (VLA) 22 GHz D-configuration radio continuum data of DR21, labelled A, along with their corresponding models labelled C. These slices were used to estimate the separation distance between the two peaks in both the observations and the models. The distance between the two peaks for the observations was calculated as 5.4″ and that of the models was corrected from the initial value of 21.3″ to 4.6 ± 0.8″. The value of R_s was deduced by taking into account the projected inclination angle of 45 degrees from the observer. The value of R_s was estimated to be 0.07 pc, as illustrated in Figure 3.10. This estimation was made by comparing it to the initial model separation of $R_s = 0.35$ pc shown in Figure 3.9. The value of $R_s = 0.07$ was adopted and used to model the observed cometary DR21 UCHII region.

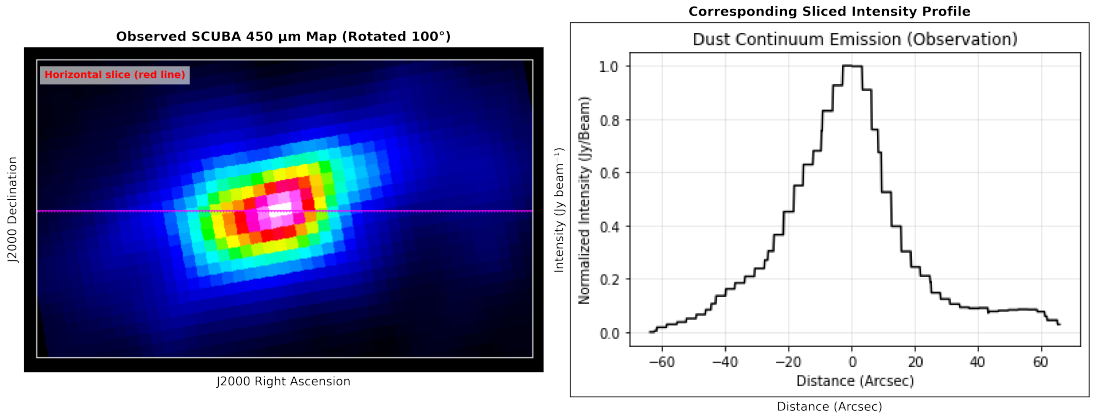


Figure 3.11: The illustration presents the dust emission from DR21 as observed by SCUBA at a wavelength of 450μm, rotated by 100 degrees, with a horizontal slice through the midpoint displayed in the left panel. The red horizontal line mark indicates the slice taken through the map to extract the flux distribution used in the analysis. The intensity profile derived from this horizontal slice is shown in the right panel. This graph illustrates the variation of flux along the slicing direction and acts as a reference for comparison with models to determine the optimal value of α.

3.7.3 Analysis of Dust Continuum Profiles and Density Power-Law Index Estimation

To estimate the density power-law index, α, for the DR21 UCHII region, the observed SCUBA 450 μm dust continuum map was rotated by 100° to align with the primary axis of the emission structure. A horizontal slice was then extracted through the midplane of the emission peak to examine the dust column density distribution along the core-envelope interface. This spatial profile was used to constrain α by comparing the observed intensity gradient to a suite of modelled dust continuum emissions.

A set of four radiative transfer models was generated with varying density power-law indices of $\alpha = 0.5,\ 1.0,\ 1.5$, and 2.0, while maintaining constant physical parameters: distance between the ionising source and the cloud core $R_s = 0.07$ pc, number density $n_0 = 1.28 \times 10^5$ cm^{-3}, inclination angle 45°, and an evolutionary

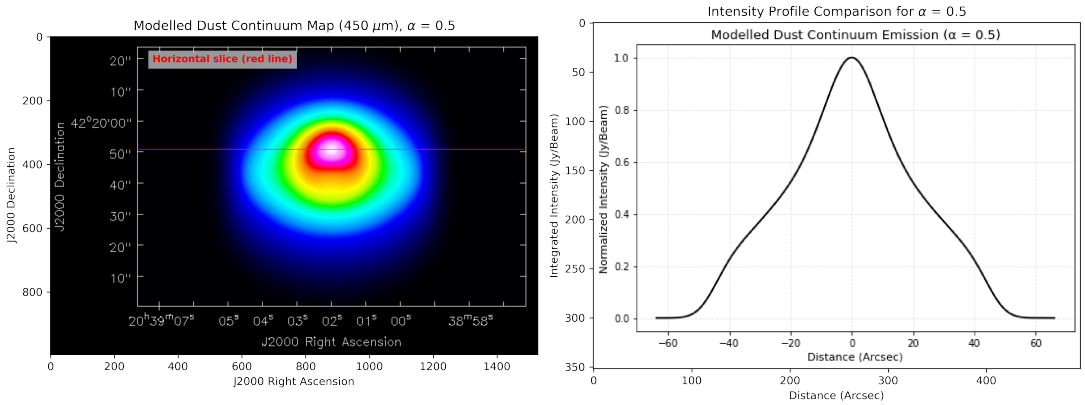


Figure 3.12: The figure shows the normalised dust column density for DR21 at 5kyrs with Rs=0.07 pc, n_o=1.28×10^5 cm^{-3}, inclination angle of 45°, and α=0.5 displayed at left-hand side. The line profile at the top-right corner shows the resulting plot for the horizontal slice through the midpoint of the modelled dust emission.

age of 5 kyrs. The resulting model intensity profiles (Figures 3.12-3.15) were compared directly to the observed dust continuum slice shown in Figure 3.11. The analysis showed a consistent pattern indicating that the spatial range of the simulated dust emission decreases with increasing α. This aligns with the anticipated physical understanding that steeper density gradients result in more compact emission structures.

The models were smoothed to 7.9″ SCUBA 450μm resolution. The combined results from the horizontal slice through the midpoint plane for the observed DR21 and the models of the dust continuum emission are displayed as seen in Figure 3.16. Each model was normalised to facilitate direct comparison with the observed profile. The reduced chi-square values (χ^2_ν) were calculated to quantify the statistical agreement between each model and the observed data. For visual clarity, the chi-square values have been included in the legend of the plot. In Figure 3.16, it is evident that the model with $\alpha = 1.0$ provides the closest match

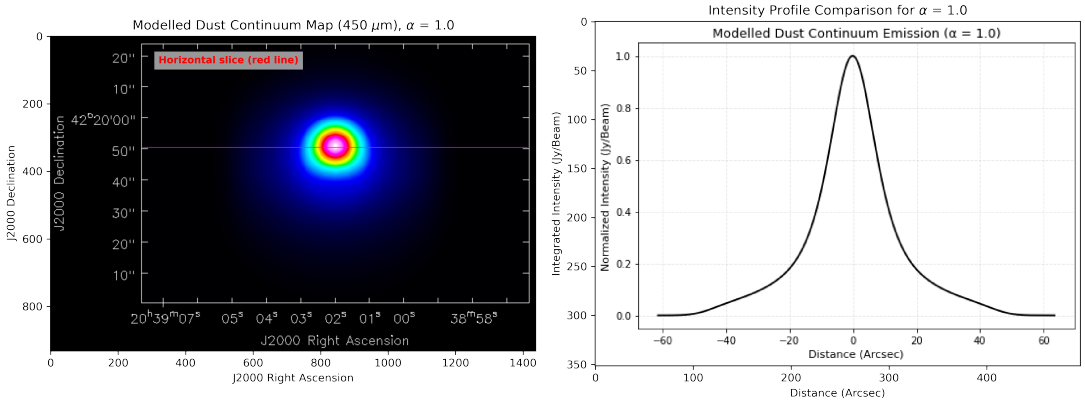


Figure 3.13: Same as figure 3.12 but with α of 1.0. The line profile at the top-right corner shows the resulting plot for the horizontal slice through the midpoint of the modelled dust emission.

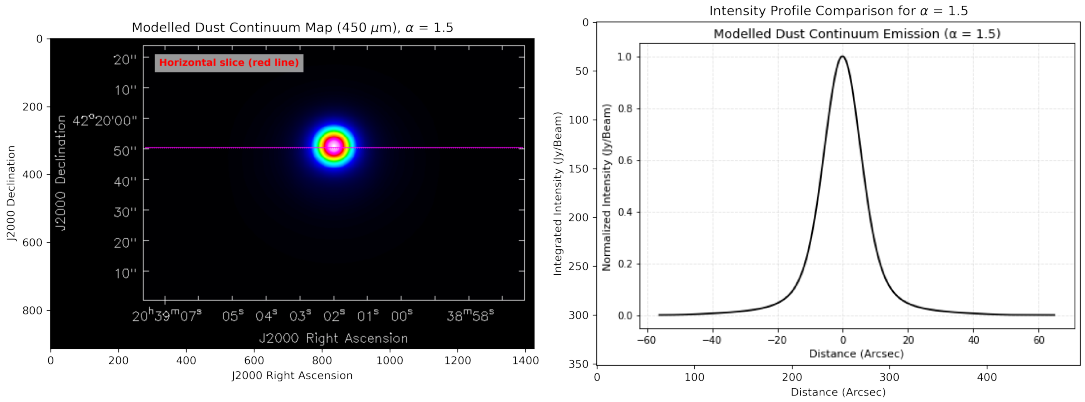


Figure 3.14: Same as figure 3.12 but with α of 1.5. The line profile at the top-right corner shows the resulting plot for the horizontal slice through the midpoint of the modelled dust emission.

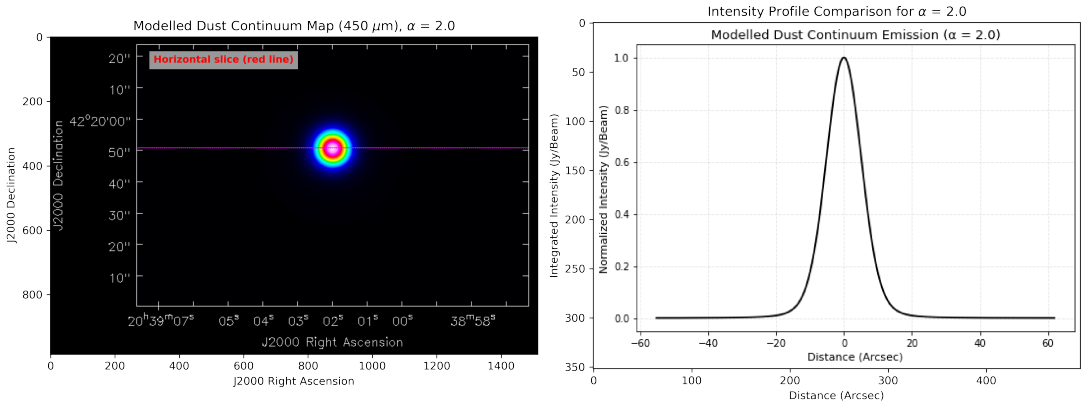


Figure 3.15: Same as figure 3.12 but with α of 2.0. The line profile at the top-right corner shows the resulting plot for the horizontal slice through the midpoint of the modelled dust emission.

to the observed profile. This is supported quantitatively by its lowest reduced chi-square value, $\chi^2_\nu = 1.57$, compared to the other models: $\chi^2_\nu = 6.27$ for $\alpha = 2.0$, $\chi^2_\nu = 4.62$ for $\alpha = 1.5$, and $\chi^2_\nu = 1.76$ for $\alpha = 0.5$.

The analysis demonstrates that a density power-law index of $\alpha = 1.0$ best reproduces the horizontal flux distribution observed in the DR21 UCH II region, indicating that the density distribution of the dust decreases with the square of the radius (r^{-2}) in the region of interest. Models with steeper ($\alpha = 1.5, 2.0$) or shallower ($\alpha = 0.5$) density profiles deviate systematically from the observed data, underestimating or overestimating the intensity at specific offsets along the slice.

Overall, this comparison confirms that $\alpha = 1.0$ provides the most statistically significant representation of the dust continuum distribution at 5 kyrs, and can be adopted as the preliminary estimate of the density structure in the DR21 UCHII region for further modelling.

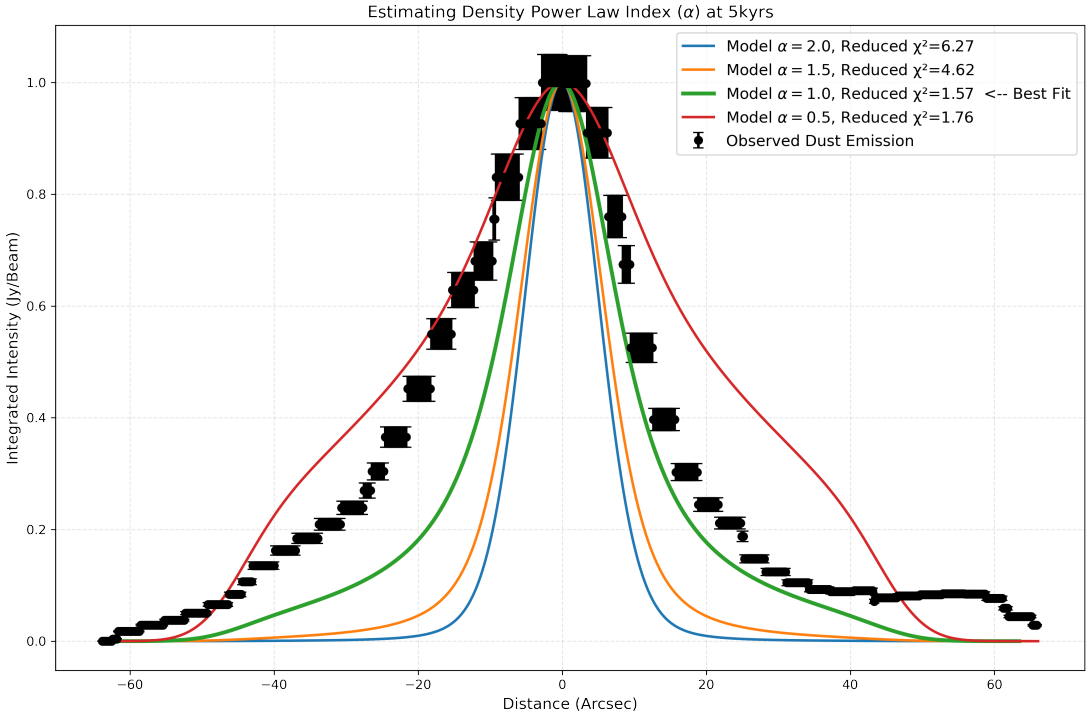


Figure 3.16: A Plot of results from slicing in the horizontal plane for the models by varying α with constant Rs and n_o with 4 different models and compared to SCUBA 450μm data to estimate the value of α using the SCUBA 450μm as reference. The plot shows the normalised spatial intensity profiles for the values of α 0.5, 1.0, 1.5, and 2.0, with α=1.0 as the best fit for the spatial intensity profile of the SCUBA 450μm data. An error margin of 0.05 was applied in the computation of χ^2_ν. Note: the SCUBA 450μm observation used as reference was rotated at 100 degrees and sliced horizontally through the midpoints to compare like terms.

3.7.4 Derivation of the Size (age) for DR21

Five different models for DR21 with ages of 5kyr, 6kyr, 10kyr, 20kyr and 40kyr were generated and compared to the observed data to estimate a reasonable age for DR21 (this was done while logically taking into account the other model parameters). To align the model with the observed data, the model intensity map for the 5kyrs was smoothed to correspond with the 22 GHz resolution of

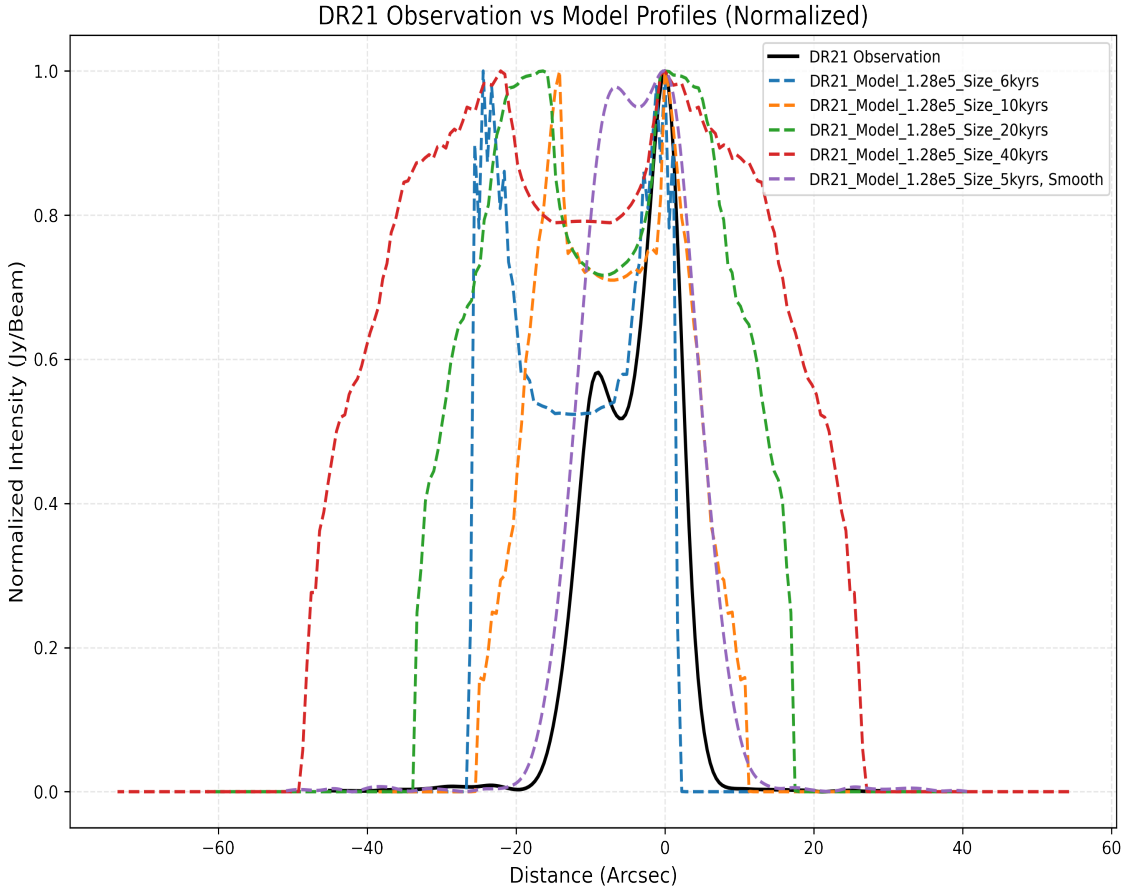


Figure 3.17: The plot shows an estimation of comparable size for the cometary DR21 UCHII region. The x-axis shows the distance from the peak intensity in arcseconds, and the y-axis shows the normalised intensity in Jy/beam. The figure displays the resulting plot from a horizontal slice through the midpoint of the observed DR21 and models at different ages (sizes) of 5kyr, 6kyr, 10kyr, 20kyr and 40kyr with constant n_o, of $1.28{\times}10^5$ cm^{-3}, Rs=0.07 pc, and $\alpha = 1.0$ at an inclination angle of 45°. Note: the observed data was rotated at 100 degrees and sliced horizontally through the midpoint to compare with the models. The model maps were not smoothed to any specific resolution or beam width, except the 5 kyr, which was smoothed to match the 22 GHz resolution of the VLA D-configuration $\approx 2.8''$ beamwidth) using the CASA task IMSMOOTH

the VLA D-configuration, with a beamwidth of $\approx 2.8''$, utilising the `CASA` task `imsmooth` while the other models were not smooth as they do not fit the size of the observed data. The models were produced at constant values for n_o, of 1.28×10^5 cm^{-3}, Rs=0.07 pc, and α =1.0 at an inclination angle of 45°. The observed data were rotated by 100° to align with the model orientation, and a horizontal slice through the midpoint was extracted for direct comparison. Figure 3.17 shows the plot of the results of the line profiles for the horizontal slicing through the midpoints for the observed DR21 and the models. The horizontal slices were selected because the tails of the models did not break out as seen in the observed radio continuum data Cyganowski *et al.* (2003); Harris & Scott (1973); Immer *et al.* (2014). Therefore, horizontal slices through the midpoint give a comparable estimate for the models and the observed DR21.

The best-fit model was investigated as shown in Figure 3.18 using the Pearson correlation coefficient (r), defined as:

$$r = \frac{\sum_i (y_i - \bar{y})(m_i - \bar{m})}{\sqrt{\sum_i (y_i - \bar{y})^2}\sqrt{\sum_i (m_i - \bar{m})^2}} \tag{3.11}$$

where y_i are the observed normalised intensities, m_i are the model normalised intensities, and $\bar{y}$, $\bar{m}$ are their respective means. A Pearson correlation coefficient r close to 1 signifies a strong positive correlation in shape; therefore, the model at 5 kyr was identified as the best-fit model with $r = 0.946$, as indicated in the legend of Figure 3.18. The resulting profiles reveal that models with larger ages (10-40 kyrs) exhibit broader emission regions and more extended peak separations than observed, indicating an overestimation of both size (age) and density. In contrast, the 5 kyrs model shows the best match to the observed profile, suggesting that the DR21 UCHII region is in an early evolutionary stage with moderate density.

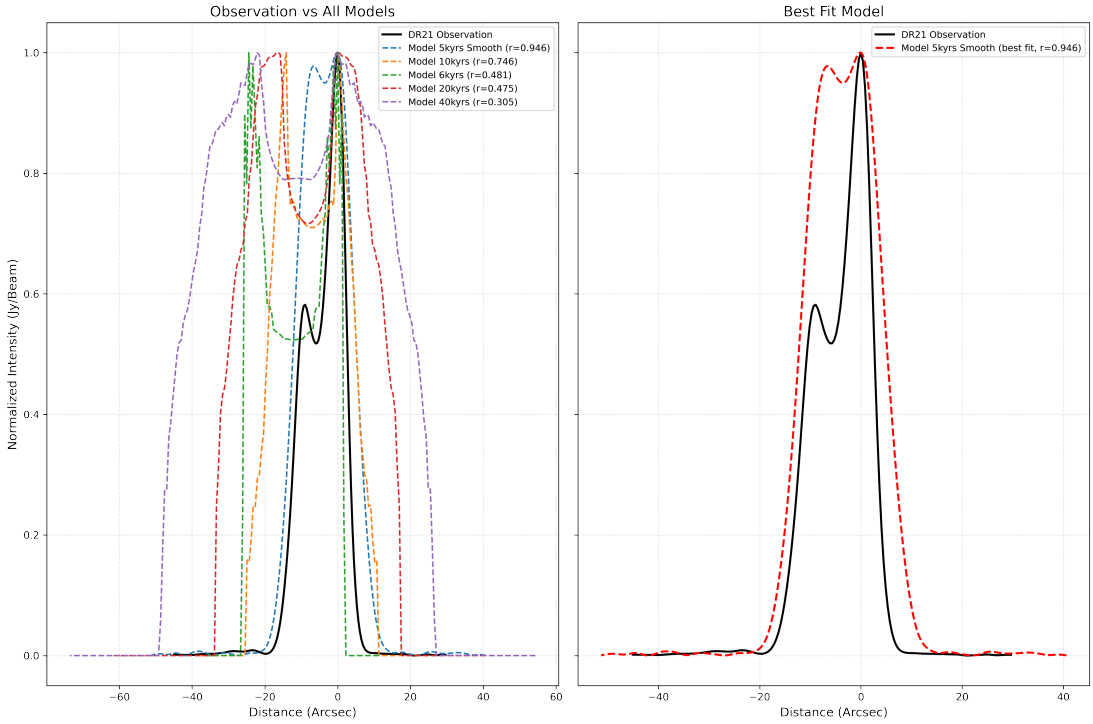


Figure 3.18: Comparison of the observed dust continuum profile of DR21 with the modelled profiles, analogous to Figure 3.17, focusing on identification of the best-fitting model. **Left panel:** Estimated size comparison of the cometary DR21 UCHII region from horizontal slices through the midpoint of observed data and models at ages of 5, 6, 10, 20, and 40 kyr. All normalised model profiles are overlaid on the observation, with Pearson correlation coefficients (r) shown in the legend. The 5 kyr model provides the best fit. **Right panel:** The best-fit model, determined by the highest Pearson correlation coefficient, is highlighted in red alongside the observed profile. This illustration allows direct comparison of model shapes and highlights the model that best reproduces the observed data.

3.8 Spectral Energy Distribution (SED) Fitting of the DR21 UCHII Region

The integrated spectral energy distribution (SED) serves as an important diagnostic tool for understanding the physical characteristics of UCHII regions. As

Table 3.5: Spectra Energy Distribution (SED) for DR21 observations and Models at 5kyr

Frequency (GHz)	Flux (Jy)	Flux1 (Jy)	Flux2 (Jy)	Flux3 (Jy)	Flux4 (Jy)
0.41	1.35	0.25	0.43	1.30	0.13
1.41	6.4	2.88	5.31	10.20	1.91
2.7	$\sim$ 16	14.69	17.91	19.80	13.12
5.0	18.5	17.09	18.91	19.82	16.73
7.8	$\sim$ 22	17.65	18.80	19.34	17.97
15.5	$\sim$ 20	17.46	18.17	18.48	18.23
31.4	18.7	16.55	17.08	17.29	17.45
85.0	14	14.49	14.91	15.06	15.35

Note: Flux = DR21 SED from Harris & Scott (1973), Flux1 = n_o= 1.28×10^5, Flux2 = n_o= 6.40×10^4 cm^{-3}, Flux3 = n_0= 3.20×10^4 cm^{-3}, Flux4 = n_e= 2.65×10^5 cm^{-3}

a final check, the comparison with the SED was repeated using the refined values of R_s, age, and α to check the turnover frequency. This approach provides an essential validation for reproducing typical SED shapes and quantitatively comparing simulated models to observations.

Table 3.6: Reduced Chi-square (χ^2_ν) values for different number densities at 5 kyr.

Model Density [n_o (cm^{-3})]	**Age [kyr]**	$\boldsymbol{\chi^2_\nu}$
3.20 × 10^4	5	**4.64**
6.40 × 10^4	5	21.13
1.28 × 10^5	5	**53.82**
2.65 × 10^5	5	103.85

The model SEDs were generated for varying number densities for 5 kyr and an inclination angle of 45°. The parameters used in the radiative transfer model include the distance between the ionising star and the cloud core, R_s = 0.07 pc and a power law index, α = 1.0. The SED reported by Harris & Scott (1973) for DR21 was used as the observational reference dataset. The values for both

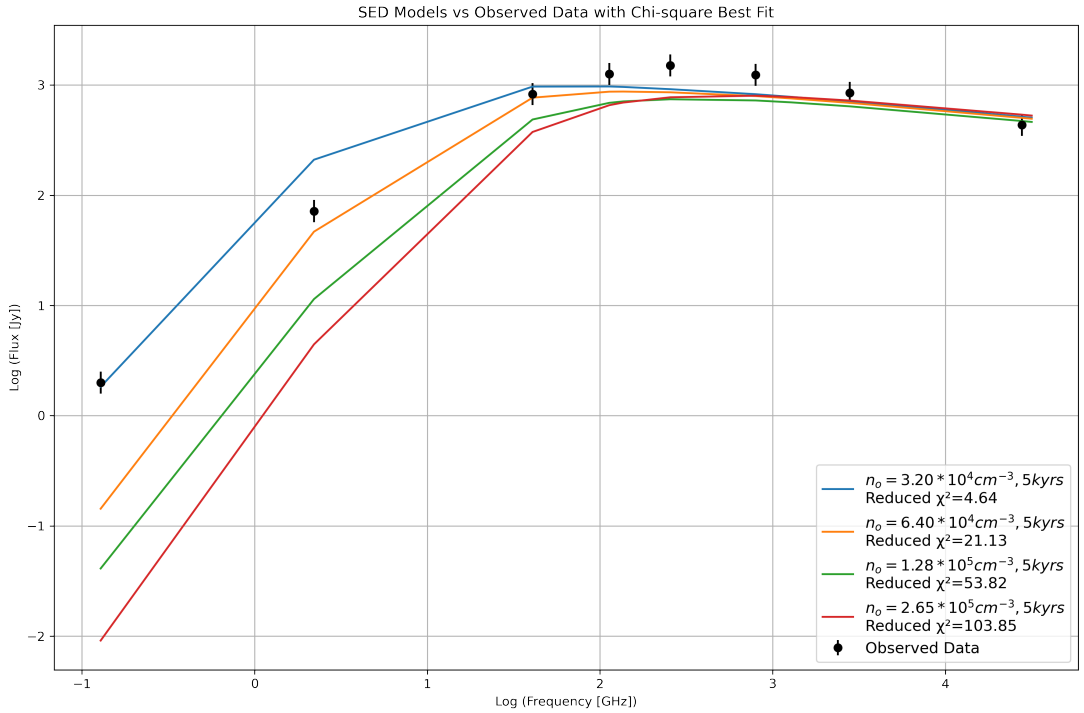


Figure 3.19: The figure shows the derived SED fitting for the cometary DR21 UCHII regions. The black circles represent observed data from Harris & Scott (1973), while the lines correspond to the model fits for varying number densities. The derived model parameters of R_s=0.07 pc, α=1.0, inclined at 45° for 5kyrs were used while varying the number density for n_o, of $3.2{\times}10^4 cm^{-3}$, $6.40{\times}10^4 cm^{-3}$, $1.28{\times}10^5 cm^{-3}$, and $2.65{\times}10^5 cm^{-3}$ with their corresponding (χ^2_ν values captured in the plot. The log of the frequency against the log of the flux was plotted from Table 3.5. The constant error bars were estimated as 10% of the derived flux.

the observed SED data for DR21 (Harris & Scott, 1973) and the corresponding values for the models are displayed in Table 3.5.

To evaluate the best-fit model, a reduced chi-square (χ^2_ν) analysis was performed for the observed data and the models. The computed χ^2_ν values for each model density are listed in Table 3.6, with the corresponding SED fits illustrated in Figure 3.19. The model with an ambient density of $n_0 = 3.20 \times 10^4$ cm^{-3} at 5 kyr

achieves the lowest reduced chi-square (χ^2_ν) value. However, the model corresponding to $n_0 = 1.28\times10^5$ cm^{-3} at 5 kyr, highlighted in green in the plot, provides the best fit to the turnover frequency, as evidenced by both Table 3.5 and Figure 3.19. At lower frequencies (see Table 3.5), the larger beamwidths encompass emission from regions beyond the compact source of interest (Dent, 1972; Harris & Scott, 1973; Ryle & Downes, 1967), resulting in contamination by external signals. This effect represents a key limitation to the measurements and must be taken into account when interpreting the data. Since accurately fitting the turnover frequency is the primary objective, the model with $n_0 = 1.28\times10^5$ cm^{-3} at 5 kyr is therefore selected as the best-fitting solution.
The comparison shows that the model SEDs reproduce the general spectral behaviour of UCHII regions, particularly the transition from the optically thick to the optically thin region at the turnover frequency. The best-fit model provides a close match to the observed SED, reinforcing the derived physical parameters for DR21. The consistency between the observed and modelled fluxes across frequencies confirms that a density of $n_o = 1.28 \times 10^5$ cm^{-3} and age of 5 kyr are representative of the physical state of the DR21 UCHII region.

3.9 Conclusion

For the first time, the continuum emission from a cometary UCHII region DR21, with appropriate estimated model parameters has been constructed tailored to DR21 observation. The model parameters estimated from the observations of DR21 deduced were the number density, $n_o = 1.28\times10^5$ cm^{-3}, the density power law index, $\alpha = 1.0$, the distance between the ionising star and the cloud core, R_s=0.07 pc with an inclination angle of 45° at 5kyrs. These values were logically and systematically obtained by comparing directly to observations and estimating one model parameter relative to the other model parameters, as changing one model parameter may affect the others. The derived model parameters were used to reproduce the radio continuum emission from DR21 with an estimated age for the cometary UCHII region DR21 of 5kyrs. The derived model with number

density, $n_o = 1.28 \times 10^5$ cm^{-3}, reproduced the SEDs HII region regular shapes and reasonably fit well to the turnover frequency in comparison with the observed DR21 SEDs using the SEDs values from Harris & Scott (1973) as observational reference. The thermal dust continuum emission from DR21 has been modelled (and the astrometry checked) and was used to estimate and constrain the model parameters for the density distribution of the modelled cometary UCHII region DR21. The distance from the star to the cloud core, Rs, was estimated using the plot from the observed and modelled radio and dust continuum emissions, as denoted. The separation distance between the two peaks of the radio and dust continuum observations was estimated by the vertical slice through the two peaks of the radio and dust continuum observations of DR21 are shown in figure 3.10. The best-fitting model, characterised by the number density of $n_o = 1.28 \times 10^5$ cm^{-3}, $R_s = 0.07$ pc, and $\alpha = 1.0$, reproduces both the observed intensity distribution and the SED turnover frequency. This consistency suggests that DR21 is in a relatively early, yet dynamically evolved, phase of ultracompact H II region evolution. A density power-law index of $\alpha = 1.0$ indicates that the density of the ionised gas decreases with the square of the radius in the region of interest. Observations indicate that the density distributions in dark clouds and UCHII regions generally follow power laws with exponents between 1 and 3 (Arquilla & Goldsmith, 1985; Arthur & Hoare, 2006; Teixeira *et al.*, 2005). Submillimeter studies of UCHII regions often find slopes from about 1.25 to 2.25, commonly near 2, consistent with isothermal, self-gravitating spheres (Hatchell & Van der Tak, 2003). Radio continuum analysis reveals even steeper gradients up to 4 in early-stage compact HII regions (**?**), though expansion over time typically smooths these gradients. For the steepest slopes, alternative density profiles such as Gaussian functions may be more appropriate. Similar power-law indices (1.6-2.4) have been reported for giant extragalactic HII regions (**?**). In comparison, the derived density power-law index of $\alpha = 1.0$ from this study is somewhat shallower than other literature values but remains consistent with the understanding that the density distribution in ionised regions flattens as the region evolves, possibly due to evolutionary effects or local conditions within the ionised gas. Such a

structure is typical of cometary UCHII regions, where the ionised gas is confined by an asymmetric density gradient or by the motion of the ionising star relative to its natal cloud (Arthur & Hoare, 2006; Franco *et al.*, 2007).

The results are consistent with previous radio continuum studies of DR21 and similar UCHII regions (Arthur & Hoare, 2006; Harris & Scott, 1973; Kurtz *et al.*, 1994; Wood & Churchwell, 1989a), which also report densities on the order of 10^5-10^6 cm^{-3}. From an evolutionary perspective, the model age of 5 kyr and the derived parameters indicate a significantly younger stage compared to the typical lifetime of several 10^4 years commonly associated with UCHII regions. However, the presence of a cometary morphology indicates ongoing dynamical interaction, possibly due to stellar winds or motion through the molecular cloud, which could further shape the observed structure over time. These results reinforce the utility of combining SED fitting with spatially resolved continuum modelling to constrain the physical conditions and evolutionary pathways of massive star-forming regions.

Chapter 4

Recombination Line Emission of Cometary DR21 UCHII Region

4.1 Introduction

Cyganowski *et al.* (2003) presented the observation of DR 21 in two hydrogen recombination lines (H66α and H53α), and two NH_3 transitions (NH_3 (1, 1) and NH_3(2, 2)) with the Very Large Array in the D configuration to investigate the cometary morphology of UCHII region DR21. The findings from Cyganowski *et al.* (2003) suggested a hybrid model (combination of bow shock and champagne flow model) with the ionised gas kinematics in the cometary head suggesting the bow shock model, whilst the cometary tail appears more of the champagne flow model. The deep hydrogen recombination line observations of the cometary UCHII region DR21 at H66α with the Very Large Array in the D configuration at rest frequency 22.364 GHz (primary beam size $\approx$ 2 arcmins by Immer *et al.* (2014) detected emissions further down the tail of the Southern UCHII region. The velocity structure deduced by Immer *et al.* (2014) shows higher velocities in the tail region of DR21 as compared to Cyganowski *et al.* (2003). The detailed investigation of the DR21 by Immer *et al.* (2014) also confirmed the hybrid model to explain the cometary morphology of DR21.

The detection and resolution of velocity structure for UCHII regions, particularly the UCHII region DR21 suggest that detailed physical models tailored to obser-

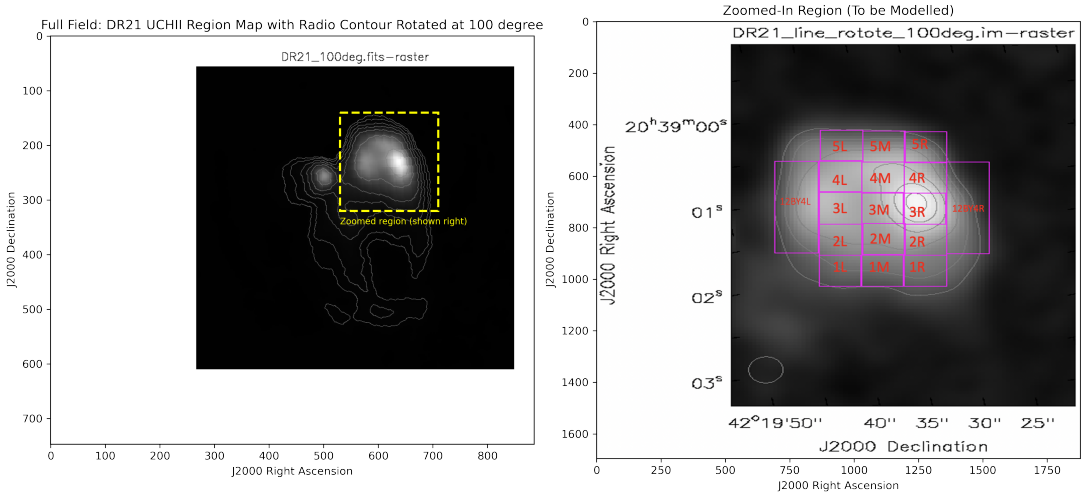


Figure 4.1: The observation of the cometary UCHII region DR21 by Immer *et al.* (2014) rotated at 100° to compare with models. The zoomed in figure region is the primary focus for the model with contour levels 0.2,0.4,0.6,0.8 Jy/beam. The figure on the right panel is the single-channel image, and the boxes show the areas of emissions summed to generate spectra for analysis in comparison with models. The synthesised beam of 3.4" is displayed at the bottom left corner of the right panel.

vations may prove helpful in investigating the internal velocity structure of DR21 (Cyganowski *et al.*, 2003; Immer *et al.*, 2014) and determining the model that best explains the cometary morphology. Figure 4.1 showcases the observation of the cometary UCHII region DR21 by Immer *et al.* (2014) with a focus on the zoomed-in region of Figure 4.1. The primary goal is to model the velocity structure within the zoomed-in region as highlighted in the right panel of Figure 4.1 of the DR21 (Immer *et al.*, 2014) to investigate the velocity structure.

4.2 The Model

To model the H66α recombination line observation of the cometary UCHII region DR21 (Immer *et al.*, 2014), TORCH developed by Steggles *et al.* (2017) is used.

TORCH has been tested by Steggles *et al.* (2017) to simulate the evolution of HII region. RadioRT developed by Steggles *et al.* (2017) is modified and tested to model the continuum emission and radio recombination line observation of cometary UCHII region DR21. The best-fit model to the continuum observation from Chapter 3 was read into the RadioRT code to model the radio recombination lines observation. The methodology section describes the process of modelling both the radio recombination line observations and the simulated spectra of the cometary UCHII region DR21.

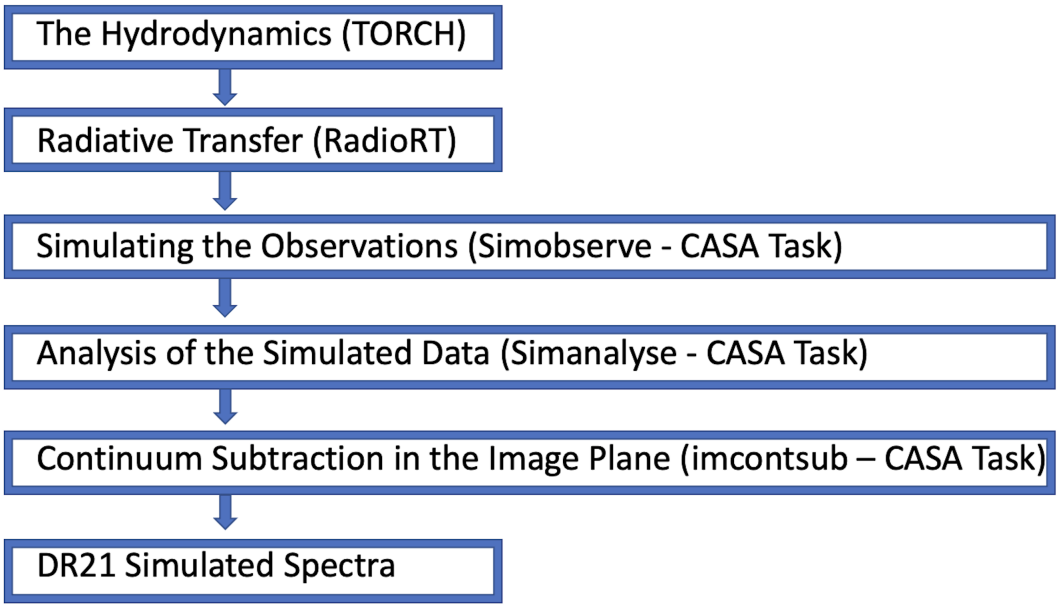


Figure 4.2: The diagram showcase the step-by-step approach in modeling the cometary UCHII region DR21.

4.3 Methodology

The diagram shown in Figure 4.2 describes the logical steps in modelling the H66α recombination line observation of cometary UCHII region DR21.

4.3.1 Hydrodynamics

Chapter 3 describes the hydrodynamics and captures the essential model parameters constrained for modelling the continuum emission from the cometary UCHII region DR21. The hydrodynamics form the initial stage and iaresubsequently processed by the radiative transfer code.

4.3.2 Radiative Transfer

Table 4.1 shows the RadioRT model parameters for modelling the cometary UCHII region DR21. The bandwidth of 25 MHz and 64 channels are selected to give the same spectral resolution as reported by Immer *et al.* (2014). Note that, the observation by Immer *et al.* (2014) for cometary UCHII region DR21 reported a 12.5 MHz bandwidth and 32 channels. The hydrodynamic models in this study were all conducted at an inclination angle of 45 degrees; however, models were tested at multiple inclination angles of 30, 45, and 60 degrees to explore their effects. The longer bandwidth selected in this case, helps to create enough channels for the continuum subtraction.

Table 4.1: The radiative transfer code (RadioRT) model parameters for the Cometary UCHII Region DR21.

RadioRT Model Parameters	
Rest Frequency	22.364 GHz
Bandwidth	25 MHz
Channel	64
Principal Quantum Number	66
Turbulence Broadening, V_{turb}	1 kms^{-1}
Line of Sight, Velocity, V_{LOS}	-2 kms^{-1}
Sampling Factor	1
Distance	1.5 kpc
Inclination Angle	(30°, 45°, 60°)

The RadioRT reproduces a general synthetic image cube of cometary UCHII re-

gion DR21 projected at a different viewing angles of 30°, 45°, and 60°. It must be noted that the viewing angles at 0° and 90° are the axis in the plane of the sky and the head-on view respectively. The inclination angle was set and run separately with the same model parameters but varying the inclination angles for each model. The turbulence broadening value was set as 1 kms^{-1} and the distance set to 1.5 kpc similar to the observations Cyganowski *et al.* (2003); Immer *et al.* (2014); Rygl *et al.* (2012). The systemic velocity of the molecular gas in DR21 ranges from -2.7 to -1.4 so the V_{LOS} was set to -2 kms^{-1} from the NH_3(1,1) and (2, 2) transition observations reported by Cyganowski *et al.* (2003) as the reference to the ionised gas and the molecular materials.

4.3.3 Simulation Observation and Analysis

The simulated image cube generated from the RadioRT is convolved to the Very Large Array (VLA) telescope beam and subsequent analysed using the tasks SimObserve and SimAnalyse from the standard Common Astronomy Software Applications (CASA; see http://casa.nrao.edu/) package. The exact antenna setup for the DR21 observation by Immer *et al.* (2014) is read into the SimObserve task to recreate the exact VLA interferometric observations at an angular resolution of 3.4" used for the cometary UCHII region DR21. The SimObserve task produced a simulated measurement set in the uv plane, which is then gridded, inverted, and deconvolved into the output cometary UCHII region DR21 at different projected angles (30°, 45°, 60°) with the SimAnalyse task.

4.3.4 Continuum Subtraction

The results from SimAnalyse have the spectral line superimposed upon the continuum, hence the intensities can be decomposed into the Line and Continuum contributions. With an interest in the radio recombination line, the CASA task Continuum Subtraction (imcontsub) in the image plane is employed to subtract the continuum from the line-free channels. The approach operates by fitting a baseline first-order polynomial to the line-free channels for the spectrum in the

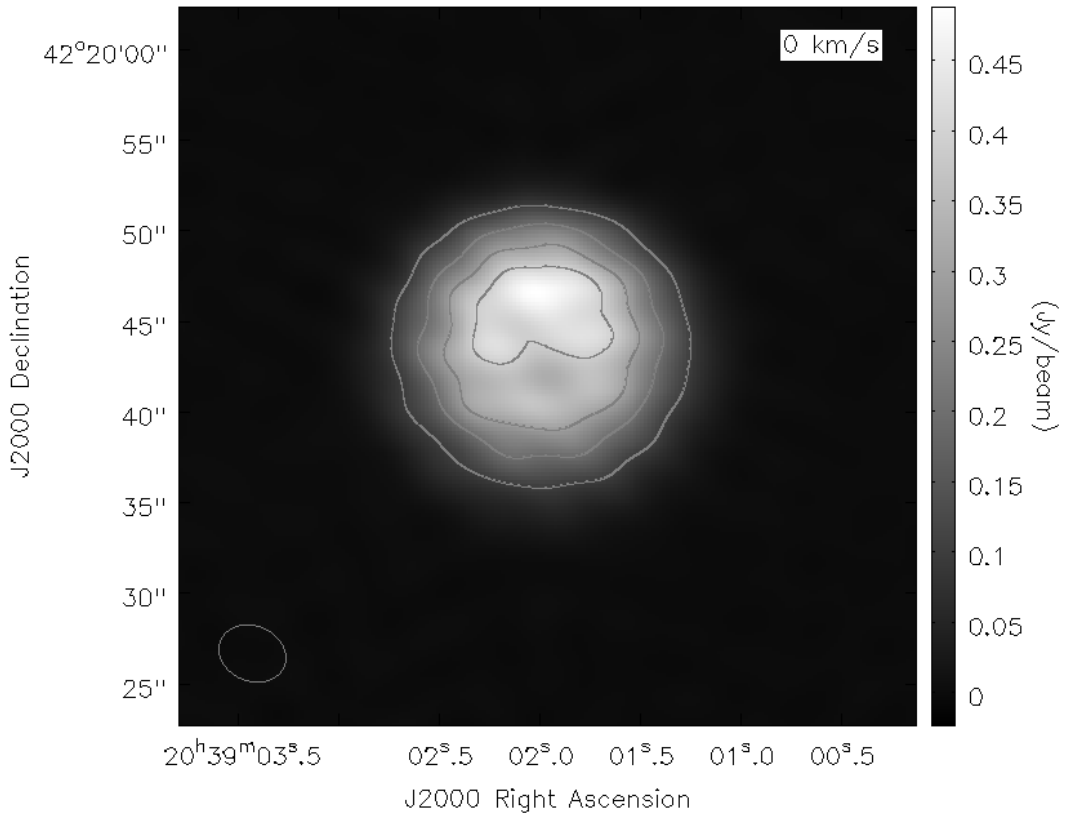


Figure 4.3: Displays the modelled cometary UCHII region DR21 projected 45° with contour levels 0.2, 0.4, 0.6, 0.8 Jy beam^{-1}. The image shows the continuum-subtracted line data at 0 kms^{-1} at channel 31 out of 64. The rms of the resulting line image cube, away from the source is 3.5 $\times$ 10^{-3} Jy beam^{-1} compared to the observed line data at 7.4 $\times$ 10^{-3} Jy beam^{-1}. The synthesised beam of 3.4" is displayed at the bottom left corner. This object is obtained by following the methodology of Figure 4.2.

image plane to decompose the line and the continuum contributions. For the 64 channels, channels 0 to 24 and 45 to 63 were selected and fitted with the baseline to the line emission-free parts of the individual line profiles. The spectral resolution corresponds to 5.2 kms^{-1}/channel to that of Immer *et al.* (2014). Figure 4.3, shows the simulated cometary UCHII region DR21 projected at 45° angle of inclination. A similar approach is followed to obtain similar models projected at

a viewing angle of 30° and 60°.

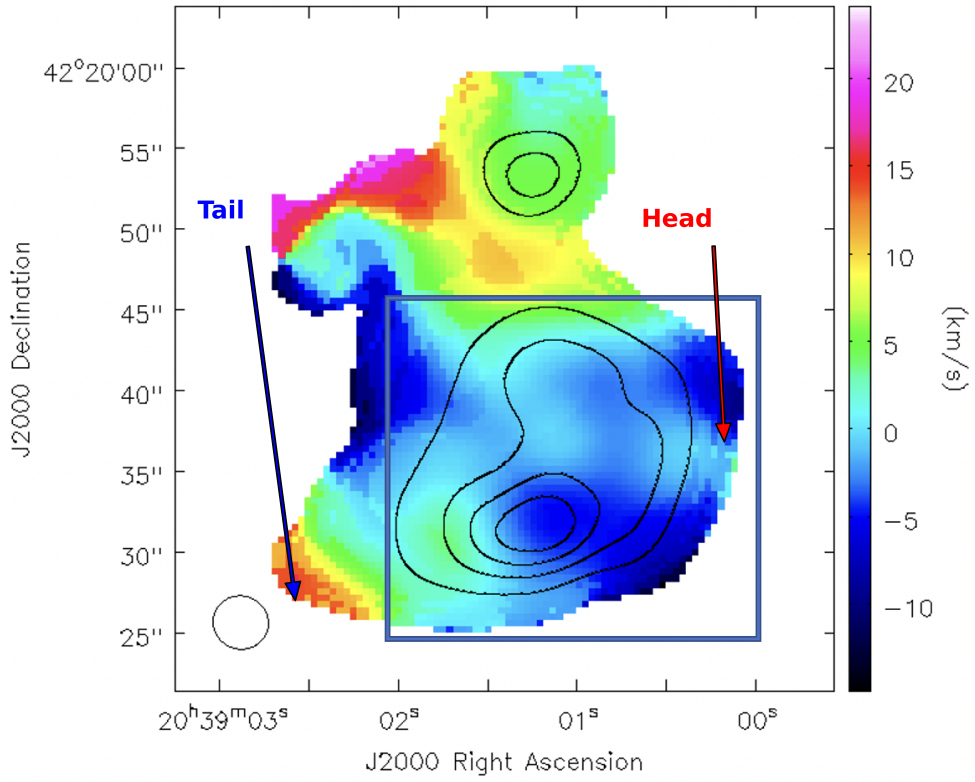


Figure 4.4: Moment 1 map showing the intensity-weighted radial velocity of the observed data by Immer *et al.* (2014) overlaid to the contour of the continuum emission to highlight the focus region of the southern area captured in the square of the cometary UCHII region compared to the models. The contour levels are 0.2, 0.4, 0.6, and 0.8 mJy beam^{-1}. Note that the Moment 1 map is not rotated.

4.4 The Velocity Structure

4.4.1 Velocity Field

The first stage to study the velocity structure of the cometary UCHII region DR21 was to investigate the moment 1 map of the observed and simulated data for the cometary UCHII region DR21. The intensity-weighted average of the velocities, (M_1), for the observed data, was generated using the CASA tool immoments task by evaluating the equation;

$$M_1 = \frac{\sum_{\iota=1}^{N_{chan}} S_\iota \times v}{\sum_{\iota=1}^{N_{chan}} S_\iota} \tag{4.1}$$

Here, the N_{chan} is the number of channels, S_ι, denotes the emission in one channel map and v, is the velocity.

The moment 1 map (velocity field) for the observed data was generated as seen in Figure 4.4 with a focus on the southern part highlighted in the square area. An observation of the moment 1 map for the observed DR21 shows a small variation in the velocity fields with relatively lower velocities within the southern area. The southern area velocity fields ranges from ≈ -15 kms^{-1} to ≈ 5 kms^{-1}. The southern cometary head has regions that are blue-shifted (dark blue as seen in Figure 4.4) and the tail has regions that are slightly red-shifted (green in Figure 4.4).

The intensity-weighted average of the velocities for the simulated DR21 projected at viewing angles of 30°, 45°, and 60° was generated and compared to the observation as seen in Figures 4.5, 4.6 and 4.7 respectively. It is observed that the overall velocity fields of the simulated DR21 exhibit increasing blue-shifts as the inclination angle increases from 30° to 45° and then to 60°. The moment 1 map for the simulated DR21 show a clear pattern variations in the velocity fields from the cometary head to the tail. The cometary head for the models exhibits blue-shifted velocities whilst the cometary tail is red-shifted. There are similarities in the low-velocity fields between the observed and the simulated DR21 data. The velocity field trend pattern for the blue-shift and red-shift of the DR21

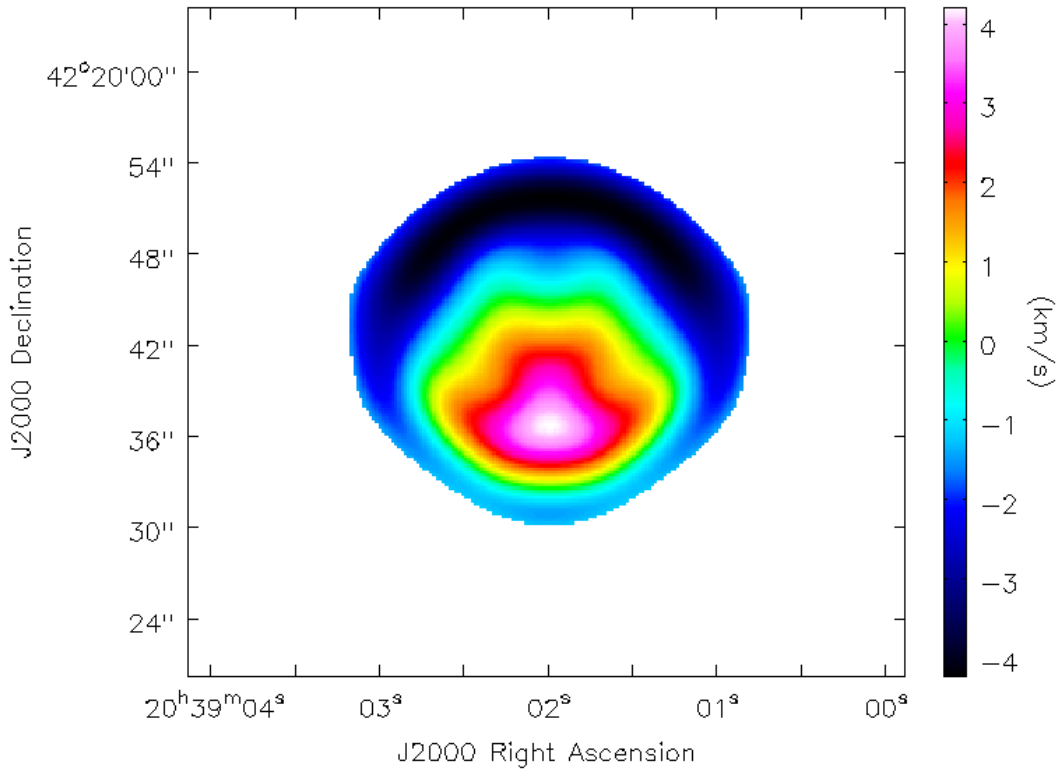


Figure 4.5: Displays the simulated Moments 1 map of the cometary UCHII region DR21 projected at a viewing angle of 30°. Note that the head is at the top and the tail at the bottom.

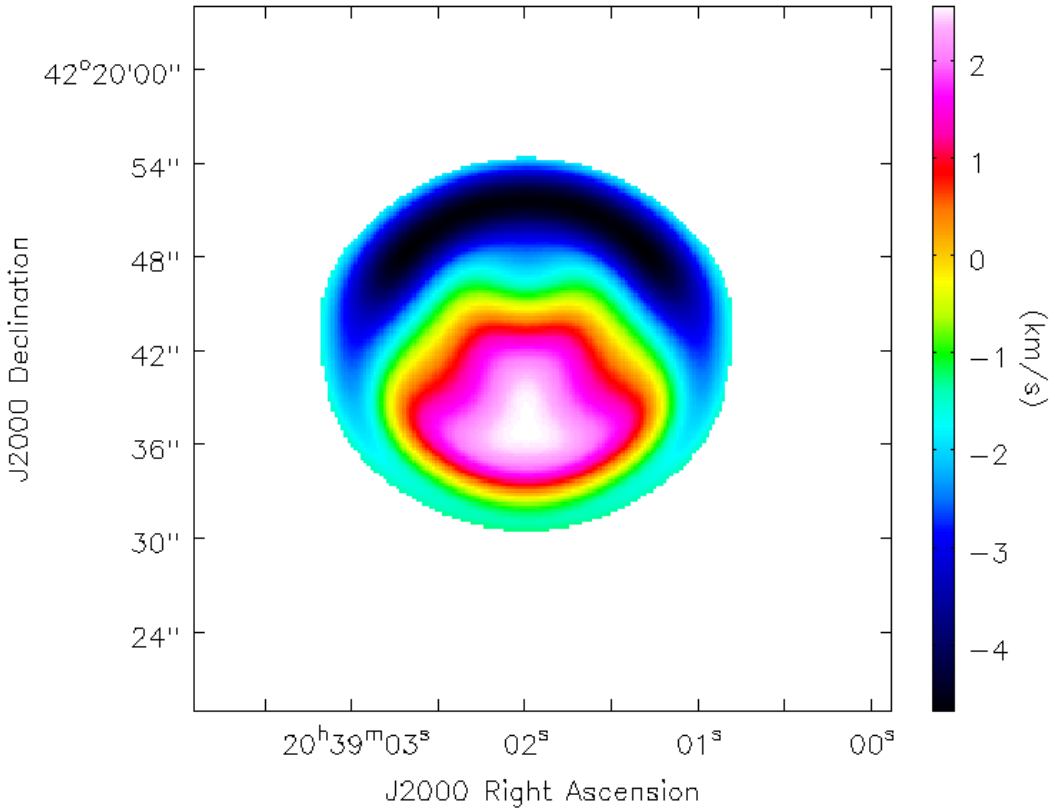


Figure 4.6: Displays the simulated Moments 1 map of the cometary UCHII region DR21 projected at a viewing angle of 45°. Note that the head is at the top and the tail at the bottom.

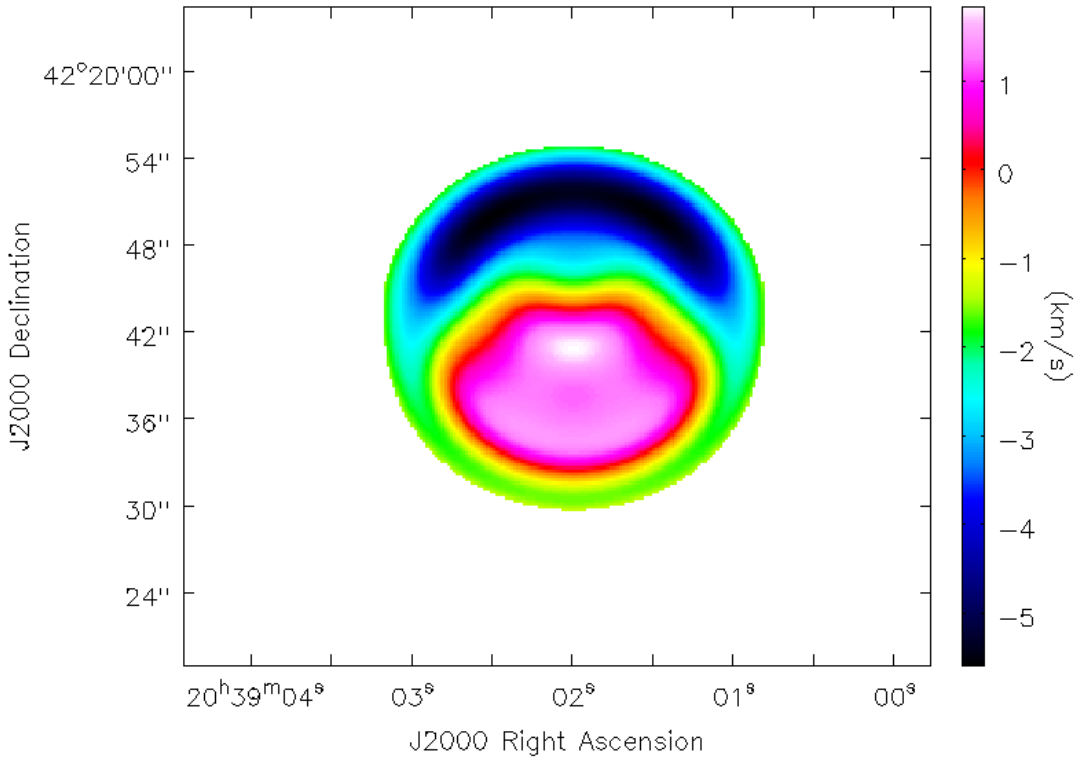


Figure 4.7: Displays the simulated Moments 1 map of the cometary UCHII region DR21 projected at a viewing angle of 60°. Note that the head is at the top and the tail at the bottom.

cometary head and tail respectively is also noticed in observed data and models. However, there is a distinction in terms of the intensity-weighted average of the velocities between the moment 1 map of the observed and the models. The observation ranges from ≈ -10 kms^{-1} to ≈ 5 kms^{-1} whiles the models ranges from ≈ -4 kms^{-1} to ≈ 4 kms^{-1}, ≈ -4.5 kms^{-1} to ≈ 2.5 kms^{-1} and ≈ -5.5 kms^{-1} to ≈ 1.5 kms^{-1} for 30°, 45° and 60° respectively. There are also distinctions in the shapes between the moment 1 map for observed DR21 and the models.

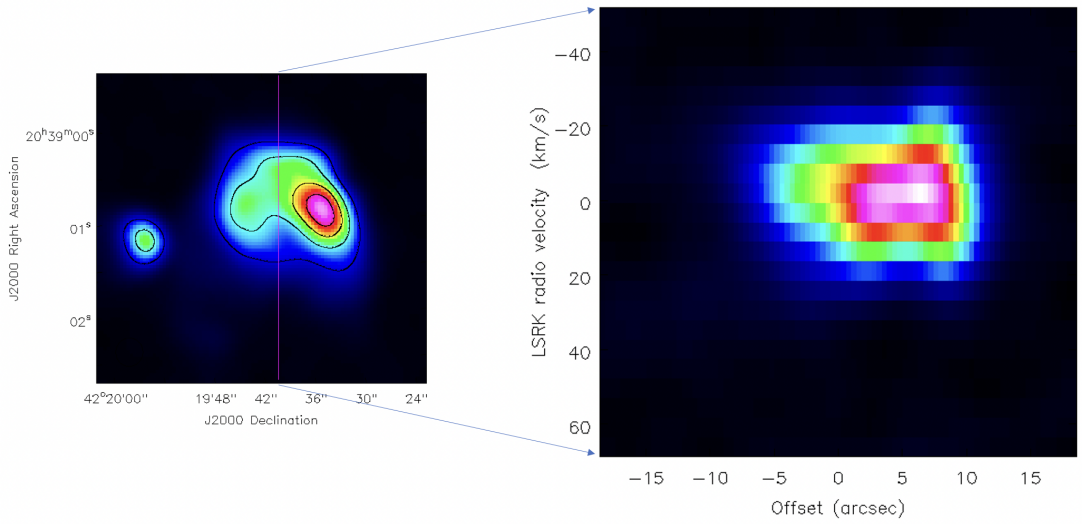


Figure 4.8: The diagram shows a slice from the cometary head (positive) through the midpoint plane to the tail (negative) of the observed DR21 on the right-hand side and the corresponding Position Velocity (PV) diagram for the slice on the left-hand side. The PV diagram displays the distance along the slice and the velocity profile. Note that, the cometary UCHII region DR21 from Immer *et al.* (2014) is rotated at 100° to compared to models

4.4.2 Position Velocity Diagram

The velocity structure of the ionised gas was investigated with the position velocity (PV) diagrams. The PV diagram was generated by slicing through the

midpoint of the observed cometary UCHII region DR21 as seen in Figure 4.8.

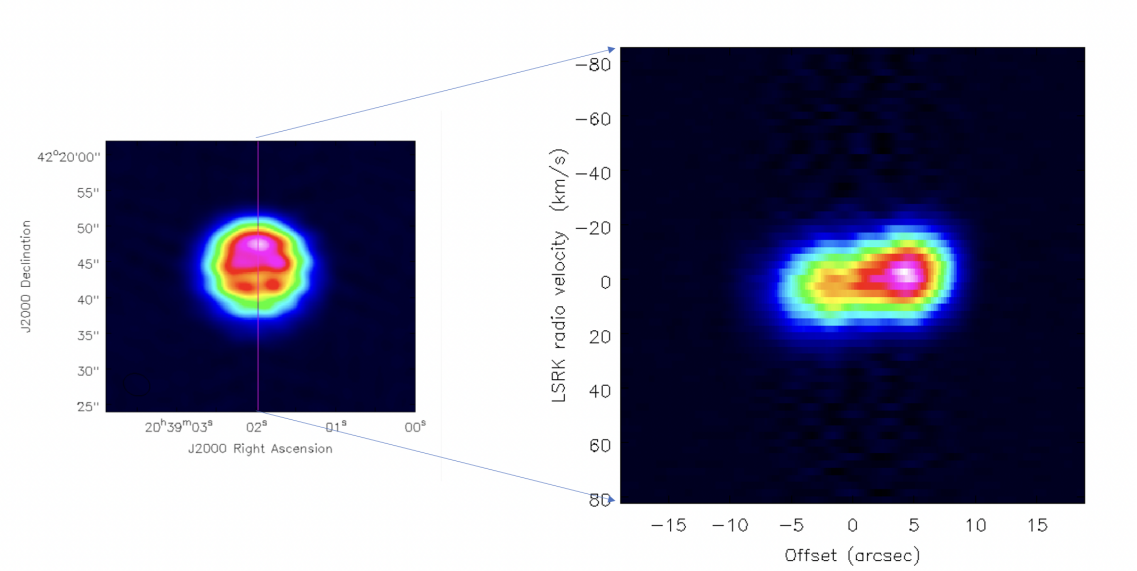


Figure 4.9: The diagram shows a slice from the cometary head through the midpoint plane to the tail of the simulated DR21 on the right-hand side and the corresponding Position Velocity (PV) diagram for the slice on the left-hand side. The PV diagram displays the distance along the slice and the velocity profile for comparison to the observed data. The simulated DR21 is projected at a viewing angle of 30°.

The figure shows two in-one plots, and in this case, the left-hand side shows the data indicating the slice from the cometary head through the mid-plane to the tail of the observed data. The corresponding right-hand-side plot shows the PV diagrams generated from the slice. A similar approach was used to generate the PV diagrams for the models of the cometary UCHII regions DR21. Figures 4.8, 4.9, 4.10 and 4.11 display the Position Velocity diagrams obtained for the observed data (rotated at 100°) and models of cometary UCHII regions DR21. The slice range of ≈ -15 to ≈ 15 offsets (arcsec) was used to investigate both the observed data and models from the cometary head through the midpoint to the tail. The PV diagrams velocity profiles (y-axis) of the ionised gas ranges from ≈

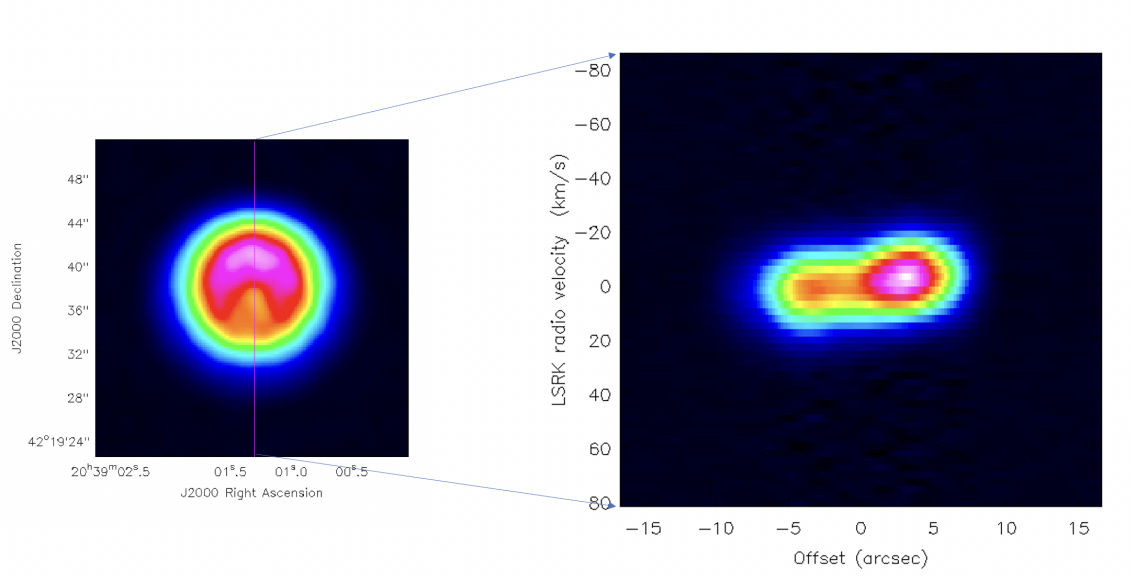


Figure 4.10: The diagram shows the slice and the corresponding PV diagram as in Figure 4.9 for the simulated cometary UCHII region DR21 projected at a viewing angle of 45°

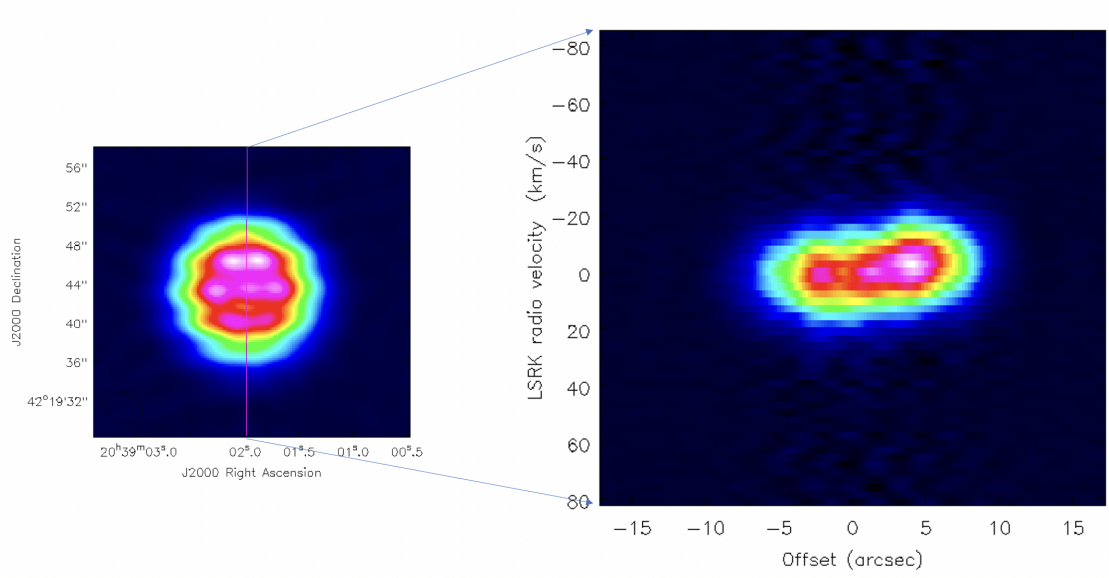


Figure 4.11: The diagram shows the slice and the corresponding PV diagram as in Figure 4.9 for the simulated cometary UCHII region DR21 projected at a viewing angle of 60°

-20 kms^{-1} to $\approx$ 20 kms^{-1} for both the observed data and model. However, the spread in the intensity distribution varies for the observed DR21 and the models. There are distinctions in the shape of the PV diagrams for the observed DR1 and the models. The PV diagrams of the models look narrower in shape, while the observed DR21 is irregular in appearance.

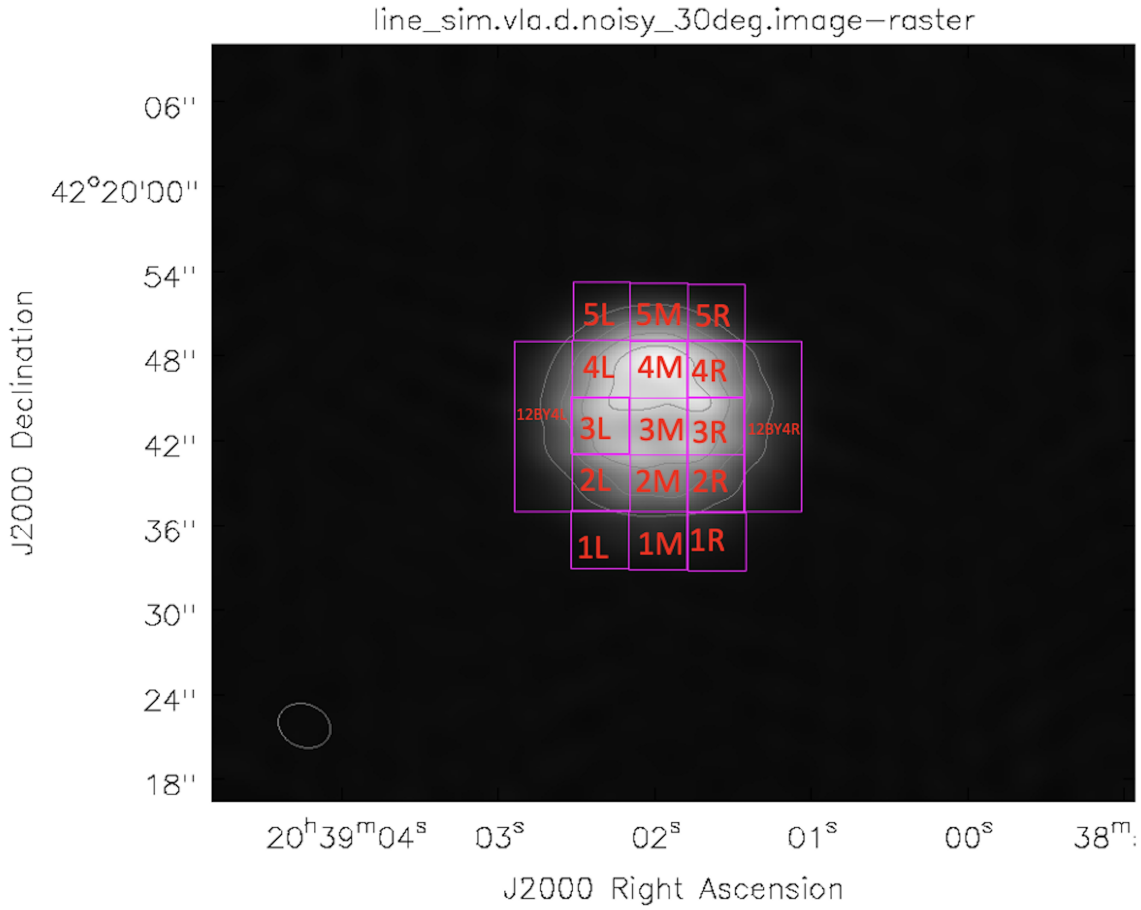


Figure 4.12: Shows the positions and box sizes of the modelled cometary UCHII region DR21 projected at a viewing angle of 30°.

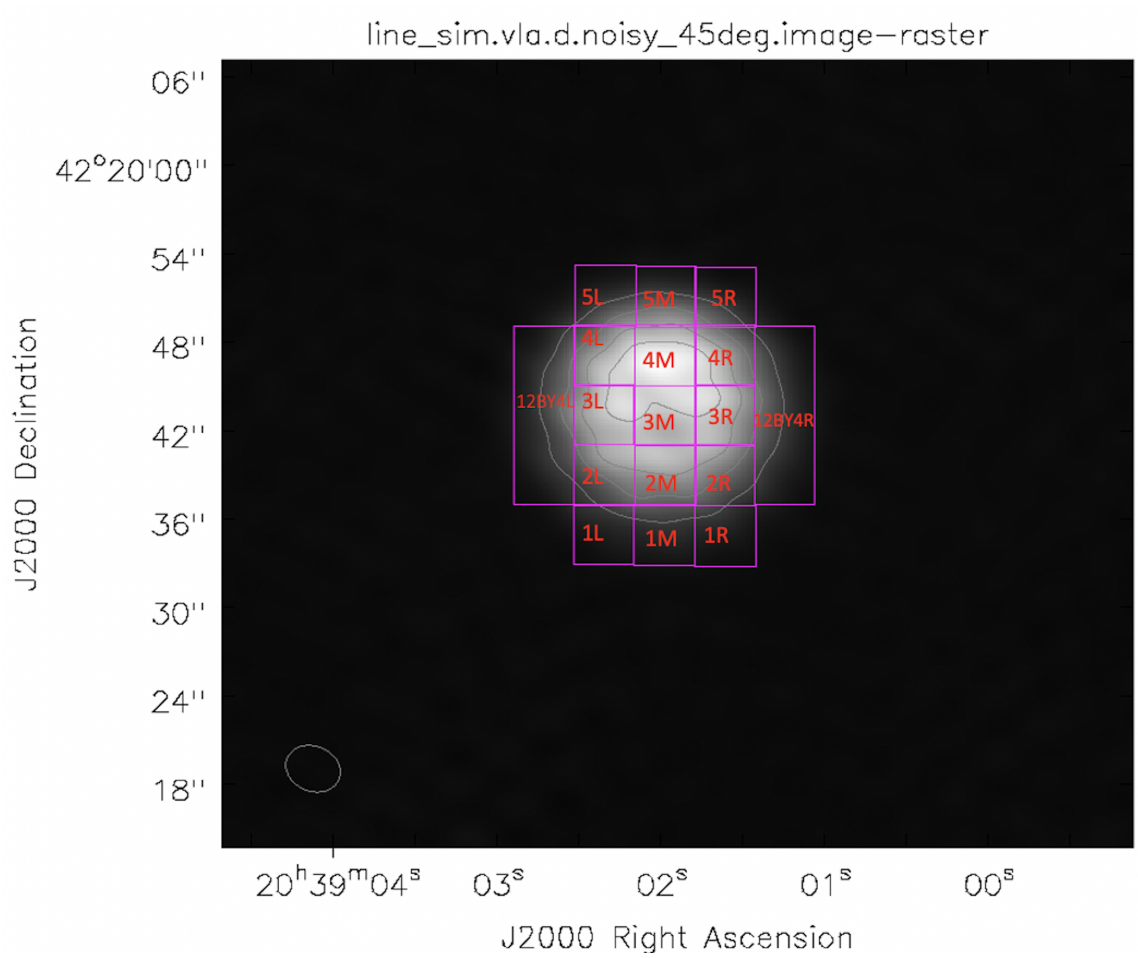


Figure 4.13: Shows the positions and box sizes of the modelled cometary UCHII region DR21 projected at a viewing angle of 45°.

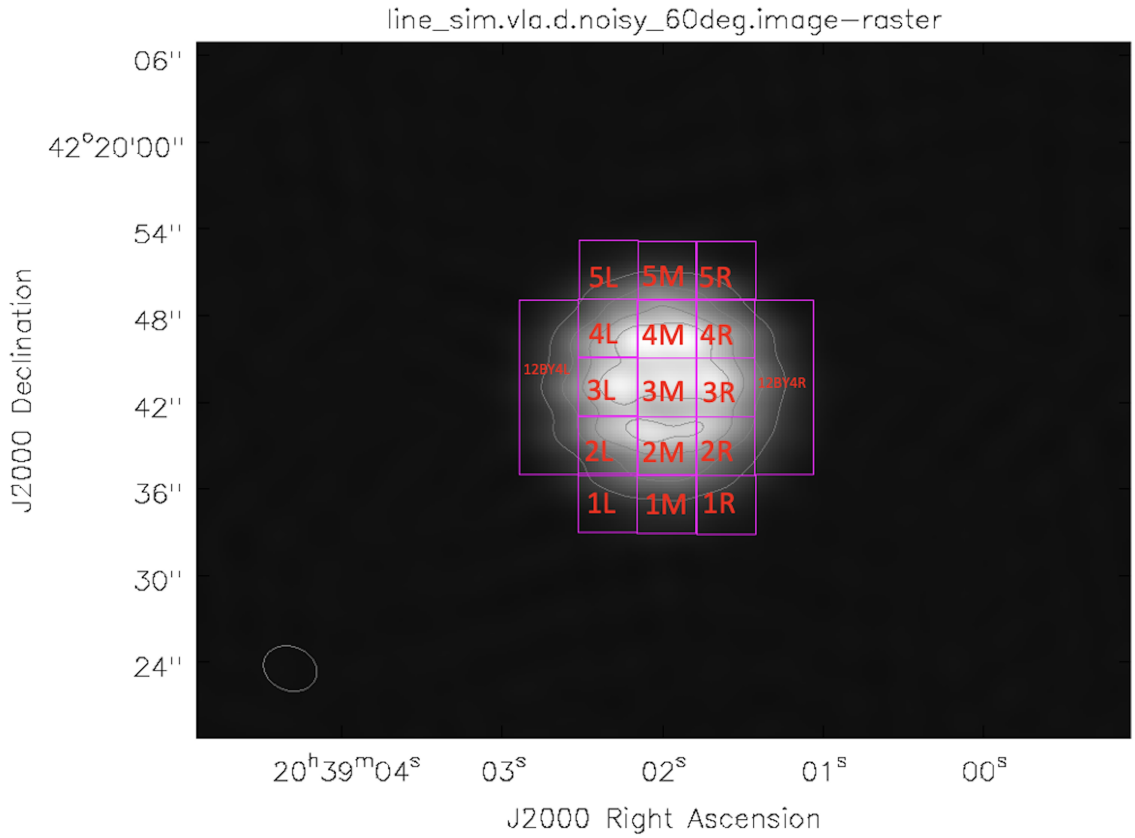


Figure 4.14: Shows the positions and box sizes of the modelled cometary UCHII region DR21 projected at a viewing angle of 60°.

4.4.3 The Ionised Gas Motion

The aim is to investigate the velocity structure of the ionised gas in the southern part by probing from the head to the tail of the cometary UCHII region and compare it to the cometary UCHII region DR21 models. To further investigate the velocity structure of the ionised gas in comparison with the models, spatially integrated spectral line profiles are generated by summing the emission over the boxes seen in the right panel of Figure 4.1. The spectral line profiles are generated by summing up emissions from the individual 17 boxes covering the emission of the southern part. The boxes are aligned from head to tail; with positions 5L, 4L, 3L, 2L, 1L (head to tail); 5M, 4M, 3M, 2M, 1M (head to tail); and 5R, 4R, 3R, 2R, 1R (head to tail), respectively. Each of these boxes is 4" × 4" (selected to match the dimensions of Immer *et al.* (2014)), while the ones labelled 12BY4L and 12BY4R are 12" × 4" to cover the regions with weaker emission. The positions and box sizes are shown in the right panel of Figure 4.1. The models have been aligned at the same box positions to allow for comparison and investigation of the velocity structure of the ionised gas motion. Figures 4.12, 4.13, and 4.14 show the positions and box sizes of the models projected at 30°, 45°, and 60°, respectively. The spectral line profiles are generated from the box positions for the models for comparison to the observed data using Table 4.2, 4.3, and 4.4.

4.4.4 Line Profile Analysis

To investigate the kinematics of the ionised gas and distinguish between the classes of models for cometary morphology, each box position as seen in the right panel of Figure 4.1, and the model's Figures 4.12, 4.13, and 4.14 is fitted independently with one Gaussian for the initial investigation. The spatially integrated line profiles were fitted with a Gaussian component for the seventeen box positions covering the emission for the observation (Southern area) and the models of DR21.

The spectral line parameters obtained from the Gaussian fitting to the line profiles

Table 4.2: DR21 Observation compared to model at 30° projection angle

Position	Amplitude / mJy		Velocity / kms^{-1}		FWHM / kms^{-1}	
	(DR21)	(Model / 30°)	(DR21)	(Model / 30°)	(DR21)	(Model / 30°)
12BY4L	92.0	84.0	0.92	−0.79	33.0	25.8
1L	42.7	36.1	−4.17	2.94	30.5	26.9
2L	117.5	180.4	−1.31	1.80	31.2	26.2
3L	174.1	334.1	−1.62	0.69	31.8	25.9
4L	168.3	326.8	−2.49	−1.01	30.7	25.6
5L	90.0	96.2	−1.55	−2.51	32.9	25.8
1M	44.9	57.6	−3.01	3.80	38.9	27.2
2M	116.7	249.2	−2.16	2.65	34.1	27.1
3M	217.4	375.1	−2.92	1.03	30.5	26.2
4M	211.3	444.9	−3.64	−1.23	30.7	25.6
5M	98.4	171.0	−2.87	−2.43	34.3	25.7
1R	60.5	34.7	0.57	3.00	38.5	26.5
2R	185.8	176.7	0.97	1.73	33.2	26.1
3R	311.0	327.7	−4.32	0.61	31.2	25.8
4R	174.2	315.6	−5.81	−1.06	32.4	25.7
5R	54.3	88.1	−6.80	−2.57	31.4	25.8
12BY4R	63.9	72.7	0.01	−0.93	30.0	25.8

Table 4.3: DR21 Observation compared to model at 45° projection angle

Position	Amplitude / mJy		Velocity / kms^{-1}		FWHM / kms^{-1}	
	(DR21)	(Model / 45°)	(DR21)	(Model / 45°)	(DR21)	(Model / 45°)
12BY4L	92.0	83.9	0.92	−0.91	33.0	25.8
1L	42.7	46.2	−4.17	2.15	30.5	26.2
2L	117.5	204.9	−1.31	1.54	31.2	26.0
3L	174.1	337.4	−1.62	0.54	31.8	25.9
4L	168.3	303.0	−2.49	−1.52	30.7	25.6
5L	90.0	81.1	−1.55	−3.22	32.9	25.5
1M	44.9	73.3	−3.01	2.36	38.9	26.5
2M	116.7	279.4	−2.16	2.10	34.1	26.7
3M	217.4	380.7	−2.92	0.75	30.5	26.3
4M	211.3	419.9	−3.64	−1.80	30.7	25.5
5M	98.4	141.9	−2.87	−3.06	34.3	25.5
1R	60.5	43.4	0.57	2.21	38.5	26.3
2R	185.8	199.7	0.97	1.53	33.2	26.1
3R	311.0	332.5	−4.32	0.40	31.2	25.8
4R	174.2	289.3	−5.81	−1.57	32.4	25.6
5R	54.3	74.2	−6.80	−3.28	31.4	25.7
12BY4R	63.9	72.0	0.01	−1.09	30.0	25.7

Table 4.4: DR21 Observation compared to model at 60° projection angle

Position	Amplitude / mJy		Velocity / kms^{-1}		FWHM / kms^{-1}	
	(DR21)	(Model / 60°)	(DR21)	(Model / 60°)	(DR21)	(Model / 60°)
12BY4L	92.0	91.7	0.92	−1.11	33.0	25.7
1L	42.7	66.3	−4.17	1.26	30.5	25.6
2L	117.5	254.4	−1.31	1.11	31.2	25.8
3L	174.1	380.6	−1.62	0.14	31.8	25.9
4L	168.3	307.7	−2.49	−2.34	30.7	25.6
5L	90.0	74.0	−1.55	−4.03	32.9	25.4
1M	44.9	104.7	−3.01	1.18	38.9	25.8
2M	116.7	344.4	−2.16	1.24	34.1	26.2
3M	217.4	432.8	−2.92	0.19	30.5	26.3
4M	211.3	428.4	−3.64	−2.61	30.7	25.5
5M	98.4	129.3	−2.87	−3.76	34.3	25.5
1R	60.5	61.5	0.57	1.19	38.5	25.8
2R	185.8	249.7	0.97	1.16	33.2	25.7
3R	311.0	372.8	−4.32	0.03	31.2	25.8
4R	174.2	290.3	−5.81	−.43	32.4	25.7
5R	54.3	69.4	−6.80	−3.96	31.4	25.6
12BY4R	63.9	78.3	0.01	−1.29	30.0	25.6

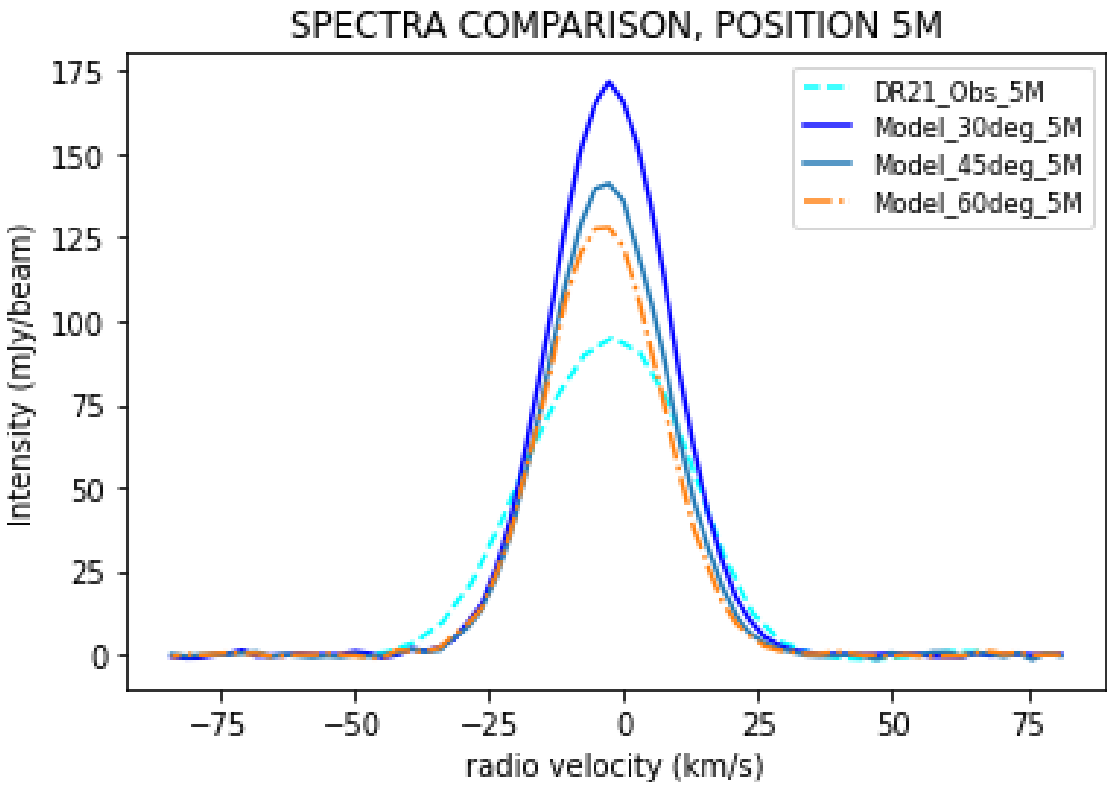


Figure 4.15: This plot corresponds to the 5M box position at the cometary head of the UCHII region DR21 and displays the overlaid spectra of the observed data alongside three model projections at inclination angles of 30°, 45°, and 60° for direct comparison.

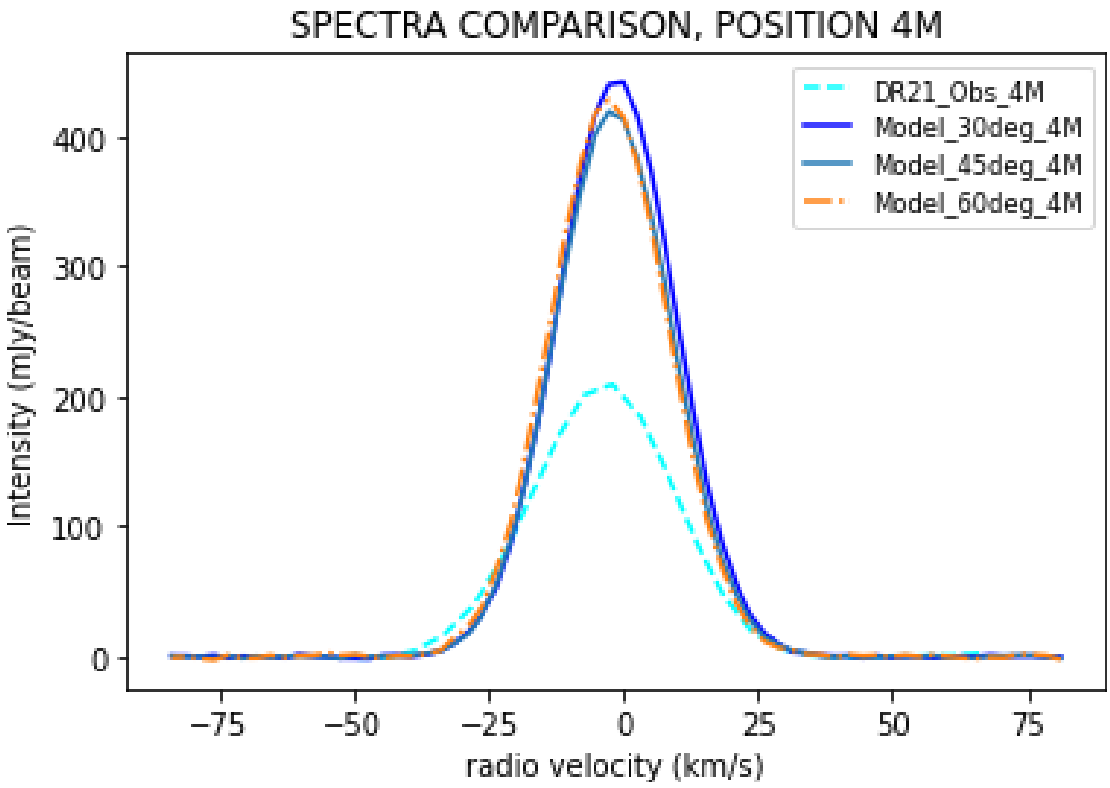


Figure 4.16: Same as Figure 4.15 but for the box position 4M of the observed data and the models.

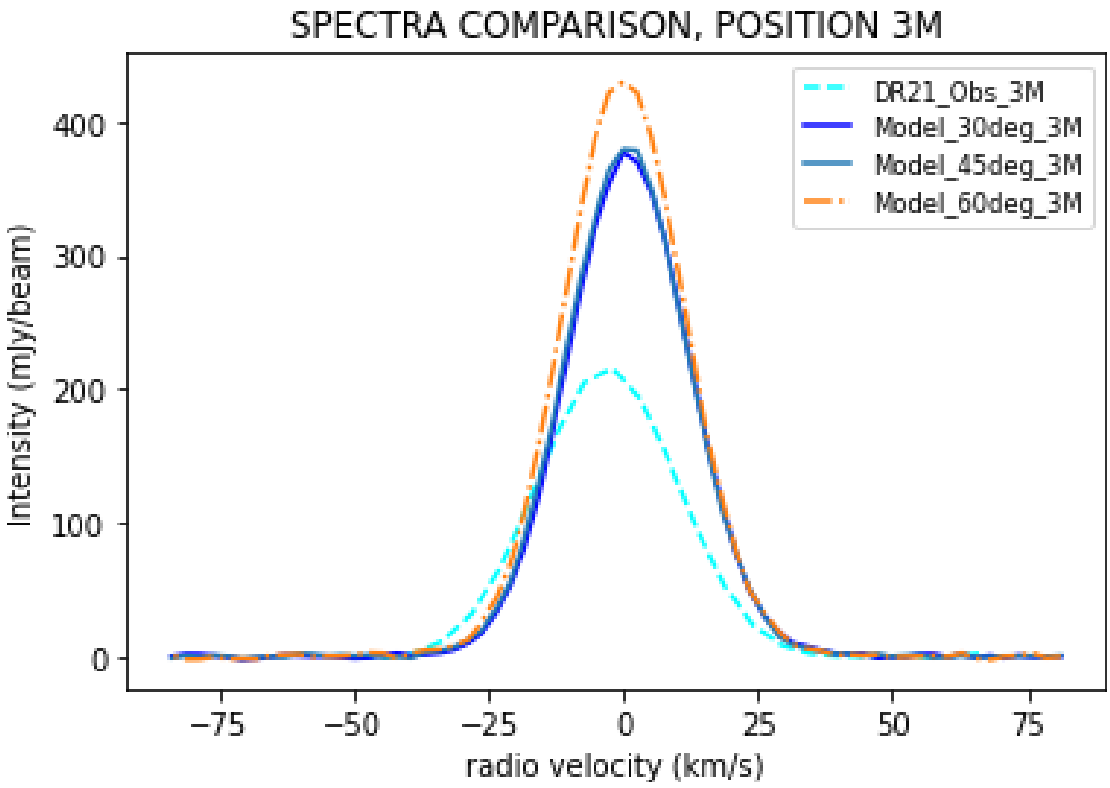


Figure 4.17: Same as Figure 4.15 but for the box position 3M of the observed data and the models.

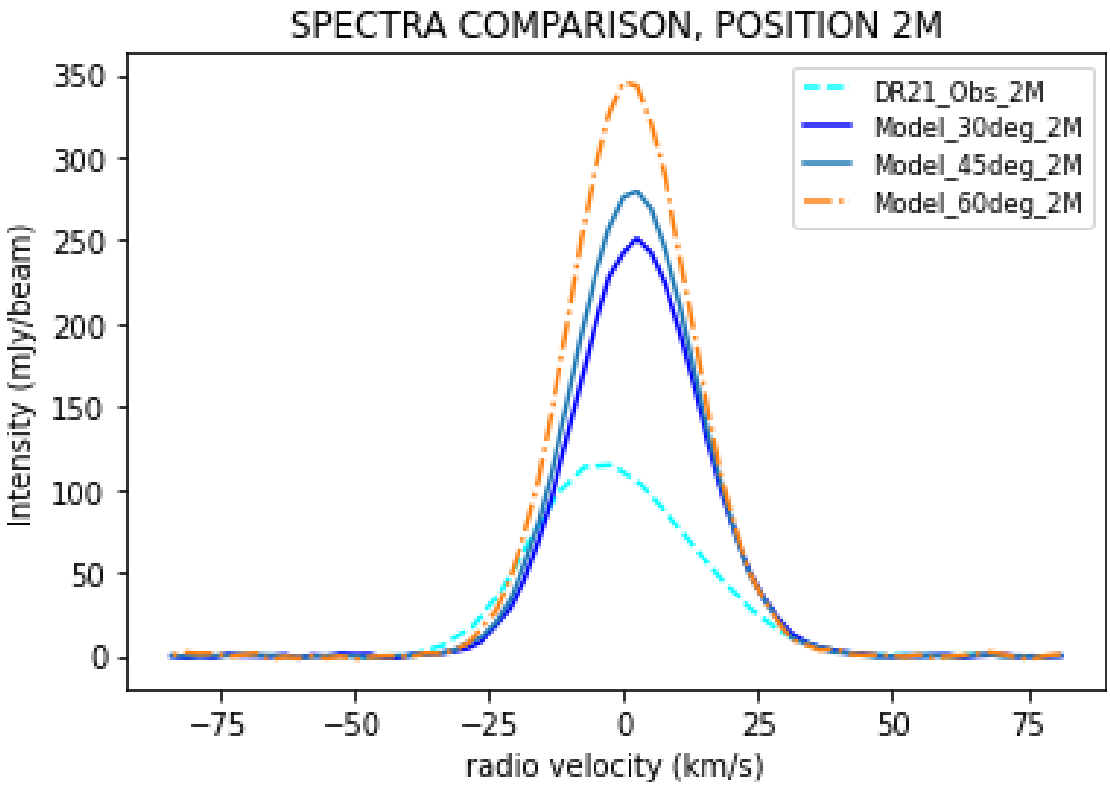


Figure 4.18: Same as Figure 4.15 but for the box position 2M for the observed data and the models

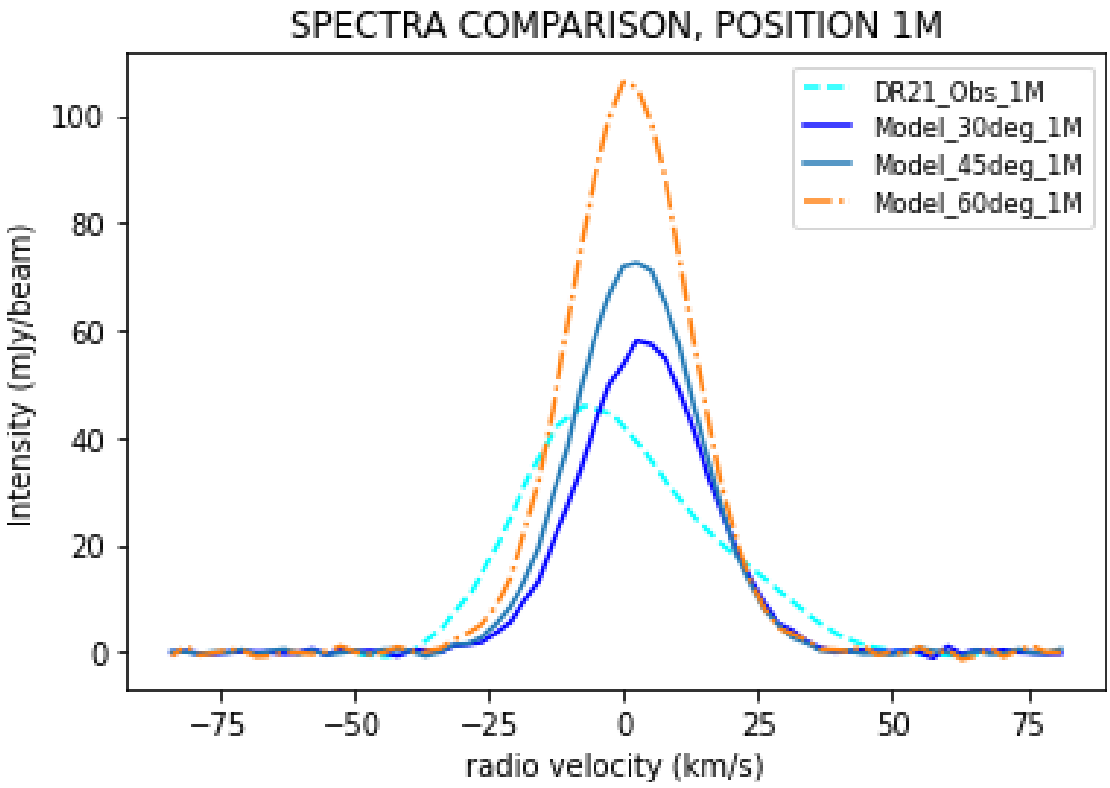


Figure 4.19: Same as Figure 4.15 but for the box position 1M for the observed data and the models

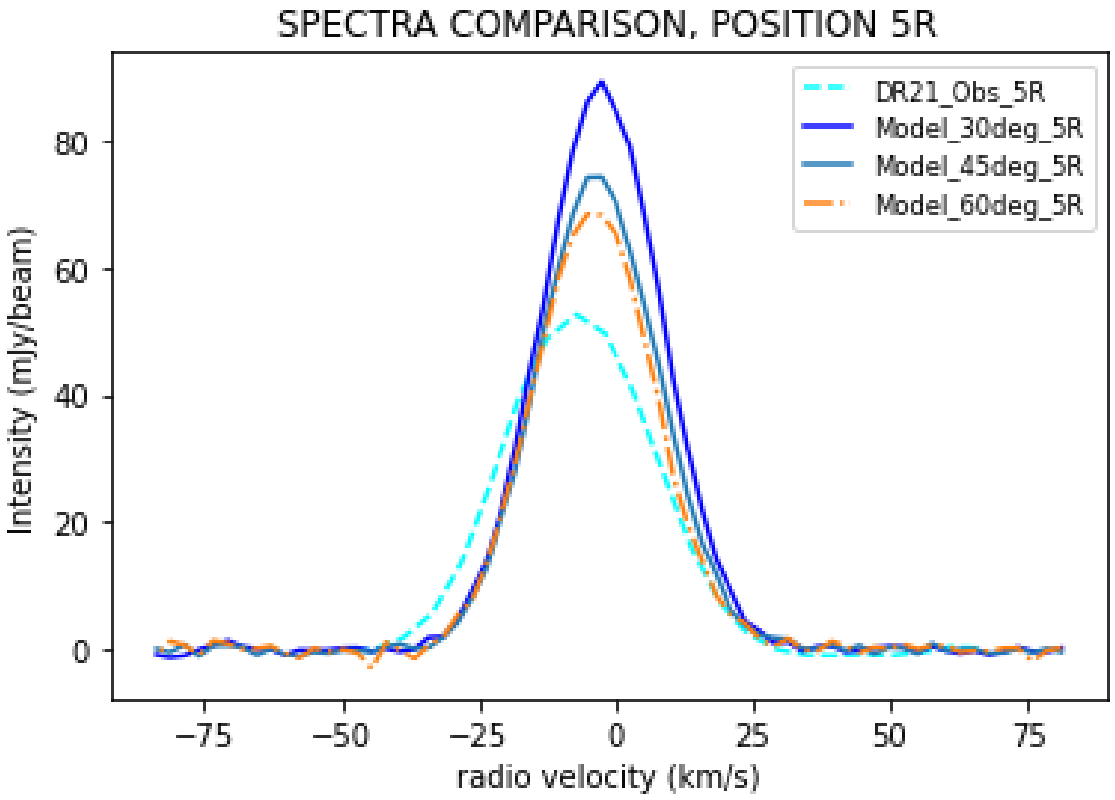


Figure 4.20: Same as Figure 4.15 but for the box position 5R of the observed data and the models.

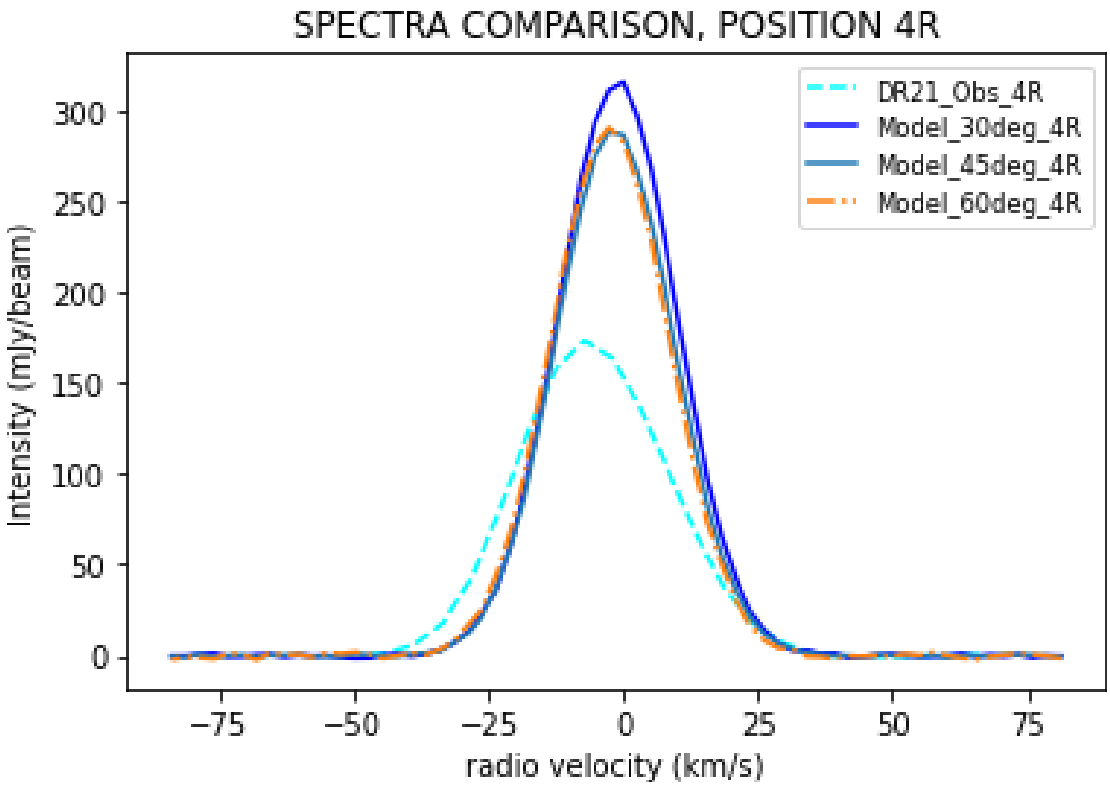


Figure 4.21: Same as Figure 4.15 but for the box position 4R of the observed data and the models.

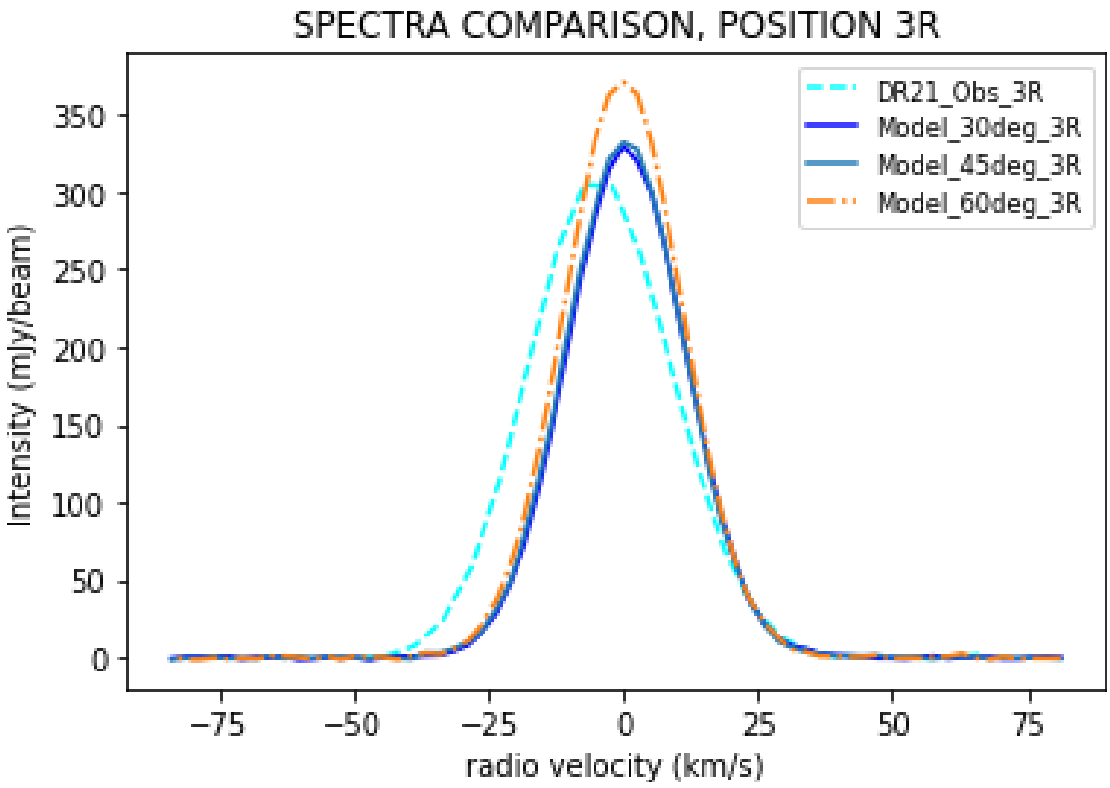


Figure 4.22: Same as Figure 4.15 but for the box position 3R of the observed data and the models.

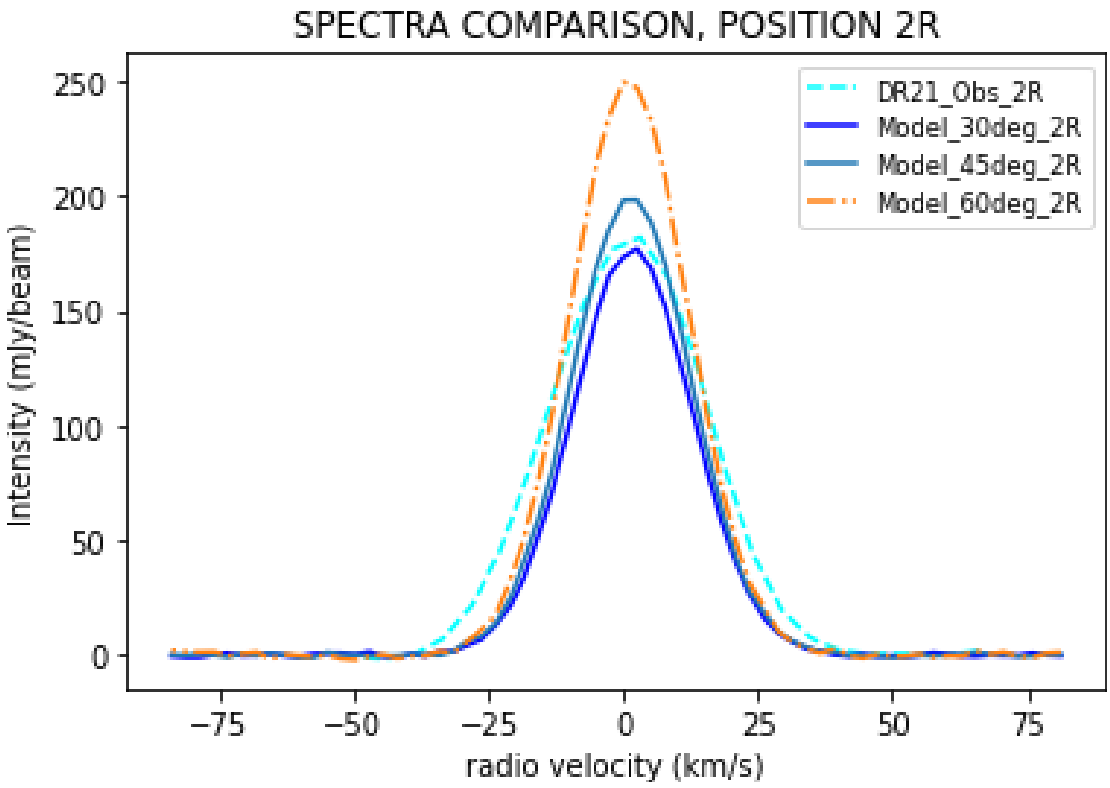


Figure 4.23: Same as Figure 4.15 but for the box position 2R for the observed data and the models.

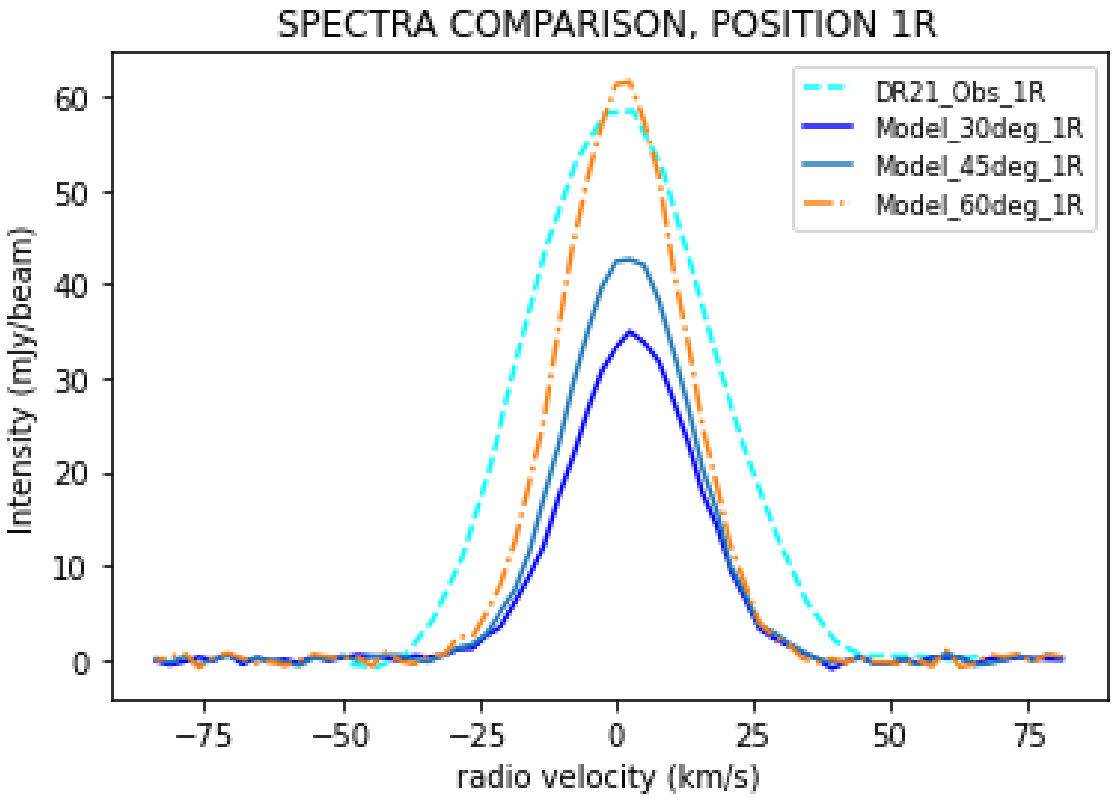


Figure 4.24: Same as Figure 4.15 but for the box position 1R for the observed data and the models.

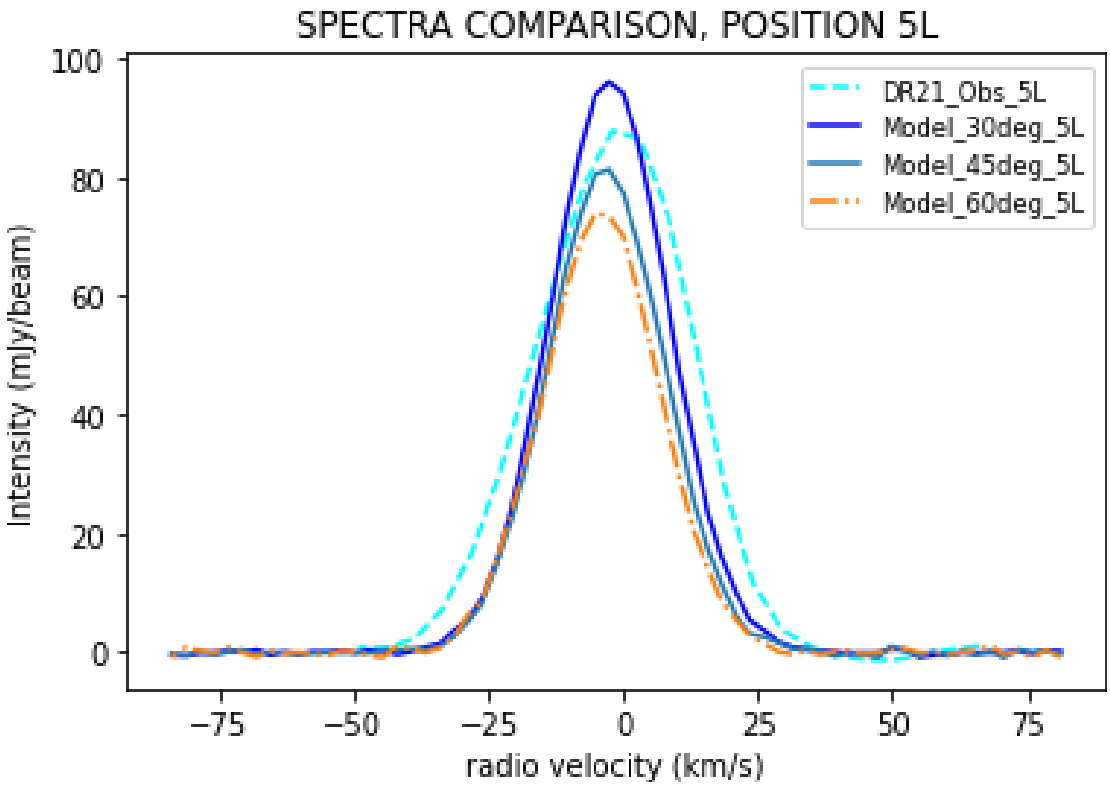


Figure 4.25: Same as Figure 4.15 but for the box position 5L of the observed data and the models.

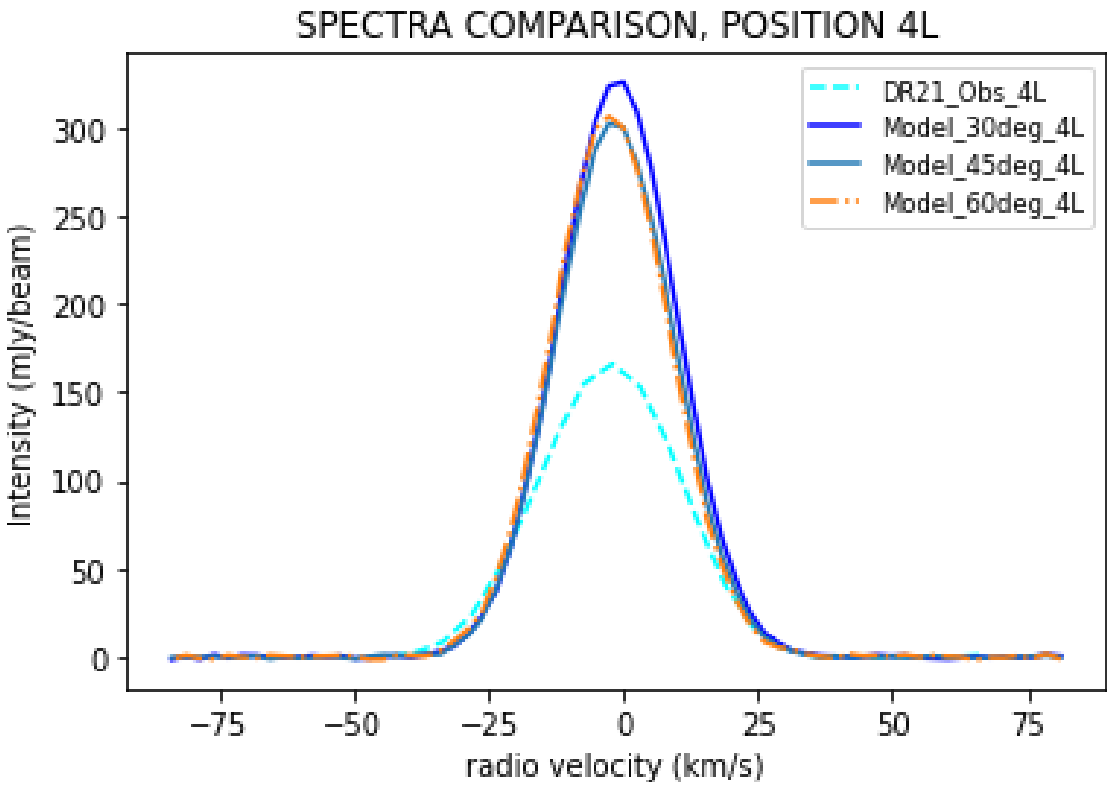


Figure 4.26: Same as Figure 4.15 but for the box position 4L of the observed data and the models.

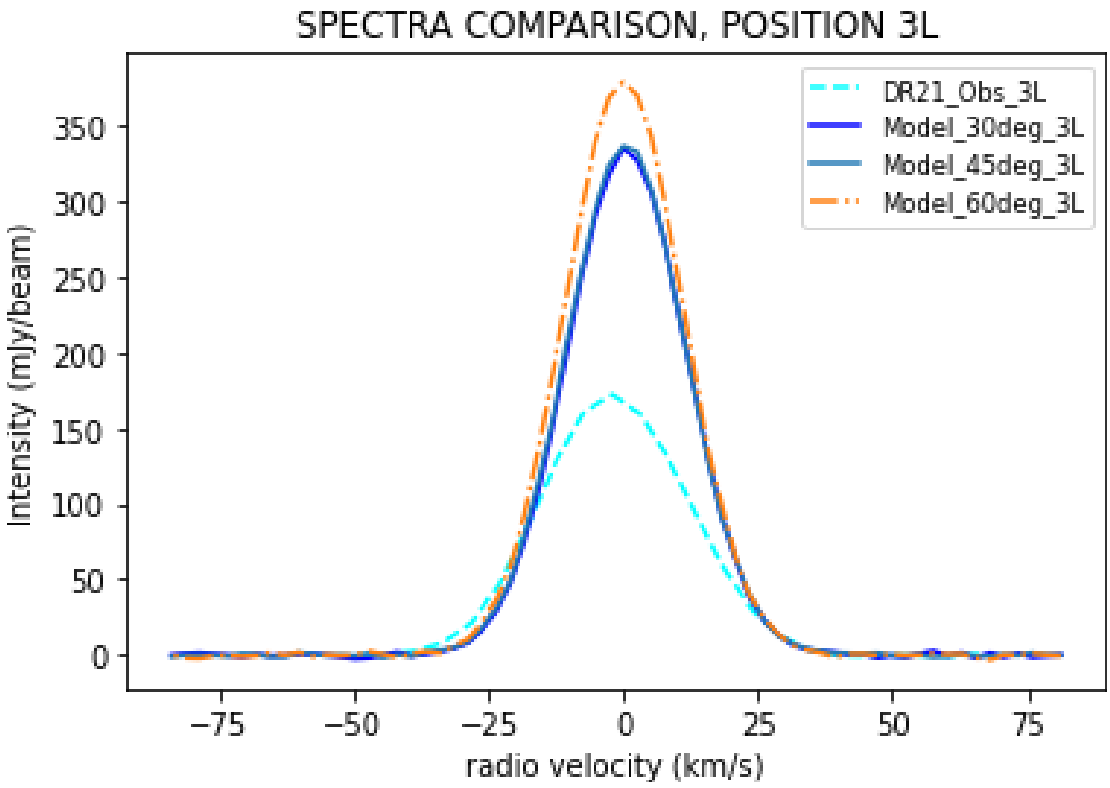


Figure 4.27: Same as Figure 4.15 but for the box position 3L of the observed data and the models.

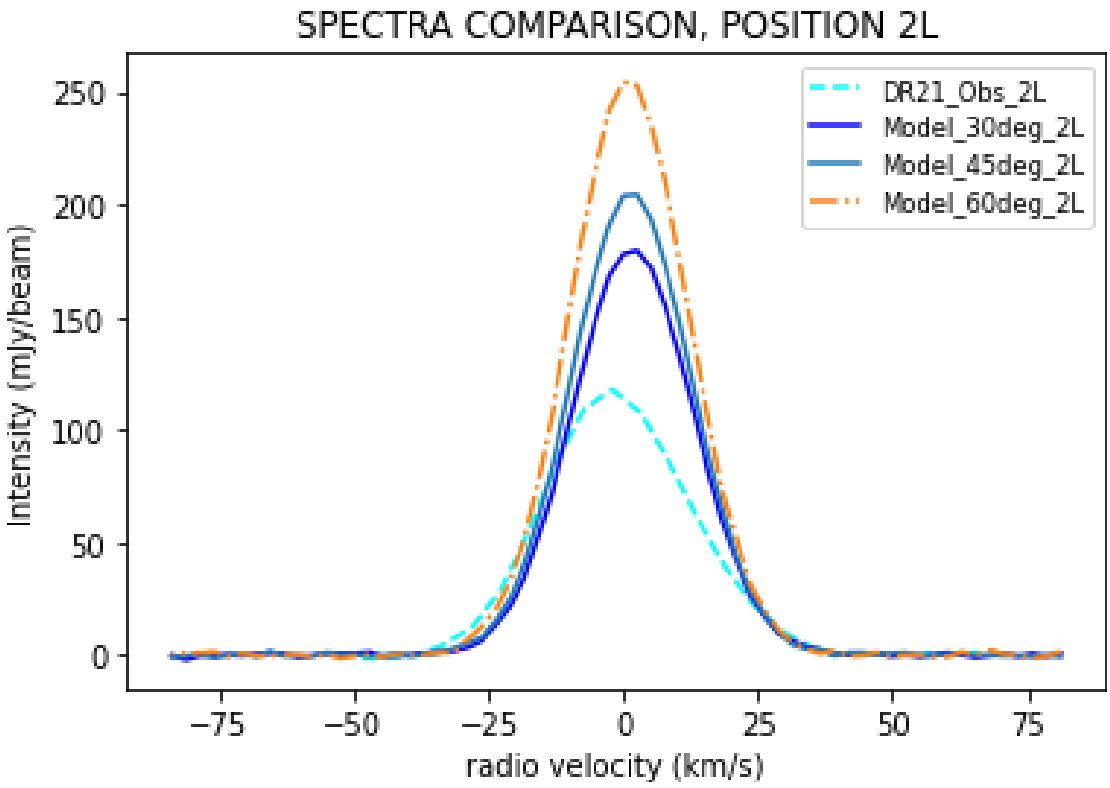


Figure 4.28: Same as Figure 4.15 but for the box position 2L for the observed data and the models.

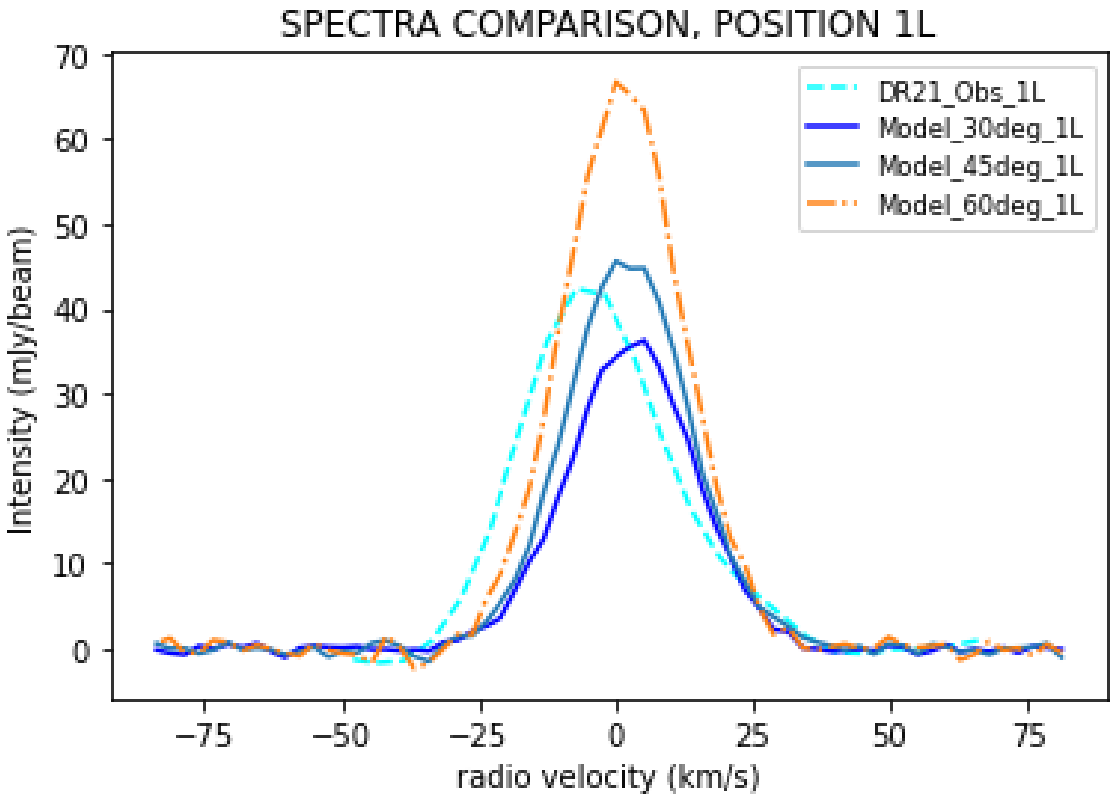


Figure 4.29: Same as Figure 4.15 but for the box position 1L for the observed data and the models.

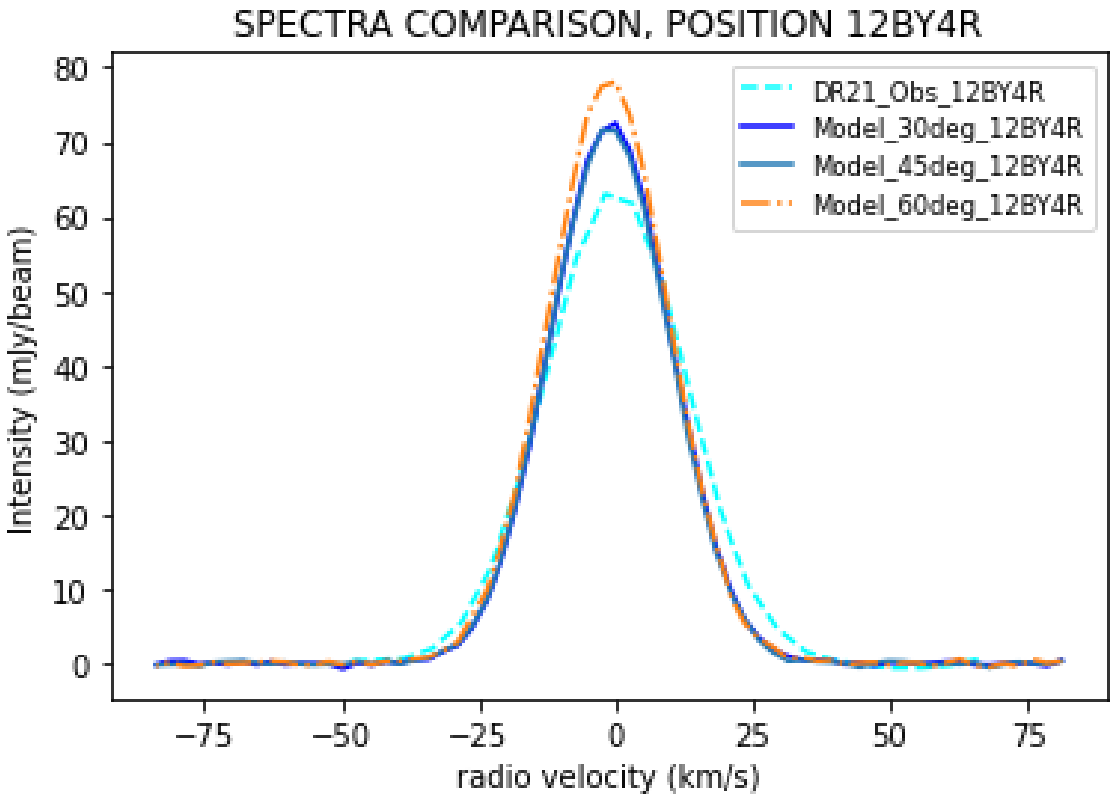


Figure 4.30: Same as Figure 4.15 but for the box position 12BY4R for the observed data and the models

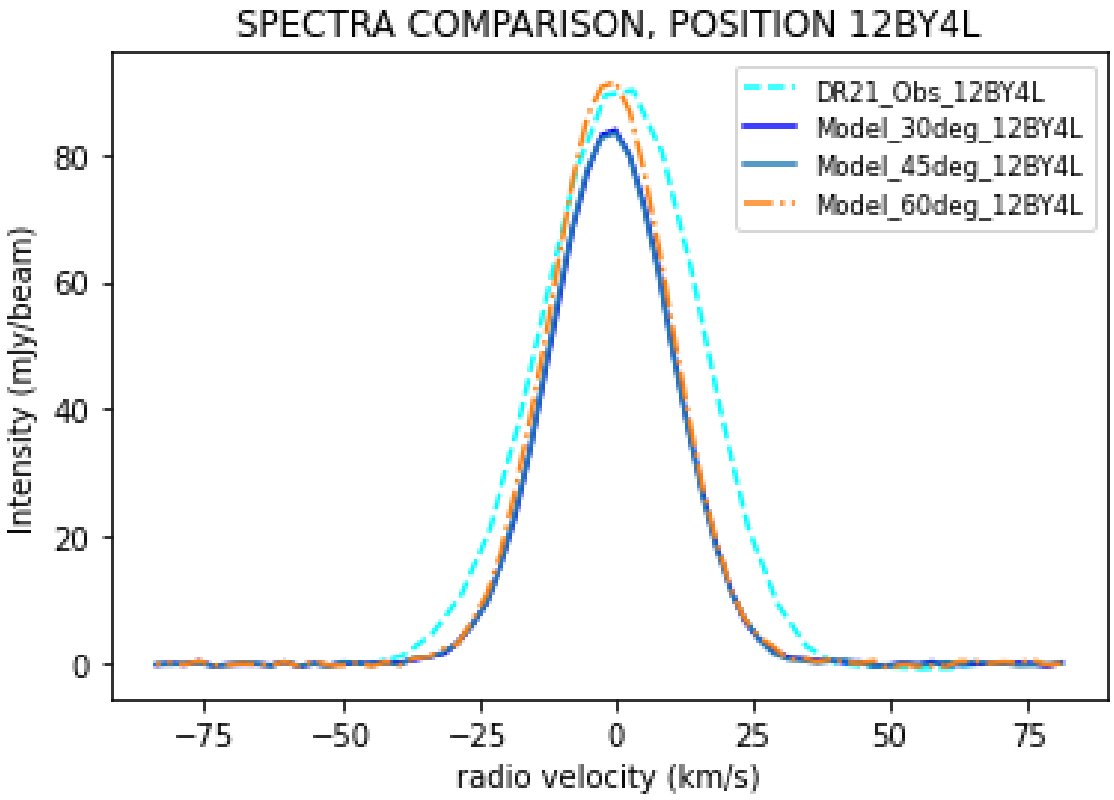


Figure 4.31: Same as Figure 4.15 but for the box position 12BY4L for the observed data and the models

are the central line velocity relative to the local standard of rest (V_{lsr}), the full width at half maximum (FWHM), and the amplitude. The spectral line profiles for the observed data and models have been compiled and compared as shown in Figure 4.15 to 4.31. Each figure shows the actual spectral line data and the Gaussian fit to the observed data and models for each located box position. The plot at the 5M position near the cometary head of DR21 compares the observed spectral data with three model spectra projected at different inclination angles (30, 45, and 60 degrees). This comparison highlights how the models reproduce the observed features across varying viewing angles, aiding in constraining the inclination and physical conditions of the region. By examining Figure 4.15, it is evident that a single Gaussian provides a reasonable fit to the model profiles, and similarly fits the observed data to a satisfactory degree. A single Gaussian was fitted to the observed data and the models for comparison as seen in Figure 4.15. The graph at the 5M box position of the cometary head shows that the model intensities decrease as the inclination angle increases from 30° to 45° and then to 60°. The intensities for the models were relatively higher than the observed data for box position 5M, while the FWHM value for the observed data is larger than the models.

For box position 4M, a single Gaussian perfectly fits both the observed data and the models. The intensities of the models are higher than the observed data, while the observed data has a larger value of FWHM than the models. The same trends were seen for box positions 3M, 2M, and 1M with higher intensities and relatively smaller FWHM for the models and observed data. From the plots' observations (box positions 5M, 4M, 3M, 2M, and 1M), the models tend to have a blue shift at the cometary head and a red shift at the cometary tail. The observed data shows a blue shift from the cometary head to the tail. The box positions 5L, 4L, 3L, 2L, and 1L follow a similar pattern as the models are blue-shifted at the cometary head and red-shifted towards the tail while the observed data are all blue-shifted. A single Gaussian fits the observed data and the models. Box positions 5R, 4R, 3R, 2R, and 1R have the same pattern for the observed data and the model, with the cometary head blue-shifted and the tail red-shifted. A single Gaussian also

fits reasonably well with the observed data and the models. The box positions 12BY4R and 12BY4L were perfectly fitted with a single Gaussian for both the observed data and models. There is a slight difference in the intensities, but more comparable in the case of 12BY4L. The FWHM of the observed data is higher than the models. (It must be noted that the blue-shifted and red-shifted were deduced using the systemic velocity of -2.0 kms^{-1} as reference measured by Cyganowski *et al.* (2003)).

The minimum and maximum amplitudes for the observed data are 43 mJy at position 1L and 311 mJy at position 3R, respectively, with an average of 131 mJy. The model projected at 30° has a minimum and maximum amplitude of 35 mJy and 445 mJy with an average of 199 mJy. The model projected at 45° has an average amplitude of 198, and the model projected at 60° has an amplitude of 220. It is observed from the plots that the peak flux from the models was relatively higher than the observed data, which may be particularly attributed to the non-LTE effects. The FWHM for the observed data has a minimum value of 30 kms^{-1} and a maximum value of 39 kms^{-1} while the models have a minimum and maximum value of 26 kms^{-1} and 39 kms^{-1}. The relatively lower values of the FWHM of the models could be attributed to the effects of the Turbulent broadening, V_{turb}, with a value of 1 kms^{-1} used for the models.

Cyganowski *et al.* (2003) reported in the long slit of their Figure 2 (S/4, S/3, S/2, and S/1), and the corresponding plots in their Figure 3 had one Gaussian fitted to the data in the Southern area (same as Figure 4.1 labelled B and models). Immer *et al.* (2014) generated spectra from the cometary head to the tail for the Southern area in their figure 1 plot labelled S/0, S/1, S/2, S/3, S/4, S/5, S/6 and S/7 used one Gaussian except for S/0 and S/5, which were fitted with 2 Gaussians. By observing the cometary UCHII regions DR21 of figure 1 (plot c) for the box positions (4" x 4"); 39, 40, 41, 42, 48, 49, 50, 51, 59, 60, 61, 62, 70, and 72 by Immer *et al.* (2014) which are considered within the Southern area (same as Figure 4.1 labeled B and models), it is debatable that one Gaussian may best fit the corresponding spectra lines. One Gaussian fit was used for comparison with models in the initial phase of the spectra analysis.

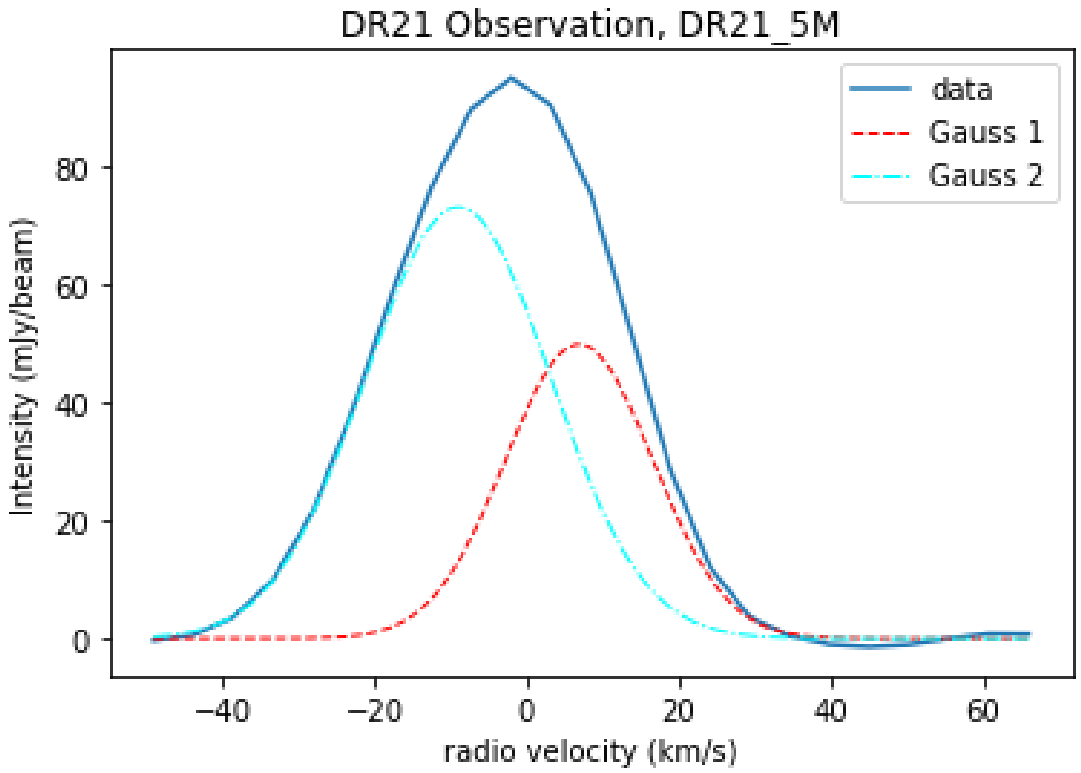


Figure 4.32: This plot shows the 2 Gaussian fits for the box position 5M for the observed data of the cometary UCHII region DR21. The velocities, V_{vls}, obtained are 6.92 kms^{-1} and -9.00 kms^{-1}

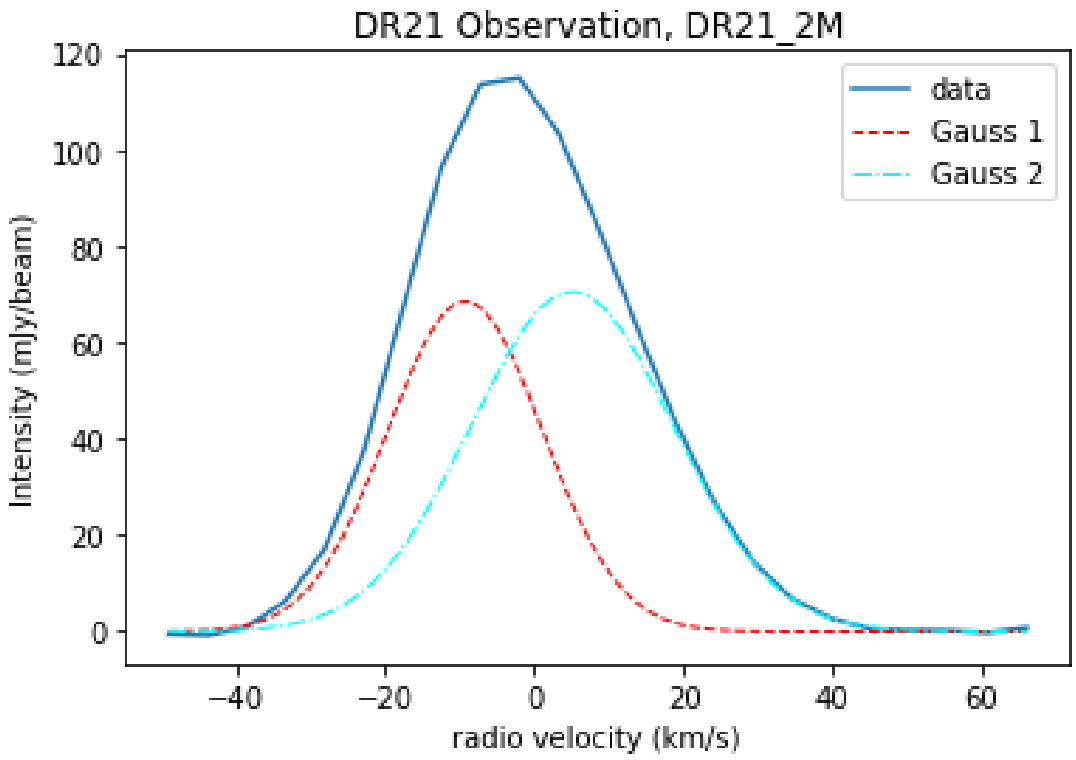


Figure 4.33: This plot shows the 2 Gaussian fits for the box position 2M for the observed data of the cometary UCHII region DR21. The velocities, V_{vls}, obtained are -9.30 kms^{-1} and 5.07 kms^{-1}

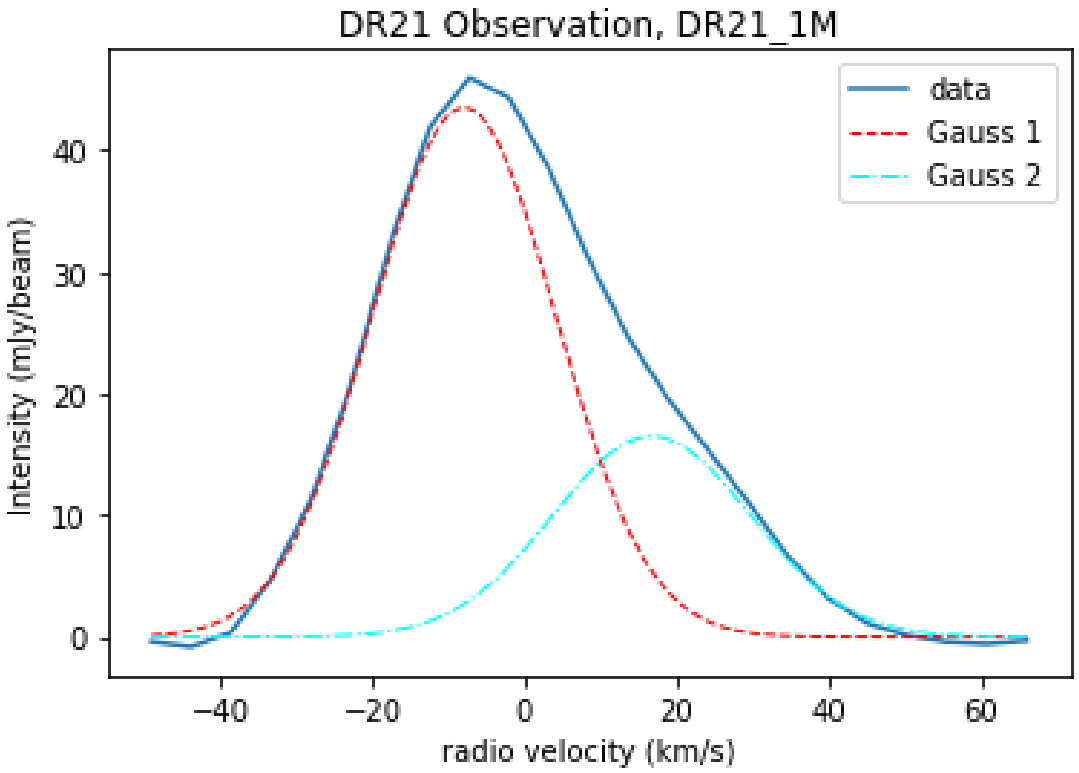


Figure 4.34: This plot shows the 2 Gaussian fits for the box position 1M for the observed data of the cometary UCHII region DR21. The velocities, V_{vls}, obtained are -7.97 kms^{-1} and 16.73 kms^{-1}

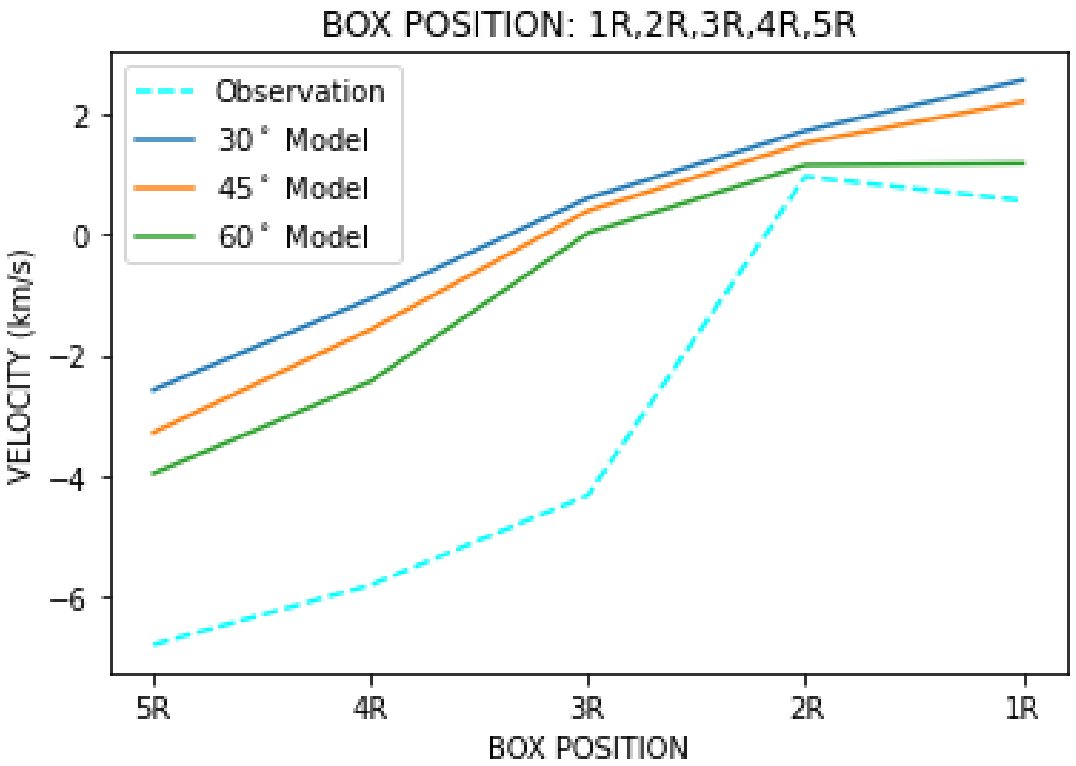


Figure 4.35: The plot displays the peak velocities for the observed data and models with respect to the box positions, to investigate the motion of the ionised gas from the head (5R) to tail (1R) of the cometary UCHII region DR21

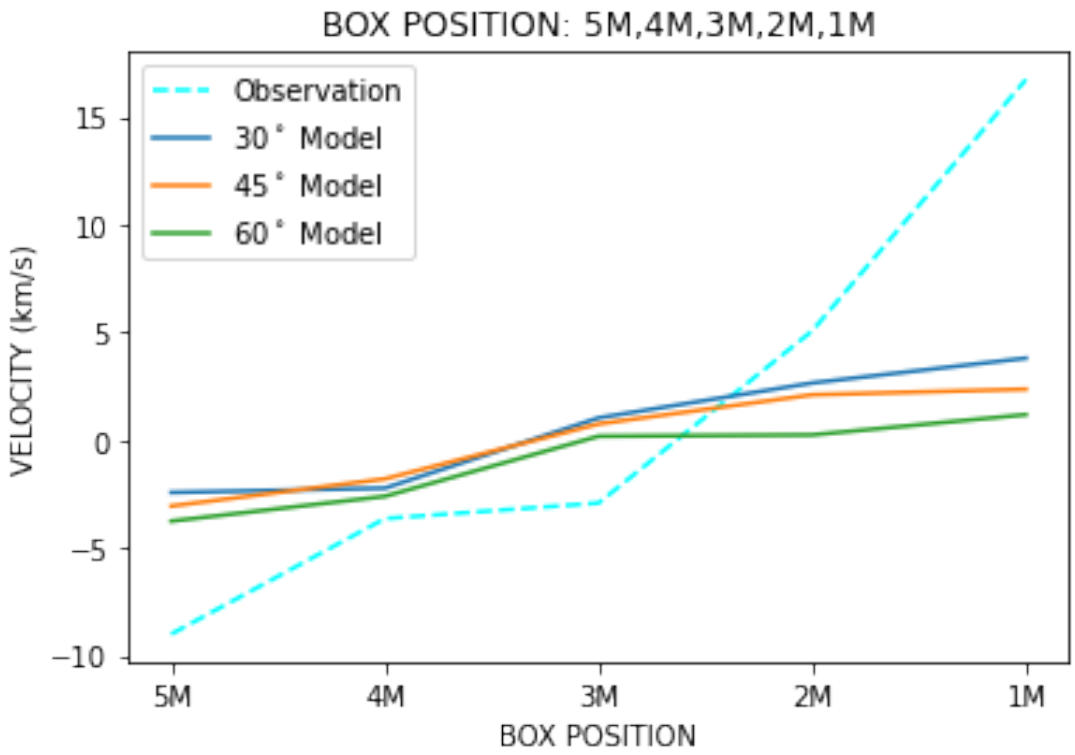


Figure 4.36: The plot displays the peak velocities for the observed data and models with respect to the box positions, to investigate the motion of the ionised gas from the head (5M) to the tail (1M) of the cometary UCHII region DR21

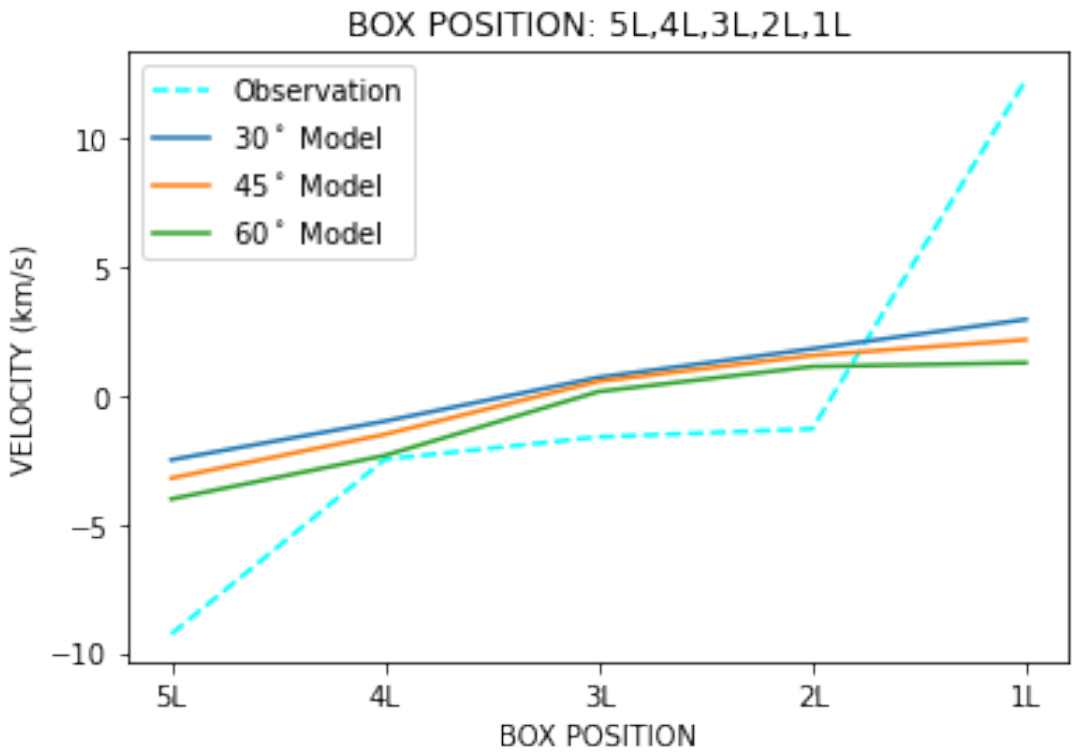


Figure 4.37: The plot displays the peak velocities for the observed data and models with respect to the box positions, to investigate the motion of the ionised gas from the head (5L) to tail (1L) of the cometary UCHII regions DR21

It was observed that 2 Gaussians could also fit the observed data for the box positions of 5M, 2M, and 1M as shown in Figure 4.32, 4.33, and 4.34. The ionised gas velocities with respect to the box positions were investigated (the value with the highest velocity between the 2 Gaussians was selected because they reasonably fit the models for box positions 5M, 2M, and 1M) to compare the observed data to the models.

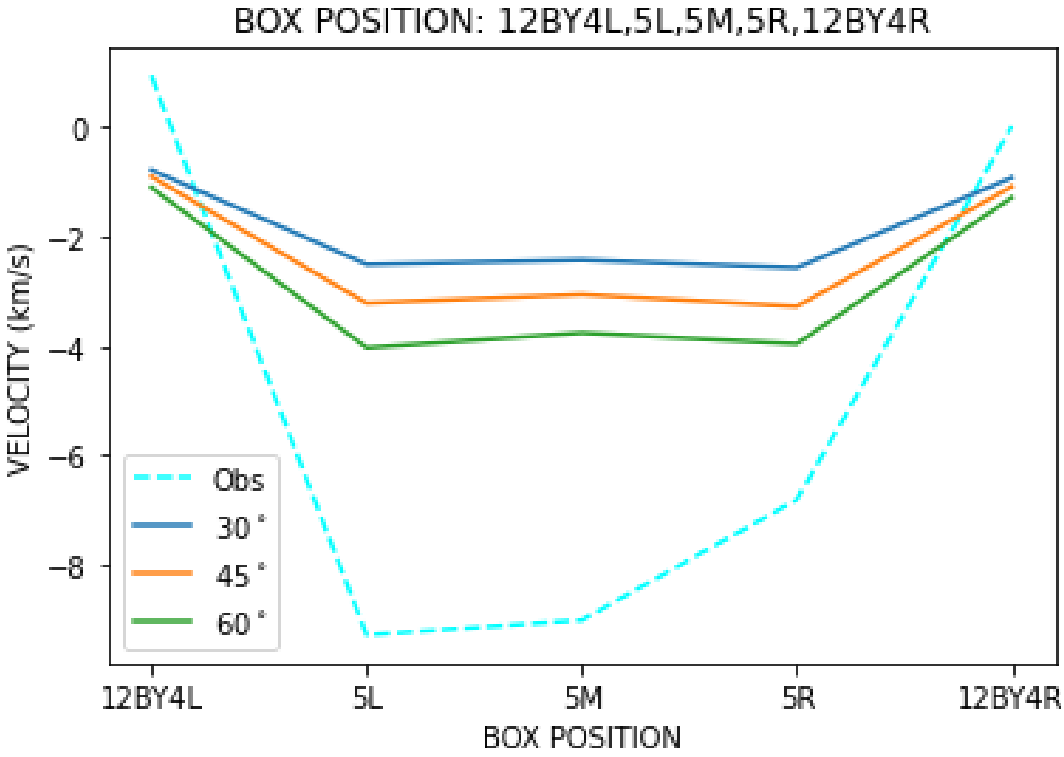


Figure 4.38: The plot displays the comparison of observed data and the models of the ionised gas motion viewed from below through the horizontal plane of the cometary UCHII regions DR21

Figures 4.35, 4.36, and 4.37 display the ionised gas velocities with respect to the box positions from the cometary head to the tail of the observed data and models for the UCHII region DR21. It is deduced from the plots that varying the inclination angles for the models from 30°, 45°, and 60° had no significant effect on the ionised gas motions. The plots also show a regular pattern for the blue-shifted

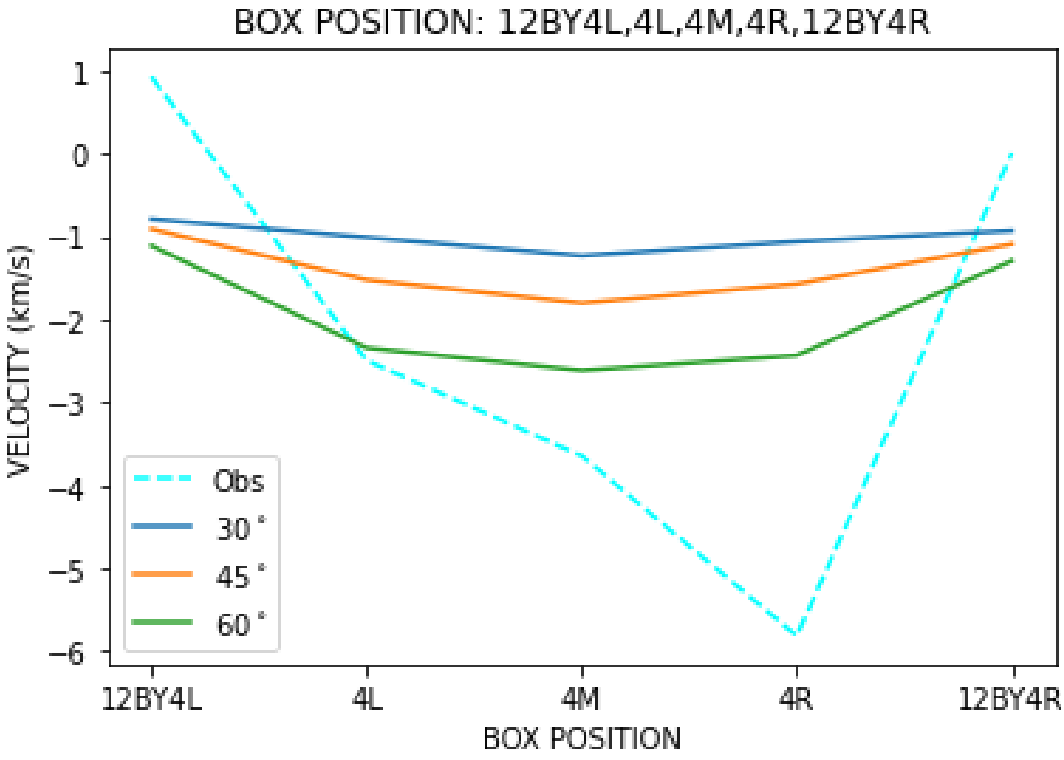


Figure 4.39: Same as Figure 4.38 at different box positions of the cometary UCHII regions DR21

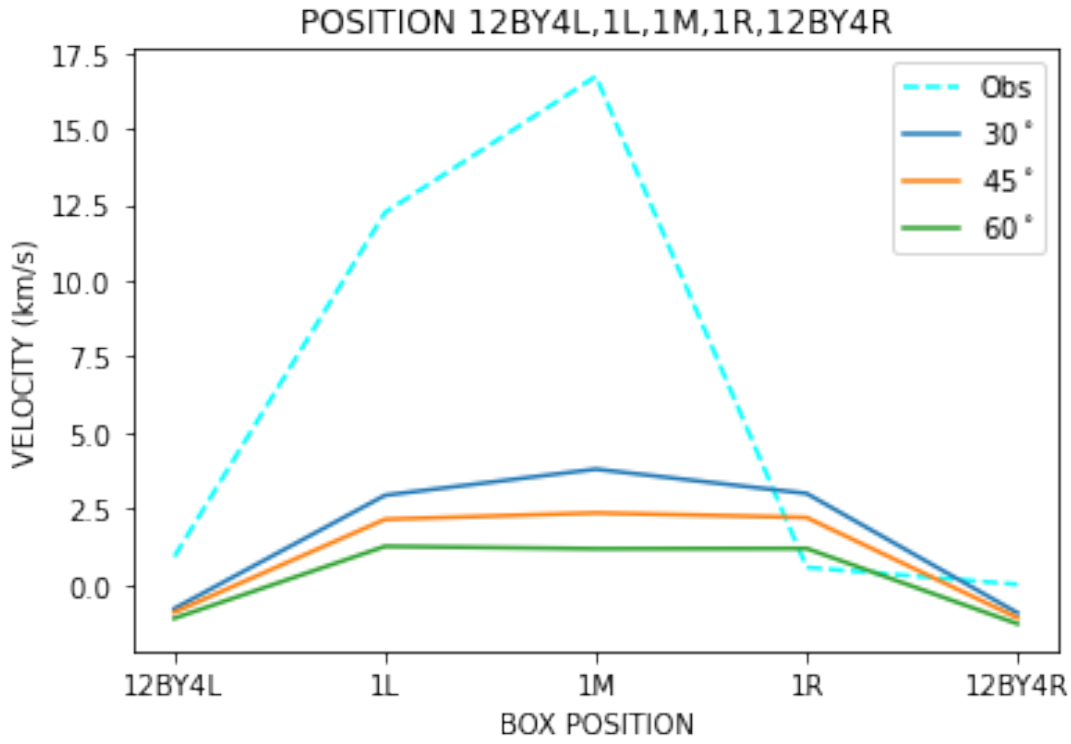


Figure 4.40: Same as Figure 4.38 at different box positions of the cometary UCHII regions DR21

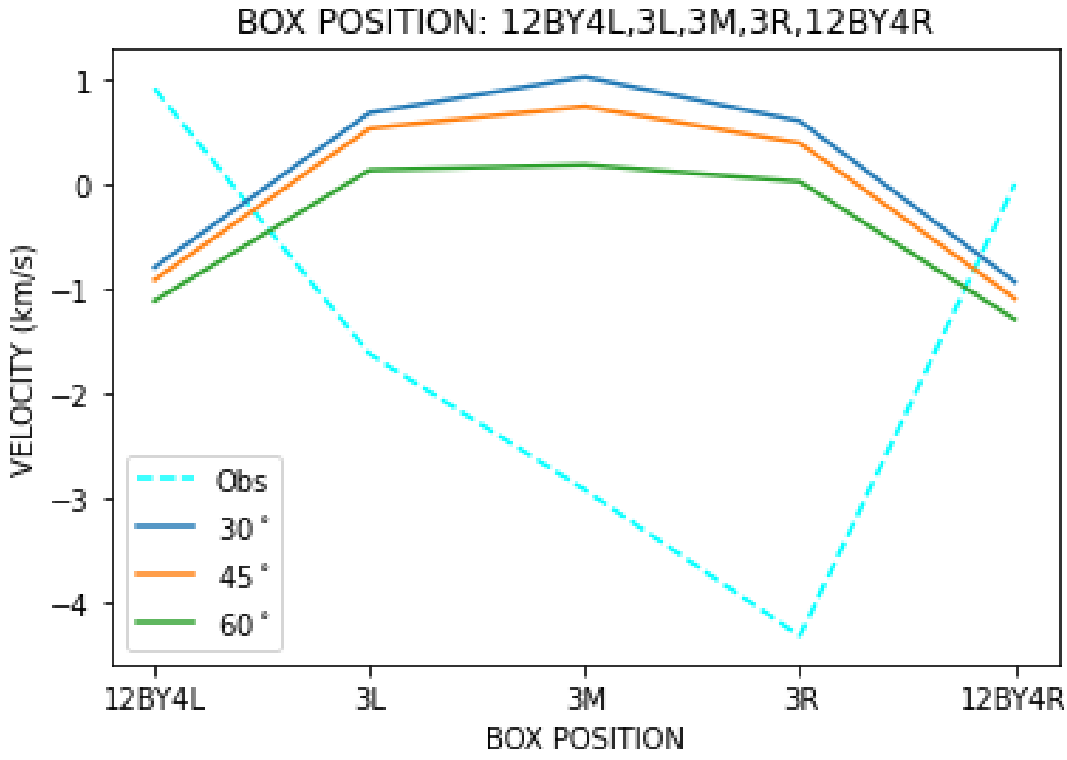


Figure 4.41: Same as Figure 4.38 at different box positions of the cometary UCHII regions DR21

at the cometary head and red-shifted at the cometary tail for both the observed data and models. In the head region (e.g., positions 5L, 5M, 5R), the models exhibit velocities $\approx 5\text{kms}^{-1}$ more redshifted than the observations. This discrepancy could potentially be resolved by incorporating the star's proper motion and the resulting bow shock of the HII region moving toward the observer, i.e., in the direction of the molecular cloud core.

At the tail positions (1L, 1M, 1R), the models fail to reproduce sufficient redshifted motion. This is because the static models do not break out along the density gradient to produce the high-velocity champagne flow observed. This discrepancy could be addressed by adopting a steeper density gradient in the tail region or by positioning the HII region further from the core within a lower-density environment. Both scenarios are consistent with the star's proper motion toward the core. In terms of analysing the velocities, V_{lsr}, for the observed data and models, plots from head to tail were analysed as well as in the horizontal plane to investigate the kinematics of the ionised gas structure. For the selected horizontal plots, there are similarities between the observed data and the model as seen from the shape of Figures 4.38, 4.39, and 4.40. However, there is a disparity in the shape between the observed data and the models as seen in Figure 4.41. The immediate explanation of the difference in the observed data and models may result from the lack of proper motion.

4.5 Numerical Methods and Code Improvements

As mentioned earlier, incorporating appropriate stellar motions could resolve the discrepancy in the shape of the cometary tail, since the current models do not reproduce the breakout observed in the tail of DR21. To develop more realistic models, it is important to update the existing hydrodynamics code or incorporate a new code that includes proper stellar motion, similar to Models G, D, and I described by Arthur & Hoare (2006). This latter approach was pursued, and a new code was implemented and tested.

The details of the new code numerical framework and computational methods

used to model the hydrodynamics and radiative transfer of cometary Ultracompact HII (UCHII) regions are described here. The simulations presented were performed using an updated hydrodynamics code named HOPE, developed by Pittard, J. (in preparation) as an extension of the TORCH code originally written by Steggles (2016). The hydrodynamic simulations were subsequently post-processed using a ray-tracing radiative transfer code, "Ray-Tracing" developed by Pittard, J. (in preparation), analogous in method to the RadioRT code by Steggles (2016), to produce synthetic radio continuum maps for direct comparison with observations.

The HOPE code retains much of the numerical architecture and physical modelling approach of TORCH, while introducing several key improvements, particularly in its treatment of variable thermodynamic quantities, pressure balance within non-uniform clouds, and the inclusion of stellar velocity effects. These enhancements enable HOPE to simulate more realistic environments in which ionising sources move through structured interstellar media.

4.5.1 Overview of the HOPE Code

The HOPE (Hydrodynamics of Photoionised Environments) code is a grid-based hydrodynamic solver designed to model the coupled evolution of ionised gas under the influence of stellar radiation and winds. The code solves the standard set of Euler equations for compressible gas dynamics, including the effects of ionisation heating, radiative cooling, and self-consistent evolution of the ionisation fraction. In its current form, HOPE incorporates several features that are broadly similar to TORCH, but with key methodological and computational refinements, as outlined below.

4.5.2 Comparison Between HOPE and TORCH

Both HOPE and TORCH employ a short-characteristics ray-tracing algorithm to compute the optical depth from the ionising source to each grid cell. This information is used to determine the ionisation rate, while an implicit solver

is applied to compute the time-averaged ionisation fraction in each cell. This approach ensures numerical stability and accurate coupling between the hydrodynamic and radiative processes.
However, the implementation of ray-tracing in HOPE differs from that in TORCH. While TORCH performed the ray-tracing sequentially in a serial fashion, HOPE parallelises this step using causal shells, significantly improving computational efficiency. This parallelisation allows for faster calculation of ionisation fronts, particularly in high-resolution simulations where causal dependencies are well-defined.

Variable Thermodynamic Quantities

One of the major physical enhancements in HOPE is the cell-dependent treatment of the ratio of specific heats (γ) and the mean particle mass (μ). In TORCH, both γ and μ were fixed global constants throughout the simulation domain. In contrast, HOPE allows these quantities to vary locally depending on the gas temperature. "Lookup tables" are used to assign γ and μ values based on the cell's pressure and density (proxies for temperature). This enables the code to represent realistic variations in gas composition and thermodynamic response across a broad temperature range from 1 K to 10^9 K. Although this modification does not produce dramatic changes in large-scale hydrodynamic structures, it ensures that the thermodynamic behaviour of the gas is treated more consistently with physical expectations.

Treatment of Non-Uniform Clouds and Pressure Balance

A more significant difference between HOPE and TORCH arises in the treatment of background density structures. In TORCH, non-uniform background clouds were initialised with a constant pressure throughout the domain. This simplification ensured that the cloud remained static but required an artificial correction to prevent motion when external dynamical processes such as expanding HII regions or stellar winds were present. HOPE replaces this with a physically motivated equilibrium model. The cloud is initialised with its equilibrium

temperature profile, such that the denser core is cooler than the outer regions. This naturally produces an outward pressure gradient. To maintain stability and prevent unphysical expansion, HOPE computes an effective cloud mass distribution, $M(r)$, required to support hydrostatic equilibrium corresponding to the pressure gradient. At each timestep, an inward gravitational acceleration associated with $M(r)$ is applied, thereby balancing the pressure gradient.

4.6 Benchmark Testing of the HOPE Code

To validate the performance and physical accuracy of the HOPE code, benchmark tests were performed against the results of Arthur & Hoare (2006), hereafter referred to as AH06. In particular, the benchmark focused on Model B of AH06, which represents a uniform-density medium through which a massive star moves supersonically, driving a bow shock and forming a cometary HII region. This test provides a stringent comparison between the hydrodynamic and ionisation structures produced by HOPE and those of a well-established model.

4.6.1 Model Setup

The benchmark simulation assumes an ionising source embedded in a uniform ambient medium of hydrogen number density $n_0 = 6000$ cm^{-3}. In contrast to AH06 Model B, where the ionising star moves at a velocity of $v_* = 20$ km s^{-1} through a static medium, the HOPE implementation adopts an equivalent but numerically convenient frame of reference: the ionising star is kept stationary at the grid centre, while the *ambient medium* is set in motion at a velocity of $v_{\rm amb} = 20$ km s^{-1} relative to the star. This approach yields an identical relative motion between the star and the surrounding gas, ensuring direct comparability of the physical outcomes while simplifying the numerical setup.

The choice of stellar velocity (or equivalently, ambient flow speed) reported by Arthur & Hoare (2006) is motivated by previous empirical and theoretical models of the ultracompact HII region G29.96-0.02 by Afflerbach *et al.* (1994); Lumsden & Hoare (1996); Martín-Pintado *et al.* (1993); Zhu *et al.* (2005), which exhibit

similar kinematic properties. The stellar parameters adopted are representative of an early-type O star, with a strong stellar wind characterised by a mass-loss rate of

$$\dot{M}_{\rm w} = 10^{-6}\, M_{\odot}\, {\rm yr}^{-1}, \tag{4.2}$$

and a terminal wind velocity of

$$v_{\rm w} = 2000 \text{ km s}^{-1}, \tag{4.3}$$

typical of an O-type star (Arthur & Hoare, 2006; Hoare *et al.*, 2007b; Mac Low *et al.*, 1991; Steggles *et al.*, 2017). These parameters generate a strong stellar wind bubble surrounded by an ionised shell, both of which interact dynamically with the surrounding neutral medium (Arthur & Hoare, 2006; Steggles, 2016).

4.6.2 Model Comparison

The results from the HOPE benchmark simulations reproduce the key morphological and dynamical features reported by Arthur & Hoare (2006). Figures 4.42, 4.43, and 4.44 present direct visual comparison between the benchmark models produced using HOPE and the corresponding Figures from AH06 (Figure 4 in their paper). The figure panels as shown in Figures 4.42, 4.43, and 4.44 are arranged vertically for three evolutionary epochs: 10,000 yr, 20,000 yr, and 40,000 yr. For each epoch, the upper panel displays the results from AH06, while the lower panel shows the corresponding HOPE outputs. Each panel from AH06 illustrates the logarithmic density distribution and ionisation fraction, highlighting the structure of the bow shock and the cometary morphology of the ionised region. The velocity field from AH06 is illustrated using a split-scale representation. The **black arrows** indicate regions of the highest velocity gas ($v > 30$ km s^{-1}), typically corresponding to the stellar wind material. In contrast, the **white arrows** depict the lower velocity components ($v \leq 30$ km s^{-1}), which are generally associated with the photoevaporated flows and the swept-up ionised shells. The **grey-scale background** represents the gas density distribution, with the darkest shades indicating the densest ionised regions, spanning a dynamic range of two orders of magnitude. Regions of **neutral gas** or very

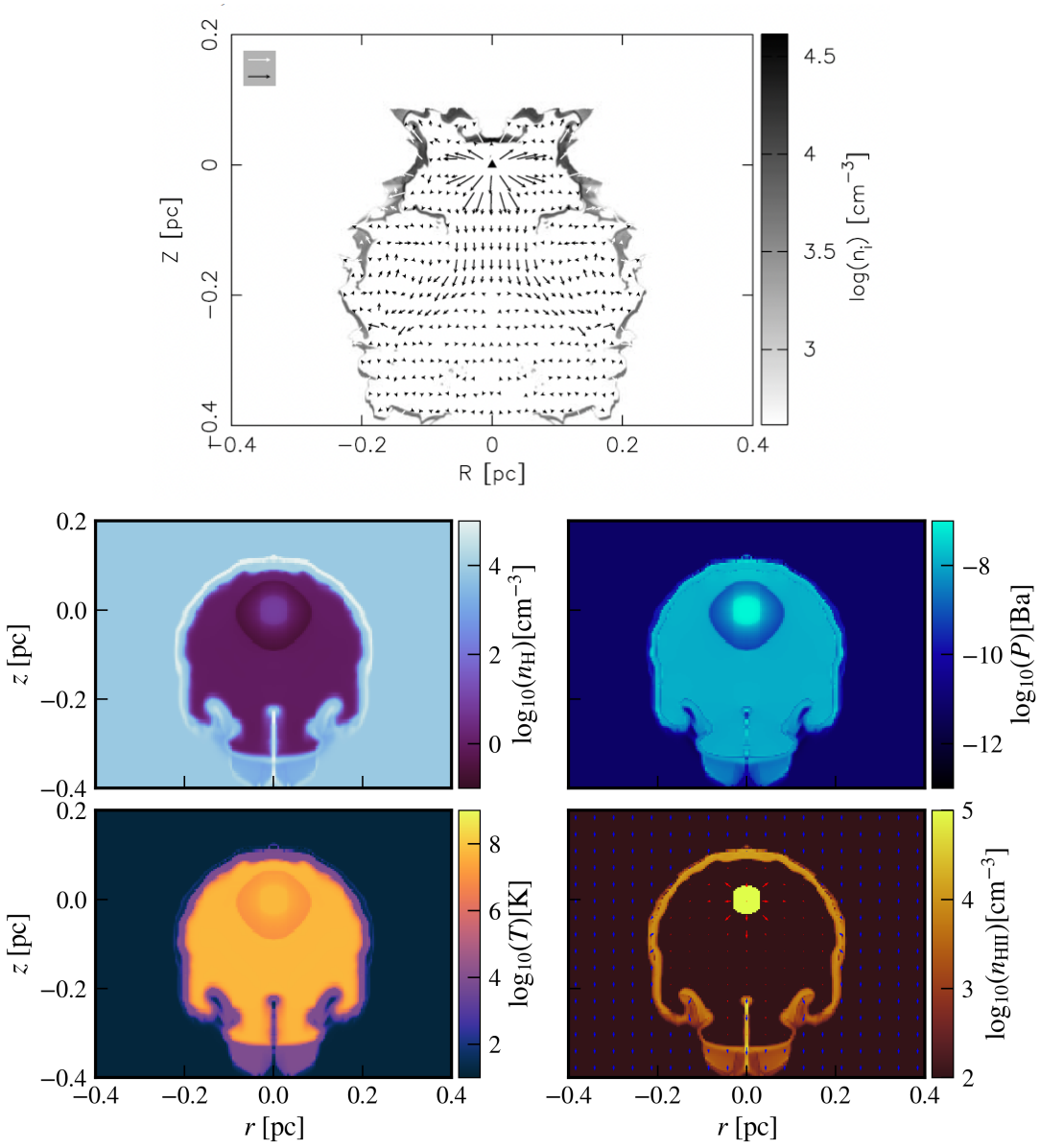


Figure 4.42: Comparison between the results of the HOPE benchmark simulation (lower panel) and the corresponding Model B of Arthur & Hoare (2006) (upper panel) after 10,000 yr of evolution. The images show the logarithmic density distribution and ionisation front morphology of the bow-shaped H II region. In HOPE, the ambient medium moves at 20 km s^{-1} relative to a stationary ionising source, whereas in AH06 Model B the ionising star itself moves through a static medium. The overall morphology and structure are consistent, demonstrating the robustness of the HOPE implementation.

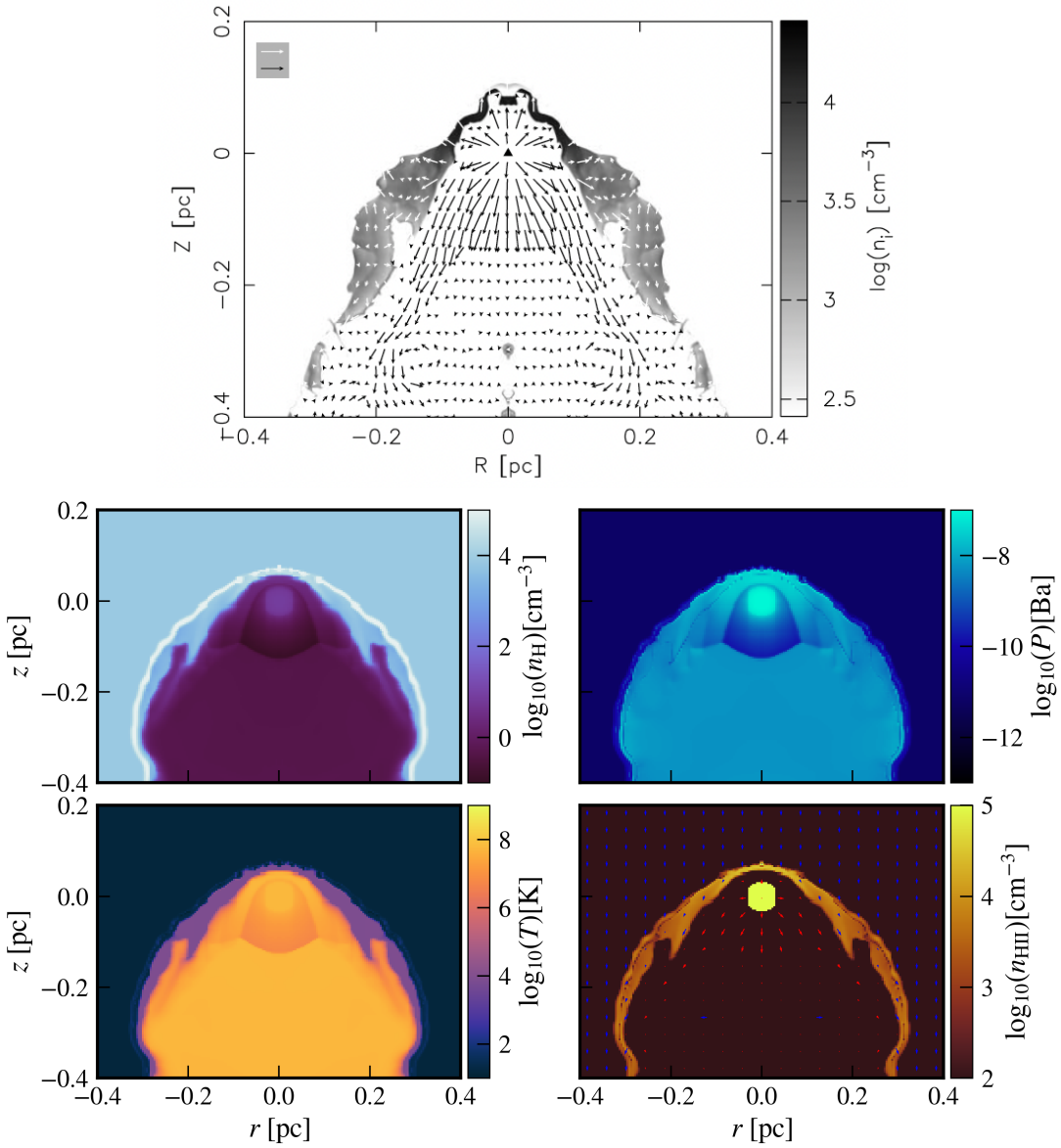


Figure 4.43: Comparison between the results of the HOPE benchmark simulation (lower panel) and the corresponding Model B of Arthur & Hoare (2006) (upper panel) after 20,000 yr of evolution. The HOPE results reproduce the dense ionised head, compressed shell, and extended tail structure seen in AH06, confirming the accuracy of the hydrodynamic and radiative transfer scheme.

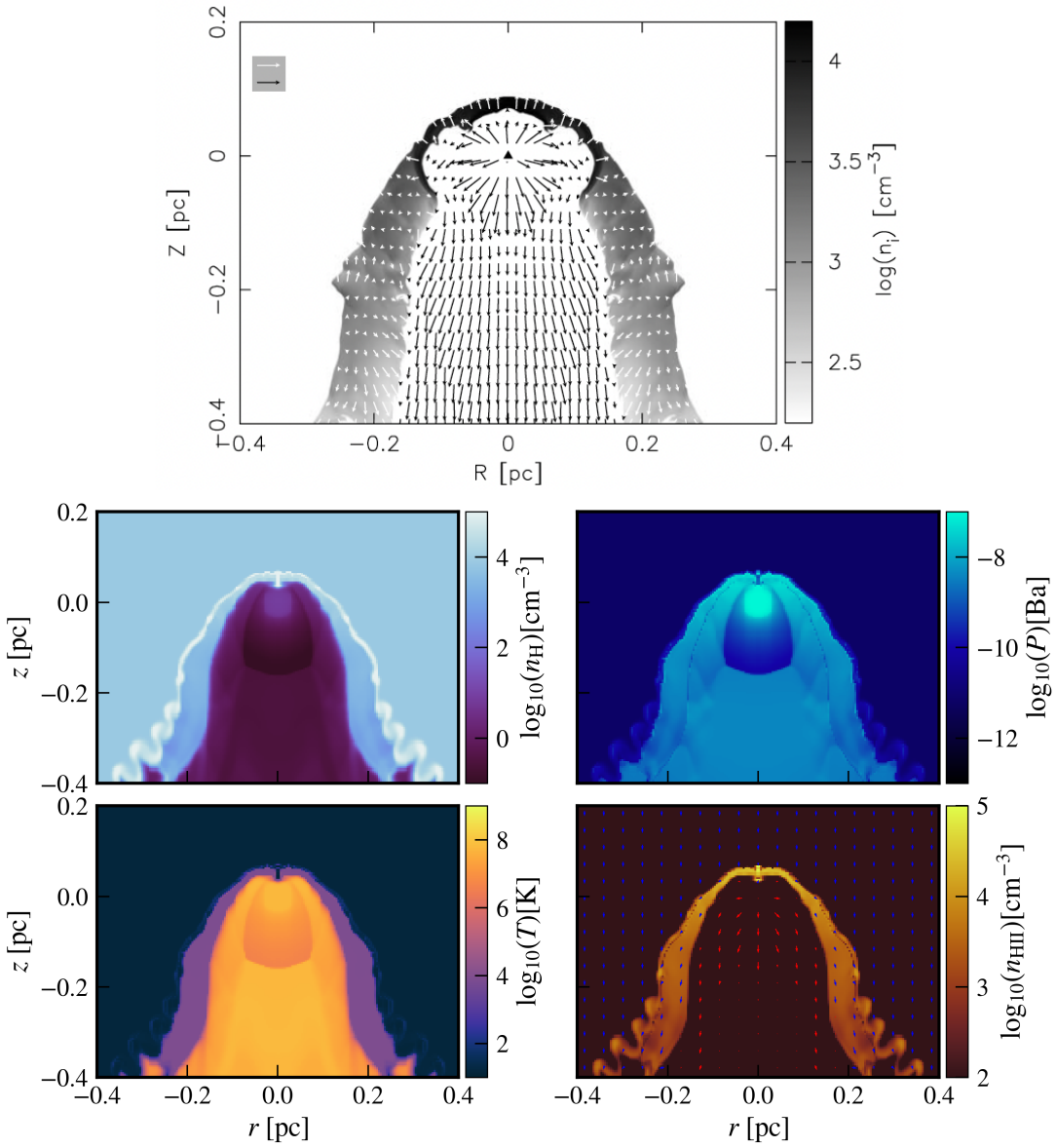


Figure 4.44: Comparison between the results of the HOPE benchmark simulation (lower panel) and the corresponding Model B of Arthur & Hoare (2006) (upper panel) after 40,000 yr of evolution. The comparison shows similar overall morphology, with consistent ionisation front structures and density contrasts, validating the reliability of the HOPE simulation for long-term evolution.

low-density ionised gas (such as the tenuous stellar wind) appear in **white**, highlighting the sharp density contrasts within the flow.
Each of the four panels (for comparison with TORCH output) in the corresponding HOPE outputs illustrates a distinct physical quantity: the **top-left** panel shows the logarithmic hydrogen number density ($\log_{10}(n_{\rm H})$ cm^{-3}), the **top-right** panel shows the logarithmic gas pressure ($\log_{10}(P)$ Ba), the **bottom-left** panel displays the logarithmic temperature ($\log_{10}(T)$ K), and the **bottom-right** panel presents the logarithmic ionised hydrogen number density ($\log_{10}(n_{\rm HII})$ cm^{-3}) which is the main focus for comparison with AH06 Model B results. The ionising star is located at coordinates $z = 0.0$ pc and $r = 0.0$ pc. The red arrows represent gas velocities in the range 30 km s^{-1} $< v <$ 2000 km s^{-1}, while the blue arrows correspond to lower-velocity gas with $v \leq 30$ km s^{-1}, shown for direct comparison with the AH06 Model B results.

4.6.3 Discussion of Results

The benchmark test demonstrates that HOPE successfully reproduces the general morphology and physical characteristics of the cometary HII region formed by a supersonic star-medium interaction in a uniform density field. In particular, the following features are in good agreement with the AH06 Model B results:

- The overall bow-shock structure is maintained, with a dense, compressed shell at the apex of the ionised region and a trailing, lower-density ionised tail.
- The stand-off distance between the ionisation front and the stellar position is consistent with analytical expectations based on ram-pressure balance.
- The evolution of the ionised shell and the increasing asymmetry over time are consistent with the relative motion between the star and the medium.
- The morphology and ionisation structure after 10,000 yr, 20,000 yr and 40,000 yr agree closely with those of AH06.

The minor difference (shape) between the HOPE results and the AH06 results arises from the use of artificial viscosity in HOPE, which suppresses instabilities that may not be well resolved. These variations do not significantly alter the global morphology or physical interpretation of the results.
This benchmark comparison confirms that HOPE produces physically consistent results for the evolution of bow-shaped, cometary HII regions resulting from the relative motion between an ionising source and a uniform medium (Arthur & Hoare, 2006). The agreement with AH06 validates the hydrodynamic, ionisation, and radiative coupling schemes implemented in the code and supports its use for more complex non-uniform density models discussed in subsequent sessions.

4.7 Inclusion of Stellar Velocity with a Non-uniform Environment

A new feature implemented in HOPE, and not present in TORCH, is the inclusion of stellar velocity together with a non-uniform environment. This allows the ionising source to move relative to the surrounding interstellar medium. It should be noted that TORCH can simulate stellar velocity by moving the background gas instead. However, it cannot accommodate time-dependent boundary conditions, which are essential for modelling non-uniform gas motion relative to the star, a feature that has been implemented in HOPE. Incorporating stellar motion is crucial for reproducing the cometary morphology of many UCHII regions, where the apparent asymmetry arises from the interaction between a moving star's ionisation front and the surrounding dense gas (Arthur & Hoare, 2006; Mac Low *et al.*, 1991; Van Buren & Mac Low, 1992; Van Buren *et al.*, 1990).
By including stellar velocities within the hydrodynamic framework, HOPE captures both the bow-shock dynamics and the resulting time-dependent structure of the ionised region. This capability represents a significant advance in simulating realistic, dynamic environments around massive young stars.

4.8 Model Development for the DR21 Ultracompact HII Region

The DR21 UCHII region presents a well-studied example of a cometary morphology, making it an ideal candidate for testing hydrodynamic and radiative transfer models of massive star formation and feedback. Following the observational constraints provided by Immer *et al.* (2014), numerical models were developed to reproduce the observed physical and morphological characteristics of DR21 using both the TORCH hydrodynamics code and the RadioRT post-processing radiative transfer tool.

4.8.1 Model Setup and Stellar Parameters

The initial set of simulations was performed using the TORCH hydrodynamics code to model the interaction between the ionising radiation from the central massive star and its surrounding dense molecular environment. The corresponding synthetic radio maps were generated using the RadioRT radiative transfer code, and the results were compared directly with the DR21 UCHII observations. Through this comparison, several key physical parameters of the source were estimated:

- Initial hydrogen number density, $n_0 = 1.28 \times 10^5$ cm^{-3};
- Distance between the ionising star and the molecular cloud core, $R_s = 0.07$ pc;
- Size (and inferred dynamical age) of the DR21 UCHII region, ~ 5000 yr;
- Density power-law index, $\alpha = 1$.

These parameters produced models that reproduced the general morphology and emission structure of DR21. However, one of the main conclusions drawn from

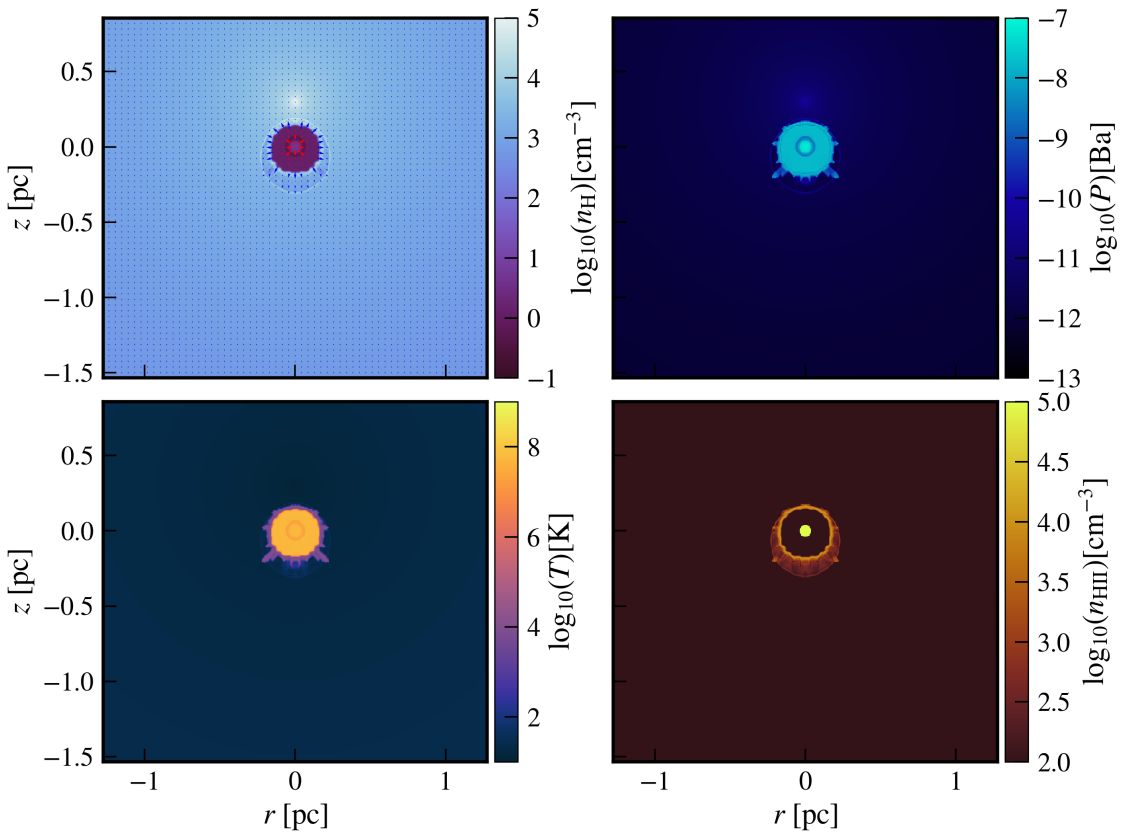


Figure 4.45: Displays of the four panels of HOPE outputs at a simulation duration of 5 kyr. The **top-left** panel shows the logarithmic hydrogen number density, $\log_{10}(n_{\rm H})$ cm^{-3}. The **top-right** panel shows the logarithmic gas pressure, $\log_{10}(P)$ Ba. The **bottom-left** panel displays the logarithmic temperature, $\log_{10}(T)$ K, and the **bottom-right** panel presents the logarithmic ionised hydrogen number density, $\log_{10}(n_{\rm HII})$ cm^{-3}. The ionising star is located at coordinates $z = 0.0$ pc and $r = 0.0$ pc. The red arrows represent gas velocities in the range 30 km s^{-1} $< v <$ 2000 km s^{-1}, while the blue arrows correspond to lower-velocity gas with $v \leq 30$ km s^{-1}.

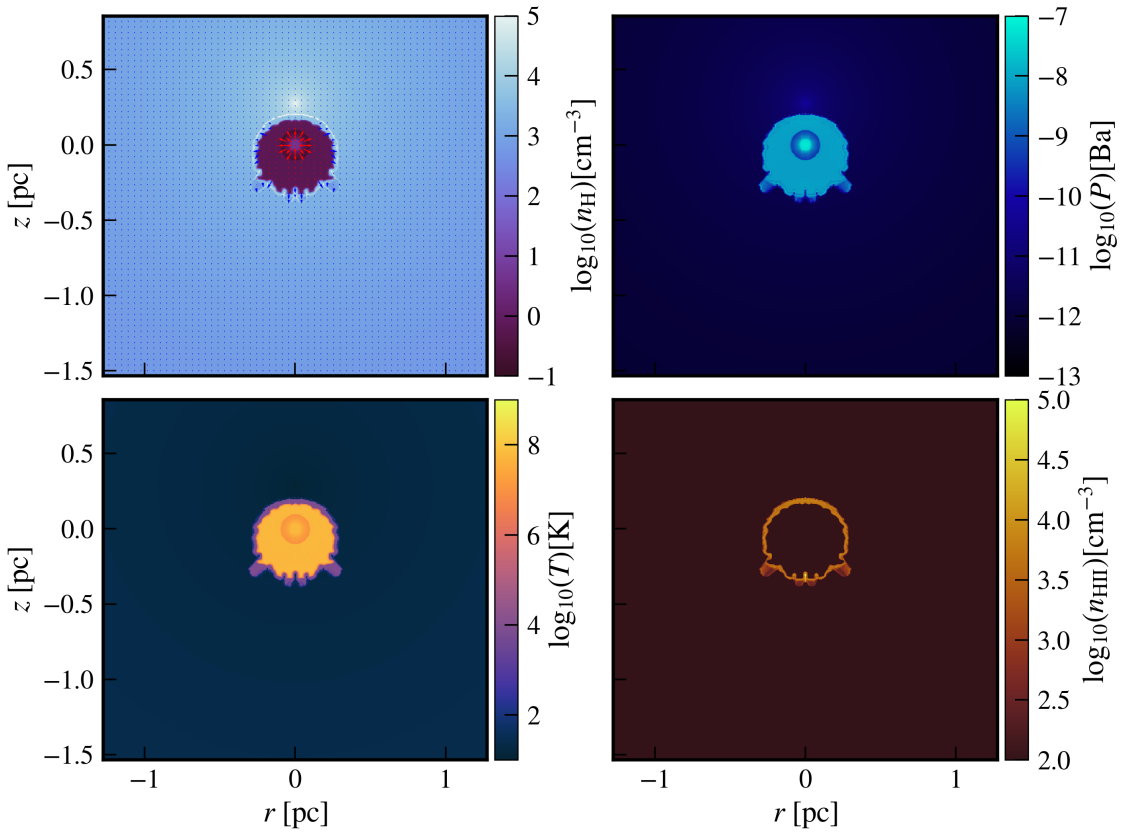


Figure 4.46: Same as Figure 4.45 HOPE output at simulation duration 10 kyr.

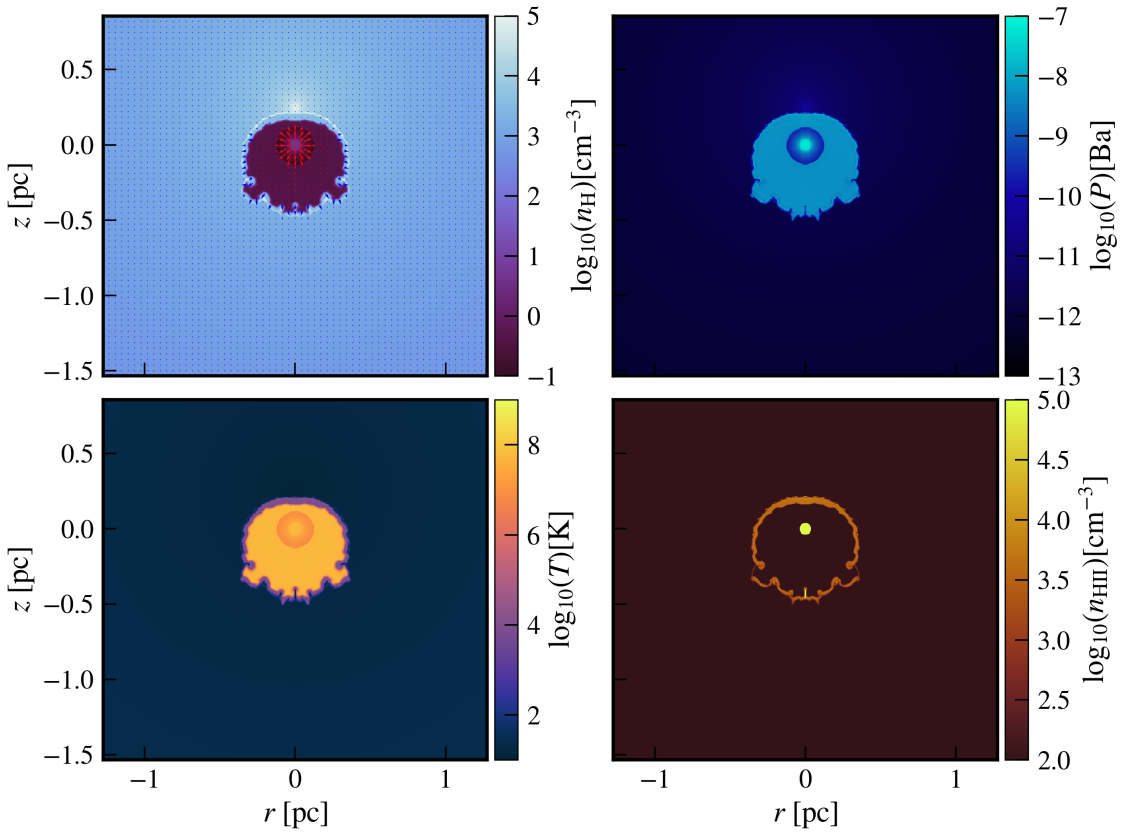


Figure 4.47: Same as Figure 4.45 HOPE output at simulation duration 15 kyr.

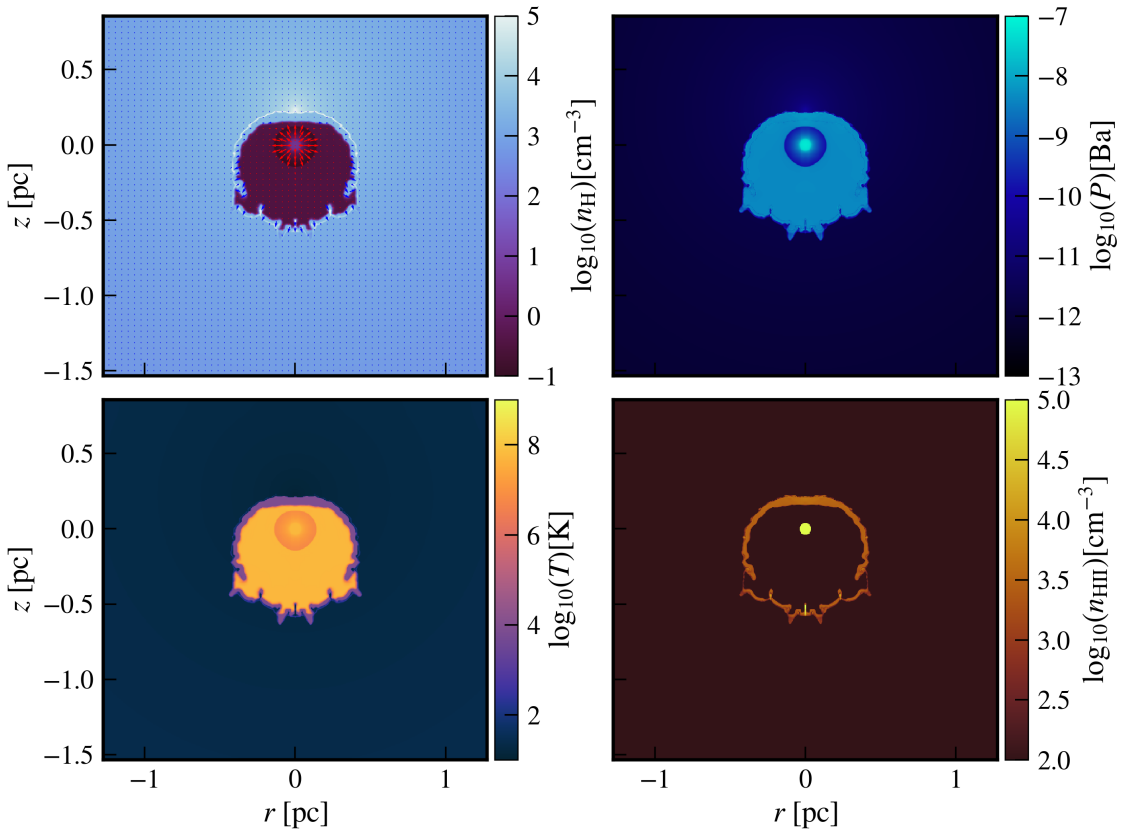


Figure 4.48: Same as Figure 4.45 HOPE output at simulation duration 20 kyr.

the TORCH models was the need to improve the treatment of stellar motion relative to the ambient medium, an aspect not originally incorporated in TORCH. To address this limitation, the HOPE code was employed to perform an updated suite of simulations incorporating stellar velocity. Unlike TORCH, where the star is stationary within the computational domain, HOPE allows the inclusion of stellar motion or, equivalently, an ambient flow relative to the ionising source. This enhancement enables the code to better reproduce the cometary morphology characteristic of the DR21 UCHII region.

The previously derived physical parameters from the TORCH+RadioRT comparison were adopted as input for the HOPE model setup. In these simulations, a stellar velocity of $v_\star = 5$ km s^{-1} relative to the surrounding medium was introduced as deduced from comparing the observations to the modelling. Please note that the value of R_s used in this simulation was 0.33 pc. This represents the star's travel over 50000 years (the duration of the simulation), assuming a stellar velocity of 5 km s^{-1}. To account for this motion, an additional 0.26 pc was added to the initially estimated 0.07 pc, resulting in the total R_s value of 0.33 pc.

The resulting output of HOPE is shown in Figures 4.45, 4.46, 4.47, and 4.48 corresponding to 5 kyr, 10 kyr, 15 kyr, and 20 kyr, respectively. The main limitation is that the code crashes at a simulation time of 26 kyr and requires further enhancement.

For emphasis and with the same approach, the code crashes when applied to a star moving at 10 km s^{-1} over a period of 50,000 years. An additional 0.51 pc was added to the initial estimate of 0.07 pc for R_s, resulting in a total value of $R_s = 0.58$ pc used in the simulation. The results are shown in Figures 4.49, 4.50, 4.51, and 4.52, corresponding to 5 kyr, 10 kyr, 15 kyr, and 20 kyr, respectively.

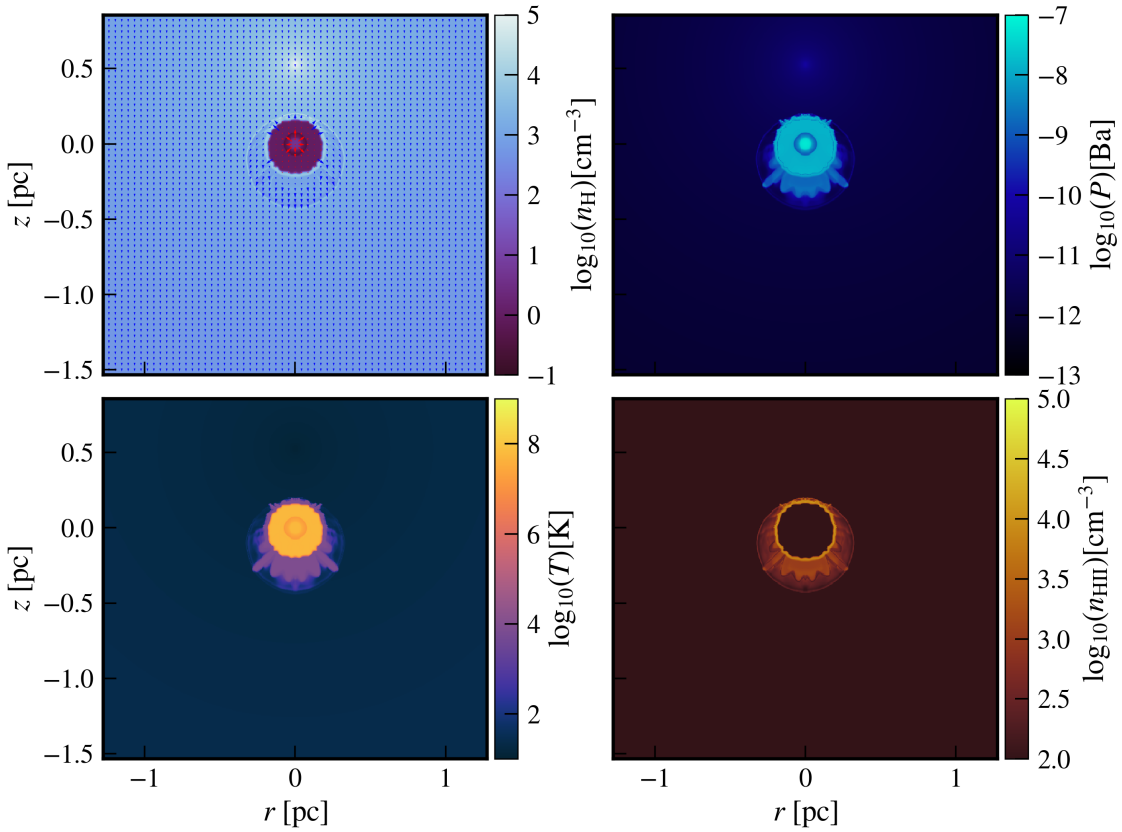


Figure 4.49: Displays of the four panels of HOPE outputs at a simulation time of 5 kyr, assuming a star moving at 10 km s^{-1}.

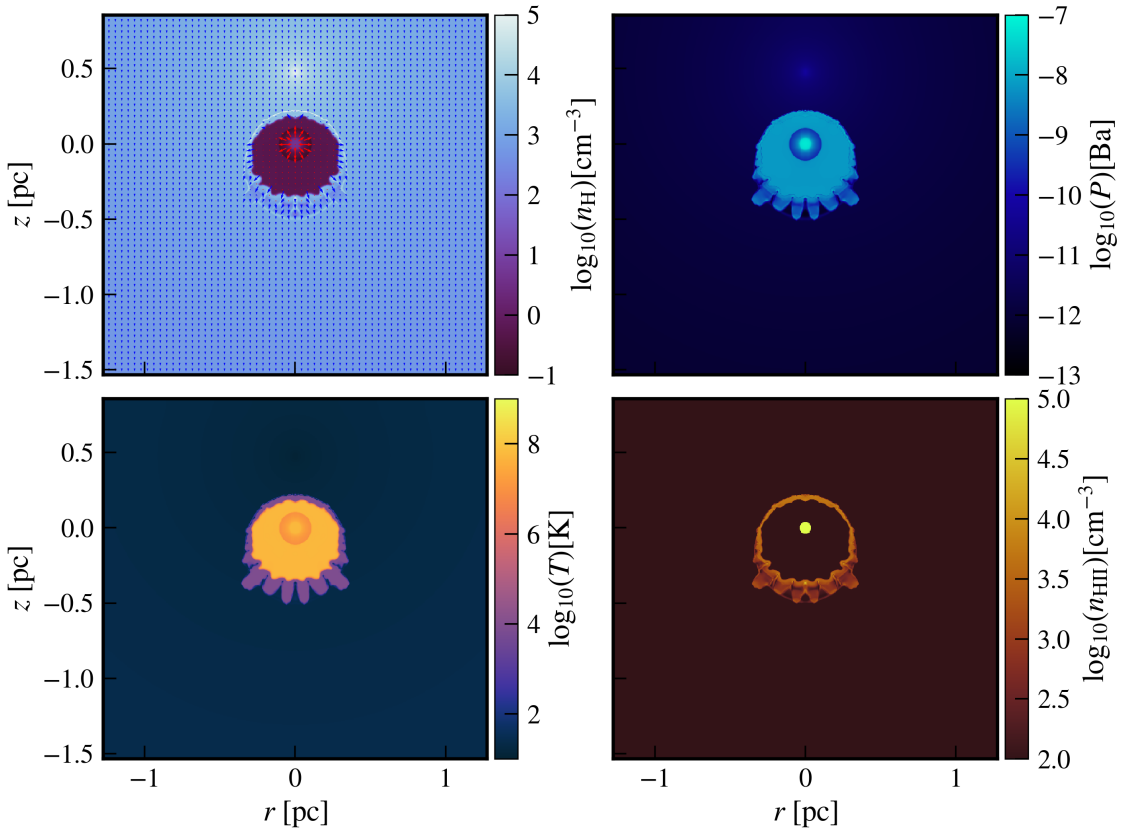


Figure 4.50: Similar to Figure 4.49 HOPE output at simulation duration 10 kyr, assuming a star moving at 10 km s^{-1}.

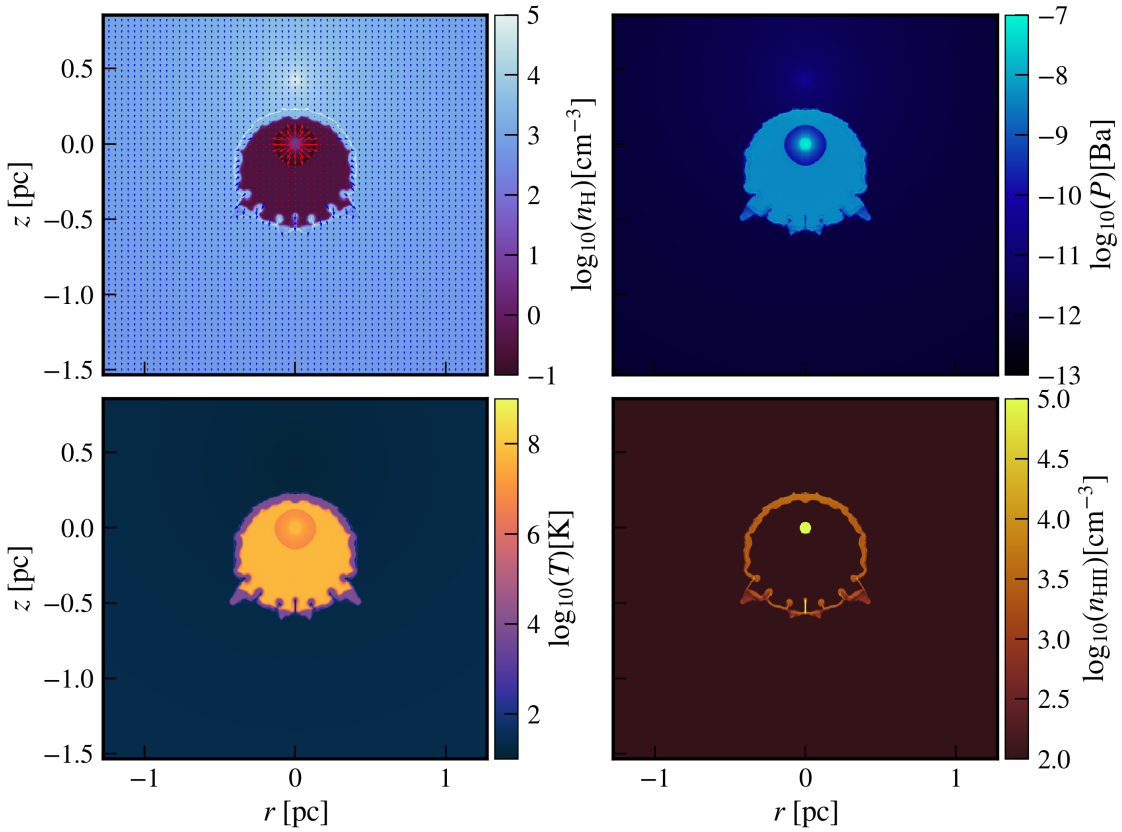


Figure 4.51: Similar to Figure 4.49 HOPE output at simulation duration 15 kyr, assuming a star moving at 10 $km\ s^{-3}$.

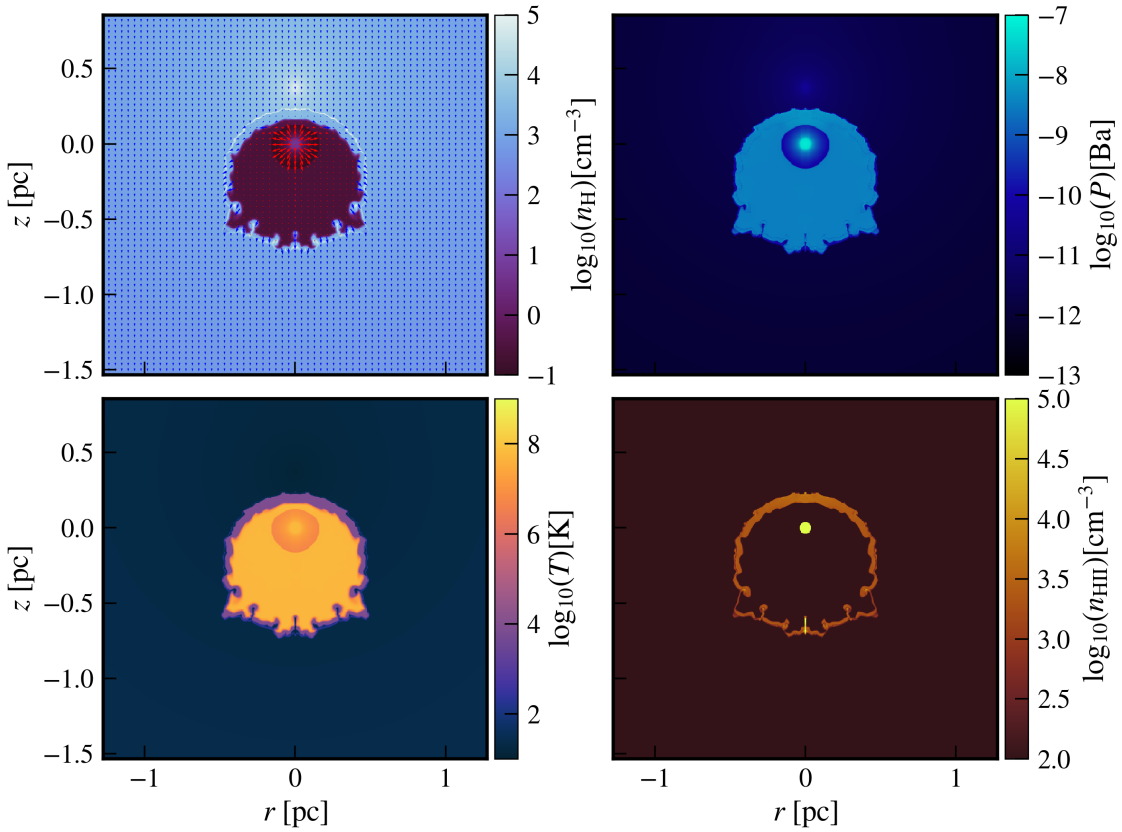


Figure 4.52: Same as Figure 4.49 HOPE output at simulation duration 20 kyr, assuming a star moving at 10 km s^{-1}.

4.8.2 Synthetic Observations and Comparison with DR21

The HOPE simulations were post-processed to generate synthetic radio continuum maps for direct comparison with the DR21 observations presented by Immer *et al.* (2014). Following the hydrodynamic simulations, the outputs from HOPE were post-processed using a dedicated ray-tracing radiative transfer code similar to the RadioRT code developed by Steggles (2016) to generate radio recombination line data.

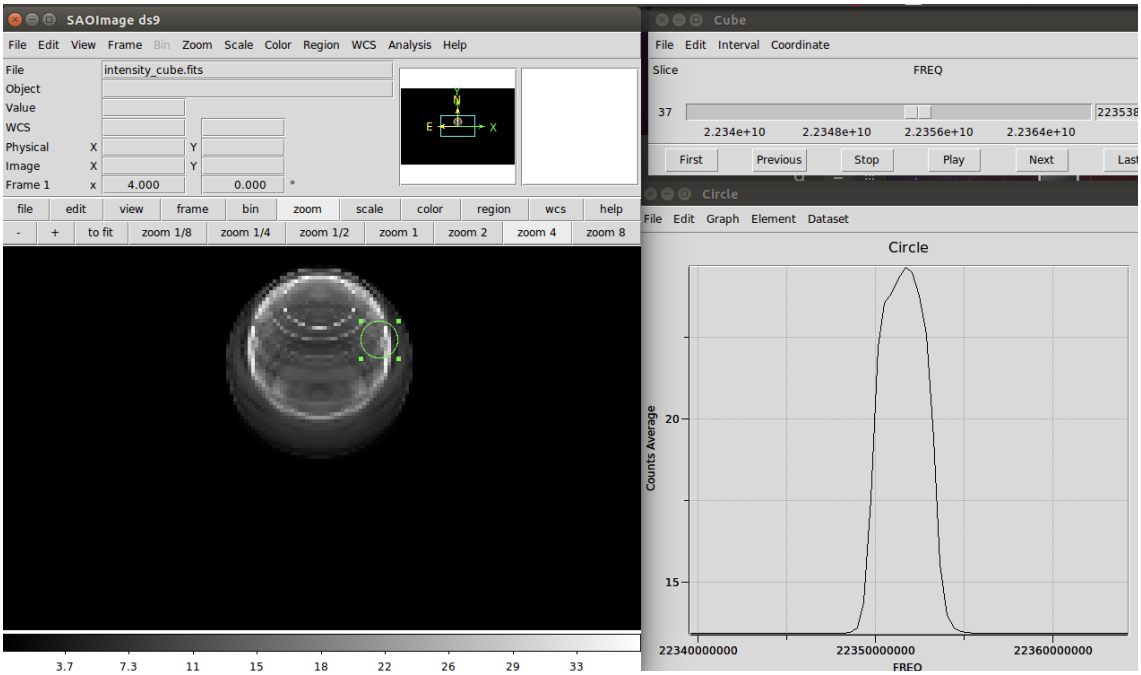


Figure 4.53: Initial output model from the "Ray-Tracing" code at 5 kyr, processed with DS9 software. Shown is the 37th slice of 64 from the image cube, with the corresponding line profile displayed on the right.

This post-processing step computes the radio free-free emission maps by integrating the line-of-sight optical depth through the simulation grid. The observational parameters for DR21 reported by Immer *et al.* (2014) were input into the Ray-Tracing code to generate the preliminary results shown in Figures 4.53, 4.54, and 4.55. A primary limitation of the Ray-Tracing code is that its output cannot be directly processed by the CASA software for further analysis, which restricts the

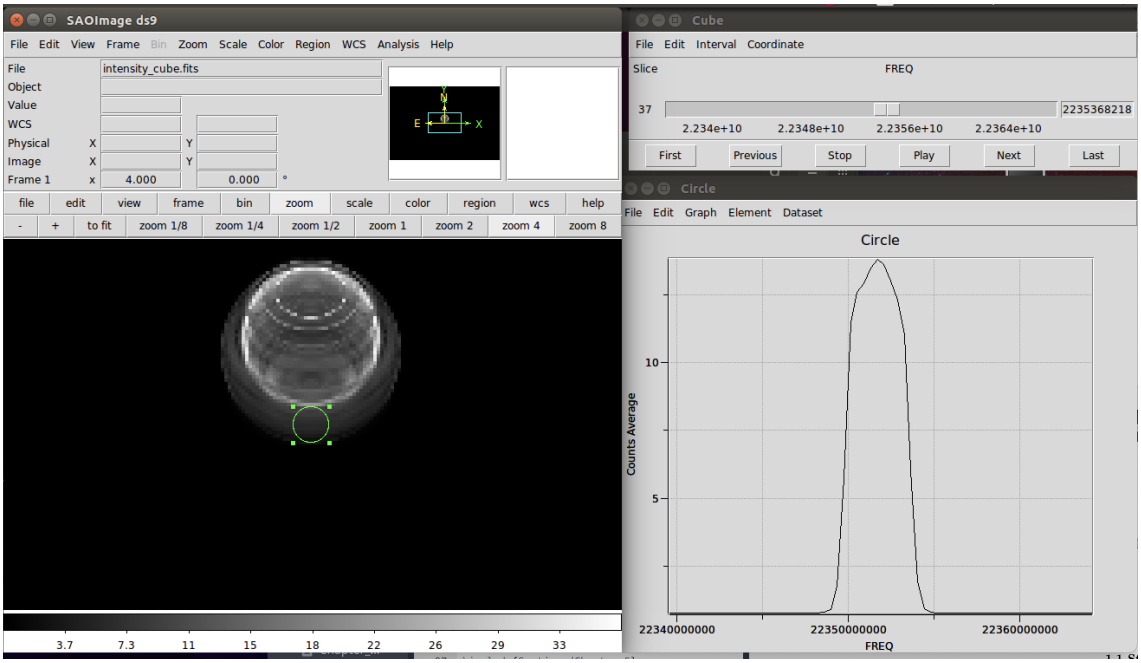


Figure 4.54: Similar to Figure 4.53, this figure displays the line profile from a different region of the resulting image cube.

ability to follow a step-by-step approach in modelling the cometary UCHII region (see Figure 4.2). This aspect of the code needs improvement.

4.9 Conclusions

For the first time, the radio recombination line data of the cometary UCHII region DR21 has been modelled and tailored to the observations. With the logical and systematic step-by-step method as shown in Figure 4.2, the models were developed. It is noticed that the models were not able to break out to form the extended tail as in the observations of the "whole" Southern part seen in Figure 1 by Immer *et al.* (2014). This disparity is seen in the illustrations in the moment 1 maps, the spectra analysis, and the PV diagrams. There were clear disparities in terms of the appearance (shape) of the observed data and the models, as they had no long tails as seen in the observed data. The most immediate interpretation of this mismatch is the lack of proper motion, but this may not be the sole

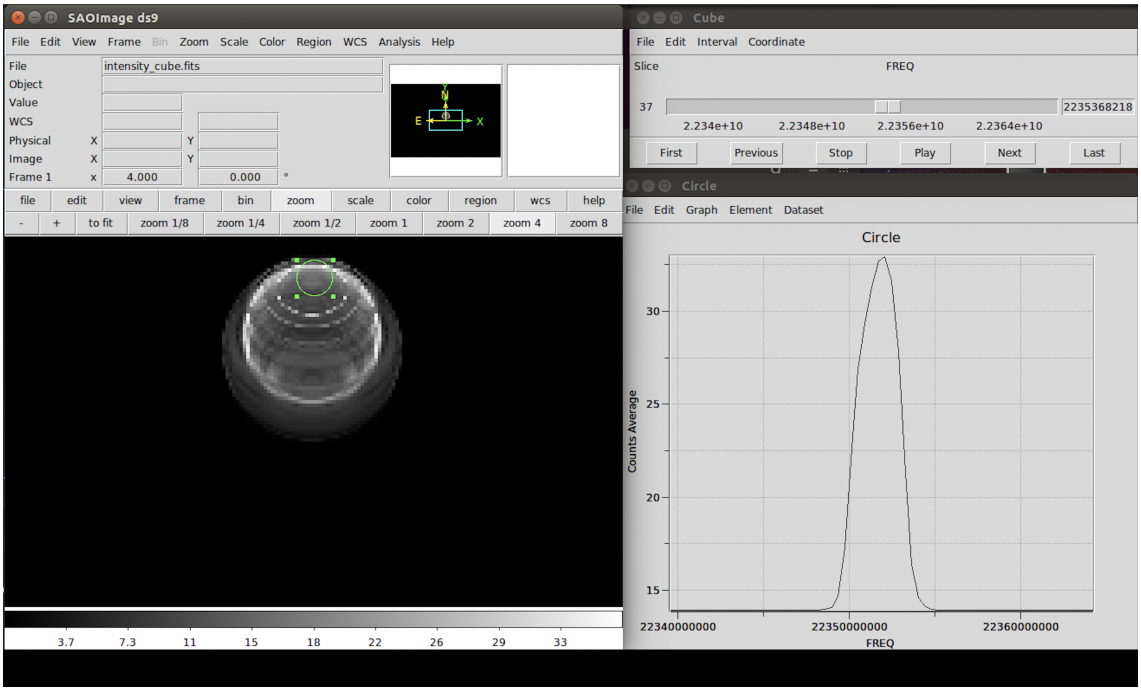


Figure 4.55: As in Figure 4.53, this figure shows the line profile from a different region of the resulting image cube.

explanation for the disparity between the observed data and models.
However, there were observed similarities between the observed data and the models. These similarities were seen in the blue-shifted and red-shifted velocities observed from the cometary head to the tail, respectively. It was also seen from the model plots that variation in the inclination angles from 30°, 45° to 60° had no significant effects on the ionised gas velocities. The two velocity component structure obtained is comparable to the spectra line profiles fitted with the 2 Gaussians by Immer *et al.* (2014). From the spectra analysis, the difference between the values of the velocity structure is attributed to the stationary nature of the ionising star and hence needs proper stellar motion.
The numerical models to simulate hydrodynamics and radiative transfer of cometary ultracompact HII regions with an emphasis on the well-studied DR21 source were improved. The development of the new code HOPE, which enhances and expands on the earlier TORCH code, marks a significant step forward in simulating UCHII regions. A key progress in HOPE include the implementation of variable thermodynamic parameters, a physically consistent approach to pressure equilibrium in non-uniform clouds, and, most importantly, the ability to incorporate stellar velocity with a non-uniform environment. These factors enable the simulations to capture more realistic physical processes and dynamic structures, especially aspects of the cometary morphology driven by the relative motion between ionising stars and their surrounding ambient medium. Benchmarking this against the well-established models of Arthur & Hoare (2006) validated the accuracy and reliability of HOPE in reproducing the features of bow shocks and ionisation fronts caused by supersonic stellar motions through uniform density environments. The application of HOPE to the DR21 UCHII region, using parameters derived from the previous TORCH models and observations, successfully validates the significance of including stellar velocity to reproduce the observed morphology and emission properties. To account for the star's travel over 50,000 years at 5 $\mathrm{km\,s^{-1}}$, the distance between the star and the cloud core parameter R_s, was adjusted accordingly to improve the model's physical realism. While the new code presented here moves significantly closer to reproducing the

observed properties of cometary UCHII regions, certain notable limitations remain. For HOPE, the hydrodynamic simulations currently crash at approximately 26,000 years, indicating the need for further code stability improvements and refinements. In addition, the output produced by the post-processing ray-tracing code does not integrate smoothly with observational analysis tools such as CASA, which limits the ability to carry out a fully comprehensive analysis. Overall, the developments and results presented in this study provide a robust foundation for subsequent studies of massive star feedback and the formation and evolution of ultracompact HII regions in diverse interstellar environments.

Chapter 5

Conclusions

5.1 Summary

This thesis presents a detailed study of the cometary ultra-compact (UC) HII region DR21. The object DR21 has been modelled and tailored to observation, and the velocity structure of the ionised gas was used to predict the classes of models that best describe the cometary morphology. The Operator-split Radiation, Cooling, Hydro-code (TORCH), which combines hydrodynamics, RadioRT, and photoionisation, developed by Steggles *et al.* (2017), was modified to investigate the density distributions of ionised and molecular gas within the context of the cometary models. In addition, the dust continuum emission from DR21 was modelled to probe the density distribution in the context of the cometary models. The results were used to constrain the model parameters and infer the density distribution.

Radio recombination line (RRL) tests are conducted using the radiative transfer code "RadioRT" developed by Steggles (2016). The first time a hydrodynamic simulation was confronted with RRL observation. The code, for the first time, was tested, modified and compared to the test cases in the literature. The results for the constrained hydro-code model parameters of the radio continuum emission and the test implementation of "RadioRT" are used to simulate and model the radio recombination line emission from DR21 to study its velocity structure. Finally, the results from the simulated spectral lines provide important insight

into the kinematics of the ionised gas structure in the context of the model classes for the cometary morphology.
This chapter summarises the main findings of the previous chapters and provides an overview of how the work is related, and reviews possible avenues for future studies.

5.2 An overview of this thesis

Chapter 2 of this study detailed the radio recombination line tests of the RadioRT code developed by Steggles (2016). This is the first time this aspect of the code has been tested and used to generate models of radio recombination lines. An error in the code was noted from the weaker line strength of $\approx 10^4$ times weaker than expected, generated from the initial run with the RadioRT code, which then calls for the code to be tested and compared with the literature. The RadioRT code was modified to test the code against the series of tests conducted by Viner *et al.* (1979) and Peters *et al.* (2012). The test of the line strength led to the correction of the value of the sampling factor from the initial value of 4 to 1. The principal quantum number was correctly set in the RadioRT code, and the checks of the departure coefficient values agree well with the literature. The emission measure results from Table 2.1 for implementation of Model 1 (varying electron density) and Model 3 (constant electron density) values were reasonably comparable to the values reported by Viner *et al.* (1979). The integrated flux values for the implementation of Model 1 and 3 of H109α, H85α and the continuum as seen in Table 2.2 were slightly higher than expected, as a result, mainly due to the sampling factor values changing from 4 to 1, as a value of 1 generated reasonable values for the emission measure test. The RadioRT code was used to verify the symmetric and asymmetric line profiles under local thermodynamic equilibrium (LTE) and non-LTE states, which showcase the significance of implementing non-LTE conditions in the models. The test implementation using RadioRT code agrees well with the expanding (Model 4) and contracting (Model 5) of gas motion as reported by Peters *et al.* (2012) with the LTE generating

identical and symmetric line profiles, while the non-LTE line profiles are distinguishable and asymmetric.

A key prediction among the models explaining the cometary morphology of UCHII regions is the Hybrid model, as proposed by Arthur & Hoare (2006); Ho *et al.* (1981). However, these authors focused primarily on the hydrodynamic features of their models, without performing direct comparisons to observational data. Observations of the cometary DR21 UCHII region by Cyganowski *et al.* (2003) and Immer *et al.* (2014) suggest that the kinematics of its cometary morphology can be explained by the hybrid model. However, it remains to be demonstrated that cometary UCHII region models have been directly tailored to observations to conclusively validate the hybrid model.

Chapter 3 of the thesis presented the simulation and modelling of the radio and dust continuum emission from the cometary UCHII region DR21. In this chapter, it was demonstrated how the density distribution of the ionised gas and dust model parameters is constrained within the context of the cometary hydrodynamical models. This is the first time the radio emission from the cometary UCHII region DR21 has been modelled tailored to observations. Comparisons of the radio continuum models were made with the literature observation, alongside the presented modelling of the dust continuum emission from DR21 using the observation of the Sub-millimetre Common User Bolometer Array (SCUBA) at 450μm of DR21 to constrain the density distribution.

To simulate and model the radio continuum emission from the cometary UCHII region DR21, the initial hydrodynamic model was selected from the grid models in Steggles *et al.* (2017) that have a star offset from the spherical molecular cloud with photo-ionisation including stellar winds. It must be noted that gravity and magnetic fields are neglected, and there is no proper stellar motion incorporated in the models. The elements of the density distribution model parameters for DR21 were strategically and logically constrained, as changing one parameter may affect others.

The modelled dust and radio continuum data were overlaid and compared with the observed dust and radio data of DR21. By examining the two peaks in both

the radio and dust emissions, along with their corresponding models and observations, the density distribution was constrained, leading to an estimated value of $R_s = 0.07$ pc between the star and the cloud core. The modelled dust continuum emission from DR21 was used to constrain the density power-law index, yielding an estimate of $\alpha = 1.0$. The age of the DR21 UCHII region was estimated at 5 kyr and was determined by comparing the size of the radio continuum emission models to the observed radio data. As a final check, a plot of the spectral energy distribution for the observed DR21 data (Harris & Scott, 1973), with the values estimated for R_s, α, and age, was used to confirm the initial number density, n_e, as 1.28×10^5 cm^{-3} at star location.

Based on these findings, we conclude that TORCH is a promising new tool for modelling the radio continuum emission from cometary UCHII regions, tailored to the level of precision needed for comparison.

In Chapter 4, the radio recombination line emission of the cometary DR21 UCHII region, for the first time, is modelled tailored directly to observation. The logical step-by-step approach in modelling the radio recombination lines for DR21 is showcased at viewing angles of 30°, 45° and 60°. The turbulence broadening value of 1 kms^{-1} set revealed the velocity structure due to the gas kinematics and potential double-peak line profiles. The systemic velocity of the molecular gas in DR21 was estimated to be approximately -2 km s^{-1} and used as a reference to the ionised gas and the molecular materials to verify the red shift and blue shift line profiles.

Three different approaches are employed in investigating the velocity structure of DR21 and are compared to the observed data. The moment maps, the position velocity (PV) diagram and the line profile are studied extensively in this chapter. The intensity-weighted average of the velocities (moment 1) maps generated show some blue-shifted regions in the southern cometary head and some red-shifted regions in the cometary tail of the DR21 observed data. There were similarities in the velocity fields between the models and observed data. The blue-shifted and red-shifted velocities at the cometary head and tail, respectively, are observed in both the models and the data, consistent with the champagne flow model resulting

from the density gradient. The overall velocity field becomes more blue-shifted as the inclination angles increase, highlighting the bow shock model. The velocity fields for the observed DR21 ranges between ≈ -50 kms^{-1} to 5 kms^{-1} while the models falls with ≈ -4 kms^{-1} to 4 kms^{-1} at 30°, ≈ -4.5 kms^{-1} to 2.5 kms^{-1} at 45°, and ≈ -5 kms^{-1} to 1.5 kms^{-1} at 60°. The offset in velocity fields shows that a hybrid model would be better in explaining the cometary morphology for the models and observed DR21.

By slicing with ≈ ± 15" offset through the midpoints, the PV diagrams were generated for the observed DR21 and models projected at viewing angles of 30°, 45° and 60°. The PV diagrams differ in shape and structure by comparing the models to the observed DR21. The intensity distribution of the observed DR21 looks complex and more spread out than the models, which look narrower and elongated. The intensity distribution for the models gets narrower towards the tail, highlighting the density gradient.

The 17 boxes covering the emission of the southern part of DR21 were used to extensively study the line profiles generated for the observed DR21 and the models. The spectra profiles generated from each box for the observed data and models at different viewing angles are investigated. The generated line profiles were independently fitted with one and two Gaussians (where possible) to extract the central line velocity, full width at half maximum (FWHM), and amplitude to investigate the kinematics of the ionised gas. It was deduced that the intensities of the models were relatively higher than the observed DR21, which was mainly attributed to non-LTE effects. The FWHM values for the observed DR21 were relatively higher than the models, which could be attributed to the turbulence broadening, V_{turb}, as a value of 1 kms^{-1} was maintained to better highlight the kinematics.

There are, however, notable similarities between the observed properties of DR21 and the models, particularly in the blue-shifted and red-shifted velocities relative to the molecular cloud at the cometary head and tail, respectively. A detailed analysis and comparison of the line widths in both the observed DR21 data and the models reveal higher line widths at the cometary tail, consistent with the

champagne flow scenario, as well as increased line widths at the cometary head, characteristic of the bow shock model. This combination of features supports the hybrid interpretation of DR21, as previously reported by Cyganowski *et al.* (2003) and Immer *et al.* (2014). Furthermore, studies of the cometary UCHII region DR21 models reinforce this hybrid picture when proper stellar motion is incorporated into the champagne flow, as demonstrated in models C, F, and G from Arthur & Hoare (2006). From Figures 4.35, 4.36, and 4.37, it is inferred that a stellar proper motion of approximately 5 kms^{-1} provides a more realistic and comparable match between the models and the observed DR21. Additionally, introducing this proper motion of around 5 kms^{-1} in the models appears to induce a breakout of the southern cometary tail, consistent with observations of DR21 and illustrated in Figures 4.35, 4.36, and 4.37.

5.3 Future Work and Improvement

This study is the first experiment of modelling the radio continuum and radio recombination lines of a cometary UCHII region directly compared to observations by means of a hydrodynamic simulation. To enhance and make the methodology described in Figure 4.2, the stability and robustness of the HOPE code must be improved to avoid runtime crashes that result in simulation failures.

Furthermore, the post-processing Ray-Tracing code will also be improved to obtain outputs that are compatible with the observational tool, CASA, which will allow for a much broader analysis and a direct comparison with observational datasets. This approach will also be generalised to other widely studied cometary UCHII regions, including G29.96-0.02, which is considered one of the best-defined elements of its domain (Arthur & Hoare, 2006). It has been observed over several wavelengths and described in detail by numerous authors (Kim & Koo, 2003; Lumsden & Hoare, 1996, 1999; Martín-Hernández *et al.*, 2003; Olmi *et al.*, 2003; Wood & Churchwell, 1989b, 1991; Zhu *et al.*, 2005), thus allowing the model to be extensively tested.

Future studies will deal with physical effects not investigated in the current re-

search, including but not limited to non-LTE phenomena and turbulence-induced line broadening. It is anticipated that the influence of these parameters will influence line strengths and kinematics of the ionised gas. Integrating these effects will facilitate a more precise determination of departure coefficients and enhance the robustness of models reproducing the line intensities and profiles seen in experimental analysis with greater precision.

References

Afflerbach, A., Churchwell, E., Hofner, P. & Kurtz, S. (1994). A multiline, multiresolution vla study of the ultracompact h ii region g29. 96-0.02. *The Astrophysical Journal*, **437**, 697–704.

Alves, M., Davies, R., Dickinson, C. *et al.* (2010). *Monthly Notices of the Royal Astronomical Society*, **405**, 1654.

Andre, P., Ward-Thompson, D. & Barsony, M. (1993). Submillimeter continuum observations of rho ophiuchi a-the candidate protostar vla 1623 and prestellar clumps. *Astrophysical Journal, Part 1 (ISSN 0004-637X), vol. 406, no. 1, p. 122-141.*, **406**, 122–141.

André, P., Di Francesco, J., Ward-Thompson, D., Inutsuka, S.i., Pudritz, R.E. & Pineda, J. (2014a). From filamentary networks to dense cores in molecular clouds: toward a new paradigm for star formation. *Protostars and Planets VI*, **27**.

André, P., Di Francesco, J., Ward-Thompson, D., Inutsuka, S.i., Pudritz, R.E. & Pineda, J. (2014b). From filamentary networks to dense cores in molecular clouds: toward a new paradigm for star formation. *Protostars and planets VI*, **27**.

Arquilla, R. & Goldsmith, P.F. (1985). Density distributions in dark clouds. *Astrophysical Journal, Part 1 (ISSN 0004-637X), vol. 297, Oct. 15, 1985, p. 436-454.*, **297**, 436–454.

Arthur, S.J. & Hoare, M. (2006). Hydrodynamics of cometary compact h ii regions. *The Astrophysical Journal Supplement Series*, **165**, 283.

Bally, J. & Zinnecker, H. (2005). The birth of high-mass stars: Accretion and outflow. *The Astronomical Journal*, **129**, 2281–2292.

Beuther, H., Schilke, P., Menten, K., Motte, F., Sridharan, T. & Wyrowski, F. (2002). High-mass protostellar candidates. ii. density structure from dust continuum and cs emission. *The Astrophysical Journal*, **566**, 945.

Bodenheimer, P., Tenorio-Tagle, G. & Yorke, H. (1979). The gas dynamics of h ii regions. ii-two-dimensional axisymmetric calculations. *The Astrophysical Journal*, **233**, 85–96.

Bonnell, I.A., Bate, M.R., Clarke, C.J. & Pringle, J.E. (1997). Accretion in stellar clusters and the initial mass function. *Monthly Notices of the Royal Astronomical Society*, **285**, 201–208.

Bonnell, I.A., Bate, M.R. & Zinnecker, H. (1998). Formation of massive stars by accretion and collisions. *Monthly Notices of the Royal Astronomical Society*, **298**, 93–102.

Bonnell, I.A., Bate, M.R. & Clarke, C.J. (2001). Formation of massive stars by competitive accretion in protoclusters. *Monthly Notices of the Royal Astronomical Society*, **323**, 785–794.

Bonnell, I.A., Bate, M.R. & Vine, S.G. (2003). The hierarchical formation of a stellar cluster. *Monthly Notices of the Royal Astronomical Society*, **343**, 413–418.

Bonnell, I.A., Vine, S.G. & Bate, M.R. (2004). Massive star formation: N-body gas dynamics. *Monthly Notices of the Royal Astronomical Society*, **349**, 735–741.

Bouvier, J., Alencar, S., Harries, T., Johns-Krull, C. & Romanova, M. (2006). Magnetospheric accretion in classical t tauri stars. *arXiv preprint astro-ph/0603498*.

Carroll, B.W. & Ostlie, D.A. (2007). *An Introduction to Modern Astrophysics*. Addison-Wesley, San Francisco, 2nd edn.

Cesaroni, R., Galli, D., Lodato, G., Walmsley, M. & Zhang, Q. (2006). The critical role of disks in the formation of high-mass stars. *Nature*, **444**, 703–706.

Churchwell, E. (2002). Ultra-compact hii regions and massive star formation. *Annual Review of Astronomy and Astrophysics*, **40**, 27–62.

Cunningham, A.J., Krumholz, M.R., McKee, C.F. & Klein, R.I. (2018). The effects of magnetic fields and protostellar feedback on low-mass cluster formation. *Monthly Notices of the Royal Astronomical Society*, **476**, 771–792.

Cyganowski, C., Reid, M.J., Fish, V. & Ho, P. (2003). Dual cometary h ii regions in dr 21: Bow shocks or champagne flows? *The Astrophysical Journal*, **596**, 344.

Dale, J.E., Bonnell, I. & Whitworth, A. (2007). Ionization-induced star formation–i. the collect-and-collapse model. *Monthly Notices of the Royal Astronomical Society*, **375**, 1291–1298.

Deharveng, L., Zavagno, A., Anderson, L.D., Mottram, J.C., Treyer, M., Andree-Labsch, S. & Hill, T. (2010). A gallery of bubbles. the imprint of massive stars on the ism. *Astronomy & Astrophysics*, **523**, A6.

Dent, W.A. (1972). A flux-density scale for microwave frequencies. *Astrophysical Journal, vol. 177, p. 93*, **177**, 93.

Dougherty, S.M., Pittard, J.M., Kasian, L., Coker, R.F., Williams, P.M. & Lloyd, H. (2003). Radio emission models of colliding-wind binary systems. *Astronomy & Astrophysics*, **409**, 217–233.

Downes, D. & Rinehart, R. (1966). Microwave observations of the cygnus x region. *The Astrophysical Journal*, **144**, 937.

Downes, D., Maxwell, A. & Rinehart, R. (1970). Flux densities of ten galactic sources in the millimeter band. *Astrophysical Journal, vol. 161, p. L123*, **161**, L123.

Dravskikh, A. & Dravskikh, Z. (1964). *Soviet Astronomy*, **8**, 833.

Elmegreen, B.G. & Lada, C.J. (1977). Sequential formation of subgroups in ob associations. *The Astrophysical Journal*, **214**, 725–741.

Emilova Kalcheva, I. (2018). *The Ultra-Compact H II Region Population of the Galaxy*. Ph.D. thesis, University of Leeds.

Falle, S. (1991). Self-similar jets. *Monthly Notices of the Royal Astronomical Society*, **250**, 581–596.

Franco, J., Tenorio-Tagle, G. & Bodenheimer, P. (1990). On the formation and expansion of h ii regions. *The Astrophysical Journal*, **349**, 126–140.

Franco, J., Kurtz, S., Hofner, P., Testi, L., García-Segura, G. & Martos, M. (2000). The density structure of highly compact h ii regions. *The Astrophysical Journal Letters*, **542**, L143.

Franco, J., García-Segura, G., Kurtz, S.E. & Arthur, S.J. (2007). From ultracompact to extended h ii regions. ii. cloud gravity and stellar motion. *The Astrophysical Journal*, **660**, 1296.

Frank, A., Ray, T., Cabrit, S., Hartigan, P., Arce, H., Bacciotti, F., Bally, J., Benisty, M., Eislöffel, J., Güdel, M. *et al.* (2014). Jets and outflows from star to cloud: observations confront theory. *Protostars and planets VI*, **451**.

Frost, A.J. (2019). *The circumstellar environment of massive young stellar objects-a multi-scale analysis*. Ph.D. thesis, University of Leeds.

Garay, G. & Lizano, S. (1999). Massive stars: their environment and formation. *Publications of the Astronomical Society of the Pacific*, **111**, 1049.

Garden, R.P. & Carlstrom, J.E. (1992). High-velocity hco (+) emission associated with the dr 21 molecular outflow. *Astrophysical Journal, Part 1 (ISSN 0004-637X), vol. 392, no. 2, June 20, 1992, p. 602-615. Research supported by Alfred P. Sloan Foundation and University of California.*, **392**, 602–615.

Gaume, R.A., Fey, A.L. & Claussen, M.J. (1994). Vla recombination line observations of the cometary h ii region g34. 3+ 0.2: Dynamics and physical properties. *The Astrophysical Journal*, **432**, 648–655.

Getman, K.V., Feigelson, E.D., Townsley, L., Broos, P., Garmire, G. & Tsujimoto, M. (2007). X-ray evidence for triggered star formation and protostars in pillars of the carina nebula. *The Astrophysical Journal*, **654**, 316–343.

Gordon, M. & Sorochenko, R. (2009a). *Radio Recombination Lines: Their Physics and Astronomical Applications*. Springer.

Gordon, M.A. & Sorochenko, R.L. (2009b). *Radio recombination lines: their physics and astronomical applications*, vol. 282. Springer Science & Business Media.

Gritschneder, M., Naab, T., Walch, S., Burkert, A. & Heitsch, F. (2009). Driving pillars and globules in turbulent clouds via ionization feedback. *The Astrophysical Journal Letters*, **694**, L26–L30.

Harris, S. & Scott, P. (1973). 5 ghz observations of small-scale structure in dr21. *Monthly Notices of the Royal Astronomical Society*, **162**, 5P–10P.

Hartmann, L. (2000). *Accretion processes in star formation*, vol. 32. Cambridge University Press.

Hatchell, J. & Van der Tak, F. (2003). The physical structure of high-mass star-forming cores. *Astronomy & Astrophysics*, **409**, 589–598.

Henney, W.J., Arthur, S.J., De Colle, F. & Mellema, G. (2009). Radiation-magnetohydrodynamic simulations of the photoionization of mag-

netized globules. *Monthly Notices of the Royal Astronomical Society*, **398**, 157–175.

Hildebrand, R. (1983). Qjr astron. *Soc*, **24**, 267.

Ho, P.T.P., Ho, L.C. & Young, L.M. (1981). Formation of high-mass stars in molecular hot cores. *Astrophysical Journal*, **245**, 23–30.

Hoare, M., Kurtz, S., Lizano, S., Keto, E. & Hofner, P. (????). Ultracompact h ii regions and the early lives of massive stars. *Protostars and Planets V*.

Hoare, M., Kurtz, S., Lizano, S., Keto, E. & Hofner, P. (2007a). Protostars and planets v. 181.

Hoare, M., Kurtz, S., Lizano, S., Keto, E. & Hofner, P. (2007b). Ultracompact hii regions and the early lives of massive stars. *Protostars and Planets V*, **181**.

Hoare, M.G., Kurtz, S.E., Lizano, S., Keto, E. & Hofner, P. (2007). Ultracompact Hii Regions and the Early Lives of Massive Stars. *Protostars and Planets V*, 181–196.

Hofner, P., Wyrowski, F., Walmsley, C. & Churchwell, E. (2000). A c17o survey toward ultracompact h ii regions. *The Astrophysical Journal*, **536**, 393.

Immer, K., Cyganowski, C., Reid, M. & Menten, K. (2014). The cometary h ii regions of dr 21: Bow shocks or champagne flows or both? *Astronomy & Astrophysics*, **563**, A39.

Isella, A. (2007). High angular resolution observations of circumstellar disks. *MEMORIE-SOCIETA ASTRONOMICA ITALIANA*, **78**, 677.

Israel, F. (1978). H ii regions and co clouds-the blister model. *Astronomy and Astrophysics*, **70**, 769–775.

Jakob, H., Kramer, C., Simon, R., Schneider, N., Ossenkopf, V., Bontemps, S., Graf, U. & Stutzki, J. (2007). The cooling of atomic and molecular gas in dr21. *Astronomy & Astrophysics*, **461**, 999–1012.

Johnston, K.G., Robitaille, T.P., Beuther, H., Linz, H., Boley, P., Kuiper, R., Keto, E., Hoare, M.G. & van Boekel, R. (2015). A keplerian-like disk around the forming o-type star afgl 4176. *The Astrophysical Journal Letters*, **813**, L19.

Keto, E. (1990). Radiative transfer modeling of radio-frequency spectral line data-accretion onto g10. 6-0.4. *The Astrophysical Journal*, **355**, 190–196.

Keto, E. & Rybicki, G. (2010). Modeling molecular hyperfine line emission. *The Astrophysical Journal*, **716**, 1315.

Keto, E., Rybicki, G.B., Bergin, E.A. & Plume, R. (2004). Radiative transfer and starless cores. *The Astrophysical Journal*, **613**, 355.

Kim, K.T. & Koo, B.C. (2001). Radio continuum and recombination line study of ultracompact h ii regions with extended envelopes. *The Astrophysical Journal*, **549**, 979.

Kim, K.T. & Koo, B.C. (2003). Molecular counterparts of ultracompact h ii regions with extended envelopes. *The Astrophysical Journal*, **596**, 362.

Krumholz, M.R., McKee, C.F. & Klein, R.I. (2005). A unified model for accretion and turbulence in self-gravitating protostellar disks. *The Astrophysical Journal*, **618**, 757–769.

Krumholz, M.R., Klein, R.I. & McKee, C.F. (2009). Radiation feedback, fragmentation, and the environmental dependence of the stellar initial mass function. *Science*, **323**, 754–757.

Krumholz, M.R., McKee, C.F. & Bland-Hawthorn, J. (2019). Star Clusters Across Cosmic Time. *Annual Review of Astronomy and Astrophysics*, **57**, 227–303.

Kuiper, R. & Hosokawa, T. (2018). First hydrodynamics simulations of radiation forces and photoionization feedback in massive star formation. *Astronomy & Astrophysics*, **616**, A101.

Kuiper, R., Klahr, H., Beuther, H. & Henning, T. (2011). Radiation pressure feedback in the formation of massive stars. *The Astrophysical Journal*, **732**, 20.

Kurtz, S. (2005). Hypercompact hii regions. *Proceedings of the International Astronomical Union*, **1**, 111–119.

Kurtz, S., Churchwell, E. & Wood, D. (1994). Ultracompact h ii regions. 2: New high-resolution radio images. *The Astrophysical Journal Supplement Series*, **91**, 659–712.

Kurtz, S., Cesaroni, R., Churchwell, E., Hofner, P. & Walmsley, C.M. (2000). Hot molecular cores and the earliest phases of high-mass star formation. *Protostars and Planets IV*, **299**.

Lada, C.J. & Lada, E.A. (2003). Embedded clusters in molecular clouds. *Annual Review of Astronomy and Astrophysics*, **41**, 57–115.

Larson, R.B. (1969). Numerical calculations of the dynamics of a collapsing proto-star. *Monthly Notices of the Royal Astronomical Society*, **145**, 271–295.

Li, Z.Y., Banerjee, R., Pudritz, R.E., Jørgensen, J.K., Shang, H., Krasnopolsky, R. & Maury, A. (2014). The Earliest Stages of Star and Planet Formation: Core Collapse, Disk Formation, and Protostellar Outflows. In H. Beuther, R.S. Klessen, C.P. Dullemond & T. Henning, eds., *Protostars and Planets VI*, 173–194, University of Arizona Press.

Lumsden, S. & Hoare, M. (1996). An ir study of the velocity structure of the cometary compact hii region g29. 96-0.02. *arXiv preprint astro-ph/9603114*.

Lumsden, S. & Hoare, M. (1999). Molecular and ionized gas motions in the compact h ii region g 29.96-0.02. *Monthly Notices of the Royal Astronomical Society*, **305**, 701–706.

Mac Low, M.M. & Klessen, R.S. (2004). Control of star formation by supersonic turbulence. *Reviews of modern physics*, **76**, 125.

Mac Low, M.M., Van Buren, D., Wood, D.O. & Churchwell, E. (1991). Bow shock models of ultracompact h ii regions. *The Astrophysical Journal*, **369**, 395–409.

Machida, M.N. & Hosokawa, T. (2020). Failed and delayed protostellar outflows with high-mass accretion rates. *Monthly Notices of the Royal Astronomical Society*, **499**, 4490–4514.

Martín-Hernández, N., Bik, A., Kaper, L., Tielens, A. & Hanson, M. (2003). A vlt spectroscopic study of the ultracompact h ii region g29. 96-0.02. *Astronomy & Astrophysics*, **405**, 175–188.

Martín-Pintado, J., Gaume, R., Bachiller, R., Johnston, K. & Planesas, P. (1993). Simulated ratio recombination line emission at 1.3 centimeters toward mwc 349. *The Astrophysical Journal*, **418**, L79.

McKee, C.F. & Ostriker, E.C. (2007). The theory of massive star formation. *Annual Review of Astronomy and Astrophysics*, **45**, 565–687.

McKee, C.F. & Tan, J.C. (2003). The formation of massive stars by accretion. *The Astrophysical Journal*, **585**, 850–871.

Mellema, G., Arthur, S.J., Henney, W.J., Iliev, I.T. & Shapiro, P.R. (2006a). Dynamical effects of ionizing radiation on molecular clouds. *The Astrophysical Journal*, **647**, 397–405.

Mellema, G., Iliev, I.T., Alvarez, M.A. & Shapiro, P.R. (2006b). C2-ray: A new method for photon-conserving transport of ionizing radiation. *New Astronomy*, **11**, 374–395.

Mezger, P. & Henderson, A. (1967). Galactic h ii regions. i. observations of their continuum radiation at the frequency 5 ghz. *The Astrophysical Journal*, **147**, 471.

Miao, J., White, G.J., Nelson, A.J., Thompson, M.A. & Morgan, L.K. (2006). Triggered star formation by ionizing radiation. i. the process of radiation-driven implosion. *Monthly Notices of the Royal Astronomical Society*, **369**, 143–155.

Motte, F., Bontemps, S., Schilke, P., Schneider, N., Menten, K. & Broguiere, D. (2007). The earliest phases of high-mass star formation: a 3 square degree millimeter continuum mapping of cygnus x. *Astronomy & Astrophysics*, **476**, 1243–1260.

Motte, F., Bontemps, S. & Louvet, F. (2018). High-mass star and massive cluster formation in the milky way. *Annual Review of Astronomy and Astrophysics*, **56**, 41–82.

Mottram, J.C., Hoare, M.G., Davies, B., Lumsden, S.L., Oudmaijer, R.D., Urquhart, J.S., Moore, T.J., Cooper, H.D. & Stead, J.J. (2011). The rms survey: the luminosity functions and timescales of massive young stellar objects and compact h ii regions. *The Astrophysical Journal Letters*, **730**, L33.

Olmi, L., Cesaroni, R., Hofner, P., Kurtz, S., Churchwell, E. & Walmsley, C. (2003). High resolution observations of the hot core in g29. 96–0.02. *Astronomy & Astrophysics*, **407**, 225–235.

Osterbrock, D. & Ferland, G. (2006). *Astrophysics of Gaseous Nebulae and Active Galactic Nuclei*. University Science Books.

Pascale, E., Auld, R., Dariush, A., Dunne, L., Eales, S., Maddox, S., Panuzzo, P., Pohlen, M., Smith, D., Buttiglione, S. *et al.* (2011). The first release of data from the herschel atlas: the spire images. *Monthly Notices of the Royal Astronomical Society*, **415**, 911–917.

Peretto, N. & Fuller, G. (2010). A statistical study of the mass and density structure of infrared dark clouds. *The Astrophysical Journal*, **723**, 555.

Peters, T., Longmore, S.N. & Dullemond, C.P. (2012). Understanding hydrogen recombination line observations with alma and evla. *Monthly Notices of the Royal Astronomical Society*, **425**, 2352–2368.

Pilbratt, G., Riedinger, J., Passvogel, T., Crone, G., Doyle, D., Gageur, U., Heras, A., Jewell, C., Metcalfe, L., Ott, S. *et al.* (2010). Herschel space observatory-an esa facility for far-infrared and submillimetre astronomy. *Astronomy & Astrophysics*, **518**, L1.

Rathborne, J.M., Jackson, J. & Simon, R. (2006). Infrared dark clouds: precursors to star clusters. *The Astrophysical Journal*, **641**, 389.

Reid, M. & Ho, P. (1985). G34. 3+ 0.2-a'cometary'h ii region. *The Astrophysical Journal*, **288**, L17–L19.

Roelfsema, P., Goss, W. & Geballe, T. (1989). Infrared and radio recombination line observations of dr 21. *Astronomy and Astrophysics*, **222**, 247–263.

Rosen, A.L. & Krumholz, M.R. (2020). The role of outflows, radiation pressure, and magnetic fields in massive star formation. *The Astronomical Journal*, **160**, 78.

Roy, A., Ade, P.A., Bock, J.J., Chapin, E.L., Devlin, M.J., Dicker, S.R., France, K., Gibb, A.G., Griffin, M., Gundersen, J.O. *et al.* (2011). The balloon-borne large aperture submillimeter telescope (blast) 2005: A 10 deg2 survey of star formation in cygnus x. *The Astrophysical Journal*, **727**, 114.

Rygl, K., Brunthaler, A., Sanna, A., Menten, K., Reid, M., Van Langevelde, H., Honma, M., Torstensson, K. & Fujisawa, K. (2012). Parallaxes and proper motions of interstellar masers toward the cygnus x star-forming complex-i. membership of the cygnus x region. *Astronomy & Astrophysics*, **539**, A79.

Ryle, M. & Downes, D. (1967). High-resolution radio observations of an intense h ii region in cygnus x. *Astrophysical Journal, vol. 148, p. L17*, **148**, L17.

Salem, M. & Brocklehurst, M. (1979). A table of departure coefficients from thermodynamic equilibrium/bn factors/for hydrogenic ions. *The Astrophysical Journal Supplement Series*, **39**, 633–651.

Salem, M. & Brocklehurst, M. (1980). *The Astrophysical Journal*, **305**, 862.

Schneider, N., Csengeri, T., Bontemps, S., Motte, F., Simon, R., Hennebelle, P., Federrath, C. & Klessen, R. (2010). Dynamic star formation in the massive dr21 filament. *Astronomy & Astrophysics*, **520**, A49.

Schuller, F., Menten, K., Contreras, Y., Wyrowski, F., Schilke, P., Bronfman, L., Henning, T., Walmsley, C., Beuther, H., Bontemps, S. *et al.* (2009). Atlasgal–the apex telescope large area survey of the galaxy at 870

\

mathsf {\mu} *m.Astronomy&Astrophysics*, **504**, 415 − −427.

Seaton, M. (1964). Recombination spectra: Iii. populations of highly excited states. *Monthly Notices of the Royal Astronomical Society*, **127**, 177–184.

Sejnowski, T. & Hjellming, R.M. (1969). The general solution of the b_ {n} problem for gaseous nebulae. *The Astrophysical Journal*, **156**, 915.

Sewilo, M., Churchwell, E., Kurtz, S., Goss, W. & Hofner, P. (2011). A vla study of ultracompact and hypercompact h ii regions from 0.7 to 3.6 cm. *arXiv preprint arXiv:1105.1107*.

Shaver, P. (1975). *Astronomy and Astrophysics*, **43**, 465.

Shu, F.H., Adams, F.C. & Lizano, S. (1987). Star formation in molecular clouds-observation and theory. *IN: Annual review of astronomy and astrophysics.*

Volume 25 (A88-13240 03-90). Palo Alto, CA, Annual Reviews, Inc., 1987, p. 23-81. NASA-sponsored research., **25**, 23–81.

Shu, F.H., Najita, J., Ostriker, E.C., Wilkin, F., Ruden, S.P. & Lizano, S. (1994). Magnetocentrifugally driven flows from young stars and disks. i. a generalized model. *The Astrophysical Journal*, **429**, 781–796.

Smith, N. (2010). The carina nebula: A laboratory for feedback and triggered star formation. *The Astrophysical Journal*, **711**, L44–L48.

Smith, N., Bally, J. & Walborn, N.R. (2010). The eagle nebula and pillars of creation revisited with hubble 2009: Hst/wfc3 emission line imaging. *Monthly Notices of the Royal Astronomical Society*, **406**, 952–973.

Solomon, P., Rivolo, A., Barrett, J. & Yahil, A. (1987). Mass, luminosity, and line width relations of galactic molecular clouds. *Astrophysical Journal, Part 1 (ISSN 0004-637X), vol. 319, Aug. 15, 1987, p. 730-741.*, **319**, 730–741.

Sorochenko, R. & Borozich, L. (1964). *Soviet Astronomy*, **7**, 778.

Stahler, S.W., Shu, F.H. & Taam, R.E. (1980). The evolution of protostars. i-global formulation and results. *Astrophysical Journal, Part 1, vol. 241, Oct. 15, 1980, p. 637-654. NSF-supported research.*, **241**, 637–654.

Steggles, H. (2016). *Ultra-compact HII regions*. Ph.D. thesis, University of Leeds.

Steggles, H., Hoare, M. & Pittard, J. (2017). Hydrodynamical models of cometary h ii regions. *Monthly Notices of the Royal Astronomical Society*, **466**, 4573–4591.

Storey, P. & Hummer, D. (1995). Recombination line intensities for hydrogenic ions-iv. total recombination coefficients and machine-readable tables for z= 1 to 8. *Monthly Notices of the Royal Astronomical Society*, **272**, 41–48.

Strang, G. (1968). On the construction and comparison of difference schemes. *SIAM journal on numerical analysis*, **5**, 506–517.

Tan, J.C., Beltrán, M.T., Caselli, P., Fontani, F., Fuente, A., Krumholz, M.R., McKee, C.F. & Stolte, A. (2014). Massive star formation. *Protostars and Planets VI*, **149**.

Teixeira, P.S., Lada, C.J. & Alves, J.F. (2005). From dusty filaments to cores to stars: An infrared extinction study of lupus 3. *The Astrophysical Journal*, **629**, 276.

Tenorio-Tagle, G. (1979). The gas dynamics of h ii regions. i-the champagne model. *Astronomy and Astrophysics*, **71**, 59–65.

Tigé, J., Motte, F., Russeil, D., Zavagno, A., Hennemann, M., Schneider, N., Hill, T., Luong, Q.N., Di Francesco, J., Bontemps, S. *et al.* (2017). The earliest phases of high-mass star formation, as seen in ngc 6334 by herschel-hobys. *Astronomy & Astrophysics*, **602**, A77.

Urquhart, J., Moore, T., Schuller, F., Wyrowski, F., Menten, K., Thompson, M., Csengeri, T., Walmsley, C., Bronfman, L. & König, C. (2013). Atlasgal–environments of 6.7 ghz methanol masers. *Monthly Notices of the Royal Astronomical Society*, **431**, 1752–1776.

Van Buren, D. & Mac Low, M.M. (1992). Bow shock models for the velocity structure of ultracompact h ii regions. *The Astrophysical Journal*, **394**, 534–538.

Van Buren, D., Mac Low, M.M., Wood, D.O. & Churchwell, E. (1990). Cometary compact h ii regions are stellar-wind bow shocks. *The Astrophysical Journal*, **353**, 570–578.

van der Tak, F.F., van Dishoeck, E.F., Evans II, N.J. & Blake, G.A. (2000). Structure and evolution of the envelopes of deeply embedded massive young stars. *The Astrophysical Journal*, **537**, 283.

Viner, M., Vallée, J. & Hughes, V. (1979). A theoretical study of the radio recombination line and continuum emission from compact inhomogeneous h ii regions. *The Astrophysical Journal Supplement Series*, **39**, 405–428.

Vink, J.S., de Koter, A. & Lamers, H. (2001). Mass-loss predictions for o and b stars as a function of metallicity. *Astronomy & Astrophysics*, **369**, 574–588.

Walborn, N.R., Maíz-Apellániz, J. & Barbá, R.H. (2002). Further insights into the extraordinary hubble space telescope ionization front images in m16. *The Astronomical Journal*, **124**, 1601–1613.

Walsh, A., Burton, M., Hyland, A. & Robinson, G. (1998). Studies of ultracompact h ii regionsâ€"ii. high-resolution radio continuum and methanol maser survey. *Monthly Notices of the Royal Astronomical Society*, **301**, 640–698.

Ward-Thompson, D. & Whitworth, A.P. (2011). *An introduction to star formation*. Cambridge University Press.

Whitworth, A.P., Bhattal, A.S., Chapman, S.J., Disney, M.J., Turner, J.A. & Watson, A.M. (1994). Preferential formation of massive stars in shock-compressed layers. *Monthly Notices of the Royal Astronomical Society*, **268**, 291–298.

Wilson, T., Rohlfs, K. & HÃ¼ttemeister, S. (2013). *Tools of Radio Astronomy*. Springer.

Wood, D.O. & Churchwell, E. (1989a). Massive stars embedded in molecular clouds-their population and distribution in the galaxy. *The Astrophysical Journal*, **340**, 265–272.

Wood, D.O. & Churchwell, E. (1989b). The morphologies and physical properties of ultracompact h ii regions. *The Astrophysical Journal Supplement Series*, **69**, 831–895.

Wood, D.O. & Churchwell, E. (1991). The dynamics and physical properties of the cometary nebula g29. 96-0.02. *The Astrophysical Journal*, **372**, 199–207.

Wynn-Williams, C. (1971). Radio maps of condensations in h ii regions. *Monthly Notices of the Royal Astronomical Society*, **151**, 397–420.

Yorke, H., Tenorio-Tagle, G. & Bodenheimer, P. (1983). Theoretical radio continuum maps of h ii regions in the champagne phase. *Astronomy and Astrophysics*, **127**, 313–319.

Yorke, H.W. & Sonnhalter, C. (2002). Formation of massive stars: A computational study. *The Astrophysical Journal*, **569**, 846–862.

Zavagno, A., Anderson, L.D., Russeil, D. & Molinari, S. (2010). Star formation triggered by the expansion of h ii regions. *Astronomy & Astrophysics*, **518**, L101.

Zhang, Q., Wang, K., Lu, X. & Jiménez-Serra, I. (2014). Hot molecular core to hypercompact hii region: Massive star formation at core scale. *The Astrophysical Journal*, **788**, 166.

Zhu, Q.F., Lacy, J.H., Jaffe, D.T., Richter, M.J. & Greathouse, T.K. (2005). Mass flows in cometary ultracompact h ii regions. *The Astrophysical Journal*, **631**, 381.

Zinnecker, H. & Yorke, H.W. (2007). Toward understanding massive star formation. *Annual Review of Astronomy and Astrophysics*, **45**, 481–563.